Research@ARL

The International Year of Light

INTERNATIONAL YEAR OF LIGHT 2015

Volume 4, Issue 1,
November 2015

Dr. Kwong-Kit Choi
and Dr. Joseph N. Mait
Editors-in-Chief

U.S. Army Research Laboratory

Editorial Board

Dr. Kwong-Kit Choi
Editor-in-Chief

Dr. Joseph N. Mait
Editor-in-Chief

Advisory Board

Dr. Kwong K. Choi

Dr. Brad E. Forch

Dr. Piotr J. Franaszczuk

Dr. Shashi P. Karna

Dr. Stephen J. Lee

Dr. Joseph N. Mait

Dr. Peter J. Reynolds

Dr. Ananthram Swami

Dr. Bruce J. West

Research@ARL can be accessed electronically at **www.arl.army.mil/ResearchARL**

Research@ARL

The International Year of Light • 2015

contents

Introduction to ARL 2

Foreword 3
Thomas Russell, Director

Introduction to the International Year of Light 4

Resonantly Pumped Single-Mode Channel Waveguide Er:YAG Laser with Nearly Quantum Defect Limited Efficiency 11
N. Ter-Gabrielyan, V. Fromzel, X. Mu, H. Meissner, and M. Dubinskiy

Conversion of Above- and Below-Bandgap Photons via InAs Quantum Dot Media Embedded into GaAs Solar Cell 15
K. Sablon, J. Little, N. Vagidov, Y. Li, V. Mitin, and A. Sergeev

P-type Interface Charge Control Layers for Enabling GaN/SiC Separate Absorption and Multiplication Avalanche Photodiodes 21
A. V. Sampath, Q. G. Zhou, R. W. Enck, D. McIntosh, H. Shen, J. C. Campbell, and M. Wraback

C-QWIPs for Space Exploration 27
K. K. Choi, M. D. Jhabvala, D. P. Forrai, J. Sun, and D. Endres

Detection and Characterization of Biological and Other Organic-Carbon Aerosol Particles in Atmosphere Using Fluorescence 35
Yong-Le Pan

Influence of Molecular Structure on the Laser-Induced Plasma Emission of the Explosive RDX and Organic Polymers 61
Frank C. De Lucia, Jr. and Jennifer L. Gottfried

A Nanosensor for TNT Detection Based on Molecularly Imprinted Polymers and Surface Enhanced Raman Scattering 71
Ellen L. Holthoff, Dimitra N. Stratis-Cullum and Mikella E. Farrell

Constellation Design for Channel Precompensation in Multi-Wavelength Visible Light Communications 87
Robert J. Drost, and Brian M. Sadler

Simple and efficient absorption filter for single photons from a cold atom quantum memory 99
Daniel T. Stack, Patricia J. Lee, and Qudsia Quraishi

Biographies of ARL Authors 111

Introduction to ARL

The Army Research Laboratory of the U.S. Army Research, Development and Engineering Command (RDECOM) is the Army's corporate laboratory. ARL's research continuum focuses on basic and applied research (6.1 and 6.2) and survivability/lethality and human factors analysis (6.6). ARL also applies the extensive research and analysis tools developed in its direct mission program to support ongoing development and acquisition programs in the Army Research, Development and Engineering Centers (RDECs), Program Executive Offices (PEOs)/Program Manager (PM) Offices, and Industry. ARL has consistently provided the enabling technologies in many of the Army's most important weapons systems.

The Soldiers of today and tomorrow depend on us to deliver the scientific discoveries, technological advances, and the analyses that provide Warfighters with the capabilities to execute full-spectrum operations. ARL has Collaborative Technology Alliances in Micro Autonomous Systems Technology, Robotics, Cognition and Neuroergonomics, Network Science, an International Technology Alliance and new Collaborative Research Alliances in Multiscale Multidisciplinary Modeling of Electronic Materials and Materials in Extreme Environments. ARL's diverse assortment of unique facilities and dedicated workforce of government and private sector partners make up the largest source of world class integrated research and analysis in the Army.

ARL Mission

Discover, Innovate, and Transition Science and Technology to Ensure Dominant Strategic Land Power.

Our Vision

The Nation's Premier Laboratory for Land Forces.

ARL's Organization

- Army Research Office (ARO) - Initiates the scientific and far reaching technological discoveries in extramural organizations: educational institutions, nonprofit organizations, and private industry.
- Computational and Information Sciences Directorate - Scientific research and technology focused on information processing, network and communication sciences, information assurance, battlespace environments, and advanced computing that create, exploit, and harvest innovative technologies to enable knowledge superiority for the Warfighter.
- Human Research and Engineering Directorate - Scientific research and technology directed toward optimizing Soldier performance and Soldier-machine interactions to maximize battlefield effectiveness and to ensure that Soldier performance requirements are adequately considered in technology development and system design.
- Sensors and Electron Devices Directorate - Scientific research and technology in electro-optic smart sensors, multifunction radio frequency (RF), autonomous sensing, power and energy, and signature management for reconnaissance, intelligence, surveillance, target acquisition (RISTA), fire control, guidance, fuzing, survivability, mobility, and lethality.
- Survivability/Lethality Analysis Directorate - Integrated survivability and lethality analysis of Army systems and technologies across the full spectrum of battlefield threats and environments as well as analysis tools, techniques, and methodologies.
- Vehicle Technology Directorate - Scientific research and technology addressing propulsion, transmission, aeromechanics, structural engineering, and robotics technologies for both air and ground vehicles.
- Weapons and Materials Research Directorate - Scientific research and technology in the areas of weapons, protection, and materials to enhance the lethality and survivability of the Nation's ground forces.

ARL Workforce in 2015

- 1,820 Civilians - 28 Military
- 1,139 Contractors (1,101 full-time/38 part-time)
- 1,303 Research Performing Workforce
- 544 (42%) hold PhDs
- 34 STs / 20 ARL Fellows

ARL's Primary Sites

- Aberdeen Proving Ground, MD
- Adelphi Laboratory Center, MD
- White Sands Missile Range, NM
- Raleigh-Durham, NC
- Orlando, FL

Visit ARL's web site at **www.arl.army.mil**

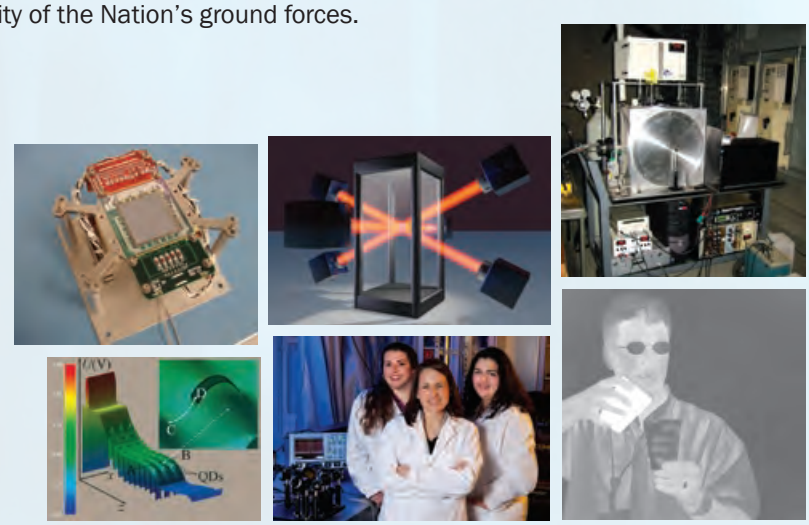

Unique ARL laboratory facilities and modeling capabilities provide our scientists and engineers with a world-class research environment.

ARL
U.S. ARMY RESEARCH LABORATORY

FOREWORD

Thank you for your interest in this latest edition of Research@ARL. This compendium is part of a series that represents the best efforts of the U.S. Army Research Laboratory (ARL). Each volume contains previously published peer-reviewed journal articles in a particular area.

This volume of Research@ARL highlights recent contributions in light-based technology being made by ARL researchers. In recognition of the central role light plays in our lives, the UN General Assembly 68th Session dedicated the year 2015 as the International Year of Light and Light-based Technologies (IYL 2015). As part of that celebration, ARL considered the role that the science and application of light has had in national defense. Significantly, ARL's predecessor organizations developed technologies in the 1950s and 1960s that allow us to see in the dark, giving the U.S. military a strategic warfighting advantage. The legacy of this work is evident in ARL's on-going contributions to infrared photodetection.

At its most fundamental level, light delivers energy from one place to another. If this energy is encoded in some fashion, light carries information and, as an information carrier, light can be used either to sense or to communicate. This volume presents papers in all of these areas: the generation of light energy; the detection of light energy; the use of light to measure and sense; and the use of light to communicate.

Our researchers take extreme pride in the quality of their work. The dedication of ARL staff to the lab's mission and that of the U.S. Army provides enhanced capabilities for our Soldiers, and influences the way the U.S. Army will operate 10, 20, and even 30 years from now.

I hope you will enjoy perusing the articles on light contained in this volume. After doing so, I'm sure you'll appreciate the advances our scientists and engineers are making to ensure our Army remains technologically superior.

Dr. Thomas P. Russell
Director, U.S. Army Research Laboratory

Introduction to the International Year of Light

All of us began our interaction with light when we first glimpsed the world. Since then, we rely upon light to bring us brightness and beauty, warmth and joy. Prompted by these comfortable feelings, one cannot help but ponder, "What is light?" Why is there something that we can see and feel but not catch and hold? The quest to understand its nature has not only fascinated scientists at every turn but also helped us uncover many of nature's deepest secrets. Each new level of understanding has inspired new applications that have changed the world. It is as though God created light not only to let us appreciate and understand his creation but also to make our lives better.

In recognition of the central role light plays in our lives, the UN dedicated the year 2015 as the International Year of Light and Light-based Technologies (IYL 2015). This year, citizens all over the world will celebrate light and light-based technologies.

As part of that celebration, the US Army Research Laboratory (ARL) has considered the role that the science and application of light has had in national defense. We commemorate IYL 2015 by publishing this research volume to recognize the contribution of light-based technologies to our mission. Indeed, optical technology provides the Army with many critical capabilities. The military's ability to "own the night" during Operation Desert Storm is the most noteworthy but there exist many others. As the premier national laboratory in utilizing and advancing light-based technologies for land power, ARL engages in a wide range of optical research that has both short- and long-term implications.

Researchers at ARL address the current needs of our military by exploiting the present understanding of light generation, propagation, light-and-matter interaction, and applying their knowledge and experience in system integration and signal processing. But ARL also strives to provide new capabilities in lethality and protection, sensors and communications, and positioning, navigation, and timing for maneuver by exploring new scientific frontiers in quantum optics, cold-atom optics, transformation optics, metamaterials, photonic crystals, nano-photonics and plasmonics. While ARL's technologies are used primarily for national defense, many will predictably contribute to solving global challenges in health, medicine, and even food safety.

At its most fundamental level, light delivers energy from one place to another. If this energy is encoded in some fashion, light also carries information and, as an information carrier, light can be used either to sense or to communicate. In this volume we present papers in all of these areas: the generation of light energy, the detection of light energy, the use of light to measure and sense, and the use of light to communicate. In the following, we provide short descriptions of recent research on light-based technologies and applications performed by ARL researchers.

1. Light Energy: Generation

1. Eye-safe solid state laser for free space application

The invention of the laser was a key milestone in mankind's engagement with light. The laser enables us to produce beams of light that propagate relatively unchanged over large distances, for example, to the moon and back, and we can generate laser light across a broad spectrum that extends from the deep ultraviolet to the long infrared. Another significant capability made possible through the invention of the laser is the generation of ultrashort light pulses on the order of femtoseconds or 10^{-15} seconds. Scientists have used such short pulses to increase our physical understanding of the interaction between light and matter.

Lasers that emit radiation with wavelengths longer than 1.4 micrometers are referred to as eye-safe because the radiation is strongly absorbed in the eye's cornea and lens and, therefore, cannot reach the highly sensitive and damage-prone retina. Given the Protocol on Blinding Laser Weapons, which bans the use of laser weapons designed specifically to cause permanent blindness to unenhanced vision, eye-safe lasers play a critically important role in military applications, such as rangefinders and designators, as well as in commercial applications, such as free-space communications and remote sensing.

To produce laser radiation, a material is excited from its lowest energy state into a higher state using an external optical source called a pump. To return to its low energy state, the material lases, or releases a photon to carry away the excess energy. The photon wavelength is a function of the energy in the material's ground state, its excited state, and the energy in the pump. The materials of choice to produce eye-safe radiation are Ytterbium (Yb) for the pump and Erbium (Er) for the lasing material.

Unfortunately, the energy levels between these two materials are such that the mechanisms to produce 1.6 micrometer radiation from a 0.98 micrometer pump are inefficient and create significant excessive heat. This complicates thermal management and leads to large, power-consuming cooling systems to manage heat. The imperfect mode matching between the pump and laser cavity further reduces the efficiency of such lasers.

ARL increased the power efficiency of the lasing process using yttrium aluminum garnet (YAG) as the pump material. Since the wavelength of a YAG pump matches closely the wavelength of the laser output, a condition referred to as resonant pumping, the pump-lase process becomes more efficient. ARL further increased the efficiency of the process by using a channel to guide the pump radiation in the gain medium and, thereby, increase the interaction between the two to improve mode matching.

ARL reported these results in the paper Ter-Gabrielyan et al, Opt. Lett. 2013, 38, 2431-2433. ARL's eye-safe solid-state laser produced coherent radiation at 1.645 micrometers with diffraction-limited beam quality and nearly quantum defect limited optical efficiency. The demonstrated efficiency of 92.8 percent is the highest ever reported for an eye-safe solid-state laser. This achievement offers the potential for considerable reductions, potentially three-fold, in size, weight and power consumption for eye-safe laser systems, and enables the development of man-portable devices for ladar, range finding, and target designation.

2. Light Energy: Detection

1. Quantum dot solar cell for broad-spectrum conversion

The Army's dependence on fossil fuel is deemed a strategic risk. Measures to mitigate this risk are being explored, including the use of renewable energy sources. Within the set of renewable sources, photovoltaic technologies represent a potential solution. Using solar energy to generate power can potentially reduce the number of batteries carried by dismounted Soldiers during an unsupplied 72 hour mission and, hence, reduce the associated weight burden.

Although there has been considerable research on the application of traditional semiconductor materials, like silicon and gallium arsenide, to photovoltaics, improvements in the performance of such materials are becoming harder to achieve as the materials near the fundamental limits on their performance. To improve energy conversion further requires materials with strong and tunable absorption and the ability to convert optical energy into electric current efficiently. It is practically impossible to achieve these properties simultaneously in homogenous materials.

Alternatively, if nanocrystalline materials, such as quantum dots (QDs), are integrated into homogeneous materials, light absorption can be enhanced while providing numerous possibilities to engineer electron processes. This makes them an attractive alternative for energy conversion applications. In fact, QD technologies show great potential to improve the performance of solar cells by reducing several loss mechanisms commonly associated with traditional material systems.

Unfortunately, the performance of QD devices has not met expectations. This is due primarily to an incomplete understanding of their electronic processes, for example, their complex band structure, electron transitions, and nonequilibrium processes. For example, the kinetics of electrons and phonons in QDs and in the spaces between quantum dots plays a critical role in photovoltaic power conversion.

To bridge this gap in understanding, as well as push the state of the art, ARL, in collaboration with the University at Buffalo, proposed a new device based on a quantum mechanical design of charged quantum dots. The design uses selective doping of the material between quantum dots to create a potential barrier. This allows greater control of the kinetics of electron processes than previously possible.

Increased control of electron processes reduces energy losses due to three different mechanisms (alignment of bandgap transitions to the solar spectrum, thermalization, and recombination) and increases the efficiency with which solar energy is converted to electrical current. Each of these is achieved via engineering the nanostructure of the device materials. Using this technique, ARL has developed new QD solar cell structures that have achieved record conversion efficiency (Sablon et al, Appl. Phys. Lett. 2014, 104, 253904).

ARL's research has shown that nanocrystalline materials are a viable material base for photovoltaic systems and, further, that device performance can be enhanced through nanoscale engineering.

2. Ultra-violet avalanche photodiode for bio-fluorescence detection and identification

In comparison to other techniques for sensing biological agents in the air or water, optical approaches operate in real-time and without requiring laboratory consumables or sample preparation. In scenarios where rapid response is required, for example, detect-to-warn, ultraviolet (UV) light spectroscopy is used. However, the development of systems that can be deployed as a network of place-and-forget sensors requires inexpensive semiconductor based UV light sources and detectors. Although UV light emitting diodes (LEDs) and man-portable lasers have addressed low-cost sources, inexpensive detectors remain an issue.

Photomultiplier tubes (PMTs) currently used as UV photodetectors can account for approximately a third of total system cost. Although PMTs offer the high gain and low noise that is critical for detecting very low optical signals, they are essentially vacuum tubes. They are fragile and easily damaged by exposure to ambient light. As a result, ARL has been actively researching semiconductor based UV sensitive avalanche photodiodes (APD) as a replacement for the PMT.

Semiconductor APDs are useful for bio-agent sensing due to their high internal gain, counting sensitivity on the order of a single photon, and low noise operation, but also for their compact, inherently rugged packaging, and low cost. Because the sensitivity and dark current performance of silicon-based APDs is generally poor in the UV spectrum, ARL has focused on wide band gap semiconductors that are more responsive in this band, such as silicon carbide (SiC) and III-Nitrides, which consist of nitrogen combined with an element from Group III of the periodic table.

Previous work by industry and academia has shown that III-Nitride-based detectors can have high quantum efficiency (QE) throughout the UV spectrum, but yield devices with high dark currents and only limited detector area. In contrast, SiC-based APDs exhibit high gain and low dark currents but high QE over only a narrow spectral range between 260-280 nanometers that is ill-suited for sensing biological agents.

In contrast to previous efforts, ARL, in collaboration with the University of Virginia, pursued the development of a device that combines both III-Nitrides with SiC APDs to leverage the advantages of each and, thereby, realize high sensitivity APDs throughout the UV spectrum. The paper in this volume (Sampath et al., Appl. Phys. Lett., 2012, 101, 093506) reports ARL's first demonstration of a GaN-SiC separate absorption multiplication (SAM) APD. The optimized GaN/SiC SAM APD exhibits large gain (>1000), dark currents comparable to the best homogenous SiC APDs, which are at least 3 orders of magnitude lower than the best GaN APDs, and active device areas at least 25 times greater than those reported for GaN APDs. This body of work demonstrates the promise for this innovative approach to provide high sensitivity APDs that operate throughout the ultraviolet spectrum and, thereby, remove a critical limitation to enabling low cost, field-able UV-sensing for Army and civilian applications.

3. Quantum well infrared photodetector for space exploration

With its surface temperature at about 5000° C, our sun emits radiation predominantly in the visible spectrum. Consequently, humans have adapted to see in these wavelengths. By comparison, objects on the earth are typically only a few tens of degrees Celsius. At these temperatures, objects, including the earth, shine in the infrared (IR) regime, whose wavelengths are roughly twenty times that of visible light. If a person could see at all wavelengths, they would see that terrestrial objects appear their brightest in the IR spectrum.

If one wishes to identify the constituent materials of an object, it is advantageous to observe the object at wavelengths it emits, which are intrinsic to the object, rather than at wavelengths produced by an external source and reflected by the object. For one thing, the object's shape and brightness are independent of the environment and the conditions of the illumination. Further, the characteristics of the emitted spectrum help us significantly to identify the object's material constituents. This is important to many applications, such as identifying cancerous tumors in medical diagnostics, locating individuals during search and rescue, and understanding the impact of climate change on the environment. The ability to identify objects without an external source is extremely useful to the military for surveillance and for navigation under low-light or no-light conditions.

ARL performs research and development on advanced IR materials and detector architectures to enhance sensitivity, increase resolution, and create new capabilities for military applications, such as, wide area surveillance, unmanned aerial vehicle detection and tracking, and missile launch and intercept observations. Working primarily with radiation that has wavelengths between 8 and 12 micrometers (i.e., long wave IR), ARL achieved these capabilities using quantum wells in gallium arsenide (GaAs), as opposed to the more conventional technology based on bulk mercury cadmium telluride (MCT).

Quantum well infrared photodetectors (QWIPs) are a promising IR technology but they have one serious drawback. To produce an electrical signal, incident light must travel sideways—i.e., parallel to the material layers, which limits the efficiency with which incident light energy is converted to an electrical signal.

To overcome this weakness, we at ARL invented the corrugated quantum well infrared photodetector (C-QWIP). In the C-QWIP structure, 45-degree inclined detector sidewalls are engineered to reflect light into parallel propagation. Because reflection is independent of wavelength, the C-QWIP preserves the natural absorption spectrum of the material. Thus, not only does the C-QWIP increase the efficiency of energy conversion but it also allows the detector to be used over a broad range of wavelengths in the long IR.

The application of C-QWIP technology to the development of the Thermal Infrared Sensor (TIRS) for NASA's Landsat-8 Earth-observing satellite is described in the paper (Choi et al, Infra. Phys. & Tech., 2011, 54, 170–176) presented in this volume. The Landsat-8 was launched in February 2013 to monitor a wide range of earth and atmospheric parameters including cloud distribution, air quality, volcanic activity, biomass burning, industrial pollution in the atmosphere, insect breeding areas, climate change, water evaporation, crop species and health, and a variety of agricultural variables. ARL led the design of the detector material such that its optical absorption spectrum matched precisely the mission requirement to detect radiation with wavelengths between 10.5 and 12.5 micrometers. The C-QWIP can also play an important role in future studies of cold objects in space. The paper presents a C-QWIP design that will be useful for searching Jupiter's moon, Europa, for oceans of water and possible habitants.

The computational methods presented in this paper allowed ARL to model the propagation of light inside a three-dimensionally confined volume, which further enabled the ability to explain and predict quantitatively the optical properties of a QWIP. ARL subsequently used these methods to redesign the detector structure and increase its quantum efficiency to 70 percent, which is comparable to that of MCT-based technologies. With high efficiency and all the advantages of semiconductor processing, QWIP technology is now poised to provide increased capability in all IR applications.

3. Light Information Carrier - Sensor

1. Bio-detection based on laser-induced fluorescence signature

Spectacular natural phenomena such as rainbows, halos, and sunsets have long inspired human admiration and curiosity about sunlight and the sciences behind these phenomena. We now know that the beautiful colors displayed in these phenomena are caused by the presence of molecules, particles, droplets, and icy crystals suspended in the air. These particles interact with sunlight through different optical effects such as absorption, reflection, scattering, refraction, and diffraction, all of which give rise to a spectrum of colors under different environmental conditions. The prominence of each mechanism depends on the properties of the particles and the wavelength of light, and this mechanism may change in time when the particles undergo physical or chemical changes in air.

Besides the colorful display, atmospheric aerosol particles impact our lives at a physical level. They reduce visibility, nucleate cloud formation and determine its radiative properties, and redistribute the Earth's energy. The latter two factors affect long-term climate change. Further, some aerosol particles, such as bacteria, pollens, fungal spores, and viruses, are harmful to human health.

Consequently, it is imperative to detect and characterize aerosol particles suspended in the air. In particular, for the Army, we need to protect soldiers against the potential release of aerosolized chemical and biological agents onto the battlefield. This requires advances in science, technology, and instrumentation to detect and identify chemical and biological threats rapidly.

Although biochemical techniques can measure biological properties of aerosols accurately, they require a large quantity of samples. They are also time consuming and costly. In comparison, optical spectroscopic techniques are more efficient in detecting the presence of biological particles.

Optical techniques provide increased flexibility in measurement. Measurements can be made remotely or in situ. That is, an observer can opt to make real-time observations or detailed interrogations after samples are physically collected. Further, particles can be studied individually or collectively. For single particle measurements, individual particles are transported into an optical system where they are interrogated one-by-one, typically by a laser. Characterization can be performed either as particles flow by a detector, known as on-the-fly, or with particles being held stationary. The latter arrangement is necessary when optical signals emitted from the biological sample are weak and, therefore require more time for observation, or when the process under study is time varying.

However, without a means to hold and then release individual particles on a continual and repeatable basis, when stationary observations were desired, scientists had to manipulate individual particles manually. This is an inefficient process. It limits the number of particles one can study to only a few representatives out of a large collection of particles, which can be in the range of 1000's. Thus, continual monitoring is impossible.

To address this problem, ARL developed an optical system that can trap and release aerosol particles automatically. The system is capable of concentrating particles from the air, slow them down, capture and hold them for measurements, release them, and repeat the process for other particles. With this development, continual, real-time monitoring of aerosols is now a reality.

The paper presented in this volume (Pan, J. Quant. Spectr. & Rad. Trans., 2015, 150, 12-35) is an extensive overview of the state-of-the-art in detection and characterization of biological and organic-carbon aerosol particles. For bio-particle detection used as a bio-agent early warning trigger, most systems use laser-induced-fluorescence (LIF). LIF signatures, when combined with analytical techniques, enable the accurate detection, characterization, and identification of atmospheric aerosol particles. The overview covers the dispersed ultra-violet LIF spectra of the particles from different locations and different seasons; the comparison between these spectra and bioaerosol simulants; the absolute fluorescence cross-sections and spectral profiles between aerosolized live agents and the corresponding simulants; the change of properties of bioaerosol simulants under various atmospheric environments; and the developments of other related technologies.

2. Laser-induced breakdown spectroscopy for CBRNE threat detection

As mentioned previously, the laser is one of the most important inventions of the 20th century. Since its introduction in the early 1960s, the laser has become one of the most important light-based research tools for scientists. In particular, laser-based sensing of compounds for environmental, security, and industrial applications has become widespread. ARL is researching one such technique, laser-induced breakdown spectroscopy (LIBS), to detect chemical, biological, radiological, nuclear, and explosive (CBRNE) threats.

The recent wars in Afghanistan and Iraq made the threat of explosive devices to our warfighters abundantly clear. The ability to detect explosives in a timely manner is an extremely difficult problem, complicated by the myriad ways explosive devices can be configured and deployed. By focusing a laser pulse through the air onto a questionable object and analyzing, in real time, the subsequent emissions from that object, LIBS provides warfighters the ability to probe an area for the presence of explosive

materials from tens of meters away. The early warning provided by standoff detection, in contrast to proximate physical contact, reduces risk and increases soldier survivability.

LIBS uses a high-energy laser pulse to excite molecules in a sample material. When the pulse is over, the molecules return to their normal, low-energy state and, as they do, they release energy as light radiation. The wavelengths of light emitted are characteristic of the molecule. ARL is developing the analysis methods necessary to differentiate the signals due to the presence of explosive materials and any non-explosive background materials and other interferents.

In this paper (De Lucia and Gottfried, J. Phys. Chem. A, 2013, 117, 9555–9563), ARL explored the light emission from a laser-induced plasma formed on the explosive cyclotrimethylene trinitramine (RDX) and several non- explosive organic polymers. Light emitted from the plasma was spectrally and temporally resolved in order to identify the atomic, ionic, and molecular emissions from the ablated sample. ARL's challenge was to differentiate between the explosive and the non-explosive polymers, despite the fact that they share the same constituent atoms: carbon, hydrogen, nitrogen, and oxygen.

What distinguishes the compounds from one another is their molecular structure and composition. Since these characteristics are reflected in the atomic and molecular light emission collected from the plasma created by the laser pulse, ARL investigated whether the differences in emission characteristics were measurable with sufficient fidelity to distinguish between the two classes of materials.

In addition to performing a spectroscopic analysis of the emitted radiation, ARL also measured their decay rate. By combining spectroscopic and temporal measurements, ARL was, in fact, able to distinguish RDX from non-explosive materials. For example, ARL found that the molecular formation and subsequent decay of cyanide (a compound consisting of a carbon atom tripled bonded to a nitrogen atom) was much faster for RDX than for non-explosive materials that contained nitrogen. To mature this approach into a fieldable system, ARL is investigating the requirements on laser power and detector sensitivity to insure reliable classification as a function of distance.

3. Surface enhanced Raman scattering with molecularly imprinted polymers for chemical detection

Light-based technologies provide solutions to global challenges, including chemical sensing. Optical sensors play a vital role in military applications and a wide variety of optical techniques are being explored to detect and identify a range of chemical and explosive threats. An explosive of particular interest is 2,4,6-trinitrotolune (TNT). Although optical methodologies for TNT detection have been successfully employed, including fluorescent polymers and Raman spectroscopy, current capabilities have limitations. For example, these technologies may not always be specific or extendable to other chemical systems, and may only allow for bulk material assessment.

ARL researchers are exploring a variety of advanced optical detection and identification (i.e., spectroscopic) methods that aim to address many of the above limitations and provide the Warfighter with new strategies to achieve enhanced chemical sensing capabilities. For example, surface enhanced Raman scattering (SERS) is an extremely sensitive and selective spectroscopic technique that involves enhancements in the Raman scattering intensities of materials adsorbed on a roughened metal surface (typically, gold or silver). These enhancements can be up to 14 orders of magnitude as compared to spontaneous Raman scattering. SERS provides vibrational "fingerprint" spectra with unique chemical and structural information for a given species that can be used to determine material identity and, in some cases, even concentration. The detection capabilities of SERS make it an excellent transduction method for selective, full compound identification; however, SERS-based techniques alone have not typically proven to be useful for explosives detection. The primary concern is that any chemical components in close proximity to the metal-coated surface can potentially contribute to the resulting spectra, making real-world samples difficult to differentiate, even with advanced analysis tools.

In the paper (Holthoff et al., Sensors, 2011, 11, 2700–2714) presented in this volume, ARL reported on a method that increases the capability of SERS for explosive detection using molecularly imprinted polymers (MIPs) in combination with the spectroscopic technique. MIPs can be utilized as artificial recognition elements for target chemicals of interest. The MIP developed in this paper includes components that significantly improve selectivity and affinity for TNT. In chemical sensing applications, a MIP alone does not meet the requirements for a sensor without some form of detector. There is increasing evidence in the literature of a variety of optical detection techniques applied to convert a MIP into a sensor for TNT detection. In this paper, SERS was used as the detection method to achieve a high level of selectivity. By employing the developed approach, the MIP concentrates the target to the SERS-active metal surface, thereby making the combined approach more highly selective than a SERS-only detection platform and free from errors related to background or chemical interference.

The data presented in this paper suggest that it is possible to distinguish species similar to TNT based on their molecular composition, and therefore unique SERS spectral "fingerprints", thus successfully demonstrating the excellent selectivity of the MIP-SERS sensor. The first-generation integrated MIP-SERS sensor exhibits a reversible response to TNT and is stable in a variety of environments. The MIP showed excellent adhesion and stability, with no apparent degradation in sensing performance, which is necessary for practical field use. This research significantly advances the state of a MIP-SERS hybrid

sensing combination, allowing for the rapid, sensitive, and accurate detection of TNT in a novel operative, robust, stable, and reusable sensor modality. The results suggest that the MIP-SERS combination is an effective and robust chemical nanosensing scheme that can be extended to other chemical and explosive hazards.

4. Light Information Carrier - Communications

1. Optical communication using light-emitting diode

Motivated by advances in light-emitting diode (LED) technologies, ARL researchers have extensively studied the use of unconventional optical communications to provide the Warfighter with new means of communications and networking that can supplement traditional radio-frequency (RF) systems. Such capabilities may provide increased network throughput and robustness to challenging tactical communication environments that may include complex (e.g., urban or mountainous) terrain or RF congestion or denial. For example, the unique characteristics of the atmospheric propagation of deep-ultraviolet radiation make possible the novel capability of establishing non-line-of-sight (NLOS) optical communication links. ARL research into ultraviolet communications (UVC) has spanned from the theoretical and experimental characterization of the complex atmospheric propagation communication channel to the development of prototype systems. ARL published an extensive review on NLOS UVC (Drost and Sadler, Semicond. Sci. Technol., 2014, 29, 084006). Similarly, the use of visible-light LEDs for communications offers unique communication advantages and challenges, and ARL researchers have been equally active in exploring and developing this technology for the Warfighter.

Visible-light LEDs are particularly relevant to the 2015 International Year of Light and Light-based Technologies, which recognizes the critical importance of optical technologies to society in wide-ranging applications. For example, “the future development of society in both developed countries and emerging economies around the world [is] intimately tied up with the ability to effectively light our cities, homes, schools and recreation areas.” As “lighting represents nearly 20% of global energy consumption (International Energy Agency),” it is clear that improved efficiency of lighting devices can, through reduced demand, have a major impact on the environmental effects of energy production. Relative to traditional lighting sources, LEDs offer a significant reduction in energy consumption and environmental impact, and recent advances in LED technologies have resulted in LEDs being characterized as the light source of the future.

Communications and access to the internet are recognized as critical societal resources, and the ability to modulate visible-light LED lighting components provides an efficient method for wireless connectivity. In fact, LEDs can be used in a variety of applications, such as signage and vehicle headlights, all of which could be augmented with visible-light communications (VLC) functionality at virtually no energy cost. Such functionality could allow, e.g., convoys of vehicles or teams of robots to maintain network connectivity while sparing RF bandwidth, a potentially strained or unavailable resource.

For an LED that has a primary function of lighting, it is clear that the addition of VLC capabilities should not degrade the lighting quality. This is primarily achieved by modulating the LED at a sufficient rate so that the human eye cannot discern the fluctuations that carry information, instead sensing only the average output of the device. Hence, a VLC modulation scheme must be designed so that the average output is appropriately constrained, and additional design constraints (such as a constant-intensity constraint of color-shift keying) that distinguish VLC modulation from traditional RF modulation may also be present.

In the paper (Drost and Sadler, IEEE Trans. Commun., 2014, 62, 1995–2005) presented in this volume, ARL developed a general VLC system model that encompasses a broad range of system configurations and applications. A novel VLC modulation design approach is then proposed that respects imposed design constraints while optimizing communication performance given varying degrees of knowledge regarding the communication channel. Simulation results demonstrate the performance enhancement that can be achieved with this approach relative to standard modulation methods in the literature. Finally, an experimental system with modulation reprogrammability is described, and measurements taken with this system verify the simulation results, providing real-world evidence of the benefits of the proposed framework.

2. Single photon filter for quantum communication

Modern networks have revolutionized our ability to communicate and light has revolutionized communications. Consider the fiber optic connections that provide our homes with fast internet and cable television. Such networks require many components, from receivers and transmitters necessary to launch and receive information, to the storage of information at server locations, and to the connectivity to our homes enabled through fiber optics or free-space broadcast in the air.

Quantum networks improve upon these networks by providing enhanced security. Presently, when we transmit information, for example, in on-line purchases, we use data encryption to provide security. In theory, the encryption is always susceptible to compromise. In practice, strong encryption is used to insure that the time required to crack a code is so long that it becomes a deterrent.

In contrast, the security of a quantum network is embedded in the physics of its information transmission. The power of quantum information lies in its ability to entangle two or more physical systems. When systems are entangled, a change to

one causes all systems to change, even when they are far from one another. Thus, the presence of an unauthorized user on a quantum network is quickly evident.

A network of quantum devices processing information across multiple nodes offers significant advantages over present networking technology. For Army applications, we envisage quantum-enhanced remote sensing for improved imaging, eavesdrop evident communications for secure information transfer, timing synchronization at the quantum, not classical, limit for high-coordinated maneuvering, and networks of quantum sensors for unprecedented navigation accuracy. However, such capabilities lie well into the future. It is necessary first to demonstrate that quantum states are viable carriers of information.

ARL's goal is to develop the building blocks of a quantum network, beginning with an essential component, the node itself. A node must be capable of retrieving, storing, and processing information. We are interested in developing a so-called quantum memory, similar in function to the memory in a conventional computer.

To establish a two-node quantum network, we extract a single photon from a quantum memory. If this photon is entangled with the quantum memory, it carries information about the memory and, when detected (measured) in a different location, it casts the memory into a known quantum state.

A crucial aspect of a quantum network is the need to prepare and control the quantum memories using laser light with wavelengths typically in the 400-800 nm range. The quality of the optical beam in terms of its wavelength purity and noise affects the fidelity of the signal transmitted. In the paper presented in this volume (Stack, et al., Opt. Express, 2015, 23, 6822-6832), we demonstrated improved performance in a fiber-based quantum memory by filtering unwanted background light. This produced a beam with a cleaner signature than previously reported.

Summary

The International Year of Light highlights the importance of light in our daily lives, and also recognizes the tremendous possibilities ahead. ARL conducts a full range of optical research to improve Army capabilities. The above examples illustrate its central role in our mission. Our research into advanced optical materials has yielded highly efficient eye-safe lasers, solar cells, UV bio-detectors, and IR night vison sensors. We developed new precision optical measurement techniques to detect aerosolized chemical and biological agents and hidden explosives. We created new device functionality from common UV and visible-light LEDs to achieve tactical communications for soldiers, and networking and teaming for robots. We explored the quantum nature of light to build the foundation for an intrinsically secured communication network. These technologies, while intended for military applications, are undoubtedly useful to society. They can be used, for example, in renewable energy, humanitarian search and rescue, environmental protection, harmful bacterial detection, and ubiquitous secure communications. Therefore, our optical technologies also contribute to sustainable development and provide solutions to worldwide challenges in energy, education, agriculture, communications, and health as emphasized in the 2015 Year of the Light celebration.

Resonantly Pumped Single-Mode Channel Waveguide Er:YAG Laser with Nearly Quantum Defect Limited Efficiency

N. Ter-Gabrielyan, V. Fromzel, X. Mu, H. Meissner, and M. Dubinskiy

Optics Letters, 38 (2013)

Resonantly pumped single-mode channel waveguide Er:YAG laser with nearly quantum defect limited efficiency

N. Ter-Gabrielyan,[1,*] V. Fromzel,[1] X. Mu,[2] H. Meissner,[2] and M. Dubinskii[1]

[1]*US Army Research Laboratory, 2800 Powder Mill Rd., Adelphi, Maryland 20783, USA*

[2]*Onyx Optics, Inc., 6551 Sierra Lane, Dublin, California 94658, USA*

**Corresponding author: nikolay.e.ter-gabrielyan.civ@mail.mil*

Received April 19, 2013; revised May 31, 2013; accepted June 8, 2013;
posted June 10, 2013 (Doc. ID 189218); published July 5, 2013

We demonstrated the continuous-wave operation of a resonantly pumped Er:YAG single-mode channel waveguide laser with diffraction-limited output and nearly quantum defect limited efficiency. Using a longitudinally core-pumped, nearly square (61.2 μm × 61.6 μm) Er^{3+}:YAG waveguide embedded in an undoped YAG cladding, an output power of 9.1 W with a slope efficiency of 92.8% (versus absorbed pump power) has been obtained. To the best of our knowledge, this optical-to-optical efficiency is the highest ever demonstrated for a channel waveguide laser. © 2013 Optical Society of America

OCIS codes: (140.3580) Lasers, solid-state; (140.3500) Lasers, erbium; (230.7380) Waveguides, channeled.
http://dx.doi.org/10.1364/OL.38.002431

Fully crystalline channel waveguide lasers are very promising as efficient and compact sources for many laser applications requiring significant power scaling with nearly diffraction-limited beam quality. In a double-clad implementation, they are direct analogs of conventional (glass-based) fiber lasers with the same ability to maintain high clad-pump intensity and tight confinement of both pump and laser modes along the entire length of the gain medium. Analysis of conventional glass fiber laser power scaling [1,2] indicates that, due to low glass thermal conductivity, heat generation associated with pumping is still strong. As a result, fibers may reach fracture threshold before nonlinear scaling limits, while nonlinearities, e.g., stimulated Brillouin scattering (SBS), will be prime power scaling limiters for very narrowband [especially single-longitudinal-mode (SLM)] fiber lasers. As opposed to conventional fibers, fully crystalline double-clad waveguides are more suitable for laser power scaling due to their ~10 times higher thermal conductivity as well as an order of magnitude higher absorption and emission cross sections of common rare-earth dopants [3]. In addition, yttrium–aluminum–garnet (YAG) waveguides have an extremely low SBS gain coefficient from 9×10^{-15} to 5×10^{-12} m/W (variation is based on data from different sources [3]), versus that of silica glass (5×10^{-11} m/W). Estimates indicate that fully crystalline double-clad fiber lasers can be scaled to tens of kilowatts of power even in the most demanding SLM laser design [3,4]. Therefore, small-core waveguide laser development is of great importance.

Recently, a resonantly cladding-pumped, Er:YAG double-clad waveguide laser, fabricated by an adhesive-free bonding (AFB), has been demonstrated [5]. Taking advantage of the large numerical aperture (NA) of the inner cladding, the laser was efficiently pumped by a conventional laser diode bar stack with poor beam quality and delivered 25.4 W of continuous-wave (CW) output at 1645 nm with 56.6% optical efficiency (limited by high cladding loss). This double-clad crystalline laser had a free-space open cavity, and, due to the large core size (500 μm × 500 μm), it was sufficiently multimode. A nearly diffraction-limited output has been demonstrated from a side-pumped multimode small-core (100 μm× 80 μm) Yb:YAG channel waveguide [6]. This effort also used a free-space open cavity, and despite a very short (10 mm) waveguide length, the achieved slope efficiency was relatively low for resonant pumping (43%) due to imperfect matching of the pump and laser modes. To the best of our knowledge, the highest reported slope efficiency of 80.4% was achieved in a 22 μm thick $KY(WO_4)_2$:Yb planar waveguide [7].

In this Letter, we demonstrate a small-core, resonantly pumped, single-mode, Er:YAG channel waveguide laser with diffraction-limited output and nearly quantum defect limited efficiency. This first core-pumped (Er^{3+}:YAG-core/undoped YAG cladding) waveguide laser delivered a 9.1 W CW output with a slope efficiency of 92.8% (versus the absorbed pump power) and $M^2 = 1.05$.

The investigated 41.3 mm long channel waveguide, manufactured by AFB [8,9], had a 61.2 μm × 61.6 μm cross section Er^{3+}(0.25%):YAG core embedded in a 3 mm × 5 mm YAG cladding; see Fig 1(a). The channel was buried in the cladding only 30 μm deep under the 5 mm × 41.3 mm surface. The small refractive index difference, Δn, between the Er-doped YAG core and undoped YAG cladding provides sufficient waveguiding with low NA [9]. This Δn was measured (with the accuracy of $\sim 10^{-6}$) by the interferometric method with specially prepared adhesive-free bonded (Er:YAG/YAG) test samples for several Er^{3+} concentration values [10]. Given the refractive index of the undoped YAG cladding at 1532 nm of 1.8073 [11] and the measured $\Delta n = 5.2 \times 10^{-5}$ between the Er^{3+}(0.25%):YAG and undoped YAG, the core NA was derived to be $NA_C \sim 0.014$. Such an ultralow NA should lead to a single transverse mode operation of the channel waveguide despite its relatively large (on the scale of step-index conventional fibers) core cross section. However, the ultralow NA presents a challenge for achieving efficient pump launching into the core from sources with large angular divergence.

 © 2013 Optical Society of America

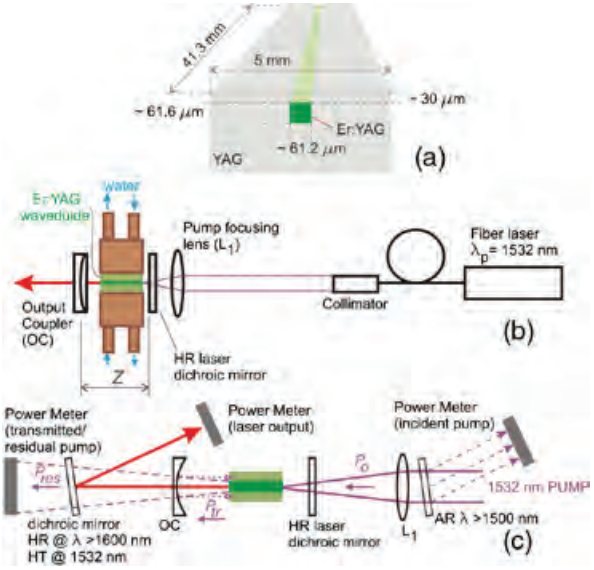

Fig. 1. (a) Er:YAG/YAG waveguide rendering (not to scale). (b) Experimental layout of the Er:YAG-core waveguide laser pumped by a single-mode Er-fiber laser. (c) Optical layout used for simultaneous measurements of the incident and transmitted pump power along with the laser output power.

To mitigate this problem, a single mode Er-fiber laser was used as a pump source. Both ends of the Er:YAG waveguide were antireflection (AR) coated for both laser and pump wavelengths ($R = 0.25\%$ at 1525–1650 nm). The waveguide was mounted on a water-cooled plate and conductively cooled at 18°C.

The experimental layout is shown in Fig. 1(b). A CW, 20 W rated Er-fiber laser, with ~0.3 nm full width at half-maximum (FWHM) at ~1532 nm, was used to longitudinally pump the Er:YAG core. A collimated, unpolarized pump with a divergence of ~1 mrad was focused into the waveguide by an aspheric lens $L_1(f_1 = 50$ mm) through a plano–plano dichroic mirror (HR at 1600–1650 nm, AR for the pump). The lens provided a ~50 μm pump spot diameter that fits well into the waveguide core cross section of 61.2 μm × 61.6 μm. This pumping geometry corresponded to an NA_F ~0.019 of the incident pump beam and yielded the best pump launching efficiency.

The laser cavity was formed by the above-mentioned dichroic mirror and a plano-concave output coupler (OC). Both mirrors were placed as close as possible (~40 μm) to the waveguide ends. This configuration provided the maximum output power. An analysis of open-cavity modes shows that excitation of the TEM_{00} laser mode in such a cavity is impossible due to the high diffraction loss, and only a waveguiding mode can be supported [12].

The laser beam divergence was determined with an IR CCD camera (Spiricon, model LW230) placed in the focal plane of the spherical lens with a focal length of 150 mm.

Due to the short length of the waveguide, not all of the incident power is absorbed on the first pass. In order to derive the maximum achievable optical-to-optical efficiency, one has to measure the unabsorbed pump power reflected off the OC back into the waveguide. Figure 1(c) depicts the optical layout used for simultaneous measurements of the incident and transmitted pump power along with the laser output power. The accuracy of the entire derivation also relies on precise knowledge of the transmissions and reflections of all optical components used in the setup shown in Fig. 1(c).

In the case of single-pass pumping schemes, we determined the absorbed pump power (P_{abs1}) by measuring the incident pump power (P_0) and the residual pump power behind the OC (P_{res}) when the laser is above the threshold; see Fig. 1(c):

$$P_{\mathrm{abs1}} = P_0 - \frac{P_{\mathrm{res}}}{1 - R_{\mathrm{OC}}(\lambda_{\mathrm{PUMP}})}. \tag{1}$$

The first pass pump absorption A_1 is determined as

$$A_1 = \frac{P_{\mathrm{abs1}}}{P_0}. \tag{2}$$

This same method cannot be easily used for the second pass (in the counterpump direction) due to the poor measurement accuracy. Instead, we assumed that the relative pump absorption in the waveguide, defined as the ratio of the absorbed pump power to the incident one, $\alpha = P_{\mathrm{abs}}/P_{\mathrm{inc}}$, was equal for both beam directions; i.e., $\alpha = A_1$. Such an assumption is acceptable when the pump saturation effect is negligible, which was the case in our experiments. This approach can only overestimate the total absorbed pump power because pump absorption on the second pass can only be lower due to the counterpropagating beam geometry, but not higher. The close proximity of the OC to the waveguide end simply ensures that the pump beam is reflected right back into the waveguide core.

The pump incident on the core entrance end further propagates in two distinct ways: (i) the pump that becomes confined inside the core (launched pump) is absorbed over the entire core length before leaving through the opposite end; (ii) the pump that escapes the core due to the mismatch between the pump NA (NA_F) and the core NA (NA_C) (where NA_F~0.019, $\mathrm{NA}_C = 0.014$) propagates in the cladding. The launching efficiency, to a first approximation, scales as the squared ratio of the core and the pump beam NAs, and in our case is $(\mathrm{NA}_C/\mathrm{NA}_F)^2 = 0.54$.

Figure 2(a) shows the CW output power of the Er:YAG waveguide laser versus the incident pump power at 1532 nm. The maximum output power of 9.1 W and the best optical-to-optical efficiency of 49.2% were achieved with $R_{\mathrm{OC}}(\lambda_{\mathrm{LASER}}) = 80\%$, $R_{\mathrm{OC}}(\lambda_{\mathrm{PUMP}}) = 85\%$, and RoC = 50 cm. With this OC full absorption of the launched power was achieved by double passing the 41 mm long Er:YAG core. On this condition, Fig. 2(b) depicts the output power of the waveguide laser plotted versus the absorbed pump power. The observed laser efficiency is near the quantum defect limited value for resonant pumping at 1532 nm.

The Er:YAG-core waveguide was designed to be a single-mode device. The criterion of single-mode operation for square waveguides is $B<1.37$, where the B number is the "square analog" of the V number for round fibers [13]:

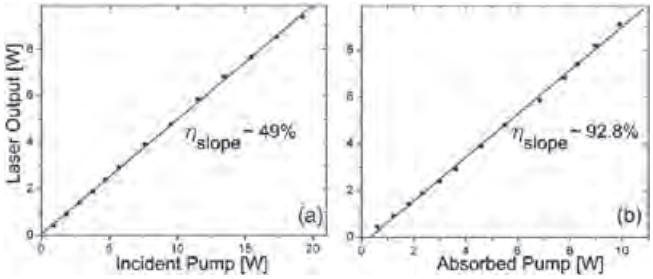

Fig. 2. (a) CW output power of the resonantly pumped Er:YAG-core waveguide laser versus the incident pump power. (b) CW output power versus the absorbed pump power. Laser cavity: length $Z = 41.3$ mm, $R_{OC}(\lambda_{LASER}) = 80\%$, $R_{OC}(\lambda_{PUMP}) = 85\%$, and RoC = 50 cm.

$$B = \frac{2a}{\lambda}\mathrm{NA}. \tag{3}$$

Based on the Er:YAG core NA of 0.014, the core size of $a \sim 62$ μm and $\lambda \sim 1.6$ μm, the B number of our waveguide is ~1.1; hence, a purely single-mode laser operation should be expected. The beam quality of the waveguide laser has been assessed at the maximum CW output power of 9.1 W by analyzing the beam intensity distribution in and near the focal plane of a spherical lens with a focal length of 150 mm. The beam was nearly Gaussian, and its far-field angular divergence was estimated at ~28 mrad (at e^{-2} level). If one compares this value to a diffraction-limited divergence of the beam from the 62 μm square aperture, $\lambda/a \sim 26$ mrad, one can conclude that this Er:YAG waveguide laser operated in a single transverse mode.

The measured beam diameter as a function of the position of the imaging plane relative to the location of the beam waist is plotted in Fig. 3. It can be seen that the collected data are in agreement with predictions based on Gaussian beam divergence with d_0 set to 67 μm:

$$d(z) = d_0 \cdot \left[1 + \left(\frac{4 \cdot \lambda \cdot z}{\pi \cdot d_0^2}\right)\right]^{1/2}, \tag{4}$$

where d_0 is the beam waist diameter and z is the distance. The beam quality M^2 derived from the above measurements was around 1.05, which proves that our laser is a purely single-mode device.

The Er^{3+}:YAG waveguide laser operated simultaneously at two wavelengths, 1617 and 1645 nm, if the R_{OC} was greater than 75%. It operated at 1617 nm only if the R_{OC} was below 70%. This observation is in agreement with the well-known interplay between the room-temperature emission cross sections and ground-state absorptions of the 1617 and 1645 nm transitions and population inversion of Er^{3+} in YAG (best explained in [14]). The maximum bandwidth of the laser emission at the maximum pump power was ~3.6 nm (FWHM) for both 1617 and 1645 nm laser lines.

The laser output was linearly polarized parallel to the 5 mm side of the cladding facet. The polarization extinction ratio was around 1000:1. This result can be tentatively explained by the asymmetric positioning of the buried channel inside the cladding described above. A corresponding asymmetric cooling causes the observed polarization preference.

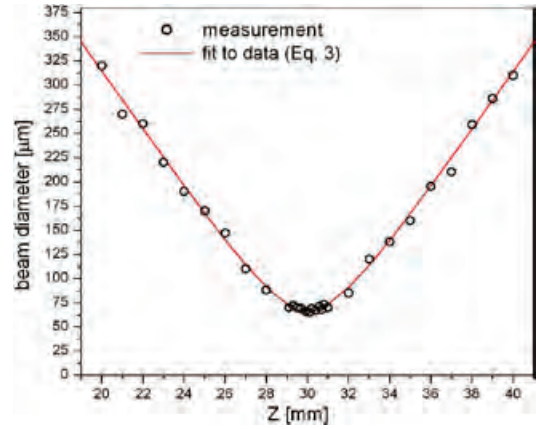

Fig. 3. Er:YAG waveguide laser beam diameter at e^{-2} level as a function of the imaging plane position near the focal plane of the lens $f = 150$ mm.

In summary, we demonstrated the CW operation of a resonantly pumped (Er^{3+}:YAG-core/undoped YAG cladding), single-mode channel waveguide laser with nearly quantum defect limited efficiency. A core-pumped waveguide delivered 9.1 W of output power at 1617 and 1645 nm with a slope efficiency of 92.8% (versus the absorbed pump power) and a nearly Gaussian output beam with $M^2 = 1.05$. The demonstrated efficiency is believed to be the highest optical-to-optical efficiency ever demonstrated for a channel waveguide laser.

References

1. D. C. Brown and H. J. Hoffman, IEEE J. Quantum Electron. **37**, 207 (2001).
2. C. D. Stacey, R. M. Jenkins, J. Banerji, and A. R. Davies, Opt. Commun. **269**, 310 (2007).
3. J. W. Dawson, M. J. Messerly, J. E. Heebner, P. H. Pax, A. K. Sridharan, A. L. Bullington, R. J. Beach, C. W. Siders, C. P. J. Barty, and M. Dubinskii, Proc. SPIE **7686**, 768611 (2010).
4. T. A. Parthasarathy, R. S. Hay, G. Fair, and F. K. Hopkins, Opt. Eng. **49**, 094302 (2010).
5. N. Ter-Gabrielyan, V. Fromzel, X. Mu, H. Meissner, and M. Dubinskii, Opt. Express **20**, 25554 (2012).
6. U. Griebner and H. Schonnagel, Opt. Lett. **24**, 750 (1999).
7. Y. E. Romanyuk, C. N. Borca, M. Pollnau, U. Griebner, S. Rivier, and V. Petrov, Opt. Lett. **31**, 53 (2006).
8. X. Mu, H. Meissner, H.-C. Lee, and M. Dubinskii, Proc. SPIE **8237**, 82373M (2012).
9. R. J. Beach, S. C. Mitchell, H. E. Meissner, O. R. Meissner, W. F. Krupke, J. M. McMahon, W. J. Bennett, and D. P. Shepherd, Opt. Lett. **26**, 881 (2001).
10. H. Lee, X. Mu, and H. Meissner, in *CLEO:2011—Laser Applications to Photonic Applications*, OSA Technical Digest (CD) (Optical Society of America, 2011), paper AMB4.
11. http://refractiveindex.info/?group=CRYSTAL&material=Y3Al5O12
12. L. A. Vainshtein, *Open Cavities and Open Waveguides* (Golem, 1969).
13. K. S. Chiang, Appl. Opt. **25**, 2169 (1986).
14. S. Setzler, M. Fransis, Y. E. Young, J. R. Konves, and E. P. Chicklis, IEEE J. Sel. Top. Quantum Electron. **11**, 645 (2005).

Conversion of Above- and Below-Bandgap Photons via InAs Quantum Dot Media Embedded into GaAs Solar Cell

K. Sablon, J. Little, N. Vagidov, Y. Li, V. Mitin, and A. Sergeev

Applied Physics Letters, 104 (2014)

Conversion of above- and below-bandgap photons via InAs quantum dot media embedded into GaAs solar cell

K. Sablon,[1] J. Little,[1] N. Vagidov,[2] Y. Li,[3] V. Mitin,[3] and A. Sergeev[3]
[1]*U.S. Army Research Laboratory, Adelphi, Maryland 20783, USA*
[2]*Optoelectronic Nanodevices LLC, Amherst, New York 14226, USA*
[3]*EE Department, University at Buffalo—SUNY, Buffalo, New York 14260, USA*

(Received 16 May 2014; accepted 13 June 2014; published online 24 June 2014)

Quantum dots (QDs) provide photovoltaic conversion of below-bandgap photons due to multistep electron transitions. QDs also increase conversion efficiency of the above-bandgap photons due to extraction of electrons from QDs via Coulomb interaction with hot electrons excited by high-energy photons. Nanoscale potential profile (potential barriers) and nanoscale band engineering (AlGaAs atomically thin barriers) allow for suppression of photoelectron capture to QDs. To study these kinetic effects and to distinguish them from the absorption enhancement due to light scattering on QDs, we investigate long, 3-μm base GaAs devices with various InAs QD media with 20 and 40 QD layers. Quantum efficiency measurements show that, at least at low doping, the multistep processes in QD media are strongly affected by the wetting layer (WL). The QD media with WLs provide substantial conversion of below-bandgap photons and for devices with 40 QD layers the short circuit current reaches 29.2 mA/cm^2. The QD media with band-engineered AlGaAs barriers and reduced wetting layers (RWL) enhance conversion of high-energy photons and decrease the relaxation (thermal) losses. © *2014 AIP Publishing LLC*. [http://dx.doi.org/10.1063/1.4885113]

According to the fundamental Shockley-Queisser (S-Q) limit, the conversion efficiency of a traditional single-junction solar cell under AM1.5 radiation cannot exceed 33%.[1] The best GaAs solar cells approach S-Q limit and demonstrate 28.8% efficiency. The short circuit current in these devices reaches 29.7 mA/cm^2 and an open circuit voltage is 1.12 V.[2,3] There are many approaches proposed for engineering photon and electron states to increase the efficiency beyond the S-Q limit. Up- and down-conversion and plasmonic effects are studied to adapt solar radiation to the bandgap spectrum.[4] Photovoltaic conversion via impurity bandgap states was investigated for forty years.[5] Last decade significant efforts were devoted to quantum dot (QD) structures, which demonstrate wide possibilities for managing of IR absorption.[6] Photoelectron kinetics with multi-exciton generation strongly increases interest to QD structures.[7] In the area of high efficiency conversion, main efforts were concentrated at the development of the intermediate band solar cell (IBSC).[8] In spite of substantial technological achievements, QD IBSC efficiency in the best case increases by 1% compared with the reference cell.[9] Let us note that besides conversion of the below-bandgap photons, this improvement may be also explained by the enhanced absorption of the above-bandgap photons due to the light scattering by QDs.[10]

The main problem of photovoltaic nanomaterials is the enhanced recombination of photocarriers. More than ten years ago, Hans Queisser highlighted:[11] "Carrier lifetime is the most sensitive measure of crystalline perfection. Any deviation from an ideal single crystal reduces the lifetime, and thus lowers conversion efficiency…. Any nanocrystalline material is, therefore, in principle an inappropriate choice for a cell material." At the same time, nanoscale engineering provides various opportunities for managing electron processes.[12] To increase the photocarrier lifetime in QD media, we propose to create nanoscale potential barriers, which suppress capture and recombination processes.[13,14]

The goal of the current work is to investigate how photoelectron processes depend on structural variations in QD media. Here, we compare effects of nanoscale potential barriers created by built-in charge[13–15] and the band-engineered barriers created by atomically thin AlGaAs layers around QDs.[16] These AlGaAs layers also substantially reduce the InAs wetting layer (WL) and, in this way, suppress photoelectron capture in QDs. To exclude effects of enhanced absorption due to light scattering on QDs, we fabricated the GaAs photovoltaic (PV) devices with 3 μm base as in the optimized GaAs solar cells. Our QD solar cells comprise various 1 μm and 2 μm InAs QD media with 20 and 40 QD layers correspondingly. To investigate effects of WL on PV conversion, we have fabricated devices with conventional QD media as well as devices with thin AlGaAs barriers and reduced wetting layers (RWL).

Figure 1 illustrates the growth diagram. The structures were grown on n$^+$ GaAs (100) substrates by molecular beam epitaxy. Following oxide desorption, a 200 nm n$^+$ GaAs buffer with a doping density of 5×10^{18} cm^{-3} was grown at 595 °C. The back surface field layer, which prevents the diffusion of holes into n$^+$-contact, was formed by 50 nm n-doped $Al_{0.2}Ga_{0.8}As$ with a doping density of 5×10^{18} cm^{-3}. The 3 μm base of the reference cell consists of 2 μm n-doped GaAs with a doping density of 2×10^{17} cm^{-3} and 1 μm of undoped GaAs. The device was completed with 100 nm p-doped GaAs with a doping density of 1×10^{18} cm^{-3}, 100 nm p-doped GaAs with a doping density of 5×10^{18} cm^{-3}, 30 nm p-$Al_{0.8}Ga_{0.2}As$ with a doping density of 5×10^{18} cm^{-3} (to prevent diffusion of electrons into p$^+$-contact), and 20 nm p-GaAs contact layer.

In QD PV devices, the QD medium was placed in the base close to the p-n junction. The QD medium contains 20

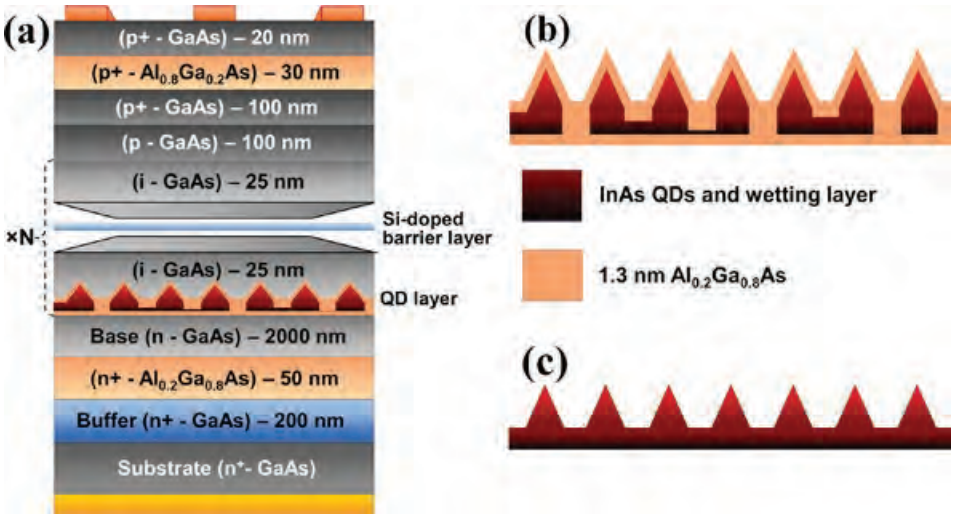

FIG. 1. Growth diagram of QD solar cells (a), QD medium with AlGaAs barriers around QDs and reduced wetting layer (b), and QD medium with wetting layer (c).

or 40 stacks of QD layers separated by GaAs spacer layers. For structures with wetting layer, InAs quantum dots were grown on GaAs layer and covered by GaAs spacer layer (Fig. 1(c)). For structures with reduced wetting layer, InAs quantum dots were grown on the bottom 1.3 nm $Al_{0.2}Ga_{0.8}As$ layer by deposition of 2.1 MLs of InAs. Then, the top 1.3 nm $Al_{0.2}Ga_{0.8}As$ layer was deposited on InAs (Fig. 1(b)). Because of the high InAs/AlGaAs interface energy, such fabrication procedure radically reduces the InAs wetting layer and creates AlGaAs barriers around QDs. To charge QDs, a plane of dopants is placed in the middle of each GaAs layer that separates the dot layers. The dopant sheet density of $3.6 \times 10^{10}\,cm^{-2}$ provides approximately three electrons per QD.

We produced PV devices employing traditional photolithography followed by etching. The structures were etched down into the n^+ GaAs substrate. The n-type blanket metallization of germanium/gold/nickel/gold was performed in an electron beam vacuum evaporator onto the back side of the substrate. Finally, the top of each device was patterned with a p-type metal. A titanium/platinum/gold top contact was deposited followed by a metal lift-off. All samples were passivated with ammonium sulfide and encapsulated with silicon nitride, which works as antireflection coating and also reduces recombination at the front and side surfaces. The devices have areas of 0.102 mm^2 (circular), 0.82 mm^2 (square), and 9.13 mm^2 (square).

To measure photovoltaic characteristics, we use the Newport Oriel PV calibrated solar simulator, which provides illumination with AM1.5G spectrum. The I-V curves were obtained with an Agilent 4156C precision semiconductor analyzer. The characteristics of the square devices with area of 0.82 mm^2 are presented in Fig. 2 and summarized in Table I. The data are obtained after averaging over five best devices made from the same wafer. As seen, all QD devices show short circuit current, J_{SC}, higher than that in the reference cell (RF1 devices), but smaller open circuit voltage, V_{OC}.

The n-doping of QD devices improves J_{SC} and V_{OC} hence increasing the conversion efficiency. The WL1 devices with InAs wetting layer and selective interdot doping of ~3 electrons per dot show the short circuit current of 27.9 mA/cm^2, which is by 1.1 mA/cm^2 higher than that in similar WL2 devices without doping of QD media. In the devices with reduced wetting layers and AlGaAs barriers around dots the effect of doping is small. The RWL2 devices without interdot doping and RWL1 devices with doping of 3 electrons per dot show approximately the same short circuit current of 28.3–28.4 mA/cm^2. In the WL2 devices with undoped QD media, the open circuit voltage, V_{OC}, is 0.83 V. Doping of this QD media (WL1 devices) increases V_{OC} to

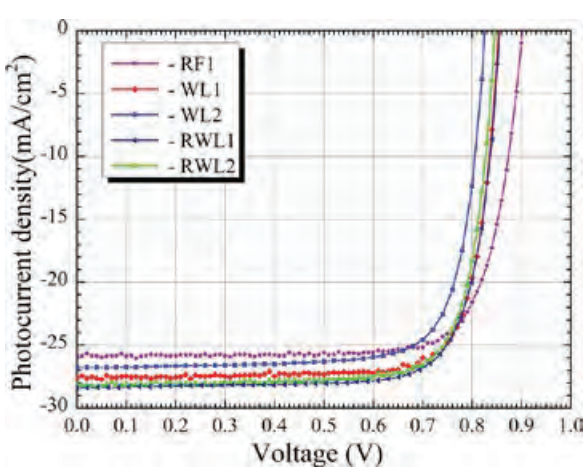

FIG. 2. Current-voltage characteristics of solar cells under 1 Sun illumination with AM1.5G spectrum.

TABLE I. Performance of QD PV devices with various QD media.

Sample	J_{SC} (mA/cm^2)	V_{OC} (V)	Fill factor (%)	Efficiency (%)
RWL1 Doped RWL	28.4	0.85	79	19.1
RWL2 Undoped RWL	28.3	0.85	78	18.8
WL1 Doped WL	27.9	0.85	79	18.7
WL2 Undoped WL	26.8	0.83	77	17.2
WL3 (40 QD layers) Undoped WL	29.2	0.78	78	17.8
RF1 GaAs ref. cell	25.8	0.9	78	18.1

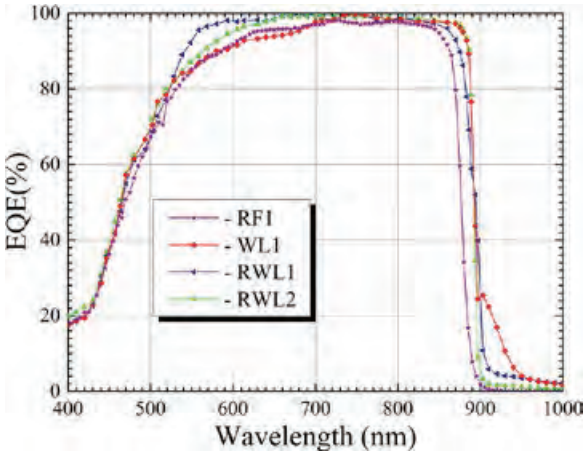

FIG. 3. External quantum efficiencies of GaAs reference cell and solar cells with various QD media.

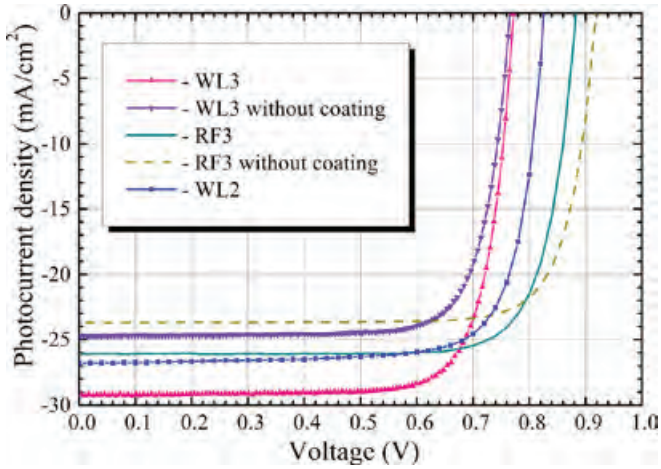

FIG. 4. I-V curves of solar cells with 20 QD layers (WL2) and 40 QD layers (WL3) with and without antireflection coating under 1 Sun illumination with AM1.5G spectrum.

0.85 V. For the RWL2 and RWL1 devices with RWL QD media the doping does not change V_{OC}, which is ~0.85 V for both undoped and lightly doped structures. These data are also confirmed by measurements of other circular and square devices with smaller and larger areas (the data scattering is ~1%). The RWL devices show conversion efficiencies of about 19.1%, the doped WL devices demonstrate 18.7% efficiency, while the efficiency of the reference cell is 18.1%.

In order to identify photoelectron processes in QD media, we measured the spectral dependence of external quantum efficiency (EQE). Such measurements require large area devices, which were fabricated from the same wafers as discussed above. According to Fig. 3, all QD devices show significant contribution to the short circuit current in the near-bandgap range of 860–900 nm. Calculating this contribution from EQE data as

$$\Delta J_{SC}^{EQE} = e \int_{\lambda_1}^{\lambda_2} EQE(\lambda)\, P(\lambda)\, d\lambda\,, \tag{1}$$

where $P(\lambda)$ is the spectral density of the AM1.5G photon flux, we get ~1.7 mA/cm^2 for RWL1 device, 1.9 mA/cm^2 for RWL2, and 2 mA/cm^2 for WL1 devices. These values exceed by 1–1.3 mA/cm^2 the corresponding value for the RF1 reference cell. This QD contribution is not sensitive to WL and AlGaAs barriers in QD media. The interdot doping of QD media slightly decreases this contribution. To exclude the bandgap shift due to InGaAs creation in the growth procedure, the devices were analyzed by Secondary Ion Mass Spectrometry (SIMS) and Energy Dispersive X-Ray Spectroscopy. The results confirm absence of In in the GaAs base and in the interdot space of QD medium matrix.

The observed QD-induced conversion of light in the range of 860–880 nm is associated with the Burstein-Moss effect. In the reference cell, the low energy states in the conduction band of n-doped GaAs are filled by electrons so the optical transitions to these states are prohibited. Dependence of GaAs absorption on the electron concentration was accurately investigated in Ref. 17. For photons with $\lambda = 870$ nm, the n-doping of 2×10^{17} cm^{-3} decreases the absorption coefficient to 0.3 μm^{-1}. In the n-doped QD media electrons populate mainly QDs and photon absorption of QD matrix becomes similar to that in the undoped GaAs. In the undoped GaAs, the absorption coefficient of photons with $\lambda = 870$ nm increases to ~0.8 μm^{-1}.[17] This provides substantial absorption in our devices. In the range of 880–900 nm, the absorption is increased due to transitions to low-energy continuous states in the minibands formed by periodically placed QD layers.[18] Various mechanisms of Urbach–Martienssen tails in nanostructured GaAs may also provide substantial contribution in this range.[19]

In the range above 900 nm, only QD devices with WLs show substantial contribution to the electric current. The 2D quasi-localized WL electron states provide effective coupling between the 0D localized QD states and 3D conducting states in the matrix. The effect of IR harvesting and conversion by QDs is proportional to the number of QD layers in the device.[20] In Fig. 4, we compare the device with 20 undoped QD layers (WL2) and analogous device with 40 undoped QD layers (WL3). As seen, the device with 40 QD layers shows the short circuit current of 29.2 mA/cm^2 (see Table I).

The most interesting observation of this work is the substantial enhancement of EQE in the wide range of 500–720 nm observed in RWL QD media. We associate the increase of EQE in this range with a two-step process shown in Fig. 5. First, a subband photon creates electron-hole pair in QD and a high-energy photon creates another pair. The second step is the ionization of the QD by the high-energy (hot) electron. Assuming that the process is localized in a dot volume, the corresponding electron extraction (QD ionization) rate may be presented as

$$\tau_{ext}^{-1} = \pi N_d\, a^3 \tau_{ee}^{-1}\,, \tag{2}$$

where N_d is the concentration of QDs, a is the QD radius, and τ_{ee} is the corresponding electron-electron scattering time in QD. Because the energy transferred in these processes is substantially larger than the level spacing, we will ignore the quantization in QD and use the electron-electron scattering rate in the bulk conductor[21] and get

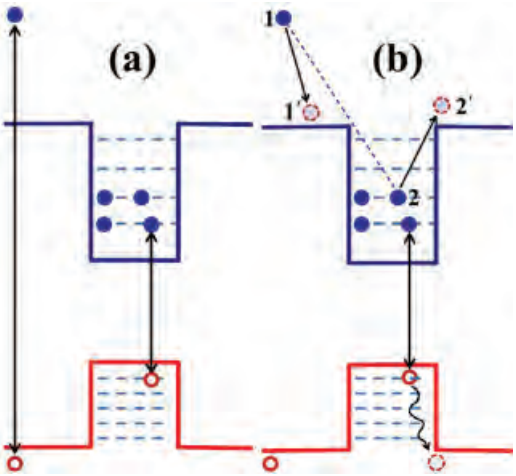

FIG. 5. Extraction of electrons localized in QD by hot electron that is excited by high-energy photon.

$$\tau_{ext}^{-1}(E) = 6\pi N_d \left(\frac{e^2}{4\pi\chi\varepsilon_0}\right)^2 \frac{n}{(2m)^{1/2}E^{3/2}}, \quad (3)$$

where χ is the material permittivity, n is the number of electrons in QD, and E is the transferred energy. The ionization rate is proportional to the number electrons per dot and it is independent on the dot radius. Let us note that the product $N_d \times n$ is equal to the concentration of dopants. The obtained ionization rate of QDs by hot electrons is of the same order as the electron-electron scattering in the bulk material with the doping level that provides n electrons per dot in Eq. (2).[21] For characteristic energy of $\sim$0.1 eV, the ionization rate turns out to be $\sim$1 ps at doping level of QD media of $\sim 10^{17}\,\mathrm{cm}^{-3}$. At this doping level, the ionization of QDs by hot electrons becomes comparable with cooling of hot electrons via optical phonon emission. Thus, doped QD media may be used to decrease relaxation losses.

The high-frequency boundary of the effect is determined by the strong absorption of high-energy photons in GaAs. The absorption coefficient of 500 nm electromagnetic quanta is $\sim 100\,\mathrm{nm}^{-1}$ and, therefore, the radiation in 400–500 nm range is strongly absorbed in the 250 nm p-doped area of our devices. The electron cooling rate is also of the order of 100 nm. Therefore, hot electrons that are created in the p-doped area do not reach QD media. The 500–720 nm wavelength photons are absorbed in QD media near p-n junction. The photoelectrons obtained in this effect should go through the whole device base. For this reason, the effect is only observed in the RWL devices with strong suppression of capture by QDs.

The efficiency of this two-step effect is proportional to the product of probabilities of two transitions. Doping suppresses the creation of electron-hole pairs in QDs due to increased filling of the dots by electrons. At the same time, the n-doping strongly enhances the electron extraction from QDs due to interaction with hot electrons. As a result of this trade-off, the effect initially increases with doping, reaches a maximum, and decreases due to filling of QDs. In the current work, the effect is investigated for undoped QD media and n-doped media with doping of $\sim$3 electrons per dot. The effect is increased with doping increase, but we did not yet reach the maximum.

In summary, it has been found that in the near-bandgap range of 860–900 nm the contribution of QDs is determined by the Burstein-Moss effect[17] and light absorption due to low-energy minibands formed by periodically placed QD layers.[18] Above 900 nm only QD media with WLs provide substantial IR harvesting and absorption. This effect is proportional to the number of QD layers. In our devices with 40 QD layers, the photocurrent increases to 29.2 mA/cm^2 which is very close to the record current in GaAs solar cells.[2] Substantial QD contribution to PV conversion is also observed in the optical range from 500 to 720 nm. We associate this effect with ionization of QDs by hot electrons (Fig. 5). In this process, the light-excited high-energy electrons extract electrons localized in QDs. In general, the electron heating, i.e., hierarchy of scattering times when electron-electron scattering dominates over the electron-phonon one, is favorable for PV conversion. For deep QDs, it leads to multiple exciton generation in QDs.[22] In doped InAs/GaAs QD media it leads to effective electron extraction from QDs by hot electrons.

In order to determine the optimal strategy, we would like to note that IR conversion is strongly enhanced in structures with large QDs due to increase of QD level degeneracy.[13,23] However, large dots efficiently capture photoelectrons and, as a result, the total photocurrent turns out to be even smaller than that in the device with small dots.[23] Therefore, devices with small dots usually show better performance.[20] At the same time, strong charging of large dots allows for both increase of IR harvesting and suppression of photoelectron capture.[13,15,24,25] According to this work, the dot charging also enhances ionization of QDs by hot electrons (Fig. 5) and minimizes the relaxation losses. Therefore, our next steps aim at studies of PV conversion by strongly charged and relatively large QDs.

The work of K.S. and J.L. was supported by ARL, work of N.V. by AFRL (FA9453-14-M-0013), work of Y. Li and A.S. by NSF (ECS-1236459), and work of V.M. by AFOSR (FA9550-10-1-0391). The authors are grateful to D. Wilt and S. Oktyabrsky for valuable discussions and highly appreciate Michael Yakimov's help in SIMS and EDXS analyses of our devices.

[1]W. Shockley and H. J. Queisser, J. Appl. Phys. **32**, 510 (1961).
[2]B. M. Kayes, H. Nie, R. Twist, S. G. Spruytte *et al.*, in Proceedings of the 37th IEEE Photovoltaic Specialists Conference, Seattle, 2011.
[3]M. A. Green, K. Emery, Y. Hishikawa, W. Warta, and E. D. Dunlop, Prog. Photovoltaics **21**, 1 (2013).
[4]H. A. Atwater and A. Polman, Nature Mater. **9**, 205 (2010).
[5]M. Wolf, Proc. IRE **48**, 1246 (1960).
[6]V. Ryzhii, Semicond. Sci. Technol. **11**, 759 (1996).
[7]A. G. Midgett, J. M. Luther, J. T. Stewart, D. K. Smith, L. A. Padilha, V. I. Klimov, A. J. Nozik, and M. C. Beard, Nano Lett. **13**, 3078 (2013).
[8]A. Luque and A. Marti, Adv. Mater. **22**, 160 (2010).
[9]A. Martí, E. Antolín, P. García Linares, I. Ramiro, I. Artach, E. López, E. Hernández, M. J. Mendes, A. Mellor, I. Tobías, D. Fuertes Marrón, C. Tablero, A. B. Cristóbal, C. G. Bailey, M. Gonzalez, M. Yakes, M. P. Lumb, R. Walters, and A. Luque, Proc. SPIE **8620**, 86200J (2013).
[10]X.-J. Shang, J.-F. He, M.-F. Li, F. Zhan, H.-Q. Ni, Z.-C. Niu, H. Pettersson, and Y. Fu, Appl. Phys. Lett. **99**, 113514 (2011).
[11]H. Queisser, Physica E **14**, 1 (2002).

[12]B. H. Hamadani, S. Jung, P. M. Haney, L. J. Richter, and N. B. Zhitenev, Nano Lett. **10**, 1611 (2010).
[13]K. A. Sablon, J. W. Little, V. Mitin, A. Sergeev, N. Vagidov, and K. Reinhardt, Nano Lett. **11**, 2311 (2011).
[14]K. A. Sablon, A. Sergeev, N. Vagidov, J. W. Little, and V. Mitin, Sol. Energy Mater. Sol. Cells **117**, 638 (2013).
[15]K. Sablon, A. Sergeev, N. Vagidov, A. Antipov, J. W. Little, and V. Mitin, Nanoscale Res. Lett. **6**, 584 (2011).
[16]G. Wei and S. R. Forrest, Nano Lett. **7**, 218 (2007).
[17]H. C. Casey, D. D. Sell, and K. W. Wecht, J. Appl. Phys. **46**, 250 (1975).
[18]F. T. Vasko and V. V. Mitin, Phys. Rev. B **85**, 235321 (2012).
[19]B. Pejova and B. Abay, J. Phys. Chem. C **115**, 23241 (2011).
[20]C. G. Bailey, D. V. Forbes, S. J. Polly, Z. S. Bittner, Y. Dai, C. Mackos, and R. P. Raffaelle, IEEE J. Photovoltaics **2**, 269 (2012).
[21]B. K. Ridley, *Quantum Processes in Semiconductors* (Oxford University Press, 2000).
[22]V. I. Klimov, Annu. Rev. Condens. Matter Phys. **5**, 285 (2014).
[23]D. Guimard, R. Morihara, D. Bordel, K. Tanabe, Y. Wakayama, M. Nishioka, and Y. Arakawa, Appl. Phys. Lett. **96**, 203507 (2010).
[24]X. Yang, K. Wang, Y. Gu, H. Ni, X. Wang, and T. Yang, Sol. Energy Mater. Sol. Cells **113**, 144 (2013).
[25]D. J. Norris, A. L. Efros, and S. C. Erwin, Science **319**, 1776 (2008).

P-type Interface Charge Control Layers for Enabling GaN/SiC Separate Absorption and Multiplication Avalanche Photodiodes

A. V. Sampath, Q. G. Zhou, R. W. Enck, D. McIntosh, H. Shen,
J. C. Campbell, and M. Wraback

Applied Physics Letters, 101 (2012)

P-type interface charge control layers for enabling GaN/SiC separate absorption and multiplication avalanche photodiodes

A. V. Sampath,[1] Q. G. Zhou,[2] R. W. Enck,[1] D. McIntosh,[2] H. Shen,[1] J. C. Campbell,[2] and M. Wraback[1]
[1]*U.S. Army Research Laboratory, Sensors and Electron Devices Directorate, RDRL-SEE-M, 2800 Powder Mill Road, Adelphi, Maryland 20783, USA*
[2]*Department of Electrical and Computer Engineering, University of Virginia, Charlottesville, Virginia 22904, USA*

(Received 21 June 2012; accepted 15 August 2012; published online 29 August 2012)

A p-type interface charge control layer (PICCL) is introduced that enables optimization of the net positive polarization induced interface charge at the GaN/SiC interface in GaN/SiC separate absorption and multiplication avalanche photodiodes (SAM-APDs) by varying its thickness. The response from SAM-APDs with PICCL thickness less than 10 nm has an anomalous shape at all bias attributed to the collection of carriers generated directly in the SiC layer. Devices with a 15 nm thick PICCL exhibit GaN related response at high bias that is indicative of punch-through of the electric field into the GaN absorption region due to optimization of the net interface charge. © *2012 American Institute of Physics*. [http://dx.doi.org/10.1063/1.4748793]

High sensitivity and high gain ultraviolet avalanche photodiodes (APDs) are useful for a number of applications, including compact water quality monitoring, radiation detection using scintillation, and combustion control. These applications will benefit from the availability of inexpensive, high sensitivity detectors with response that can be tailored to a portion of the visible-UV spectrum and have either a relaxed or no requirement for an external filter. Currently, significant work has been done on the development of APDs using wide band gap semiconductor materials such as SiC and GaN,[1–3] which are attractive because these detectors can be inherently solar/visible blind, have low dark current, and operate in harsh environments. State of the art SiC APDs can have high quantum efficiency (QE) in the deep ultraviolet (~60% at 268 nm), high gain, low dark current density ($J_{dark} = 63$ nA/cm^2 at a gain of 1000, which indicates primary dark current of <63 pA/cm^2), and low noise ($k = 0.10$).[1] However, the indirect band gap of SiC results in poor absorption and, therefore, reduced response near its band gap around 380 nm. GaN APDs grown on bulk GaN substrates have been demonstrated that exhibit gains of ~1000 and dark current densities of ~2.6 μA/cm^2 near avalanche breakdown.[2] However, the size of these devices is still smaller than those of SiC APDs, 30–50 μm in diameter as compared to 250 μm, presumably due to the presence of defects. Furthermore, the excess noise in GaN APDs is likely to be significantly higher than that of SiC APDs due to the near unity ratio of the ionization coefficients in GaN ($k \sim 1$), therefore, requiring structures employing impact ionization engineering.

Recently, we have reported on an alternative approach consisting of a separate absorption and multiplication APD (SAM APD) employing a III-Nitride semiconductor as the absorption region and SiC as the multiplication region.[4] The advantages of this approach include the possibility of having high QE over a widely tunable spectral range, from the visible to the deep ultraviolet, by modifying the composition of the direct band gap III-Nitride absorption region, as well as low dark current and high gain associated with the high quality SiC multiplication region. In addition, this device structure benefits from the formation of a type II heterojunction between the III-Nitride and 4H SiC layers[5] that promotes hole injection and inhibits electron injection from GaN into SiC, enabling single carrier injection of the photo-generated holes in the absorbing region into the SiC multiplication layer that is optimal since the hole ionization coefficient of SiC is much greater than that of the electron. These factors, as well as the spatial separation of the absorption and multiplication regions in these devices, should promote single carrier hole multiplication and, therefore, reduced excess noise.

However, these diodes differ from traditional heterojunction SAM APDs such as InGaAs/InP telecommunications devices in two important ways: the presence of defects in the absorption region and the use of polar materials. The defects arise from both the lattice mismatch between the III-Nitride absorption and the SiC multiplication regions as well as the initiation of heteroepitaxy at the critical interface between them, resulting in very short carrier diffusion lengths. Therefore, efficient hole injection will require an electric field in the GaN sufficient to sweep holes into the SiC multiplication region, while remaining low enough to avoid generating large dark currents due to defects. As these detectors employ polar materials, with SiC having smaller spontaneous polarization than the III-Nitride semiconductor for all compositions, a positive polarization induced charge is expected at the hetero-interface for III-face growth. Ideally, this can achieve an optimal electric field profile in the diode, an atomically sharp transition between a high field in the multiplication region desirable for high gain and a low field within the absorption region for high QE, thus eliminating the conventional doped charge layer and avoiding the concomitant voltage penalty associated with it. However, excessive interface charge will confine the electric field in the SiC and prevent punch through into the GaN absorption region prior to avalanche breakdown of the diode.

In this paper, we demonstrate that the introduction of a delta doped p-type interface charge control layer (PICCL) at

the GaN/SiC heterointerface, designed so that the total density of negatively charged ionized acceptors can partially offset the positive polarization charge, provides an effective "knob" for optimization of the net interface charge in GaN/SiC SAM APDs. In addition, PICCLs with varying thickness can be used to examine the role of polarization induced interface charge on device performance and, in conjunction with modeling, enable the extraction of the contribution to multiplication gain and hole injection efficiency of the GaN absorption region.

The structure of the GaN/SiC APDs consists of a 2 μm thick p^+-SiC layer doped $2 \times 10^{18}\,cm^{-3}$, a 480 nm thick n-SiC multiplication layer unintentionally doped $5 \times 10^{15}\,cm^{-3}$, a 300 nm thick unintentionally n-type doped GaN absorption layer, and a 10–50 nm thick n^+-GaN layer doped $2 \times 10^{18}\,cm^{-3}$. The SiC epitaxial layers grown on Si- face 4H-SiC substrates were purchased from Cree, Inc. The III-polar GaN epitaxial layers were heteroepitaxially grown by plasma assisted molecular beam epitaxy at 850 °C directly upon the SiC epitaxial layers without the use of traditional buffer layers. The role of polarization induced interface charge is examined by considering two similarly Mg doped GaN PICCLs with thicknesses of 10 and 15 nm grown with a Mg beam equivalent pressure of 7×10^{-8} Torr and placed between the SiC multiplication region and GaN absorption region. The devices containing these PICCLs will be referred to as APD10 and APD15, respectively. The SiC substrates were chemically prepared prior to growth by solvent cleaning and Radio Corporation of America (RCA) cleaning.[4] The substrate is prepared *in-situ* immediately prior to growth by periodically covering the epitaxial surface with Ga metal and then allowing the metal to desorb as described by Korakakis *et al.*[6]

The DC photoresponse of these devices was measured by illuminating the detector using a broad spectrum, laser-driven light source, and monochromator combination. The optical power was held constant over the spectral range using a motor-controlled variable neutral density filter. Capacitance-voltage measurements were taken with an Agilent 4284 LCR meter using a 100 kHz AC bias with amplitude of 500 mV.

The measured photoresponse spectra at various reverse biases for a typical APD10 are shown in Figure 1 (top, open shapes). The responsivity increases with reverse bias above ~100 V due to gain in the multiplication region. The shape of the response is constant with increasing reverse bias and exhibits a local maximum at ~372 nm and a local minimum at ~365 nm that is inconsistent with a typical GaN or SiC photodetector. All devices measured with PICCL thickness less than 10 nm exhibit similar behavior. While the photoresponse for a typical APD15 (Figure 1 bottom, open shapes) is similar to that of APD10 at low reverse bias (50–130 V), its shape changes with increasing reverse bias (>130 V) and is consistent with GaN response when biased near avalanche breakdown, above ~159 V. A responsivity of ~4.0 A/W was measured at 364 nm for a reverse bias of 160 V.

Figure 2 shows a plot of $(d/dV\ 1/C^2)^{-1}$ as a function of (1/C) for a typical APD15, where $(d/dV\ 1/C^2)^{-1}$ and 1/C are proportional to the effective carrier concentration and depletion width, respectively. The plot shows three clear regions,

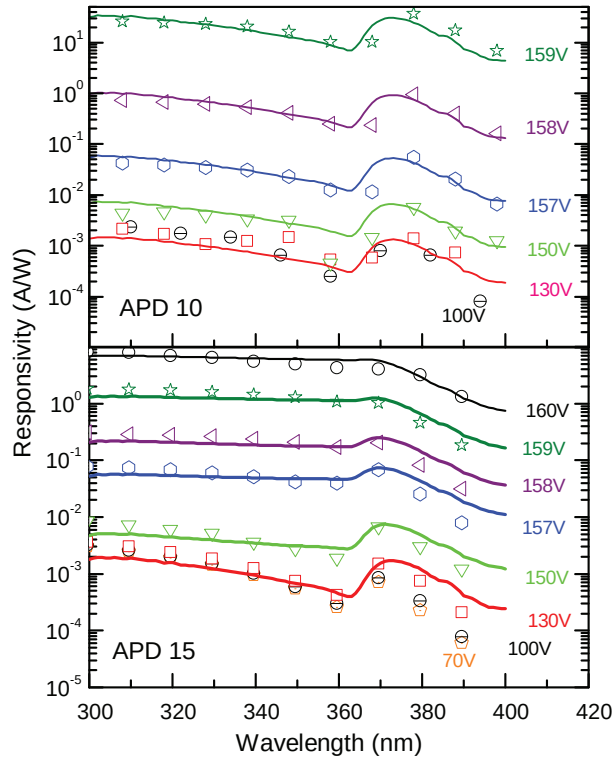

FIG. 1. Measured (open figures) and calculated (solid lines) photoresponse from APD10 (top) and APD15 (bottom).

with the effective carrier concentration nearly constant with increasing depletion width for regions 1 and 3. The carrier density softly decreases from higher to lower effective carrier density in region 2.

The origins of the observed spectral response can be understood by analyzing its components in these devices. Since GaN has a wider band gap than SiC and because of incomplete absorption in the GaN absorption region, the photoresponse has a component associated with carrier generation in the SiC multiplication region (R_{SiC}) in addition to that associated with the generation and injection of holes from the GaN absorption region (R_{GaN}). The total photoresponse can then be expressed as

$$R_{photo} = R_{SiC} + R_{GaN}. \quad (1)$$

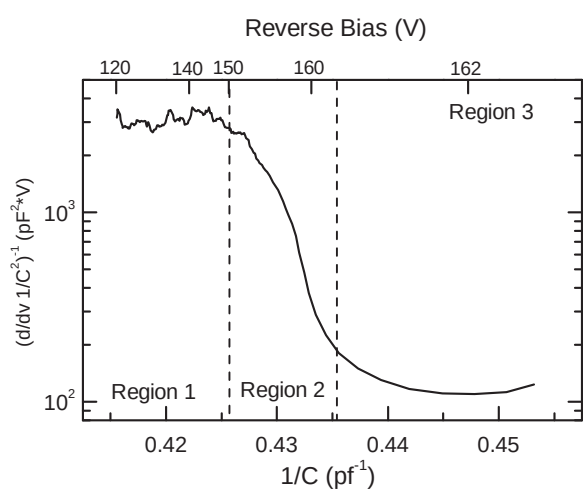

FIG. 2. CV characteristics for APD15.

The SiC component of the photoresponse is a function of both photon wavelength and reverse bias and may be expressed as

$$R_{SiC}(V,\lambda) = \frac{(1-R)q}{\hbar\nu} \cdot e^{-\alpha(\lambda)d_{GaN}} \cdot \eta_{SiC}(\lambda) \cdot g(V), \quad (2)$$

where R is the reflectance of the illuminated surface, η_{SiC} is the quantum efficiency of the SiC acting as an absorption region, α and d are the absorption coefficient and thickness of the GaN absorption region acting as an optical filter, and g is the gain in the SiC multiplication region. The product of the first and second term of Eq. (2) is the net photon flux incident upon the SiC region accounting for reflection at the illuminated surface and transmission through the GaN absorption region.

The GaN component of the photoresponse is given by

$$R_{GaN}(V,\lambda) = \frac{(1-R)q}{\hbar\nu} e^{-\alpha(\lambda)(d_{Gan}-d_{depl})}(1-e^{-\alpha(\lambda)d_{depl}}) \times \eta_{inj}(V)g(V), \quad (3)$$

where d_{depl} is the thickness of the depletion in the GaN absorption region and η_{inj} is the hole injection efficiency from the GaN into the SiC layer. This calculation assumes that only the photo-generated holes created in the depleted GaN absorption region are collected and the contribution of diffusion from the un-depleted region is negligible due to the short hole diffusion length expected in this material resulting from a high defect density. The product of the first and second terms of Eq. (3) is the incident photon flux on the depleted GaN absorption region.

The solid lines in Figure 1 top show the calculated SiC component of the photoresponse using Eq. (2). The QE of SiC, η_{SiC}, was measured using homogeneous SiC p-i-n APD structures having a 480 nm thick intrinsic region. Unity gain is assumed for reverse bias less than 130 V, while *g(V)* at higher bias is a fitting parameter. The agreement between the experimental results and the modeling is excellent, indicating that photoresponse for APD10 at all bias voltage prior to avalanche breakdown is from the collection of carriers generated directly in the SiC multiplication region with the GaN absorption layer acting as an optical filter and negligible GaN related photocurrent. The local maxima at 374 nm and minima at 365 nm are due to slowly increasing absorption in the SiC at wavelengths shorter than 380 nm superimposed with the initially rapid increasing absorption in the direct bandgap GaN region as the excitation wavelength approaches the band gap at ~363 nm.

However, Eq. (2) cannot on its own explain the change in response shape observed in APD15 with increasing bias. The solid lines in Figure 1 bottom show the calculated total photoresponse (Eq. (1)). In addition to the SiC component, the GaN component of the photoresponse is calculated from Eq. (3), where d_{depl}, η_{inj}, and g are fit to the experimentally measured data. This model agrees well for APD15, indicating that the GaN contribution to the photoresponse is responsible for the change in shape observed (Figure 1 bottom). Further, insight can be gained by considering the effect of the difference in net charge at the hetero-interface on the punch-through voltage

$$V_{Punch} \approx \frac{\sigma_n - N_A d}{\varepsilon_{SiC}} d_{SiC}. \quad (4)$$

where σ_n is the total density of interface charge, d_{SiC} is the depletion region thickness in the SiC, N_A is the density of acceptor dopants, and d is the thickness of the PICCL. The critical field for the onset of avalanche breakdown in the SiC multiplication region limits the reverse bias that can be applied on the diode to achieve punch-through of the electric field into the GaN absorption region. Therefore, excessive interface charge density will confine the electric field to the multiplication region and inhibit the collection of holes generated in the GaN, as observed through the lack of GaN photoresponse in APD10 despite the presence of a 10 nm PICCL. In contrast, increasing the PICCL thickness to 15 nm sufficiently reduces the net interface charge, so that punch-through is achievable prior to avalanche breakdown. As a result, GaN response is observed in APD15 at higher reverse bias due to the non-zero depletion region thickness in the GaN absorption region that enables the collection of holes photo-generated therein.

This conclusion is supported by C-V measurements taken on both APD10 and APD15. While the effective carrier concentration as a function of depletion width is nearly constant for APD10 (not shown), the measurements for APD15 show a transition from higher to lower effective carrier concentration that indicates the depletion of two layers with different net doping. Specifically, the nearly constant carrier concentration observed in region 1 is consistent with initially depleting the p-SiC region in the presence of the large 2DEG at the hetero-interface. A soft transition occurs in region 2 as the charge density in the p-SiC depletion region approaches that of the 2DEG, resulting in both areas depleting simultaneously with increasing bias. Once the 2DEG is fully depleted, punch-through occurs and the depletion region extends into the unintentionally doped GaN absorption layer, thereby exhibiting a lower carrier concentration (region 3). In contrast, the constant effective carrier density observed for APD10 at all reverse biases before avalanche breakdown indicates that punch-through of the E-field into the GaN absorption layer does not occur in these devices. It is important to note that the constant lower effective carrier concentration in region 3 is indicative of non-instantaneous depletion of the GaN absorption region that accounts for the gradual recession of the valley in the photoresponse observed at 365 nm in APD15 as a function of reverse bias (Figure 1 bottom), as predicted by Eq. (3).

Conventionally, the multiplication gain in an APD is calculated from the unity gain response by

$$G(V_b) = \frac{I_{photo}(V_b) - I_{dark}(V_b)}{I_{photo}(V_{G=1}) - I_{dark}(V_{G=1})}, \quad (5)$$

where G is the gain at reverse bias V_b and the dark current (I_{dark}) and photocurrent (I_{photo}) are measured at V_b and at a voltage corresponding to unity gain. However, this expression does not apply to the case of these GaN/SiC APDs because it does not account for the different components of the photocurrent at unity gain, I_{SiC}, and non-unity gain, I_{SiC} and I_{GaN} as well as the different net photon flux associated

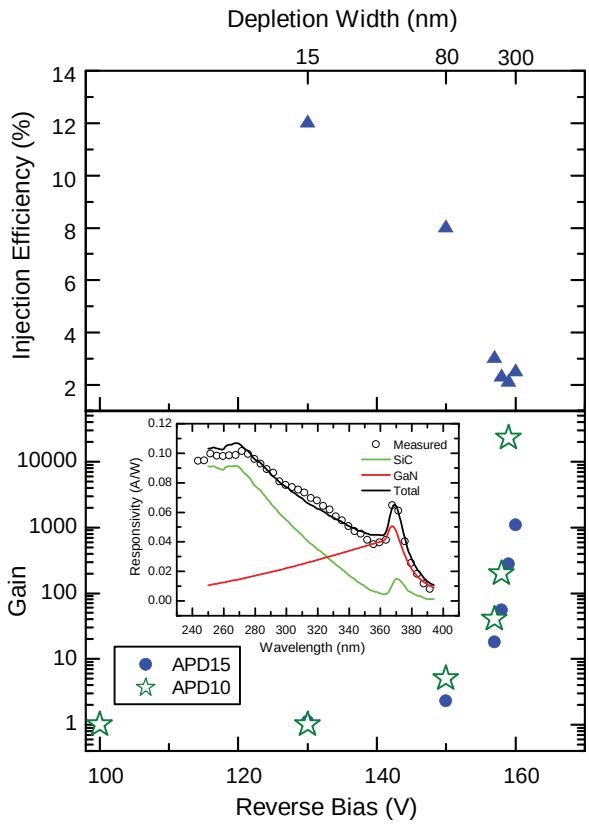

FIG. 3. Calculated hole injection efficiency (top) for APD15 and gain (bottom). For APD10 and APD15 as a function of reverse bias. Inset measured (open figures) and calculated (solid lines) photoresponse for APD15 at 157 V reverse bias. The SiC (light green) and GaN (medium red) components of the response are also provided.

with each component given by Eqs. (2) and (3). Instead, the multiplication gain from the devices is extracted from fitting the measured data to Eq. (1), as shown in Figure 3 (bottom) for both APDs. Independent of PICCL thickness, these devices exhibit a high gain greater than 1000 that is similar to that observed for homogeneous SiC APDs. However, APD10 exhibits a higher gain than APD15 at comparable biases greater than 130 V that is attributed to the component of the applied bias that is dropped across the GaN absorption region after punchthrough, which reduces the E-field in the SiC multiplication region at that bias relative to that for APD10. This effect accounts for the larger responsivity observed for APD10 over APD15 in Figure 1 at a given bias.

The hole injection efficiency and the GaN depletion width are also extracted from fitting the measured data to Eq. (1) and shown in Figure 3 (top, solid squares). The hole injection efficiency of these devices provides a practical equivalent to the external quantum efficiency (EQE), for comparison with SiC APDs. It peaks at 12% at low reverse bias and narrow GaN depletion thickness and decreases with increasing reverse bias and wider depletion to ∼3%. However, the peak injection efficiency of APD15 is larger than the EQE of comparable wholly SiC APDs in the 330–365 nm and up to 6 times larger near the GaN bandgap (363 nm), indicating that the GaN absorption region can significantly improve detector performance in the near ultraviolet spectral range[7] The observed low injection efficiency is attributed to the confluence of extended defects originating at the hetero-interface and the diminishing magnitude of the electric field with increasing distance from the hetero-interface associated with non-instantaneous depletion of the absorption region. As a result, the probability of collecting holes is less likely the farther from the interface they are generated, as is clearly evidenced by the SiC component dominating the total response of APD15 at wavelengths shorter than ∼330 nm (Figure 3 inset). A significant defect density in the GaN absorption region is expected due to the requirement for transport across the hetero-interface that restricts the use of commonly employed buffer layers such as AlN. In addition, impurities residing at the hetero-interface despite the surface preparation process may also play a role.

In summary, we have demonstrated that p-type PICCLs provide an effective means of optimizing the positive polarization induced interface charge in GaN/SiC SAM APDs to achieve high gain, low dark currents, and high responsivity in the near ultraviolet spectrum. Studies of the DC photoresponse on APDs with insufficient PICCL thickness indicate that hole injection from the GaN absorption region to the SiC multiplication region is negligible prior to avalanche breakdown due to the inability to achieve punch-through of the electric field into GaN in the presence of excess positive interface charge. With increasing PICCL thickness, punch-through can be achieved, and the resulting hole injection efficiency from the GaN can be larger than the EQE from 4H-SiC photodiodes in the 330–365 nm spectral range.

[1]X. G. Bai, X. Y. Guo, D. Mcintosh, H. D. Liu, and J. C. Campbell, IEEE J. Quantum Electron **43**, 1159 (2007).
[2]J. B. Limb, D. Yoo, J. H. Ryou, W. Lee, S. C. Shen, R. D. Dupuis, M. L. Reed, C. J. Collins, M. Wraback, D. Hanser, E. Preble, N. M. Williams, and K. Evans, Appl. Phys. Lett. **89**, 011112 (2006).
[3]R. McClintock, J. L. Pau, K. Minder, C. Bayram, P. Kung, and M. Razeghi, Appl. Phys. Lett. **90**, 141112 (2007).
[4]Q. G. Zhou, D. McIntosh, Z. Lu, J. C. Campbell, A. V. Sampath, H. Shen, and M. Wraback, Appl. Phys. Lett. **99**, 131110 (2011).
[5]E. Danielsson, C. M. Zetterling, M. Ostling, K. Linthicum, D. B. Thomson, O. H. Nam, R. F. Davis, Solid-State Electron. **46**, 827 (2002).
[6]D. Korakakis, A. V. Sampath, H. M. Ng, G. Morales, I. D. Goepfert, T. D. Moustakas, MRS Proc. **395**, 151 (1995).
[7]H. D. Liu, D. Mcintosh, X. G. Bai, H. P. Pan, M. G. Liu, J. C. Campbell, and H. Y. Cha, IEEE Photon. Technol. Lett. **20**, 1551 (2008).

C-QWIPs for Space Exploration

K. K. Choi, M. D. Jhabvala, D. P. Forrai, J. Sun, and D. Endres

Infrared Physics & Technology, 54 (2011)

Contents lists available at ScienceDirect

Infrared Physics & Technology

journal homepage: www.elsevier.com/locate/infrared

C-QWIPs for space exploration

K.K. Choi [a,*], M.D. Jhabvala [b], D.P. Forrai [c], J. Sun [a], D. Endres [c]

[a] US Army Research Laboratory, Adelphi, MD 20783, USA
[b] NASA Goddard Space Flight Center, Greenbelt, MD 20771, USA
[c] L3-Cincinnati Electronics, Mason, OH 45040, USA

ARTICLE INFO

Article history:
Available online 25 December 2010

Keywords:
QWIP
FPA
NEΔT

ABSTRACT

We have extended our investigation of corrugated quantum well infrared photodetector focal plane arrays (C-QWIP FPAs) into the far infrared regime. Specifically, we are developing the detectors for the thermal infrared sensor (TIRS) used in the NASA Landsat Data Continuity Mission. This mission requires infrared detection cutoff at 12.5 μm and FPAs operated at ~43 K. To maintain a low dark current in these extended wavelengths, we adopted a low doping density of 0.6×10^{18} cm^{-3} and a bound-to-bound state detector in one of the designs. The internal absorption quantum efficiency η is calculated to be 25.4% for a pixel pitch of 25 μm and 60 periods of QWs. With a pixel fill factor of 80% and a substrate transmission of 70.9%, the external η is 14.4%. To yield the theoretical conversion efficiency CE, the photoconductive gain was measured and is 0.25 at 5 V, from which CE is predicted to be 3.6%. This value is in agreement with the 3.5% from the FPA measurement. Meanwhile, the dark current is measured to be 2.1×10^{-6} A/cm^2 at 43 K. For regular infrared imaging above 8 μm, the FPA will have a noise equivalent temperature difference (NETD) of 16 mK at 2 ms integration time in the presence of 260 read noise electrons, and it increases to 22 mK at 51 K. The highest operability of the tested FPAs is 99.967%. With the CE agreement, we project the FPA performance in the far infrared regime up to 30-μm cutoff, which will be useful for the Jupiter-Europa deep space exploration. In this work, we also investigated the C-QWIP optical coupling when the detector substrate is thinned.

Published by Elsevier B.V.

1. Introduction

We have developed the corrugated quantum well infrared photodetector focal plane array (C-QWIP FPA) technology for a number of years. At present, both the theoretical model and the production processes are sufficiently mature such the FPA properties are well understood in the quantitative manner while high production yield is consistently maintained. In this work, we applied this technology to the NASA Landsat project and obtained satisfactory results. In view of the agreement between theory and experiment in these and other detectors in the long wavelength regime, we extend the C-QWIP model to the far infrared and predict its performance up to 30-μm cutoff. In this work, we also perform a three-dimensional (3D) finite element electromagnetic (EM) field simulation to investigate the effects of substrate thickness on the C-QWIP optical properties.

2. TIRS5 FPA

In this section, we apply the classical geometric-optical (GO) C-QWIP model [1] to one of the FPAs developed for a thermal infrared sensor (TIRS) instrument [2]. To predict the external quantum efficiency η of a C-QWIP FPA, the absorption coefficient $\alpha(\lambda)$ of the QWIP material is first calculated for parallel propagating light with a proper polarization. $\alpha(\lambda)$ is given by

$$\alpha(\lambda) = \sum_n \frac{N_D W}{L} \frac{\pi e^2 \hbar}{2\sqrt{\varepsilon_h}\varepsilon_0 m^* c} f_n \rho_n(\lambda), \tag{1}$$

where N_D is the doping density in the well, W is well width, L is the QW period length, f_n is the oscillator strength from the ground state to the nth excited state, and ρ_n is the normalized Gaussian broadening for each optical transition. The values of f_n are obtained after solving the eigen energies and eigen functions of the structure. The C-QWIP pixel structure reflects the normally incident light into parallel propagation, with which η under the GO model is given by

$$\eta(V,\lambda) = t_s f_p \eta_{\text{int}} = t_s f_p \kappa \frac{1}{p}\left[t + \frac{e^{-\alpha p}}{2\alpha}(1 - e^{2\alpha t})\right]\gamma(V). \tag{2}$$

In Eq. (2), t_s is the substrate transmission, f_p is the pixel fill factor, η_{int} is the internal quantum efficiency, κ is a factor proportional to the thickness of the active layer inside a corrugation [1], p is the pixel linear dimension, t is the corrugation height, and

* Corresponding author. Tel.: +1 301 394 0495; fax: +1 301 394 1157.
E-mail address: kwongkit.choi@us.army.mil (K.K. Choi).

$\gamma(V)$ is the transmission coefficient of a photoelectron traveling out of the QW at a bias V. The resulting photocurrent J_p generated within a C-QWIP pixel is then

$$J_p(V,T_B) = \frac{\pi}{4F^2+1} eg(V) \int_{\lambda_1}^{\lambda_2} \eta(V,\lambda) L(T_B,\lambda) d\lambda, \tag{3}$$

where T_B is the scene temperature, $g(V)$ is the photoconductive gain obtained from noise measurement, λ_1 and λ_2 are the lower and upper wavelengths encompassing the detector absorption spectrum, F is the f-number of the optical system, and $L(T_B, \lambda)$ is the photon spectral radiance.

The QWIP material described in this section is labeled as TIRS5. It is made of 60 periods of 700-Å $Al_{0.172}Ga_{0.828}As$ and 60-Å GaAs. To avoid dopant migration during the material growth, only the center part of the well is doped such that the equivalent N_D is 0.6×10^{18} cm^{-3} in the well. The active QW material is sandwiched between two GaAs contact layers. The top layer is 3.67 μm thick and the bottom layer is 4.15 μm thick. Applying Eq. (1) to this material, the value of α is shown in Fig. 1. Its peak value is 0.17 μm^{-1}. The calculation shows that the structure is a bound-to-bound (B–B) state detector because its peak is below the barrier height. The combination of a low doping density and the B–B detector structure ensures a low dark current for this long wavelength detector.

Inserting $\alpha(\lambda)$ into Eq. (2), η_{int} and η can be obtained. With $p = 25$ μm, $t = 11$ μm and $K = 0.69$ for 60 QWs, the peak η_{int} is 25.4%. For the present uncoated FPA, $t_s = 0.709$, and assuming $f_p = 0.80$ and $\gamma = 1$ at high bias, the calculated external η is shown in Fig. 2 with a peak value of 14.4%. To know the external conversion efficiency CE ($\equiv \eta g$), the photoconductive gain $g(V)$ was obtained from the noise measurement and is shown in Fig. 3. At the substrate bias of 5 V, g was measured to be 0.25, with which the peak CE is predicted to be 3.6%. The material was processed into C-QWIP FPAs and the arrays were hybridized to Indigo 9803 640 × 512 readout circuits (ROICs). The measured CE from one of the FPAs is shown in Fig. 4. It increases with the applied bias, and at 5 V, it was measured to be 3.5%, agreeing with the prediction at 3.6%. The dashed curve in Fig. 4 is the same curve shown in Fig. 2 but was shifted to a shorter wavelength by 0.35 μm to match the experimental spectrum. From the agreements on both the magnitude and lineshape, one can assess the accuracy of the detector model in predicting the C-QWIP optical properties. Using the fitted CE spectrum (dashed curve in Fig. 4), the calculated detector photocurrent from Eq. (3) is 1.19×10^{-4} A/cm^2 (or 4.62×10^9 e/s/pixel) with $F/2$ optics and 294 K background when imaging at $\lambda > 8$ μm.

In addition to the optical properties, the dark current of a C-QWIP can also be modeled and predicted in sufficient accuracy.

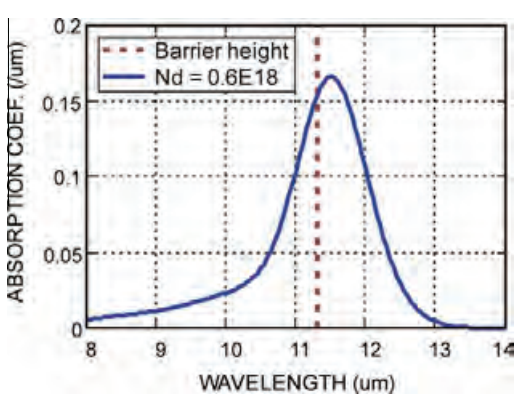

Fig. 1. The calculated absorption coefficient α of TIRS5. The straight line divides B–B transitions on the right and bound-to-continuum transitions on the left.

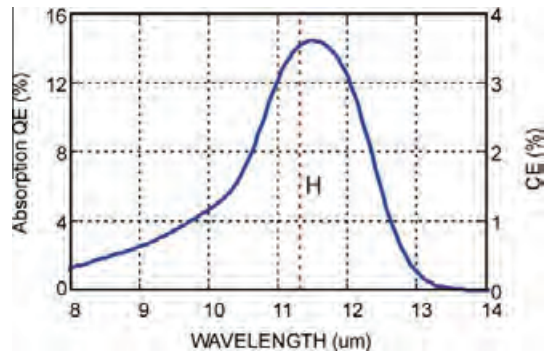

Fig. 2. The calculated η and CE spectra of TIRS5 for $g = 0.25$.

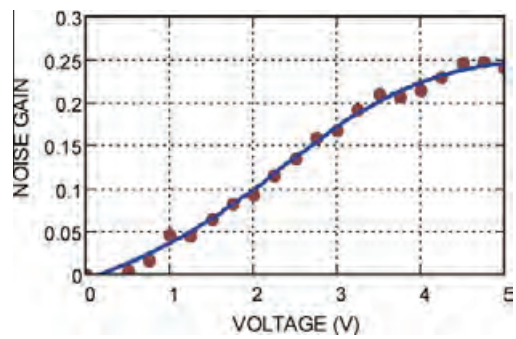

Fig. 3. The photoconductive gain of TIRS5 obtained from noise measurement.

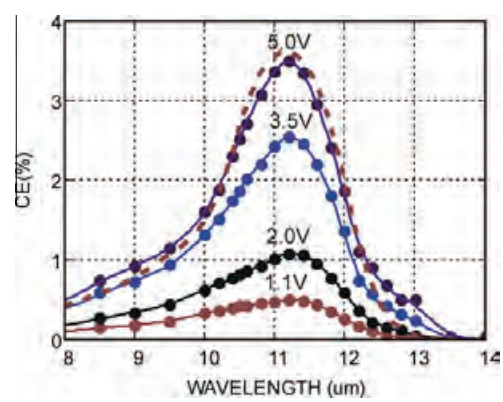

Fig. 4. The measured spectral conversion efficiency of a TIRS5 FPA at different bias (circles) and the calculated CE (dashed curve) at 5 V, which has been blue shifted by 0.35 μm.

The dark current transport can be classified into three main mechanisms, which are direct tunneling (DT) between adjacent QWs, thermally assisted tunneling (TAT) near the tip of a tilted barrier under bias, and thermionic emission (TE) over the barrier. All of these three transport mechanisms can be incorporated into a single expression [3], in which

$$\begin{aligned} J(V,T) &= \int_{E_1}^{\infty} J(E,V,T)dE, \\ &= \int_{E_1}^{\infty} e\rho f(E,T)\gamma(E,V)v(V)dE, \\ &= \int_{E_1}^{\infty} e\frac{m^*}{\pi\hbar^2 L}\frac{\gamma(E,V)}{1+\exp\left(\frac{E-E_F-E_1}{kT}\right)}\frac{\mu V/L}{\sqrt{1+\left(\frac{\mu V}{Lv_{\text{sat}}}\right)^2}}dE. \end{aligned} \tag{4}$$

In Eq. (4), $J(V,T)$ is the measured dark current density, $J(E,V,T)$ is the current density per meV, ρ is the effective 3D density of states in the QW, $f(E,T)$ is the Fermi–Dirac energy distribution, γ is the tunneling probability out of the QW, and $v(V)$ is the electron drift velocity. The value of γ is given by the usual WKB expression, and $v(V)$ is related to the low field mobility μ at low bias and the saturation velocity v_{sat} at the high bias as shown in Eq. (4).

At very low T, when $f(E,T)$ is essentially 1 for $E < E_F$ and 0 when $E > E_F$, Eq. (4) describes the DT process. When T increases, the finite $f(E,T)$ above E_F creates the TAT current. At the very high T, more electrons can be excited above the barrier with which $\gamma = 1$. TE process then dominates. To visualize their relative contributions at different T, the normalized $J(E,V,T)$ for the present TIRS5 structure is plotted in Fig. 5 at $V = 83$ mV/period and different T. It is shown that the carrier distribution moves up quickly in energy as T increases and at $T \sim 43$ K, the dark carriers are conducting just below the tip of the tilted barrier.

Fig. 6 shows the measured and fitted dark current for TIRS5 C-QWIP test detectors. The three fitted parameters in Eq. (4) are $H = 157.1$ meV in the WKB expression, $\mu = 400\ \mathrm{cm^2/V\,s}$ and $v_{sat} = 1 \times 10^7$ cm/s. The value of H is close to the 163.5 meV deduced from the spectral response measurement and v_{sat} is the same as the known saturation velocity for GaAs. We found that the present fitted values of μ and v_{sat} are the same for all detectors having λ_c ranging from 9 to 13 μm, showing the consistency of the model. Only for shorter wavelength QWIPs, such as the one at $\lambda_c = 8.6$ μm, a smaller μ of 120 $\mathrm{cm^2/V\,s}$ was observed. Fig. 6 also shows the background generated photocurrent J_p of the test detector. At 5 V, J_p is observed to be 3.24×10^9 e/s/pixel, which is 70% of the predicted value of 4.62×10^{-9} e/s/pixel. Since the transmission loss of the KRS-5 window in the optical dewar is 70%, the two measurements thus agree to within experimental error.

With the known $J_p = 4.62 \times 10^9$ e/s/pixel, the measured J_d in Fig. 6 and $g = 0.25$ at 5 V, the NEΔT of a TIRS5 FPA can be estimated from [4]

$$NE\Delta T = \frac{1}{C}\left[\left(\frac{2gN_{tot} + n_{rd}^2}{N_{tot}^2}\right)\left(1+\frac{1}{r}\right)^2 + u^2\right]^{1/2}, \tag{5}$$

where $C = 0.0149$ is the thermal contrast, N_{tot} is the total number of electrons collected in an integration time τ_{int}, $n_{rd} = 260$e is the measured number of read noise electrons, and $r = J_p/J_d$ is the photocurrent to dark current ratio. The parameter u is the spatial nonuniformity, which is assumed to be zero here. Eq. (5) thus considers only two noise sources, which are the detector g–r noise from both the photocurrent and the dark current and the ROIC noise. The presence of other noise sources such as cooler induced noise and target thermal fluctuations are ignored. Fig. 7 shows the expected NEΔT as a function of operating temperature T for different τ_{int}. NEΔT is 16 and 22 mK at $T = 43$ and 51 K, respectively, for $\tau_{int} = 2$ ms. This result assumes the use of the full spectrum at $\lambda > 8$ μm. With different adopted filter bandwidth, $f/\#$ and detector bias in the TIRS instrument, a different τ_{int} may be needed to achieve the same NEΔT. We also note that the fabricated FPAs typically have very high operability, being in the range of 99.96%.

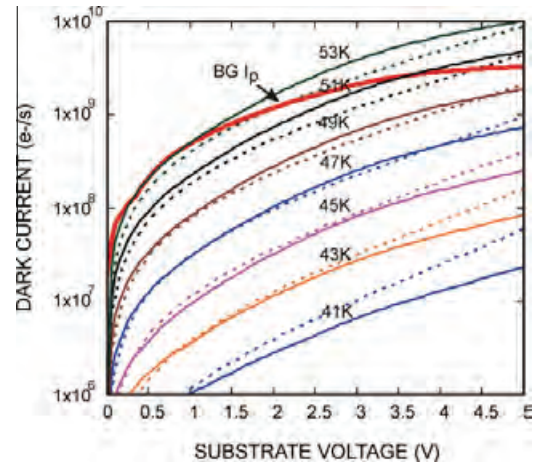

Fig. 6. The measured dark current (solid curves) of a large area C-QWIP test detector normalized to the pixel area. The dashed curves are the fitted current using Eq. (4). The thick solid curve shows the measured background photocurrent of the test detector.

3. LC9 FPA

To further substantiate the detector model, we apply the same analysis to another FPA in this section. This FPA is labeled as LC9. The material is made of 60 periods of 700 Å $Al_{0.19}Ga_{0.81}As$ and 50 Å GaAs. The center part of the well is doped with the equivalent N_D of $1.7 \times 10^{18}\ \mathrm{cm^{-3}}$ in the well. Since it is a bound to quasi-bound plus (B–Q+) detector, the spectral width of $\alpha(\lambda)$ is wider than that of TIRS5, while the peak value is about the same at 0.18 $\mu\mathrm{m}^{-1}$ despite a higher N_D. The calculated peak η_{int} and η are thus about the same as that of TIRS5 and they are 26.1% and 18.8%, respectively. In the η estimation, we have assumed $t_s = 0.9$ for the present AR-coated FPA, and $f_p = 0.80$. The calculated η is shown in Fig. 8 as a solid curve. By measuring the noise gain at dif-

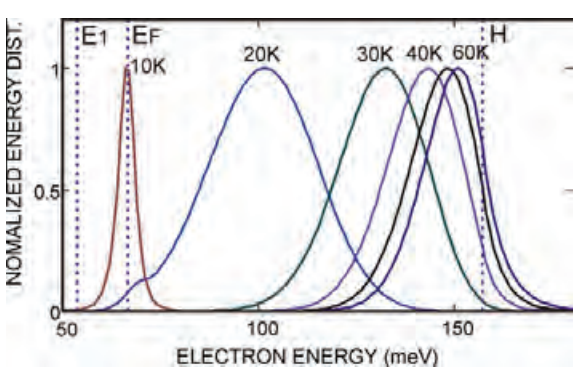

Fig. 5. The plot shows the normalized energy distribution of the conducting dark electrons at different temperatures. The assumed bias is at 5 V or 83 mV/period. In this plot, E_1 is the ground state energy relative to the GaAs band edge, E_F is the Fermi energy, and H is the barrier height of the QW. TAT current dominates in the entire calculated temperature range except at 10 K.

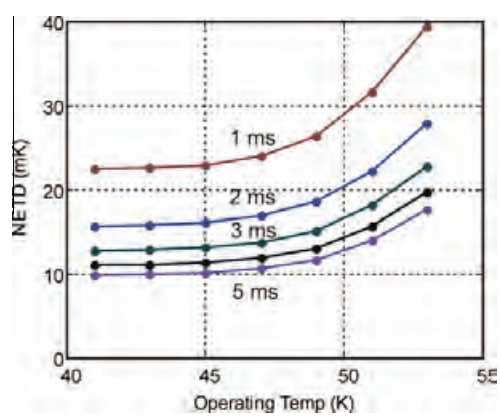

Fig. 7. The calculated NEΔT of a TIRS5 FPA operated under different temperatures and integration times for 260 noise electrons, $F/2$, and 5 V based on the measured photocurrent and dark current.

ferent bias, the value of CE can be obtained. At $V = -3$ V, $g = 0.25$ and thus the calculated CE is 4.7% at this bias.

The material was processed into 1024 × 1024 C-QWIP FPAs and the arrays were hybridized to L3-Cincinnati Electronics ROICs. The measured CE from one of the FPAs is shown as circles in Fig. 9 up to −2.5 V. By fitting this data with the trend of the background photocurrent, CE at −3 V is deduced to be 4.9%, which agrees with the 4.7% from calculation. The measured FPA CE spectrum is shown as circles in Fig. 8. It agrees quite well with the calculated spectrum. The sharp decrease of signal in approaching 8 μm was caused by the presence of an 8-μm cold filter in the camera. The measured η as a function of bias is shown in Fig. 9. The average value of 20% is in agreement with the 18.8% from calculation.

The current–voltage (I–V) characteristics of this QWIP material are asymmetric with respect to bias polarity. Under negative bias where the present ROIC operates, the material has a larger dark current than that under positive bias. As a result, the FPA shows background limited performance (BLIP) at a lower temperature of 50 K at −3 V rather than 55 K at +3 V. The calculated NEΔT based on the observed dark current at $-V$ is 12 and 20 mK, respectively, at $T = 45$ and 52 K for $\tau_{int} = 2$ ms. Fig. 10 shows an infrared image taken at $T = 52$ K, 1 V and $\tau_{int} = 2.0$ ms.

Fig. 10. Shows a 1-megapixel infrared image taken by an LC9 FPA at $T = 52$ K, −1 V and $\tau_{int} = 2.0$ ms.

4. Far infrared C-QWIP FPAs

From the previous examples, one can observe that most of the C-QWIP FPA properties can be designed and predicted in high accuracy. In the following example, we attempt to predict the FPA performance in the far infrared. The band structure of the material design is shown in Fig. 11. By varying the QW thickness within the superlattice between the two 1000-Å blocking barriers, a wide detection spectrum can be achieved. The cutoff wavelength λ_c of this structure is determined by the bandgap of the two lowest minibands, which can be made small by changing the QW thicknesses. This material design allows a very long λ_c (30 μm, in this case) to be reached without having a very low barrier height to maintain the material uniformity. Fig. 12 shows the calculated η_{int} for 63 QW periods, which will fill up a corrugation having a period of 25 μm. (Each pixel may contain several corrugations in these very long wavelength FPAs.) The peak η_{int} is calculated to be 35% for a doping of 0.9×10^{18} cm^{-3}. Fig. 12 also shows the radiation spectrum of a 110-K blackbody as, for example, encountered on the surface of one of Jupiter's moons, Europa. The proposed detector will be adept in observing such a cold scene.

The dark current can be similarly calculated using $\mu = 400$ cm^2/V s, $v_{sat} = 1 \times 10^7$ cm/s and $H = 101$ meV, and it is shown in Fig. 13 also shows the background generated photocurrent under $F/2$ for two background temperatures T_B. In estimating J_p, we have assumed the same gain in Fig. 3 for TIRS5 as they have a similar number of QWs. In this example, we also assumed a 100% fill factor and unity substrate transmission for simplicity. Due to the broadband characteristics of this material, the detector photocurrent is about eight times larger than that of TIRS5 at the same T_B of 300 K. Furthermore, because of its very long λ_c, J_p is reduced only by 100 times when T_B is reduced to 110 K and it still maintains a substantial level at $\sim 1 \times 10^{-5}$ A/cm^2. Since the dark current decreases exponentially in T, the reduction of J_p translates to less than 10-K reduction in the BLIP temperature from that with the 300-K back-

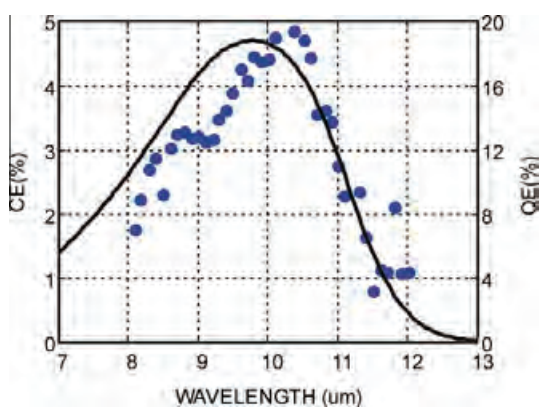

Fig. 8. The figure shows the measured spectral conversion efficiency of an LC9 FPA at different bias (circles) and the calculated η and CE (solid curve) at −3 V.

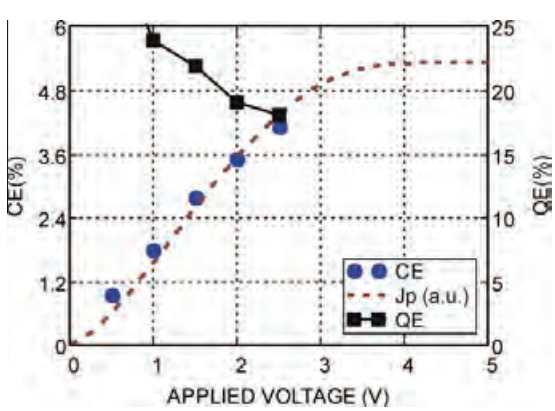

Fig. 9. The figure shows the measured FPA CE (circles) and the deduced η (squares). The dashed curve is the measured background photocurrent and was scaled to fit the CE data. The maximum CE is expected to be 5.3% occurred at −4 V.

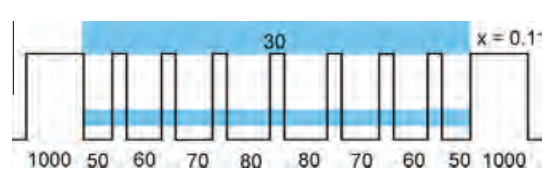

Fig. 11. The band structure of a quantum well period of a broadband QWIP with λ_c equal to 30 μm. The numerals are the layer thicknesses in Å. The aluminum molar ratio is 0.11. The figure also shows the two lowest minibands.

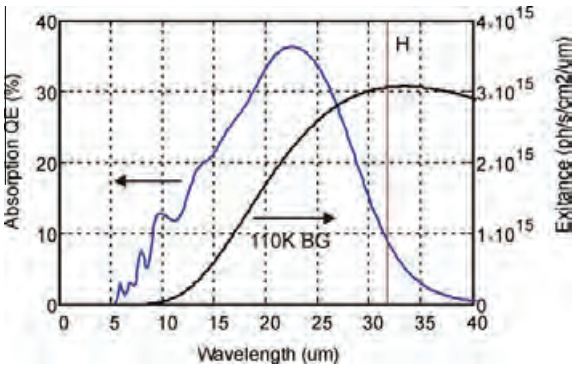

Fig. 12. The absorption spectrum of the proposed material and the emission spectrum of a 110-K blackbody.

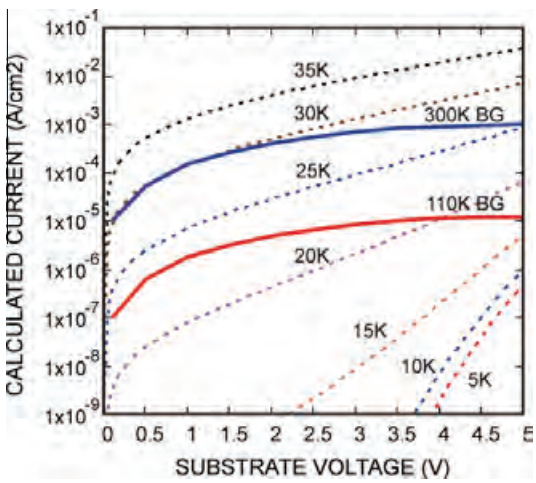

Fig. 13. The calculated dark current (dashed curves) and the calculated background photocurrent (solid curves) under two background temperatures for a C-QWIP FPA.

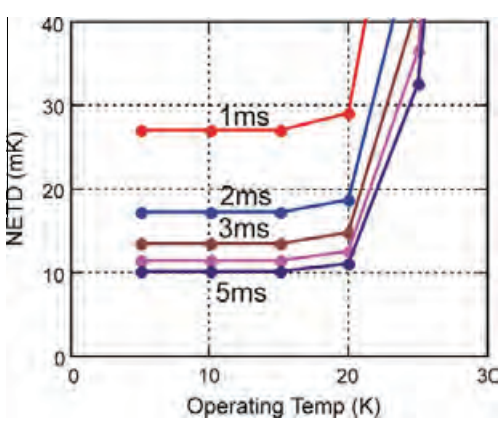

Fig. 14. The calculated NEΔT of a hypothetical C-QWIP FPA with $\lambda_c = 30\ \mu m$ operated under different temperatures and integration times for 260 noise electrons, $F/2$ and 3 V in viewing a 110-K scene.

ground. In the present example, it shows BLIP at about 21 K at +3 V. The corresponding NEΔT for this hypothetical FPA is shown in Fig. 14, assuming 260 noise electrons and a thermal contrast C of 0.0478 between 5 and 35 μm at $T_B = 110$ K. Such a camera is expected to resolve a 10-mK temperature difference when operated below 20 K.

5. C-QWIPs with thin substrate

In this section, we discuss the C-QWIP optical coupling when all the detector dimensions are comparable to the optical wavelength. When the substrate is thick, the light reflected from the substrate is incoherent with the incoming light. The only optical interference is between the light reflected from the two opposite detector sidewalls. We have shown in such case [5] that the classical GO model of Eq. (2) agrees well with the electromagnetic (EM) field simulation when the linear pixel size is larger than 10 μm. This is true for the LC9 FPA, which has a ~30-μm-thick substrate. But when the substrate is completely removed, as in the TIRS5 FPA, the optical interference from the tightly confined optical field within the detector volume should change the classical absorption, and yet the TIRS5 FPA continues to agree well with the classical model. To understand the detector characteristics in this case, a 3D EM field simulation was performed using a commercial EM solver. The investigated detector structures are shown in Fig. 15. They are either prism-shaped C-QWIPs (labeled as prism-QWIP or PR-QWIP), as adopted in TIRS5 and LC9 FPAs, or pyramid-shaped C-QWIPs (labeled as pyramid-QWIP or PY-QWIPs), as adopted in some of the previous FPAs [5]. The detectors are assumed to be surrounded by air with proper boundary conditions. The incoming light is polarized diagonal to the pixels to represent unpolarized light.

Fig. 16 shows the external unpolarized absorption η for 25 μm pixel pitch FPAs. In this case, the pixel sizes (L, W, H) are $25 \times 25 \times 11\ \mu m^{-3}$ for the PR-QWIP and $25 \times 25 \times 11\ \mu m^{-3}$ for the PY-QWIP. In order to compare these detector structures to the typical grating structure, we also performed a calculation on a $24 \times 24 \times 1.5\ \mu m^{-3}$ cross grating-QWIP. All the detectors have the same common contact layer thickness of 1.5 μm. The entire

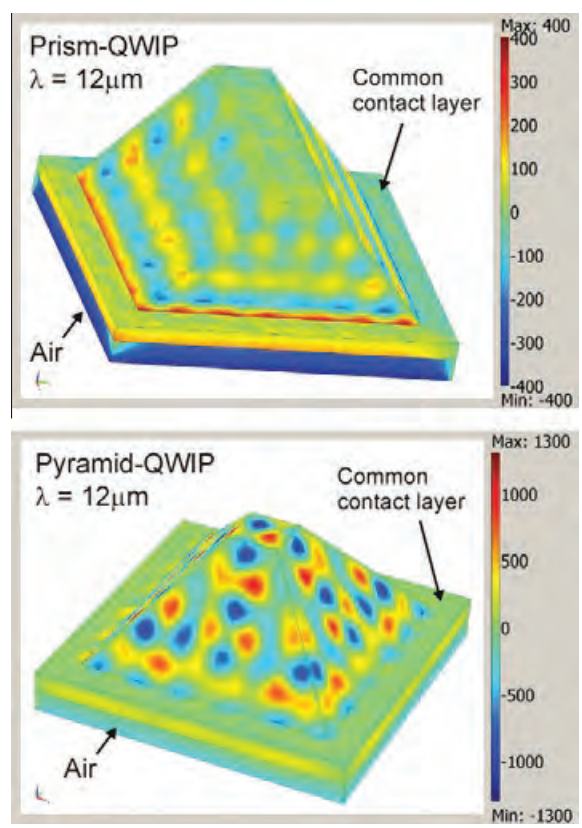

Fig. 15. The detector structures used in the EM field simulation. The left-hand panel shows the PR-QWIP, and the right-hand panel shows the PY-QWIP. The contour pattern shows the optical E_z distribution on the detector surface.

pixel volume is assumed to be filled with active material and the absorption coefficient is assumed to be constant at 0.15 μm^{-1}. There are no AR-coatings in these detectors.

Fig. 16 shows that without a substrate, C-QWIP coupling is also dependent on wavelength. A more detailed examination shows that the locations of these η peaks can be accurately described by the Fabry–Perot resonances applying to the corrugation structure. For the PR-QWIP, these oscillations are centered about the classical value of 24.5% (for $t_s = 0.709$, $f_p = 1$ and $\kappa = 1$) near the 11-μm regime. This proximity to the classical value explains the applicability of Eq. (2) to the TIRS5 FPA data, and the substrate thinning in this case does not affect the overall FPA performance. On the other hand, the PY-QWIP shows a much more pronounced resonant effect and the η oscillates mainly above its classical value [5],

$$\eta = t_s f_p \eta_{\text{int}} = t_s f_p \kappa \frac{e^{-\alpha p}}{\alpha^2 p^2}\{\, 1 + \alpha p + 2\alpha^2 t(p-t)e^{\alpha p} + [\alpha(2t-p)-1]e^{2\alpha t}\}, \quad (6)$$

of 30.9% (for $t_s = 0.709$, $f_p = 1$ and $\kappa = 1$) within the displayed wavelength range. At 8.2, the peak value can reach 43%. This calculation thus shows that the PY-QWIP benefits more from substrate removal. However, we should emphasize that this large theoretical η assumes total phase coherence within the detector volume. The actual enhancement will rely on the degree of coherence of infrared radiation within the detector and has yet to be determined by experiments.

Fig. 16 also shows the simulation result on grating coupled QWIPs. The grating period is either 3 or 5 μm, and the grating depth is 0.75 μm. Following the grating formula, the 3-μm grating is optimized for 10-μm detection. Surprisingly, the simulation did not yield a 10-μm peak. Instead, it shows that the detector pixels, due to their small and finite sizes, behave more like resonators than gratings. A large η is observed when one of the eigen-modes of the resonator is excited by the incoming light. The three peaks appear at 13.0, 11.0, and 8.4 μm, which, upon examining the vertical electric field distributions, correspond to the first, second, and third harmonics of the eigen-modes, respectively. The grating features on top of the pixel in this case facilitate the excitation of these modes by individually dispersing the incoming light into different directions. The grating period thus does not relate to the detection wavelengths, as Fig. 16 shows. When the fundamental mode is excited, the resonator can provide a large η of ~11.3% at 11 μm. However, the coupling decreases rapidly at higher harmonics and, near the typical 8–9 μm detection, it is only about 3.3% via the third harmonic for the assumed α of 0.15 μm^{-1}. The value of η can be improved by adopting higher doping density, thicker detector material, and possibly AR-coating. Nevertheless, the present η is within the same range as that observed in some commercial QWIP FPAs, and the calculated lineshape is in agreement with a grating-QWIP coupled to a broadband detector material [2] and explains the narrow 8–9 μm lineshape of typical QWIP FPAs with 25 μm pixel pitch. The agreements obtained in the PR-QWIP and the grating-QWIP cases thus lend experimental support to the present EM field simulation.

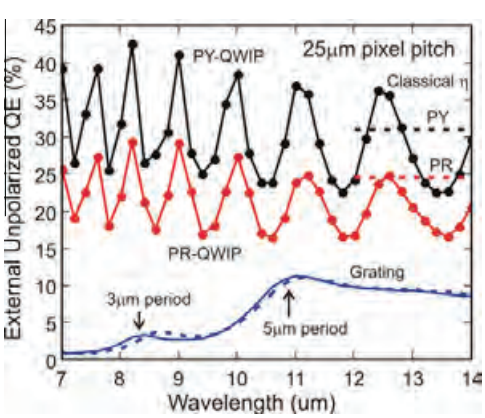

Fig. 16. The theoretical η for QWIPs with different detector geometries when the substrate is absent. The assumed pixel pitch is 25 μm and the common contact layer thickness of 1.5 μm. The straight lines are the classical values.

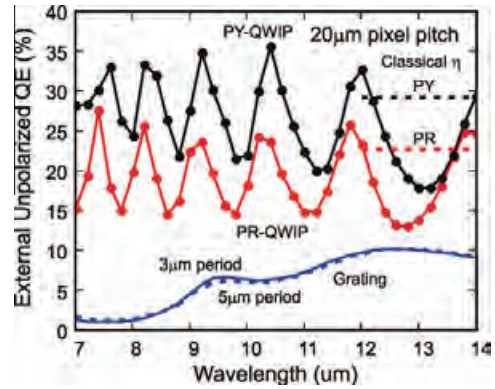

Fig. 17. The theoretical η for QWIPs with different detector geometries when the substrate is removed. The assumed pixel pitch is 20 μm and the common contact layer thickness of 1.5 μm. The straight lines are the classical values.

The trend of FPAs is toward high density and small pixels. The case for a 20-μm pixel pitch is examined in Fig. 17. The assumed pixel sizes are $20 \times 20 \times 8.8\ \mu m^{-3}$ for the PR-QWIP, $20 \times 20 \times 9.1\ \mu m^{-3}$ for the PY-QWIP and $18 \times 18 \times 1.5\ \mu m^{-3}$ for the grating-QWIP. The classical η for the PR-QWIP and the PY-QWIP of these sizes are 22.8% and 29.1%, respectively. As in the previous case, η of the PR-QWIP oscillates close to its classical value near 11 μm. At the shorter λ of 8.2 μm, the peak η can reach 25.4%. For the PY-QWIP, it is higher at 33.3% in the same λ range. For the grating-QWIP, the smaller cavity dimensions lead to shorter resonant wavelengths. The second harmonic peak, now at 9.6 μm instead of 11 μm, produces a η of 6.7% at this wavelength. Overall, the resonant C-QWIP structures are shown to be more capable for 8–14 μm detection.

6. Conclusion

We have applied a classical geometric-optical model and a dark current model to describe the opto-electronic properties of C-QWIP FPAs and obtained quantitative agreement. Both the TIRS5 and LC9 FPAs are competent in high-speed imaging with NEΔT in the order of 20 mK at a 2-ms integration time and $T \sim 50$ K. The LC9 FPA, which has an AR-coating and a higher doping density, exhibits a higher external quantum efficiency of 20% and a broad spectral band of 4 μm. By applying the same detector model to far infrared detection, we found that a C-QWIP FPA is capable of providing 10-mK sensitivity in observing a 110-K scene. Such a sensitive FPA, together with the promise of reliability, affordability, and uniformity of the GaAs material, will be very useful for space explorations particularly in detecting and observing cold objects. In this work, we also adopted a 3D finite-element EM field simulation to study the detector properties when the detector substrate is absent. It turns out that the performance of the prism-shaped C-QWIP structure, which is used in the present C-QWIP FPAs, is less dramatically affected by the substrate thickness. On the other hand, the pyramid-shaped C-QWIP shows a stronger resonant effect and its theoretical value can be as high as 42%. If the thermal radiation within the C-QWIP shows a high degree of coherence, as assumed in the theory, the detector structure will be very useful for infrared detection. Experimental effort is underway.

References

[1] K.K. Choi, D.P. Forrai, D.W. Endres, J. Sun, Corrugated quantum well infrared photodetector focal plane arrays, IEEE J. Quant. Electron. 45 (2009) 1255.

[2] M. Jhabvala, D. Reuter, K. Choi, M. Sundaram, C. Jhabvala, A. La, A. Waczynski, J. Bundas, The QWIP focal plane assembly for NASA's Landsat Data Continuity Mission, Proc. SPIE 7660 (2010) 76603I-11.

[3] B.F. Levine, C.G. Bethea, G. Hasnain, V.O. Shen, E. Pelve, R.R. Abbott, S.J. Hsieh, High sensitivity low dark current 10 μm GaAs quantum well infrared photodetectors, Appl. Phys. Lett. 56 (1990) 851.

[4] K.K. Choi, C.J. Chen, A.C. Goldberg, W.H. Chang, D.C. Tsui, Performance of corrugated quantum well infrared photodetectors, Proc. SPIE 3379 (1998) 441.

[5] K.K. Choi, K.M. Leung, T. Tamir, C. Monroy, Light coupling characteristics of corrugated quantum well infrared photodetectors, IEEE J. Quant. Electron. 40 (2004) 130.

Detection and Characterization of Biological and Other Organic-Carbon Aerosol Particles in Atmosphere Using Fluorescence

Yong-Le Pan

Journal of Quantitative Spectroscopy & Radiative Transfer, 150 (2015)

Contents lists available at ScienceDirect

Journal of Quantitative Spectroscopy & Radiative Transfer

journal homepage: www.elsevier.com/locate/jqsrt

Detection and characterization of biological and other organic-carbon aerosol particles in atmosphere using fluorescence

Yong-Le Pan*

U.S. Army Research Laboratory, Adelphi, MD 20783-1197, USA

ARTICLE INFO

Article history:
Received 24 February 2014
Received in revised form
5 June 2014
Accepted 13 June 2014
Available online 5 July 2014

ABSTRACT

This paper offers a brief review on the detection and characterization of biological and other organic-carbon (OC) aerosol particles in atmosphere using laser-induced-fluorescence (LIF) signatures. It focuses on *single individual particles or aggregates* in the micron and super-micron size range when they are successively drawn through the interrogation volume of a point detection system. Related technologies for these systems that have been developed in last two decades are also discussed. These results should provide a complementary view for studying atmospheric aerosol particles, particularly bioaerosol and OC aerosol particles from other analytical technologies.

Published by Elsevier Ltd. This is an open access article under the CC BY-NC-ND license (http://creativecommons.org/licenses/by-nc-nd/3.0/).

1. Introduction

Organic-carbon (OC) aerosols, including bioaerosols, play an important role in atmospheric aerosols. They are essential to fields of science ranging from Earth climate to human health. Extensive research over many years has been aimed at detecting and characterizing the OC and bioaerosol fraction of atmospheric aerosols using a variety of techniques ranging from bacteria cultures, to single particle mass spectrometry (MS), to chromatographic studies of extracts of collected particles. Typically, the various methods provide very different information, each affording a different view of the extremely complex mixture of atmospheric aerosols. Optical and electron microscopy imaging can supply particle size and shape directly, whereas elastic scattering uncovers morphology information, as well, even from single-moving particles. Laser-breakdown (LIBs) and X-ray fluorescence spectroscopy can determine the elemental compositions of the particles, while MS reveals the elemental composition along with some molecular fragments of particles, representing the most widely used techniques in aerosol characterization. Infrared (IR) absorption and Raman spectroscopy provide rotational and vibrational information on the molecular compositions of the particles, and laser-induced fluorescence (LIF) spectroscopy focuses on the electronic, ro-vibrational structures of molecules within particles. Culturing of bacteria, other microorganisms, and viruses collected in air samples can, in some cases, impart definitive information relating to the viability and identification of the genus or species through various biochemical analyses. Other methods, like nuclear magnetic resonance (NMR), can be used to estimate the fractions of hydrogen atoms bound, e.g., C=O, and C–O. Collections of aerosol particles can be fractionated on the basis of their physiochemical properties, such as solubility, tendency to elute into specific solvents, retention times in chromate-graphic columns and electrophoretic mobility. Among these technologies, MS, LIBs, LIF, and elastic scattering can rapidly record the properties of a single airborne aerosol particle when the particle is successively drawn through the interrogation volume of a system. Single aerosol particle diagnostic techniques have the advantages of avoiding definitive inferences, obtaining the compositions of individual particles and detecting the rapid time variations of specific, low concentration aerosol species that

* Tel.: +1 301 394 1381; fax: +1 301 394 4797.
E-mail address: yongle.pan.civ@mail.mil

are generally obscured by other dominated aerosol particles in the collected samples.

Atmospheric aerosol particles are mainly composed of viruses (~50–200 nm), smoke (~50 nm–1 μm), dust (~0.5–10 μm), bacteria (~0.5–10 μm), pollen, and fungi (~5–100 μm). OC aerosols in atmosphere range from small molecules such as oxalic acid or phenols, to polycyclic aromatic hydrocarbons (PAHs), to viable bacteria, fungi and spores (each of which are composed of many thousands of different kinds of organic molecules), to highly complex mixtures of decomposition products of biological materials (e.g., humic substances), to secondary OC (SOC) aerosols formed initially by oxidation of volatile organics. OC aerosols can include alkanes, alkenes, carboxylic acids, ketones, phenols, furans, terpenoids, PAHs, aromatic polyacids, lignans, cellulose, humic and fulvic acids, humic-like substances (HULIS), pollens, bacteria, bacterial spores, viruses and fungal spores. The relative contribution of primary organic aerosols (particles directly injected into the atmosphere) and secondary organic aerosols (particles formed by gas-to-particle conversion) is highly variable and can be affected by meteorological factors. Processes that generate OC aerosols include biomass combustion; residential wood and coal burning; cooking; the nucleation and growth of new particles in urban environments; microbial decay of plant matter; the emission of volatile OCs by vegetation and bacteria followed by oxidation, and then condensation into SOC aerosols; microbial and biochemical degradation of organic debris in the soil; wind action around dairy and cattle feedlots; farming operations; sewage wastewater treatment plants; and bubbles bursting from the ocean's surface through wave action. Most airborne bacteria are derived from plants, soil and water bodies. Both primary OC and SOC aerosols may be aged in the atmosphere. Bioaerosols and humic materials tend to be very complicated even before they undergo aging in the atmosphere. Although the far simpler types of primary OC aerosols, the chemical reactions that age these aerosols and the resulting aged aerosols can be extremely complex. This suggests that we have much more to learn about OC aerosols in the Earth's atmosphere. Some review papers, even when just dealing with primary biological aerosol particles (PBAPs) in the atmosphere, experience big challenges in atmospheric aerosol study. Després et al. summarized the sampling methods, specifically, the physical, chemical and biological techniques for PBAP analysis, which included cultivation, microscopy, DNA/RNA analysis, chemical tracers, optical and mass spectrometry [16]. Another paper discussed the large variation in PBAPs based on different seasons and locations, even just the contributions from fungi display significant variation for OCs in atmosphere [3]. A more broad review article summarized the current understanding in the properties and interactions of atmospheric aerosols and their effects on climate and human health [81].

Studies show that fluorescence spectroscopy can be used effectively to broadly classify organic compounds, including biological materials, while non-organic compounds are, in general, only weakly fluorescent in atmospheric aerosols. A number of rudimentary measurements of the fluorescence excitation and emission matrix (EEM) spectra of a variety of samples aimed at characterizing atmospheric OC aerosols have been reported. These fluorescence signatures include (a) integrated signatures from particles or water-soluble extracts of atmospheric aerosol particles/droplets collected on filters or substrates (e.g., [17,49,60,90]); (b) integrated signatures from a plume of atmospheric aerosol particles measured by fluorescence light detection and ranging (LIDAR) (e.g., [57,94,15,7,51,99,22,43,56,102]); and (c) signatures from individual single aerosol particles drawn into fluorescence point sensors (e.g., [78,79,63,64,68,71,24,25,26,34,101,100]). The integrated fluorescence spectra obtained from a group of aerosol particles, or the partial extracts from them, provide some information about the compositions of the particles in (a) and (b), but it is far from what we can get from the fluorescence spectra measured from individual single aerosol particles in (c). In addition, regardless of whether or not they are water-soluble, the fluorescence spectra from individual single atmospheric aerosol particles include SOC particles and PBAPs such as plant, animal, and insect debris, fungal spores, pollens, and bacteria that may not be soluble in water. Therefore, this paper focuses on the measurement of LIF from *single individual particles or aggregates* in a size range around 1–100 μm in diameter here. These results should provide a complementary view in the detection and characterization of biological and other OC aerosols in the atmosphere.

2. Fluorescent molecules and their excitation-emission matrix (EEM) spectra in bioaerosols

The molecules responsible for most of the fluorescence in most biological cells [52,33] are amino acids, nucleic acids, and some of the coenzymes (e.g., the reduced form of nicotinamide adenine dinucleotide (NADH) and its phosphate (NADPH), flavins (flavin mononucleotide (FMN) and flavin adenine dinucleotide (FAD)), and the B6 vitamers), and vitamins K and congeners. Particularly, such molecules are

1) The amino acids tryptophan, tyrosine and phenylalanine. Each of these constitutes 1–5% of the dry weight of some typical bacteria. The excitation and emission maxima of these fluorophors in solution are about 255 and 282 nm for phenylalanine; 275 and 303 nm for tyrosine, and 280 and 348 nm for tryptophan. In proteins that contain tryptophan as well as one of these other fluorescent amino acids, it is common for the energy absorbed by phenylalanine and tyrosine to be transferred to tryptophan, and emit fluorescence around 350 nm.
2) The reduced NADH and NADPH, which have excitation and emission maxima around 340 and 450 nm.
3) The flavin compounds such as riboflavin, FAD and FADH, FMN, and a variety of flavoproteins. In aqueous solutions flavins have excitation and emission maxima around 450 and 520 nm, respectively, but with a red-shifted emission peaked at 560 nm for dried flavins.

The excitation and emission maxima from biological materials can be much more complex than the absorption and emission peak wavelength of primary fluorophors listed above. Because (1) the fluorescence of the primary biological

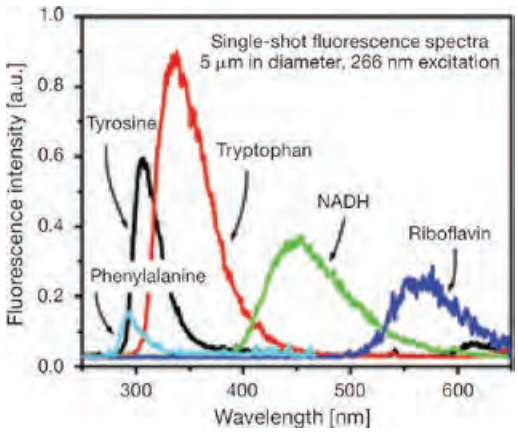

Fig. 1. Single-particle 266-nm-excited fluorescence spectra of common fluorophors found in biological particles. Each spectrum is for a nominal 5 μm diameter.

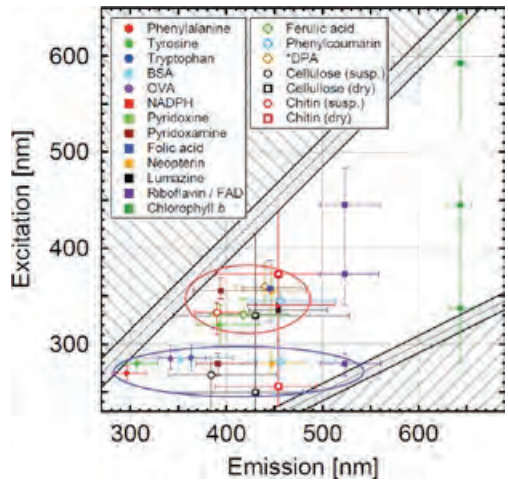

Fig. 2. Overview EEM mapping the spectral position of biological fluorophores. Protein fluorophores are represented by solid circular markers, coenzyme fluorophores by solid square markers and structural fluorophores by open markers. Full width at half maximum (FWHM) of the emission peaks is represented by horizontal and vertical bars. Differences in relative fluorescence intensity are neglected. For multi-modal fluorophores, all modes are shown. Data refer to measurements of solved fluorophores in PBS. For cellulose and chitin, results of solid-state and suspension-state spectra are shown [80].

fluorophors depends upon their local environment, e.g., the pH value, concentrations of certain ions, temperature, relative humidity, and the relative connection with other different molecules. Many biological molecules are polymers or oligomers of smaller building blocks. For example, (a) RNA is a polymer of ribonucleic acids, (b) glycogen, starch and cellulose are polymers of sugars, and (c) proteins are polymers of amino acids, where the number of common amino acids is in the low 20's. In a protein, different tyrosine or tryptophan molecules can exhibit different fluorescence depending upon their proximity to other amino acids in the same or other protein molecules. Because of this, the amount of variation in fluorescence of mixtures can be much larger than would be expected when looking only at the individual fluorophors [33].

One example of this effect of the local environment is that the EEM from different biological materials are not necessarily the same in a dried aerosol as in solution, because the aerosols are often dry or somewhat dry (e.g., [32]). Fig. 1 shows the single-shot, fluorescence spectra from individual (nominal 5-μm-diameter) dried particles of these fluorophors, measured on-the-fly by 266 nm excitation. Phenylalanine has weak fluorescence emission peaked around 280 nm; tyrosine and tryptophan have peak emission at about 310 and 340 nm. The NADH emission peaks around 450 nm. The riboflavin emission from dry particles peaks near 560 nm, which is strongly red-shifted from its emission when in an aqueous solution, where it peaks near 520 nm.

There are many other fluorescent molecules in various biological systems, e.g., the chlorophylls in plants and blue-green algae, the fluorescent compound in the bacterium *Pseudomonas fluorescens*, and the green fluorescent protein, but their contribution is less relevant to aerosol characterization. Although there is an enormous amount of chlorophyll in the environment, it shows little fluorescence in atmospheric aerosols. It may be that the chlorophylls have been rapidly decayed and modified enough to fluoresce little, as when a leaf degrades enough to have parts of it blown up as an aerosol particle [80].

The amount and composition variations of fluorescent molecules in different bioaerosol particles offer the possibility of detection and discrimination. Many other fluorescent molecules in biological particles (e.g., chlorophylls, lignins, lignans, ferulic acid) [32] can provide distinct spectral features for better differentiation among fluorescence spectra from various species. Viruses and protein toxins, which typically are not associated with flavins or nicotinamide compounds, commonly contain one or more of the fluorescing amino acids. The spectra of fluorescent molecules also depend upon the intracellular environment. The fluorescence EEM from numerous possible atmospheric bioaerosols illustrates the fundamental idea of using them to select the excitation and detection wavelength in instrumentations. Hill et al. [32] reported the fluorescence EEM spectra of quite a few types of biological materials, including bacteria, pollens, spores and grass leaves; some inorganic particles; and an oil. Pohlker et al. [80] summarized the fluorescent biomolecules and potential interferences in atmospheric bioaerosol particles, as shown in Fig. 2. The others, such as the early EEM spectra reported for seed pubescence, pollen and spores, and senesced plant materials [92,86], humic acid bands from coral reefs [55], fresh and aged biogenic SOC [54] are also a good reference for bioaerosol characterization based on fluorescence. Saari et al. [88] also reported the fluorescence spectra of atmospherically relevant bacterial and fungal spores and potential interferences.

3. Development of single-particle laser-induced-fluorescence techniques

Single-particle fluorescence detection systems have been developed based on pioneering studies by several groups (e.g., [77,27,19,29,83,62,65,93,41,42,44,45,95,97]).

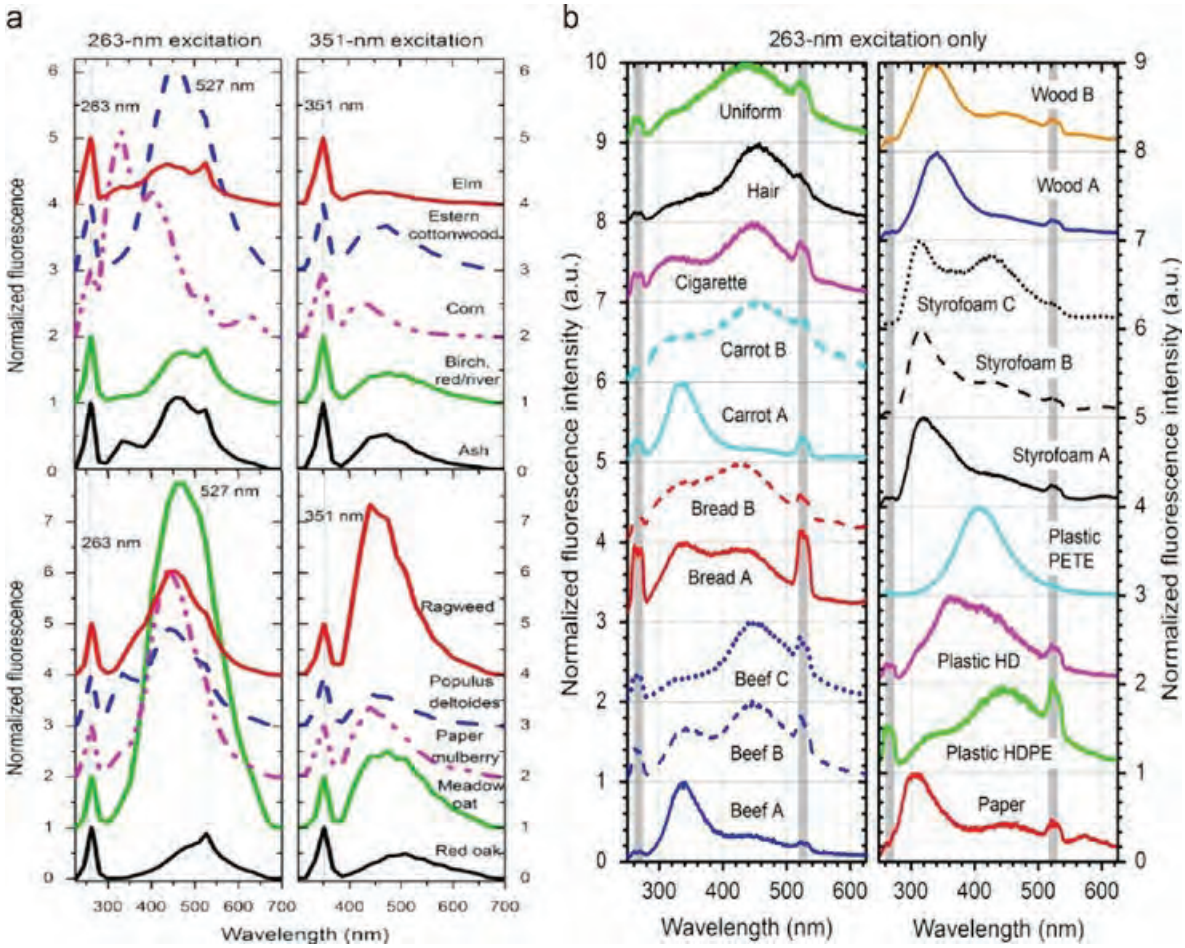

Fig. 3. (a) Fluorescence spectra measured by the DPFS for various pollens. Each spectrum is an average for 100 individual particles and is normalized to the elastic scattering intensity for easy comparison [71]. (b) Average (1000 laser-shot) UV-LIF spectra of particulate emissions from various burning materials. If the fluorescence spectral profiles undergo only small changes during the burn process (as for the battle-dress uniform, human hair, cigarette, plastic water bottle, plastic spoon, plastic cup, and shredded white paper samples), only one average UV-LIF spectrum is shown. If the profiles change significantly during the burn process (as for shredded carrots, potato-roll bread, cooked hamburger meat, wood shards, and Styrofoam cup), two or more average UV-LIF spectra are presented [73].

These systems, which are typically combined with measurements from elastic scattering for each particle to estimate size, are employed in most of the biological agent early warning systems. Such systems have also been used to study the fluorescence of bioaerosols; and other fluorescent particles in the laboratory (e.g., [29,32,10,97]), and to make continuous reagentless fluorescence measurements of atmospheric aerosols on several continents (e.g., [78,79,65,68,71,72,34,24,25,26,101,100,80,104]). Pan et al. [67] summarized how to select the illuminating light source (laser, light-emitting diode (LED), or flash lamp); choose the most suitable detector (charge-coupled device (CCD), intensified CCD (ICCD), linear arrays of avalanche photodiodes, or multianode photomultiplier tube (PMTs)); and generate the test bioaerosol. They also reviewed the instrumentation of a few well-known detection systems.

The representative fluorescence-based bioaerosol detection and characterization systems are the biological agent warning sensor (BAWS) (e.g., [83]), the ultraviolet aerodynamic particle sizer (UV-APS) (e.g., [27]), the waveband integrated bioaerosol sensor (WIBS) (e.g., [42]), the dual-wavelength-excitation multiple-fluorescence-band system (e.g., [97]), and the dual-wavelength-excitation or single wavelength excitation single particle fluorescence spectrometer (DPFS or SPFS) (e.g., [63,64,65,66,70,44,45]). UV-APS supplies total particle and fluorescence particle concentration as well as the relative fluorescence intensity by 355-nm excitation in each of the aerodynamic size bins (0.532–20 μm), and is a good particle sizer and fluorescence particle counter. BAWS extracts information from the scattering particle size and fluorescence intensities in the UV (300–400 nm) and visible bands (400–600 nm), and can discriminate bioaerosols particles from other non-bioaerosol particles with higher specificity than UV-APS. Most of the commercialized or laboratory instruments based on one or two broad fluorescence bands using one wavelength excitation have some degree of discrimination ability similar to UV-APS and BAWS (e.g., [77,27,83,93,19,41]).

The two-wavelength-excitation multiple fluorescence bands systems (e.g., [42,95,97]) are able to provide more specific discrimination between various bioaerosol particles.

WIBS-4, in particular, has a parameter called the asymmetrical factor (AF), which is related to the particle's shape and is derived from the angular elastic scattering intensity distribution, which should greatly help distinguish particles when they are all in single particle forms (e.g., [26,101]). Comparing a single *B. subtilis* (BG) spore and a single polystyrenes (PSL) sphere, their AFs show a huge difference, but the AFs are similar when sphere-like aggregates are formed from the two different primary particles. The AF values for the particles formed by the same primary particles are different when they are in singlet, doublets, triplets, or big aggregates. Therefore, AF, in some situations, will confuse the discrimination.

The fluorescence spectra based systems, such as DPFS, which supplies particle size and two dispersed fluorescence spectra (280–700 nm) using dual wavelength excitation (263/266 and 351/355 nm), provide the richest information for every detected particle, leading to the highest discrimination capability [63–65,70,44,45]. In general, LIF based systems promise to be able to differentiate bioaerosol particles from most non-bioaerosol particles (e.g., [27,29,19,83,62,65,41]); discriminate biothreat agents from atmospheric aerosol particles; and classify different bioaerosol species such as pollen versus fungi, as shown in Fig. 3(a) [42,58,71,97,44,45,28]. But keep in mind, not all fluorescent particles are bioaerosols, and also some biomolecules contained aerosol particles may be below the fluorescence detection threshold. For example, if a not-suitable illuminating wavelength is selected, the resulting fluorescence signal may escape detectable.

In general, the fluorescence spectral profiles from atmospheric particles always show very broad fluorescence structures, covering tens to hundreds nm wavelengths. This makes it possible to use a few bands in atmospheric aerosol discrimination with reasonable spectral resolution. For a particular sample, the overall fluorescence spectral profiles from 12 different fresh supermicron particulate emissions of burning materials in a tube furnace exhibit either one or two broad bands peaked from 300 to 500 nm within the 280–650 nm spectral range when the particles are illuminated with a 263-nm laser. Different burning materials have different profiles; some of them (cigarette, hair, uniform, paper, and plastics) show small changes during the burning process, and while others (beef, bread, carrot, Styrofoam, and wood) show large variations. These initially exhibit a single UV peak (around 310–340 nm) and a long shoulder in visible, and then gradually evolve into a bimodal spectrum with another visible peak (around 430–450 nm) with intensity increasing during the burning process (Fig. 3(b)). These spectral profiles could mainly derive from polycyclic aromatic hydrocarbons combined with tyrosine-like, tryptophan-like, and other humic-like substances. Particularly, about 70% of these single-particle fluorescence spectra have been observed from the spectra of millions of atmospheric aerosol particles in three locations in the US; while the others, particularly these bimodal spectra, show bigger difference from the common atmospheric aerosol particles. Therefore, these spectra from particulate emissions of burning materials can be easily discriminated from that of common atmospheric aerosol particles. It also implies that fluorescence would be a good tool for monitoring fresh burn pit emissions and possibly for distinguishing them from aged atmospheric aerosol particles [73].

4. UV-LIF spectra and absolute cross section from aerosolized live agents and surrogates

The commercial availability of bioaerosol detection and characterization systems makes atmospheric aerosol measurements and deployments for routine continuous monitoring feasible. However, the development and initial testing of these systems (including their detection algorithms) for infectious agents is often done with simulants or, less commonly, with the killed agents. For example, BG and *B. thuringiensis kurstaki* (Btk) are often used as simulants for *B. anthracis*. Some questions regarding agents and simulants are as follows. (1) For any given live agent and simulant pair, do they have the same detection-relevant properties? In the case of fluorescence detection systems, spectrally resolved fluorescence cross sections and spectral profiles would be the most important parameters at the relevant excitation wavelengths. (2) Do the relevant properties of agents and simulants change in the same way after they are aerosolized, released into the atmosphere, and subjected to sunlight, water vapor, and reactive molecules such as ozone and hydroxyl radicals?

Fig. 4 shows the averaged UV-LIF spectra of 1000 individual aerosol particles for different measured samples excited at 266, 273, 280, 365 and 405 nm [74]. As the live bioagents measured are very dangerous, all the measurements were required to carry out in a biological safety level 3 (BSL3) laboratory. Such a system supplies a great tool for important spectral profile and cross-section measurements from live agents and surrogates. The five excitation wavelengths were selected to closely match the most popular wavelengths in various light sources for fluorescence excitation (laser, LED, flash lamp) in the developed bioaerosol detection systems. These fluorescence profiles and the corresponding cross sections listed in Table 1 could be a good source for developing fluorescence-based detection systems.

The reported samples include (1) bacterial spores: *Bacillus anthracis* Ames (BaA); *B. atrophaeus* var. *globigii* (BG) (formerly known as *Bacillus globigii*); *B. thuringiensis israelensis* (Bti); *B. thuringiensis kurstaki* (Btk); *B. anthracis* Sterne (BaS); (2) vegetative bacteria: *Escherichia coli* (*E. Coli*); *Pantoea agglomerans* (Eh) (formerly known as *Erwinia herbicola*); *Yersinia rohdei* (Yr); *Yersinia pestis CO92* (Yp); and (3) virus preparations: *Venezuelan equine encephalitis TC83* (VEE) and the bacteriophage *MS2*. The sharp peaks around the corresponding wavelengths, particularly at 266 nm (first row), 365 nm (the fourth row) and 405 nm (the fifth row), are the leakages of elastic scattering, which have not been totally blocked by the corresponding filters. The spectra excited at 266, 273 and 280 nm were normalized to the same peak intensities for easy spectral profile comparison. However, the spectra excited by 365 and 405 nm had not been adjusted, other than subtracting the background and applying the spectral response calibration, because the fluorescence from some samples (e.g., BtK) is too weak and too noisy to be adjusted for comparisons of the spectral shapes.

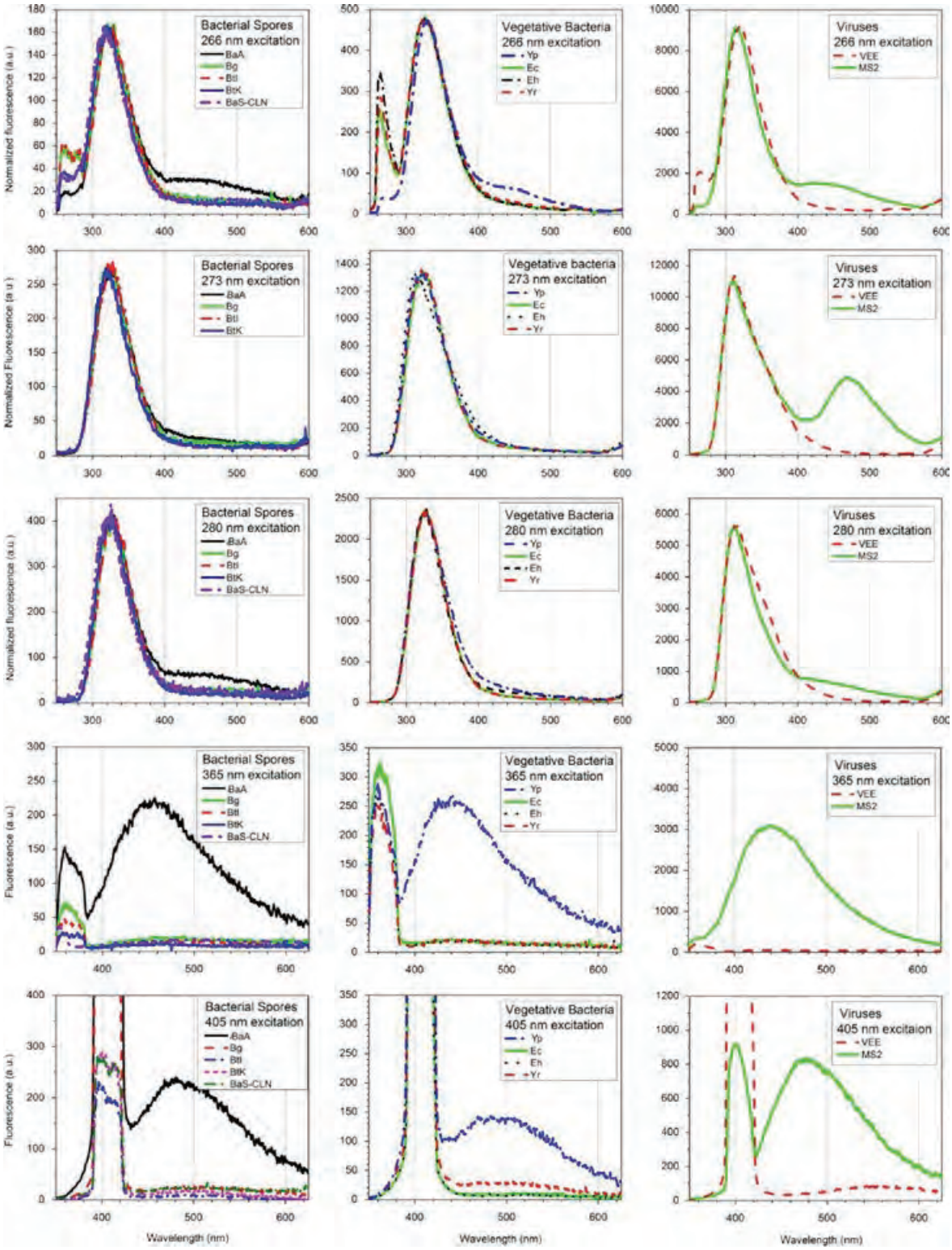

Fig. 4. Averaged UV-LIF spectra of 1000 single aerosol particles from various live agents and surrogates excited at 266, 273, 280, 365 and 405 nm. The peaks around the excitation wavelengths are the leakages of the elastic scattering. The spectra excited by 266, 273 and 280 nm are normalized to the same peak intensities at about 330 nm for easy comparisons of spectral profiles. The spectra excited at 365 and 405 nm have not been normalized [74].

Table 1
Averaged total and peak fluorescence cross sections from about 2000 (range 1000–3000) particles of various aerosolized live agents and surrogates excited at 5 different wavelengths [74].

Excitation wavelength (nm)	Name of agent	Fluorescence cross section (10^{-12} cm^2/sr particle)	Peak fluorescence cross section (10^{-12} cm^2/sr nm particle)	Average particle diameter (μm)
266	BaA	2.62	0.0291	1.66
266	BaS, unwashed	1.08	0.0143	1.47
266	BaS, washed 1 ×	1.16	0.0161	1.55
266	BaS, clean	0.97	0.014	1.35
266	BG	0.74	0.0099	1.56
266	Bti	0.93	0.0127	1.37
266	Btk	1.75	0.025	1.36
266	Yp	17.94	0.2574	1.89
266	*E. coli*	3.05	0.0486	2.68
266	Eh	2.22	0.0344	2.79
266	Yr	2.45	0.0371	2.76
266	VEE	14.09	0.2217	2.08
266	MS2	43.05	0.5530	2.43
273	BaA	3.59	0.0492	1.96
273	BG	1.11	0.0156	1.66
273	Bti	1.21	0.0182	1.45
273	Btk	1.14	0.0178	1.36
273	Yp	25.87	0.3891	3.38
273	*E. coli*	6.94	0.1101	3.31
273	Eh	5.43	0.0807	3.26
273	Yr	8.00	0.1244	3.32
273	VEE	25.94	0.4401	3.5
273	MS2	80.34	0.8193	3.39
280	BaA	6.09	0.0707	1.95
280	BaS, unwashed	1.05	0.0123	1.63
280	BaS, washed 1 ×	1.10	0.0144	1.5
280	BaS, clean	1.14	0.0154	1.51
280	BG	1.98	0.0248	1.57
280	Bti	1.90	0.0268	1.57
280	Btk	3.08	0.0448	1.49
280	Yp	24.00	0.3400	2.73
280	*E. coli*	11.66	0.1928	2.19
280	Eh	8.40	0.1355	2.22
280	Yr	14.96	0.2469	2.25
280	VEE	39.21	0.6006	3.27
280	MS2	57.94	0.8344	3.22
365	BaA	1.370	0.0103	1.73
365	BaS, unwashed	0.30	0.0022	1.28
365	BaS, washed 1 ×	0.21	0.0014	1.19
365	BaS, clean	0.14	0.0009	1.19
365	BG	0.14	0.0008	1.53
365	Bti	0.14	0.0011	1.34
365	Btk	0.09	0.0006	1.3
365	Yp	1.30	0.0098	2.63
365	*E. coli*	0.14	0.0008	2.02
365	Eh	0.12	0.0007	1.99
365	Yr	0.17	0.0010	2.7
365	VEE	0.40	0.0023	3.01
365	MS2	15.44	0.1290	2.33
405	BaA	0.93	0.0071	1.87
405	BaS, unwashed	0.17	0.0011	1.45
405	BaS, washed 1 ×	0.12	0.0007	1.42
405	BaS, clean	0.11	0.0007	1.36
405	BG	0.13	0.0008	1.69
405	Bti	0.07	0.0005	1.3
405	Btk	0.11	0.0008	1.56
405	Yp	0.60	0.0046	2.94
405	*E. coli*	0.06	0.0005	2.89
405	Eh	0.05	0.0004	3
405	Yr	0.11	0.0008	3.01
405	VEE	0.32	0.0026	2.92
405	MS2	2.98	0.0264	2.95

All samples show strong fluorescence emission in the 280–400 nm range when excited at 266, 273 and 280 nm. The bacteria fluorescence peaks around 320–330 nm. The viral particle fluorescence, which is probably dominated by the fluorescence of the lysate of the Vero cells (in the case of VEE), or *E. coli* cells (in the case of MS2), and some of the spent culture medium in which they were grown, peaks around 310–320 nm. BaA, BaS, Yp and the MS2 sample have strong fluorescence emission at 400–600 nm when excited at any of the five wavelengths. The peak intensity of this visible emission (400–600 nm) is about 1/5 to ~1/10 of the UV band (280–400 nm) when excited by 266, 273 and 280 nm. It peaks around 450 nm when excited at 365 nm, and is red-shifted to 475–500 nm when excited at 405 nm. Other samples have little fluorescence emission above 400 nm.

Table 1 summarizes the total fluorescence cross sections averaged from the data set with 1000, 2000 or 3000 particles, most commonly from 2000 particles of various aerosolized live agents and surrogates excited by 266, 273, 280, 365 and 405 nm lasers. Note that each data row is from a different group of aerosol particles with a different size distribution and mean size value. Even slightly different aerosol generation conditions may result in different fluorescence cross sections. For bacterial spores (prepared under the conditions as stated in the reference by [74]), Btk has optical properties similar to BaA, based on particle size and total fluorescence intensity via 266-, 273- or 280-nm excitation. But BG, Bti or Btk are not good simulants for BaA if the system is using particle size and total fluorescence by 355-, 365- or 405-nm excitation. None are very suitable for a system based on particle size and two bands or multiple bands of fluorescence intensities either via single wavelength excitation or two wavelength excitation. Further, BG, Bti and Btk do not have spectral profiles similar to BaA, as none of these simulants has as strong a fluorescence emission in the visible as BaA. This result implied that live agents don't need to have the same optical properties as simulants; we have to choose the best simulants that have the closest properties to the corresponding agent for a particular fluorescence-based bioaerosol detection system (certain excitation wavelength and collection fluorescence wavelength range, as well as the related discrimination algorithm). These data can aid in the design and evaluation of bioaerosol detection systems, and the choice of the most suitable simulants for system development and field testing.

The difficulty in system calibration and the complication that fluorescence intensity strongly depends on the particle size, growth conditions, dried degree of the particles, intensity of the illuminating laser, and even the signal collection direction ([30,31,33,6,40,51,47]) cause the measured fluorescence cross sections to have large variations. Even two similar systems based on the same fluorescence band with slightly different excitation wavelength and system design, the detected fraction of fluorescence particles could be quite different, such as the study for BioScout (405-nm ex.) and UV-APS (355-nm ex.) carried out recently [89]. Table 2 summarized the available results for bacterial spores and vegetative cells. For example, Faris et al. [20,21] reported spectra for aerosolized *B. subtilis*, with peak 270-nm excited fluorescence cross sections of 1.5×10^{-14} cm^2/(nm sr spore) for wet aerosol and 0.3×10^{-14} cm^2/(nm sr spore) for dry

Table 2
Fluorescence cross sections measured by several groups. In some cases, the numbers shown were estimated from figures or from other reported numbers.

Researcher (s)	Sample	Fluorescence cross section	Peak fluorescence cross section	Excitation wavelength (nm)	State and size of sample
[21], Fig. 8	*B. subtilis* spores	Wet: 1×10^{-12} cm^2/(sr · particle) estimated from spectrum in Fig. 8 Dry: 0.2×10^{-12} cm^2/(sr · particle)(est)	1.5×10^{-14} cm^2/(nm sr spore) for wet aerosol; 0.3×10^{-14} cm^2/(nm sr spore) for dry aerosol	270	Aerosol
[53], Fig. 2	*B.thuringiensis* spores in dry PBS	0.4×10^{-12} cm^2/(sr · particle) est. from number at right	0.6×10^{-14} cm^2/(nm sr spore) for aerosol (cross section divided by 4π sr)	280	Aerosol
[95]	*B. globigii* (BG) spores, Dugway, washed	0.7×10^{-12} cm^2/(sr · particle)		266	Aerosol 1 μm Converted with fluor-elastic assumption
[50]	*B. subtilis* spores, washed	0.65×10^{-12} cm^2/(sr · particle)	1.1×10^{-14} cm^2/(sr · nm · particle) est. from number at left	280	Dried spores on quartz slide 1.1 μmx.48 μm
[98]	*B. globigii* spores	0.3×10^{-12} cm^2/(sr · particle)	0.8×10^{-14} cm^2/(nm sr particle)	270–290 from lamp	Aerosol held in electrodynamic trap Broad dist. Avg > 1 μm
[1]	*B. globigii* spores	0.03×10^{-12} cm^2/(sr · particle)	0.08×10^{-14} cm^2/(nm sr spore)	266	Dilute aqueous suspension 1 μm x 0.5 μm
[103]	*M. luteus*	3×10^{-12} cm^2/(sr · particle)	8×10^{-14} cm^2/(nm sr particle) (cross section divided by 4π sr)	280	Aerosol dry 1 μm
[74]	Bacillus spores in Table 1.	$0.91–3.2 \times 10^{-12}$	$1.2–3.6 \times 10^{-14}$	266	1.35–1.66 μm
		$1.1–3.6 \times 10^{-12}$	$1.6–5.0 \times 10^{-14}$	273	1.36–1.96 μm
		$0.54–3.0 \times 10^{-12}$ cm^2/(sr · particle)	$0.06–3.5 \times 10^{-14}$ cm^2/(nm sr particle)	280	1.49–1.95 μm avg. diameter

aerosol. Different spore sizes were used by different groups in calculating the cross sections. For examples, Atkins et al. [1] used spores measured as 1 μm × 0.5 μm; Faris et al. [20,21] used 1.25 μm × 0.75 μm; and Manninen et al. [53] used 1.1 μm × 0.48 μm. Carrera et al. [9] found the size of *B. subtilis* spores to be 1.07 μm × 0.48 μm using electron microscopy. Comparisons among the values in Table 2 are complicated by the variations in preparation methods and the differences and uncertainties in sizes. Considering all the difficulties and uncertainties, the values summarized in Table 2 from different groups appear to be within reasonable agreement.

5. The evolution of optical property of bioaerosols in atmospheric environments

Atmospheric aging and processing of bioaerosols in the natural environment (such as exposure to gases, sunlight, temperature and humidity) may involve many different chemical reactions, which occur on different time scales (minutes, hours, days). Different sizes of bioaerosols may respond differently to various environmental conditions because of the different surface/volume ratios of the particles, and result in different diffusion and reaction rates with interacting gases. There have been many studies of atmospheric aging and processing of OC aerosols and bioaerosols, particularly on the effects of ozone and simulated open air factors (OAFs) (e.g., [2,87,14,18]). Changes in fluorescence spectra from pollens (not aerosolized) treated with ozone have been measured [85]. Some correlation between ozone and naturally occurring aerosols including fungi, pollen and other organic materials have been observed [105]. The long-term chemical aging of model biogenic secondary organic aerosol (SOA) prepared from ozonolysis of terpenses was observed to have strong changes of absorption and fluorescence spectra [5]. Humic substances showed big difference between fresh, reduced and aged aerosols [46,54]. Exposure to ozone was reported to change the absorption and fluorescence of the aromatic amino acids in solution and in animal tissues. N-formyl kynurinene (NFK) and kynurenine (KN) were found to be the primary products from oxidation of tryptophan [36,37,61,23,4,59,48]. These measurements were carried out in aqueous solutions or on samples collected from air onto substrates.

Continuous inspection of bioaerosols collected on a substrate or trapped in the air could be a good analytical path for understanding how bioaerosols change in the atmosphere. However, the repeat interactions on the same particle may create additional changes rather than from the atmosphere, e.g., photo-degradation [63,64]. Therefore, injecting bioaerosol particles into a rotating chamber to keep particles aloft for long-term aging and observation could be another very powerful method in studying bioaerosol aging in various atmospheric conditions. Fig. 5 shows how the 263-nm (a, b) and 351-nm (c, d) excited UV-LIF spectral changes with time with different ozone concentration and at various relative humidities for octapeptide (Arg-Phe-Tyr-Val-Val-Met-Trp-Lys) aerosol particles. This 340-nm fluorescence band decreased to about one-half of its initial value after 4 h at RH ~ 20% and ozone < 5 ppb (left 9a)), but decreased faster (reduced by approximately 90%) after 4.5 h at higher RH (50%) and ozone (150 ppb) (left (b)). Initially, the 351-nm excited fluorescence (left (c)) has a peak intensity about 500 times weaker than the 263-nm excited fluorescence, it changed little at 20% RH and < 5 ppb ozone concentration for 4 h. However, at 50% RH and 150 ppb ozone it increased to 20-fold stronger than its initial intensity (left (d)). This increase occurs primarily within the first 1.5 h. Given the composition of the peptide and what is already known about reactions of ozone with tryptophan, this increase in 351-nm excited fluorescence indicates that in these octapeptide particles the ozone caused the oxidation of tryptophan to NFK and/or KN, molecules that fluoresce in the visible when excited at 351 nm.

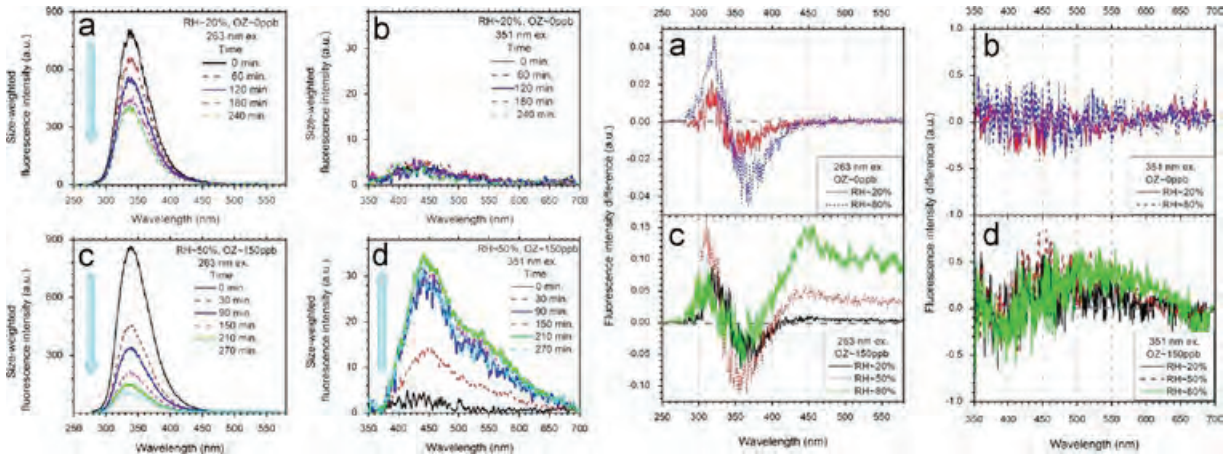

Fig. 5. Typical time-dependent UV-LIF spectra (left) and difference spectra (right) of octapeptide aerosol particles under different RH and ozone concentrations (OZ). Where the difference spectra are the subtracted spectra between the normalized average fluorescence spectrum at the end of the experiment and that when the particles were initially released in the chamber. In the cases listed at 150 ppb, the ozone increased from approximately 0 ppb to 150 ppb in the first approximately 30 min. The spectra have been weighted by particle diameter as $1/d^{2.05}$ for 263-nm excitation and as $1/d^{2.8}$ for 351-nm excitation, and so the averaged spectra shown are the converted counts from the measurements of the ICCD that is estimated to be if all particles were 1 μm diameter [75].

Fig. 6. A system, which was developed to study the transformation of optical properties and viability of bioaerosols exposed to different atmospheric environments, was carried out a field measurements at the High-Bay, ARL during September 27th through October 19th.

The right part in Fig. 5 presents the difference spectral profiles measured initially and after 4 h (with no ozone) or 4.5 h (when ozone is added) of aging in the chamber. All 263-nm excited spectra, with or without ozone, exhibit slight blue shifts in the 340-nm band for an increase in intensity at shorter wavelengths and a decrease at longer wavelengths. These changes in intensity are less than 5% when particles were not exposed to ozone (right (a)) but up to about 10–15% when particles were exposed to ozone at various RH (right (b)). The relative increase in intensity in the visible wavelength range (400–600 nm) during the exposure to 150 ppb ozone confirmed that one or more new fluorescent molecules have been generated, and that this oxidation product can also be excited at 263 nm to fluoresce at visible wavelengths. The primary new molecules are mostly NFK, KN and possibly further-modified variants of these such as hydroxykynurenine. The *E. coli*, *B. thuringiengis*, *Yersinia rohdei*, ovalbumin and MS2 (bacteriophage) demonstrated similar phenomena when the interacting with ozone [91]. The fluorescence emission peak around 340 nm appears to decrease in intensity and become slightly blue-shifted. It decreases much faster at high ozone concentration especially associated with high humidity. The fluorescence peak in the 400- to 550-nm range decreases less rapidly than the 330-nm tryptophan peak. There are significant changes in the UV-LIF spectra for the single MS2 particles when they are exposed to ozone, especially at high relative humidity.

The changes become more complicated when these bioaerosol particles are released into real atmospheric air with various weather conditions such as under different sunlight, humidity, temperature, pollution and trace gases. A system shown in Fig. 6, which was developed by a group of scientists from US Army Research Laboratory (ARL), Texas A&M University (TXA&M), Johns Hopkins University Applied Physics Laboratory (JHU/APL) and Sandia National Laboratories (SNL), composed of two equivalent rotating chambers, has made this study more feasible in finding the possible correlation between the changes in the viability, fluorescence and various atmospheric environmental condition parameters. The two chambers are sealed by UV transparent Teflon films and rotate at 1 rpm to keep the particles aloft for long-term aging. They are on a platform that rotates during the day tracking the sun for maximizing exposure to sunlight without shading. The ends of the inner volume of each drum (i.e., the drum heads) is a membrane of porous expanded tetrafluoroethylene (ePTFE), which prevents any particles larger than about 20 nm from entering or leaving the drum, but allows gases to pass into and out of the drums.

In one operation mode, both drums are injected with the same bioaerosol simultaneously, while one of the drums is allowed to equilibrate with atmospheric gases and the other drum equilibrates with highly cleaned atmospheric air (with humidity adjusted back to atmospheric level) in which volatile organics, ozone, NOx and other trace gases have been removed. Several instruments are used to monitor the aerosol properties sampled from the drums including (1) a DSPF system for measuring single particle fluorescence spectra excited by a 263- or 351-nm laser; (2) a TSI UVAPS for particle size, concentration and total fluorescence by 355-nm excitation; (3) two DMAs for monitoring the growth of small particles injected into the chamber (for indication of secondary organic aerosol formation); (4) a solar pyrometer, ozone, humidity, and temperature sensors for continuously recording atmospheric environmental conditions; and (5) bioaerosol viability measurement, where aerosol particles,

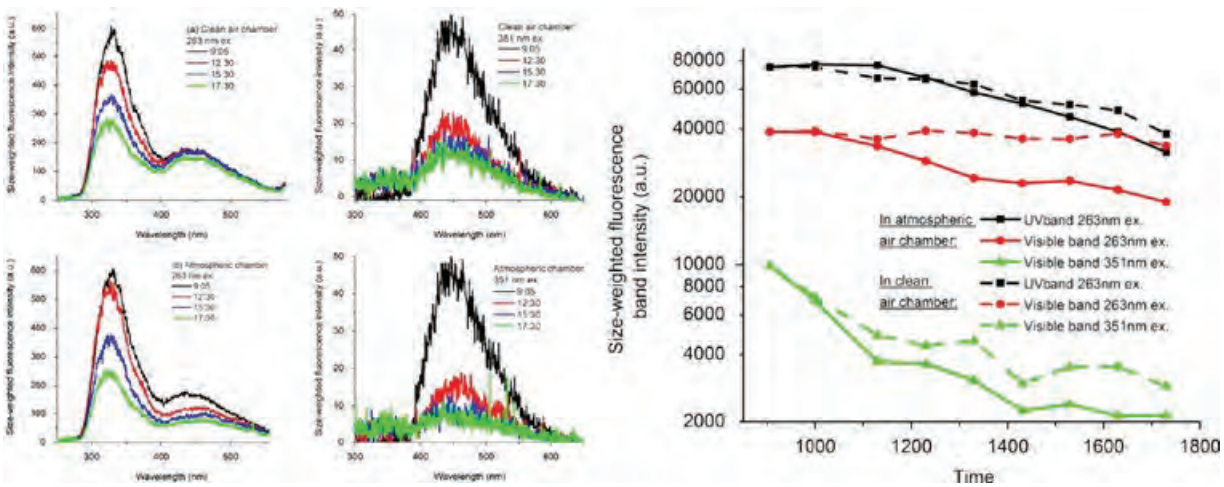

Fig. 7. Time-dependent changes of UV-LIF (263- and 351-nm excitation) fluorescence spectra of MS2 particles within a clean chamber and atmospheric chamber measured on Oct 18, 2012, during 0900–1730 on a sunny day $\sim 18 \pm 4$ °C temperature, $\sim 45 \pm 9\%$ relative humidity and $\sim 40 \pm 16$ ppb ozone concentration at ARL, Adelphi, MD.

at different times, are collected into water by all-glass impingers (AGIs) and analyzed for colony forming units (in the case of bacteria) or plaque-forming-units (in the case of virus), as well as for total bacteria (live+dead) or virus (infectious+non-infectious) using q-PCR. The first field measurement for this study was carried out from September 27th through October 19th, 2012 at the High-Bay parking lot of U.S. Army Research Laboratory, Adelphi, MD. Fig. 6(a) shows a photo of the whole system; (b) and (c) show the essential devices for bioaerosol, clean air and air flow generation and controlling, the DPFS for obtaining two UV-LIF spectra from every individual aerosol particles, and the solar radiation, ozone concentration, relative humidity and temperature monitors.

Fig. 7 shows one of the typical results measured on Oct 18, 2012, during 0900–1730 in a sunny day with temperature around 18 ± 4 °C, relative humidity around $45 \pm 9\%$ and ozone concentration around 40 ± 16 ppb. The time-dependent intensity variation of all fluorescence bands is summarized in the right column of Fig. 7. Basically, all the UV and visible fluorescence bands decrease with time in the atmospheric chamber whether they are excited by a 263- or 351 nm laser; they all decrease faster than that in the clean air chamber. All emission bands show blue-shift. The visible fluorescence band excited by the 263-nm laser has little change in the clean air chamber. Similar or different variations in different days with different change rates under different atmospheric conditions show complex correlations. Details of these results are still under analysis. The process could be very complicated, even just by sun illumination. For example, bacterial bioaerosols (E. coli and BG) can be thermally inactivated to produce various degrees of cellular culturability. Their UV- and Vis-fluorescence intensities can decrease with increasing deactivation temperature; it has a much faster decreasing rate in the UV-band than that in the visible band, which is similar to the observed phenomena from atmospheric aging as shown in Fig. 7 [38].

These changes in fluorescence intensity and spectral profile under different atmospheric environmental conditions have significant impact on fluorescence-based detection of biological aerosols. It would be wise to include these OAFs into the discrimination algorithms in the development of bioaerosol detection systems according to different environmental conditions.

6. Fluorescence spectra from atmospheric aerosol particles

Atmospheric aerosol particles contain complex external and internal mixtures of organic and non-organic compounds. There is an enormous variability in the composition of particles containing OC, especially in the biological fraction of OC aerosols. Single-particle fluorescence spectral measurements should be useful for improving our understanding of the OC-particle fraction of atmospheric aerosol, including sources, sinks, chemistry, variations with season and time of day, location (urban, remote), local wind fields, air mass trajectories, atmospheric stability conditions, etc. The ability to measure single particle fluorescence is particularly useful for studying a minority population of (fluorescing) particles entrained in a dominant background of non-fluorescent particles. During last 10 years, many measurements have been carried out in Asia, Europe and North America using various bioaerosol (more precisely fluorescence aerosol) detection and characterization systems, such as by UV-APS (e.g., [39,34]); WIBS [42,24–26,101,84]; and using one wavelength or dual-wavelength excitation fluorescence spectra like SPFS or DFPS [65,68,70,72,78,79,100].

Fig. 8 (upper) shows one of the typical 263-nm excited UV-LIF spectra from a series of 1000 consecutively arriving particles measured during 23 October 2006 in CT, over a 16-min period [68]. Spectra of the small fraction of particles that have the largest fluorescence emission dominate this compressed view of the data; most of the particles have weak fluorescence emissions and the fluorescence peaks at different wavelengths. It presents significant diversity of the fluorescence intensity and

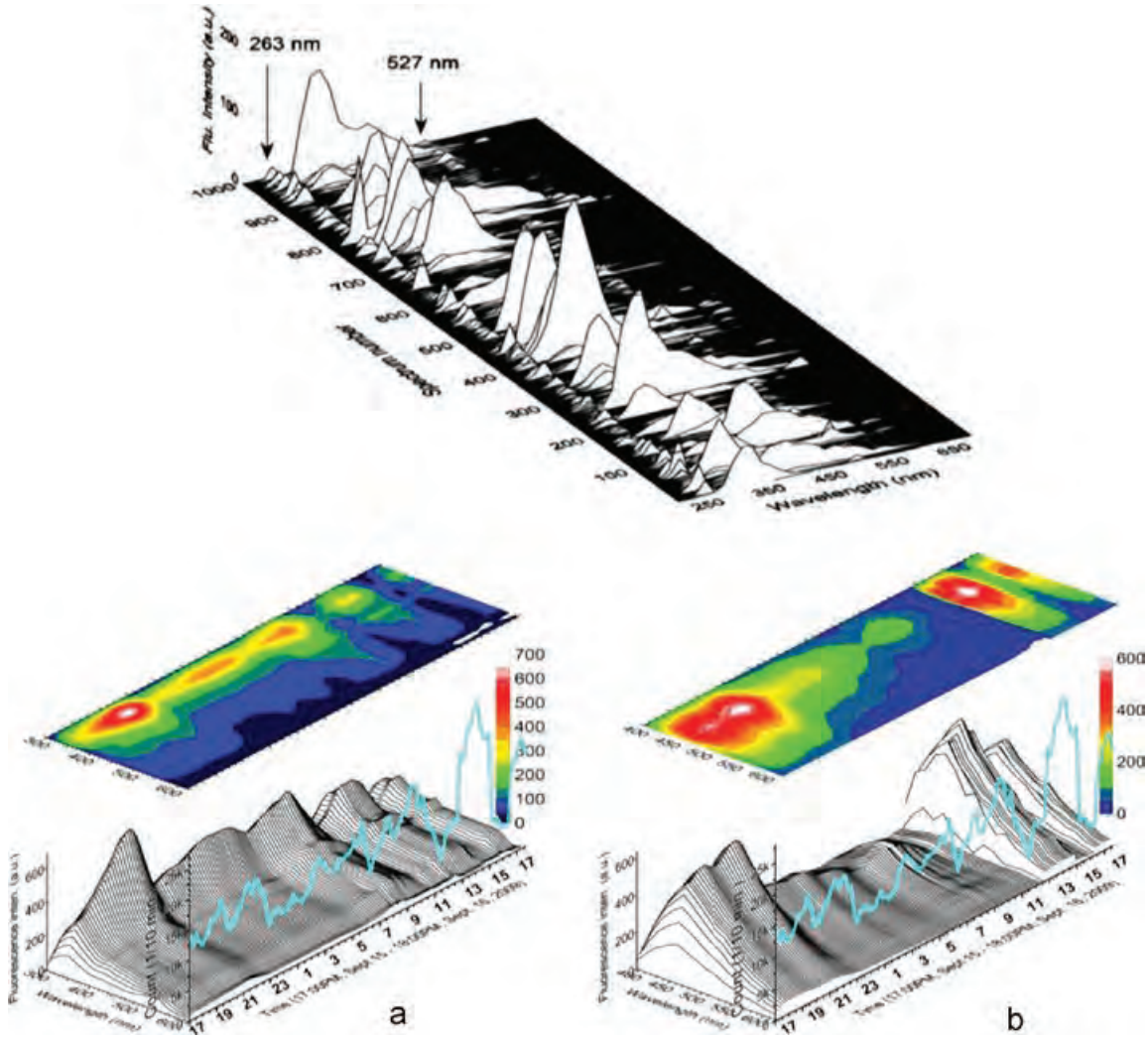

Fig. 8. (Upper) raw fluorescence spectra of 1000 typical atmospheric particles measured on Oct. 23, 2006, 10:00–10:16 am at New Haven, CT. Most particles have very weak fluorescence. The fluorescent particles emit mainly in the 300–600 nm wavelength range. The peaks at 263 nm are the scattering leakage between the UV pulsed laser and the particles, which is used as the measurement of scattering particle size; the peak at 527 nm is from the second order of grating [68]. (Bottom) Integrated UV-LIF spectra from atmospheric aerosol particles, the associated intensity contour map, and total number of detected aerosol particles for every 10-min interval during 17:00, Sept. 15–18:00, Sept. 16, 2009, in Adelphi, MD, using 263-nm (left) and 351-nm (right) excitation [72].

profile in atmospheric aerosol particles even just from a 16-min sampling of 1000 detected particles. It is a huge challenge to analyze and further to identify the chemical compositions of each particle only through UV-LIF spectra.

Detection and characterization of individual aerosol particle is crucial for revealing the appearance of low concentration particles. The UV-LIF information from samples collected using, for instance, a rotating drum impactor (RDI) find it difficult to search out trace particles. Fig. 8 (bottom) shows the integrated UV-LIF spectra from atmospheric aerosol particles, the associated intensity contour map and total number of detected aerosol particles for every 10-min interval during 17:00, Sept. 15–18:00, Sept. 16, 2009 in Adelphi, MD, using 263-nm (left) and 351-nm (right) excitation. They are the sum of all the fluorescence emissions from a few thousands to a few ten thousands of the particles detected within each 10-min period by DPFS. These integrated spectral profiles have small variation during 25 h, although individual particles have huge spectral diversities as shown in the upper part of Fig. 8. The strong fluorescence particles peaked around 350 nm by 263-nm excitation and that peaked around 450 nm by 351-nm excitation dominated the fluorescence particle populations.

However, the integrated UV-LIF spectra, which merge all the divinity of individual spectra, provide spectral profiles similar to those obtained by florescence LIDAR or a fluorescence detection system based on collected samples [57,94,15,7,51,99]. The data from integrated UV-LIF spectra should help in the evaluation and development of LIDAR systems, as well as point detection systems based on the fluorescence properties of collected particle on a substrate or filter [72,79]. These integrated spectral profiles had small variations from time to time, but are still distinguishable from that of the bacterial simulant *B. subtilis*. Therefore, some particular bioaerosol of interest should be detectable from

background aerosol if it appears in a high enough concentration. When excited by the 263-nm laser, the spectra always have a broad fluorescence emission from 280–700 nm, strongly peaked around 330–370 nm with another weaker peak around 410–480 nm. The fluorescence intensities of these integrated spectra are always weaker at visible than that at UV in Adelphi, MD, and New Haven, CT, but have compareable intensities in the two wavelength regions in Las Cruces, NM, where occasionally the UV peak is stronger than the visible peak. This is undersanable that the two sites at the East Coast have more bioaersol related emissions than the New Mexico area with a lot of desert. The integrated fluorescence spectra excited by 351-nm peaks around 420–470 nm; these were mostly from biological and OC-containing compounds. Pearson product correlation coefficients of the integrated fluorescence spectral profiles between New Haven, CT, and Adelphi, MD, both show strong correlation with high similarity [72,79].

The Hierarchical Cluster Analysis (HCA) and Nonhierarchical Cluster Analysis (NHCA) have been applied to treat fluorescence spectra obtained from millions of atmospheric aerosol particles. This simplified the very complex data sets by grouping all spectra into 8–10 clusters according to their spectral profiles, and tried to assign the possible types of compounds that might contribute to the fluorescence emission of each clusters [78,79,68,70,72]. Other data measured by WIBS (e.g., [84]) and fluorescence spectra-based detection systems (e.g., [100]) indicated that HCA and principal component analysis (PCA, e.g., [71]) are powerful tools for the classification of fluorescence aerosol particles.

These measurements carried out by SPFS or DPFS in the three sites (Adelphi, MD; New Haven, CT; and Las Cruces, NM, USA) covered quite a different regional climate and different season, and gives an example of how the fluorescence property of atmospheric aerosol particles might look [78,79,68,70,72]. Adelphi and New Haven have moderately

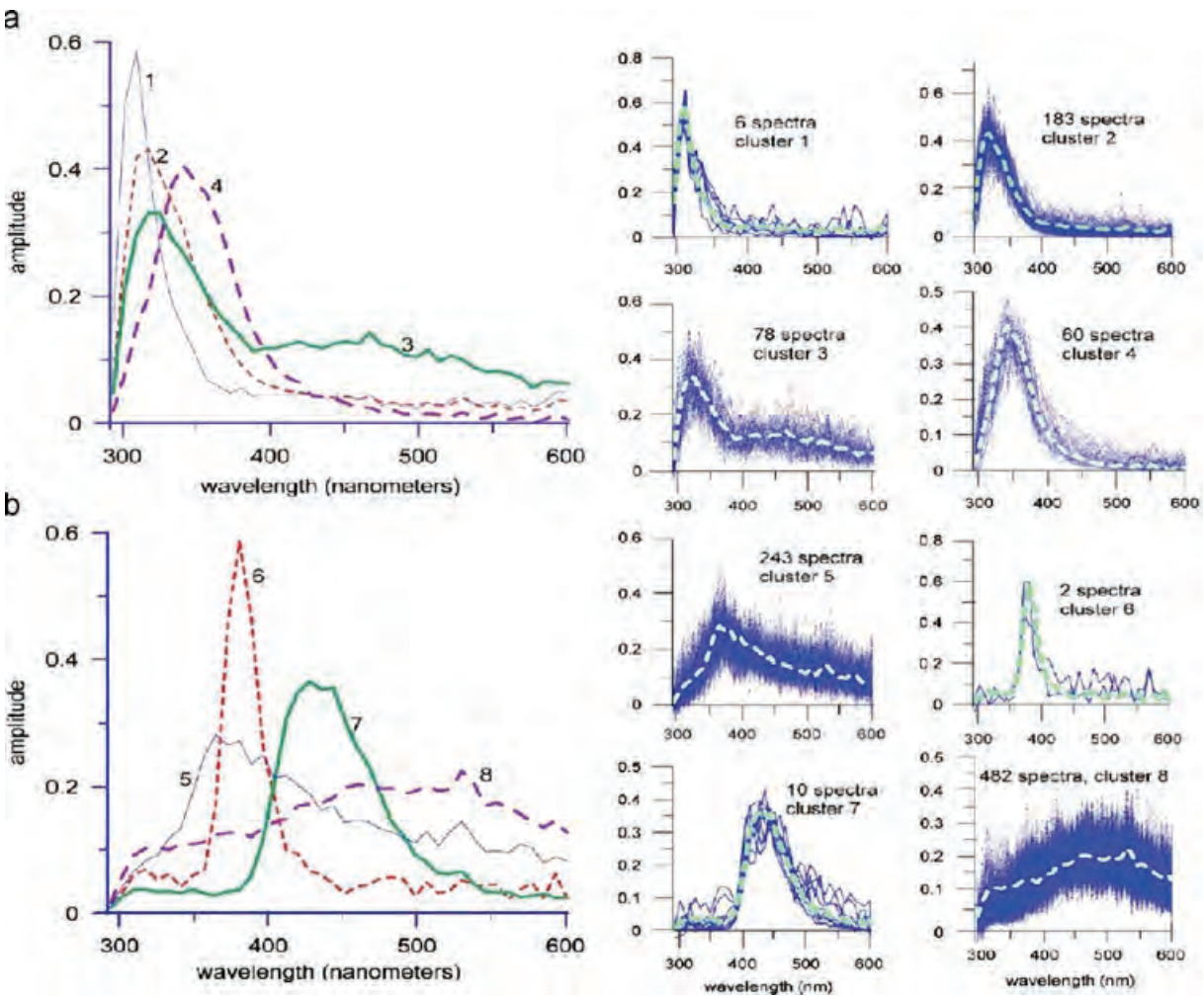

Fig. 9. Left shows the representative (template) spectra from Adelphi, MD. The spectra are labeled in order of increasing peak wavelength. Right is an example of the normalized fluorescence spectra of atmospheric aerosols (solid lines) measured on 28 March 2003 from 12:52 to 13:18 and the template spectra (dashed lines) they are similar to, i.e., have a dot product (between the normalized cluster spectrum and the normalized spectrum of the particle) greater than 0.9 [78].

high precipitation and large deciduous forests with tall trees and other vegetation. Las Cruces is near isolated riparian areas with very low precipitation, where there are essentially no trees, but dust storms are common. The left part of Fig. 9 shows the representative (template) spectra generated by HCA from 16 ensembles of measured data at Adelphi in 2003. The template spectra are labeled in order of increasing peak wavelength. The cluster number 8 was *selected artificially* to indicate the diversity of fluorescence spectra from atmospheric aerosol particles, but not to make the clusters number too high to be complicated. The right part of Fig. 9 shows an example of the normalized fluorescence spectra of atmospheric aerosols (solid lines) measured on 28 March 2003 from 12:52 to 13:18 and the template spectra (dashed lines) they are similar to, i.e., have a dot product (between the normalized cluster spectrum and the normalized spectrum of the particle) greater than 0.9. Of the 10,000 total spectra measured, 1127 spectra above the preset fluorescence threshold used in the analysis, and of these, a total of 1064 were similar to at least one of the template spectra [78].

By examining and comparing with the well-known fluorescence spectra from possible chemistry in atmosphere, the template spectra are considered to be the compounds that might contribute to them as follows [78].

Cluster 1's spectrum (peaking near 308 nm) rises sharply toward shorter wavelengths but appears to be cut off by the filters used to block the 266-nm laser scattering. Compounds having a single aromatic ring could fall into this cluster. Compounds that have been found in OC aerosols and that may contribute are the benzoic acids, dibenzoic acids, phenols, and benzaldehydes.

Cluster 2's spectrum peaks at 317 nm. This spectral type occurs frequently and has high fluorescence intensity. Particles in this cluster may include single-ring aromatics, as well as single-ring aromatics having additional conjugated bonds. Double-ring aromatics such as napthalene and its derivatives, or heterocyclic compounds such as tryptophan in proteins may contribute.

Cluster 3's spectrum is bimodal with a peak near 321 nm and a very broad shoulder between 400 and 500 nm. It covers a pretty high percentage of fluorescent particles but with relatively low intensity. It is similar to the spectra of some bacterial samples, especially ones that have not been washed well. The spectrum appears to be a mixture of compounds. The broad hump is similar to that of some mixtures of humic acids or HULIS compounds.

Cluster 4's spectrum (peaking near 341 nm) occurs on reasonably high percent of fluorescent particles. Particles in this group tend to have moderate fluorescence intensity. This spectrum is similar to that of pure tryptophan. Other double ring aromatic compounds (e.g., napthalenes) and heterocyclics may have similar spectra.

Cluster 5's spectrum (peaking near 350–360 nm, but with a long tail extending to 600 nm) has some similarity to spectra of collections of marine aerosol. It may include bacterial or other biological particles, but the peak emission is further to the red than for laboratory-grown bacteria. Particles in this fraction have small fluorescence intensity and a comparable percentage as Cluster 3 and 4.

Cluster 6's spectrum (peaking near 380 nm) is strikingly narrow and weak, and looks like sharp Raman or atom emission with very small populations, but does appeared at all three sites within one of the 10 highest populated clusters.

Cluster 7's spectrum (peaking near 430 nm) is similar to spectra of cellulose, although any fluorescence from completely pure cellulose should be very weak. Aromatic and polycyclic aromatic compounds, nicotinamide adenine dinucleotides, and humic acids could also be candidate compounds. The fluorescence intensity is generally the largest of all fractions but has low fraction.

Cluster 8's spectrum, with its very broad hump, is similar to some spectra recorded for fulvic or humic acids or HULIS. A complex distribution of aromatic and polycyclic aromatic compounds could look similar. Overall this fraction has the most fluorescent particles in all measurement, while typically it has the lowest fluorescence intensity of any cluster.

The collected UV-LIF spectra from atmospheric aerosol particles in three sites were processed using HCA independently; the similarity of the resulting clusters suggests an underlying similarity of particle formation and behavior in the three sites. It shows that fluorescent particles are around 5–10% of total particles detected by either SPFS or DPFS. More than 90% of the fluorescent particles can be grouped into 8–10 clusters, and the majority of the 8–10 spectral clusters (or the highest populated clusters) are remarkably similar to each other independently derived from the spectra at each site, although the proportions of particles in the various clusters are different. Fig. 10 shows the fluorescence spectral templates derived from HCA for Adelphi, MD, New Haven, CT, and Las Cruces, NM data. The percentage of (fluorescent) particles that cluster into each template is also shown. The most highly populated cluster is that characteristic of humic acid/HULIS (cluster 8); the least populated is cluster 6. The measurement and analysis of UV-LIF spectra from atmospheric aerosol particles carried out by a Japanese group with their own developed system observed similar spectral phenomena [100].

The fluorescence spectra excited by 351 nm from atmospheric aerosol particle from New Haven, CT, and Adelphi, MD, show similar phenomena as 263-nm excited fluorescence spectra in long emission wavelength, as presented in Fig. 11. It shows the UV-LIF spectra from the first 3000 fluorescent particles at each site and how they are grouped into the different clusters. Only the first 300 fluorescent particles are shown for clusters 3, 4, and 5, because there are so many spectra in these clusters. The spectra in cluster 1 and 2 may be cut off at the short-wavelength end by the long-pass filter (cut-off wavelength is 380 nm). We also cannot tell what the actual particle composition is for each cluster since these particles have not been sorted for biochemical identification. However, taking the well-known UV-LIF spectra of compounds that are present in the atmosphere and these clusters might fall into [72].

Clusters 1 and 2 are peaked at 425 nm or shorter. Compounds containing the biological fluorophores pyridoxine, pyridoxamine, ferulic acid, ergosterol, and cellulose may have fluorescence emission profiles like cluster 1 and 2 when excited by a 351-nm laser. Pyrene, phenanthrene, naphthalene, mulberry pollen, and corn pollen mixed with a small portion of other compounds can also generate fluorescence similar to clusters 1 and 2.

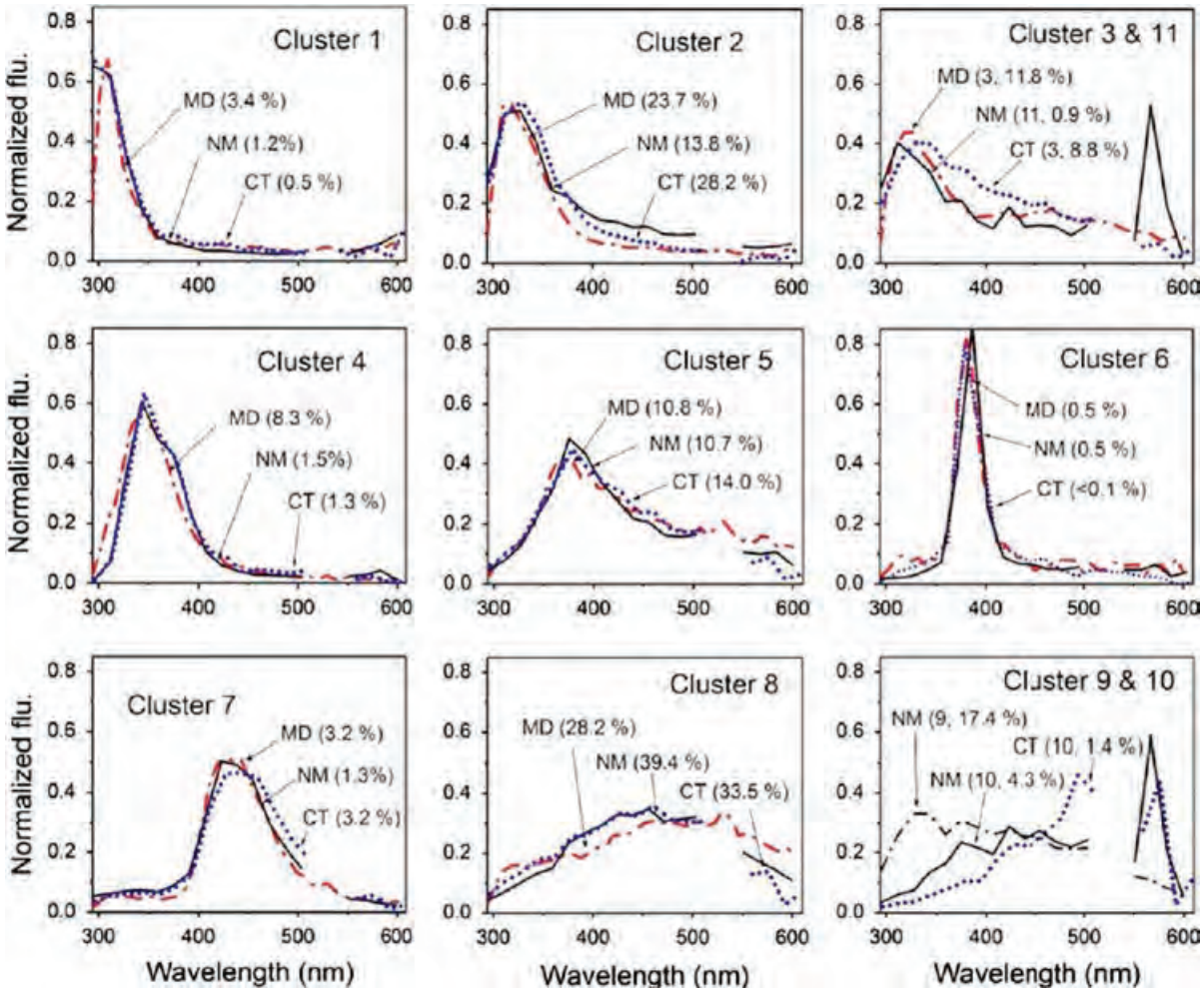

Fig. 10. The 266- or 263-nm excited fluorescence spectral templates derived from hierarchical cluster analyses for Adelphi, MD, New Haven, CT, and Las Cruces, NM, data. The percentage of (fluorescent) particles that cluster into each template is also shown [68].

Clusters 3–5 are peaked around 440–470 nm with increasing green and red fluorescence. Compounds containing the biological fluorophores NADH, neopterin, lumazine, and chitin may have fluorescence emission profiles like clusters 3, 4, and 5. Diesel soot, biomass burning, *S. cerevisiae*, vegetative bacteria, bacterial spores (e.g., *B. subtilis*), some pollens (e.g., these pollens from ragweed, elm, cottonwood, birch, and populus deltoides) and some fungi (e.g., *Penicillum chrysogenum*, Johnson grass smut spores, *Cladosporium herbarum*, *Aspergillus flavus*) by themselves or mixed with a small portion of other compounds may also fluoresce similarly to cluster 3, 4 and 5. Many non-biological compounds found in the atmosphere, including a very significant fraction of PAHs and their oxidation products, are highly fluorescent in this emission region. HULIS materials are also fluorescent in this emission wavelength.

Clusters 6 and 7 have a fluorescence peak around 520–560 nm. Compounds containing the biological fluorophore riboflavin may have fluorescence profiles similar to clusters 6 and 7. Under some conditions, pollen (e.g., red oak), aged fulvic acid, and humic acid may also fluoresce with a similar spectral profile.

Cluster 8 has a broad emission band spanning from blue to red and may be from a mixtures of different compounds. Clusters 4 and 6 are similar, but with different peak wavelengths.

Some possible factors contributing to the similarities between clusters at the different sites and seasons by two different excitation wavelength are (1) long-range atmospheric transport and turbulent mixing tend to homogenize the ambient aerosol; (2) combustion (biomass, engines, etc.) emissions, both the primary and secondary organic aerosol, and the new compounds generated as these aerosols aging, may be similar at different geographic locales; and humidity, temperature and atmospheric turbulent structure may affect the formation of aerosol particles, partitioning of combustion products between gas and particle phases, and processing of particles; and (3) the predominant fluorophors in biological materials (tryptophan, NADH or similar compounds, and flavins) are preserved across species. Some of the main

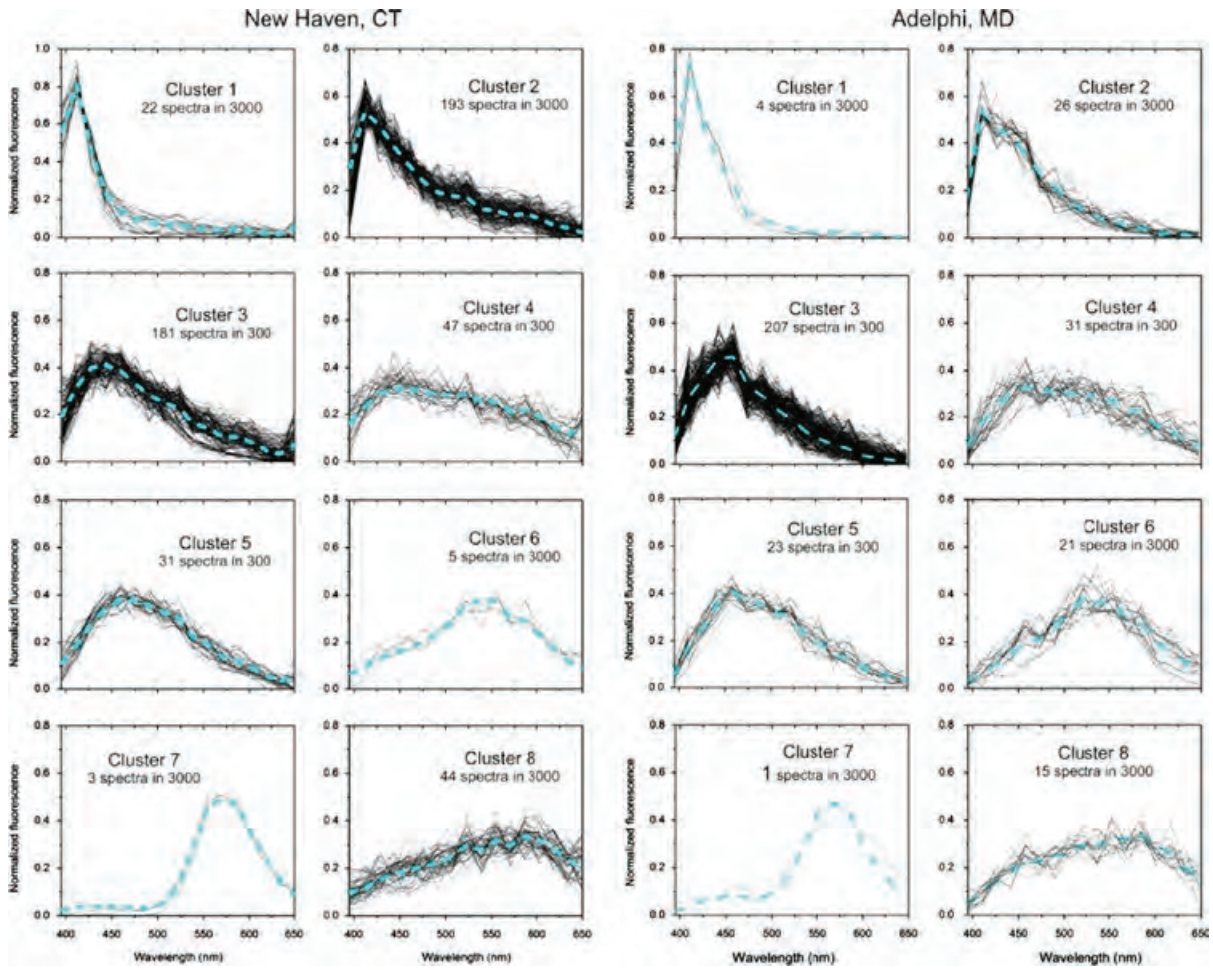

Fig. 11. Normalized fluorescence spectra of single atmospheric aerosol particles excited by a 351-nm laser (thin solid lines) measured at New Haven, CT, and Adelphi, MD. The template spectrum for each cluster (derived from a HVA) is shown in thick dashed line.

fluorphors in plant cell walls (e.g., ferulates), and wood (lignans, sinapyl alcohols, etc.) are common in diverse environments [78,79,68,70,72].

7. Time series of aerosol population in different fluorescence clusters

The population of particles in each cluster varies from more than 10^4 counts (e.g., cluster 8) to only a few counts (e.g., clusters 1, 6, and 7) in a 10 min period observed by SPFS. The time series of aerosol measurements for May 3–4, 2007 in New Mexico are presented in Fig. 12; Nephelometer data are presented in dark red, which is shown as the ratio of aerosol scattering to molecular Rayleigh scattering, are averaged over 4-min periods. The SPFS data are presented as total counts accumulated over 24-min periods. They include the total aerosol particle count (for sizes greater than about 1 μm), the fluorescence particle count above preset threshold, and the counts for particles having spectra falling in various spectral clusters. The shaded areas in the figures indicate a gap in data collection [79].

It is noticeable that the most populated cluster of fluorescent particles is cluster 8 in all locations and seasons. The next most populated clusters are 5, 9, and 2. Weakly populated clusters are those with bacteria-like spectra (cluster 4), cellulose/pollen-like spectra (cluster 7), cluster 10, and clusters 6 and 1. The fraction of fluorescent particles populating the various clusters is in general remarkably similar for the different data sets with a few exceptions. The concentrations of particles in the most populated clusters (8, 5, 9, 2) appear highly correlated for all time-series of data in New Mexico.

One striking feature of these data sets is that the fraction of fluorescent particles falling in the various spectral clusters appears to remain relatively constant for periods of several weeks at a particular site. So it may not be too surprising that at least some of the concentrations of particles in different clusters might be correlated over much shorter time scales. The strong correlation of concentrations of particles in highly populated clusters could be hypothesized that these high correlated clusters must have the same source regions, or from a long travel distance with enough time to mix and age during the atmospheric transportation process.

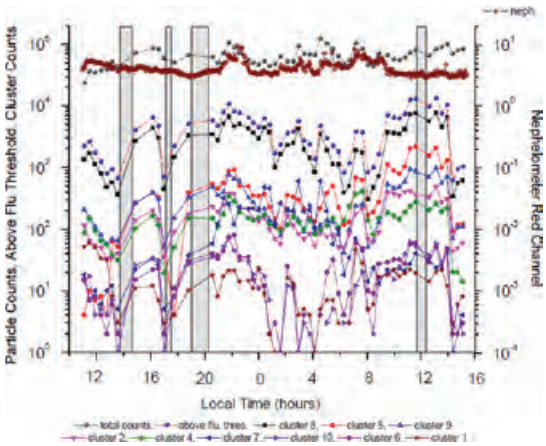

Fig. 12. Time series of aerosol measurements made with a Nephelometer (red circles with cross hairs) and the SPFS for May 3–4, 2007 in Las Cruces, NM. Nephelometer measurements shown the total particle counts averaged over 4-min periods. SPFS measurements shown are integrated over 24-min periods for total particle count (black circles), particles with fluorescence above threshold (blue circles), particles populating clusters 8 (black square), 9 (light blue triangle), 4 (green diamond), 2 (red triangle), 5 (red circle), 1 (brown star), 7 (dark blue triangle pointing left), 10 (purple triangle) and 6 (purple hexagon) [79]. (For interpretation of the references to color in this figure legend, the reader is referred to the web version of this article.)

The long-term online monitoring of PBAP at different locations and seasons also reveals some nature of time-dependent variation of fluorescence particles (e.g., [34,24,25,26,101,84,69,79,80]). The diurnal cycle of visible fluorescence particles (assigned to N_{NADH}) observed by WIBS-3 in northern France is noticeable, where the relative ratio of fluorescent particles (N_{NADH}) to the total particles (N_{TOT}) usually increases after dark before reducing again by sunrise (Fig. 13), but the relationship between N_{NADH} and N_{TRY} (tryptophan particles) in this measurement is inconsistent with other PBAP measurements using WIBS-3 [101] or SPFS [79], which have high correlation between the bacteria-like fluorescence particles (N_{TRY} or cluster 2, 3 and 4) and HULIS-like particles (N_{NADH} or cluster 7, 8) as just discussed above. It was explained to be lack of fungal spores release at this site northern France. While in the other measurement sites, the bacteria, fungal spores or pollen dominated the PBAP, the results show better time-serious correlation between various groups of fluorescence particles [26]. However, this assumption does not totally agree with the observations from Las Cruces, NM (Fig. 12), which is near isolated riparian areas with very low precipitation, essentially no trees, frequently dust storms, and has much lower population of bacteria, pollen and fugal.

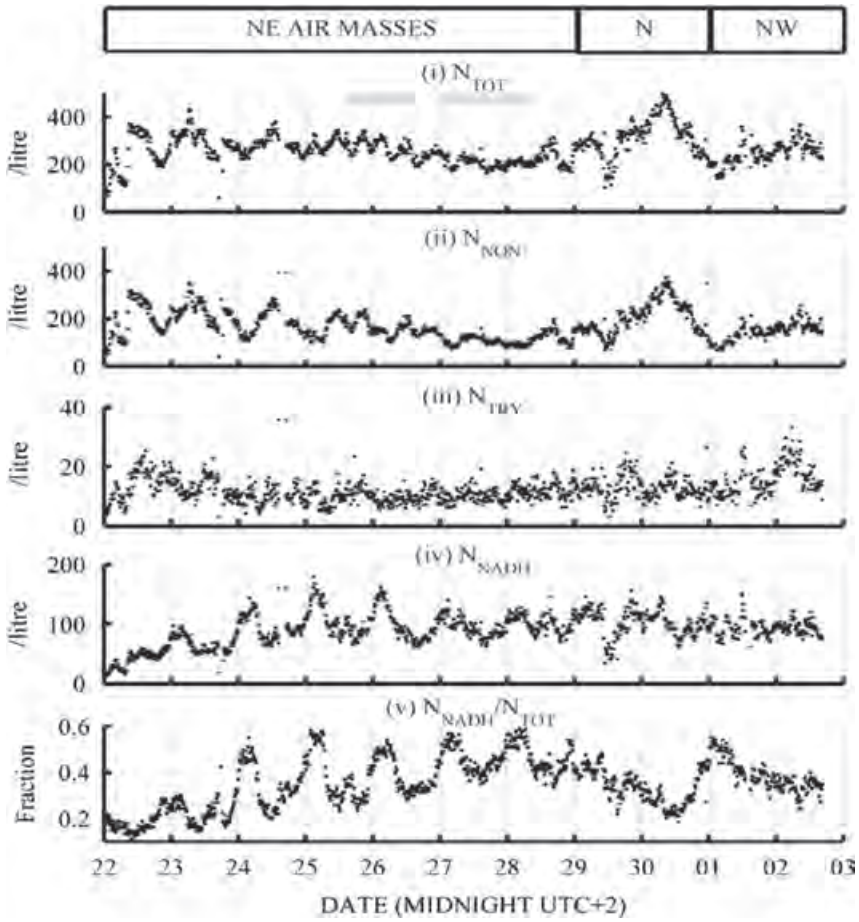

Fig. 13. (i–iv) WIBS-3 number concentrations of fluorescent and non-fluorescent particle types (v) number fraction of N_{NADH} and relative humidity time series from 22 June to 3 July 2010. Gray boxes denote when ELPI samples were running and white boxes show modeled air mass origin (Fig. 1 in [26]).

Dividing the very complex fluorescence spectra into different clusters using HCA greatly simplified the spectral analysis process; it could be a very good method for future atmospheric aerosol study. Further measurements need to be made at a single site during different seasons, and also different sites with different regional climate, to investigate the generality of the observed phenomena. The long-term bioaerosol measurements that showed some seasonally and daily time variations carried out by several research groups using different instruments further help us in the understanding of atmospheric aerosol formation and transport (e.g., [34,24,25,26,101,84,79,80]).

8. Ultrafast multi-photon-excited fluorescence of bioaerosols

Even using the information from DPFS with two dispersed fluorescence spectra and two elastic scattering intensities from every single particle, it is still impossible to identify bioaerosol particles that have similar fluorescence spectra and quantum efficiencies, e.g., between BG, *E. coli,* diesel vapor and cigarette smoke [29]. One of the possible methods of overcoming the limits of conventional linear spectroscopy is to excite the fluorescence with ultrashort laser pulses in order to access specific molecular dynamics features in the *time domain*. Recent experiments lead by Prof. J.-P. Wolf using coherent control and multi-photon ultrafast spectroscopy have shown the ability to discriminate between molecular species that have similar one-photon (e.g., by 263/266 nm) excited fluorescence spectra. This femtosecond pump-probe depletion (PPD) spectroscopic technique can distinguish biological microparticles (containing amino acids (Tryptophan, Trp) and flavins (riboflavin RBF, FMN and FAD)) from nonbiological PAH (as diesel fuel). Diesel particulate emission in atmosphere is one of the key interferents for bioaerosol discrimination; it has similar fluorescence features as bacteria. The femtosecond laser induced multi-photon excited fluorescence (MPEF) technique also showed good bioaerosol discrimination between different pollen particles (Ragweed, Pecan, Mulberry) [11,13,44,45].

PPD technique is based on the time-resolved observation of the competition between excited state absorption into higher lying excited states and fluorescence into the ground state. Fig. 14(a) shows the scheme in a tryptophan molecule. A femtosecond pump laser pulse (at 270 nm for tryptophan (Trp) and PAHs, 405 nm for flavins), resonant with the first absorption band of the fluorophores, coherently excites them from the ground state. Then the linear fluorescence emission process happens, which lasts from a few nanoseconds to more than 10 ns depending on the molecular structures. Meanwhile, a second 810-nm femtosecond probe pulse is used to transfer part of the population in the first excited state into higher lying electronic states, this depletion efficiency of the population relies on both the molecular dynamics in this intermediate state and the transition probability to higher state. By varying the temporal delay Δt between the pump and probe laser pulses, the dynamics of molecule population in the intermediate state and the fluorescence signal are therefore depleted as a function of Δt. Fig. 14(b) shows a typical PPD spectroscopy ($\lambda 1 = 270$ nm and $\lambda 2 = 810$ nm) from *E. coli*, *B. subtilis*, and diesel fuel. They demonstrated remarkable difference between bacteria and diesel fuel, although generally they have very similar one-photon excited fluorescence spectra.

9. Algorithms for discriminating particular bioaerosol from atmospheric aerosol particles

For specific applications where particular bioaerosol particles have well-defined optical properties, e.g., for a specific preparation of bacteria or viruses, or for fungal spores, the DPFS or SPFS can be highly sensitive using the information from either two or one dispersed fluorescence spectra and elastic scattering size. An optimized algorithm to distinguish the specific particles from other interferent and background aerosol particles based on UV-LIF rapidly,

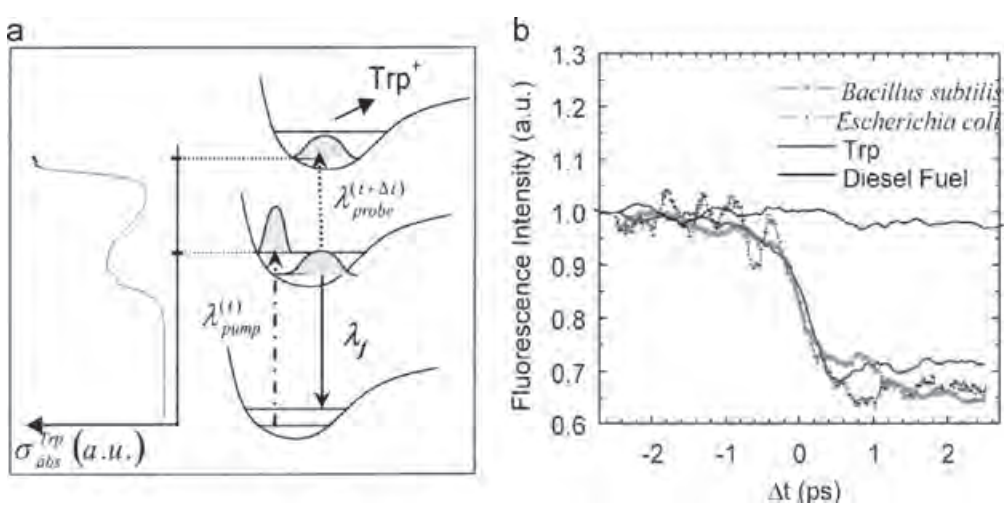

Fig. 14. (a) Pump-probe depletion (PPD) scheme in a tryptophan molecule. The pump pulse excite molecules into the first excited state, the molecules population in this state (and therefore the fluorescence) is depleted by the second probe pulse with a certain time delay; (b) discrimination between bacteria and diesel fuel using PPD ultrafast spectroscopy [11,12].

easily and clearly is always important. The spectral analysis algorithms used in the existing instruments can be grouped into three methodologies [67]. (1) Specific particle is determined by its signal location in a two- or three-dimensional space where the coordinates are the fluorescence intensity, ratio of fluorescence intensity from UV and visible bands, or the size and shape information from elastic scattering of the detected aerosol particles, generally called scatter-plot. (2) Specific particle is determined by its fast fluorescence spectral profile match through the relative intensity comparison between different wavelengths (or multiple bands) associated with its fluorescence quantum efficiency (including size, or even shape information). (3) Specific particle is determined by using PCA, HCA, discriminant function analysis (DFA), or least-square fit, etc., numerically multivariate analysis and classification. These discrimination results can also be presented in a special coordinate as (1). Taking the below parameters into consideration in the discrimination algorithm should greatly increase the discrimination ability, such as the time evolution property with particular atmospheric conditions and geographical conditions as discussed in Section 5.

For these systems, with one or two fluorescence spectral bands with or without one elastic scattering intensity, generally the discriminations can be visualized by the particles location in a space (e.g., [77,19,93,95,27,83,41,42]). Fig. 15 shows one of the typical scatter plots that frequently used to illustrate the observation of various aerosol simulants located in different positions. It indicates that some common bioaerosol simulants overlap with a small fraction of ambient particles occur in essentially all parts of the fluorescence feature space. The presence of the fluorescent atmospheric aerosol particles is significant because they establish a background threshold level that a new population of fluorescent particles would need to exceed in order to be detected by an automated algorithm [97].

Fig. 16 shows how six different mimic fluorescence-based detection systems can be used to discriminate particular particles from atmospheric aerosol particles. Here, BG (a common bacterial simulant for *Anthrax*) was used as the

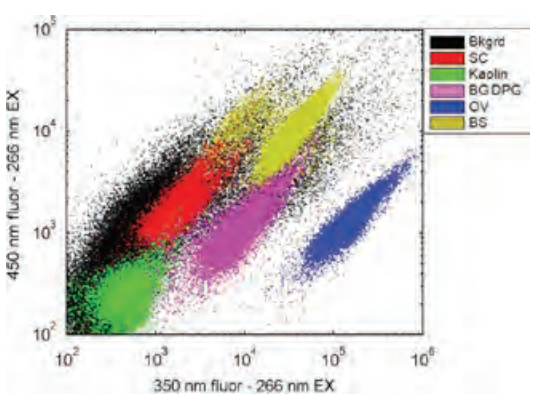

Fig. 15. The fluorescence signature in two 266-nm excited spectral bands from background aerosol particles sampled over a 2-hr period, overlaid with the signature of some of the common simulants and interferents. The background particles show substantial overlap with inorganic interferent kaolin and fungal spores (Fig. 3 in [97])

particular particle with well-defined elastic scattering and dispersed fluorescence spectra by DPFS. *Algorithm 1* and *2* for system only have information from total fluorescence and elastic scattering excited by 263 and 351 nm, respectively, such as UV-APS; *Algorithm 3* for systems have elastic scattering particle size and the integrated UV and visible fluorescence bands such as BAWS; *Algorithm 4* for systems that have elastic scattering and two-band fluorescence (ultraviolet and visible) excited by 263 and 351 nm somehow similar to the systems developed by Sivaprakasam et al. [95] and Kaye et al. [42]. *Algorithm 5* for system SPFS based on 263/266-nm elastic scattering and the 263/266-nm-excited fluorescence spectrum; and *Algorithm 6* for system DPFSs that have both 263- and 351-nm elastic scattering and both 263- and 351-nm excited fluorescence spectra. Here only the simplest method was used for discriminating BG from atmospheric particles by applying the relative ratio between multiple bands of fluorescence and elastic scattering without considering any specific algorithms such as PCA or HCA.

In general, a certain concentration is required before a particular bioaerosol can be noticeably detected within atmospheric aerosol particles, where a lot of particles may have similar optical properties as the particular bioaerosol, so the more specific the detection system, the higher discriminating ability the system will have. The specific functions of a detection system help improve the detection ability of a particular bioaerosol at low concentrations (e.g., [82,70]). Fig. 16 demonstrated the capability of six mimic systems in discriminating among BG and atmospheric aerosol particles. These particles are assigned to be either biological (for algorithms 1 and 2) or BG-like (for algorithms 3–6) particles at different time periods. They differ by about a factor of 250 for the overall averages (right) and by as much as three orders of magnitude for some time periods (e.g., 3 am–11 am). For algorithms 1 and 2 the percentages of particles detected as fluorescent are 16.2% and 16.5% on average. For algorithms 3–6, which are constructed to detect BG against the natural atmospheric background, the corresponding percentages of particles that are BG-like are: 2.49%, 1.43%, 0.46% and 0.06%. The very large differences in specificities obtained with the six algorithms illustrate the diagnostic power and potential versatility of the DPFS. These six algorithms use more of the information successively measured by the DPFS regarding the fluorescence intensities, fluorescence spectral shapes and elastic scattering, and have an ability to discriminate against an increasingly larger fraction of the atmospheric aerosol background in the case of particles having known fluorescence spectra. However, the more specific system, the lower positive alarm rate, but the more negative false alarm rate, in which particular particle that has small optical property variation, e.g., the same bioaerosol under slightly different growth conditions [51] or atmospheric environments [75], could be missed by detection.

There is always a tradeoff between the discrimination ability and negative false alarm rate, or the sensitivity (should be less confusing by using a detection threshold) and the probability of detection [67,70]. In order to reduce the positive false alarm rate, a system generally has to set at a high detection threshold, at the same time that will

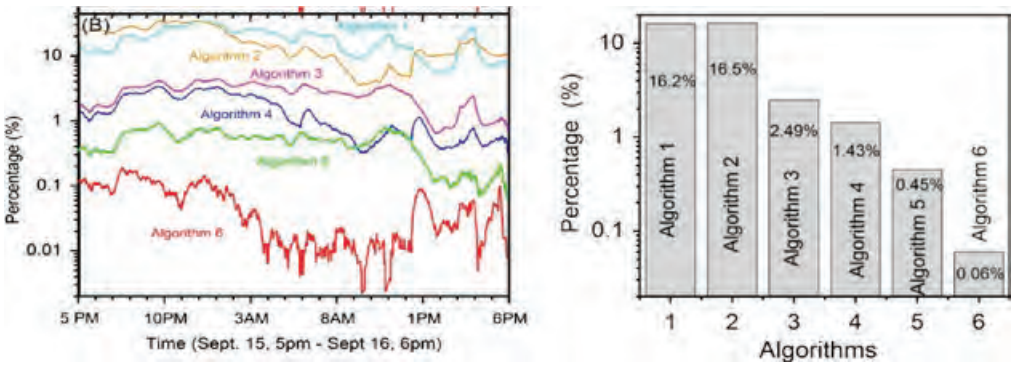

Fig. 16. (Left) percentages of fluorescent particles according to algorithm 1 (turquoise) and 2 (orange). Percentages of BG-like particles according to algorithms 3 (magenta); 4 (blue); 5 (green); and 6 (red); (b) Percentages of atmospheric aerosol particles that cannot be distinguished from one particular sample of BG using each of the six algorithms described in the text. The atmospheric aerosol sample of 1,419,127 total aerosol particles was measured by the DPFS during Sept 15, 5 PM to Sept 16, 6 PM, 2009, at Adelphi, MD [70]. (For interpretation of the references to color in this figure legend, the reader is referred to the web version of this article.)

automatically result in high negative false alarm rate. For a real-time detection system, a fast efficient discrimination algorithm has to be used, such as the simple relative band intensity comparison developed in SPFS by using 32-anode PMT as a detector [63,64]. For laboratory-generated samples prepared in some certain conditions, fluorescence spectra are more promising for bioaerosol discrimination, even between different species such as the differentials between the gas phase samples of 46 bioaerosols [8]. Their relative LIF spectra were treated chemometrically by PCA, HCA and linear discriminant analysis (LDA) to classify the microorganisms according to family, morphology and gram. In this study, the best classifications are found to be based on LDA. Fig. 17 shows a plot of the samples on the plane defined by the two first canonical discriminant functions according to the name of the bacteria [8]. This further demonstrated the discrimination power of fluorescence spectra.

10. Detecting and characterizing single aerosol particle on-line by fluorescence

Fluorescence is an inelastic optical process having a signal (for particles containing OC) about 3–6 orders of magnitude less than elastic scattering. Among all the inelastic processes, fluorescence generally has the strongest signals. The fluorescence process involves three steps: (1) transition from the vibronic states of the ground electronic manifold to some vibronic states in an upper electronic manifold caused by the absorption of an incident photon; (2) a non-radiative transition among vibronic states within or between upper electronic manifolds; and (3) lastly, a photon emission from the radiative transition of the upper electronic manifold to some vibronic states in the ground electronic manifold. Biological molecules are typically very large, and consequently the vibronic states and the electronic manifolds are dense and result in broad, diffuse emission spectral profiles. Furthermore, many similar biomolecules are ubiquitous among living organisms. Consequently, the fluorescence signal can only be used as a classifier and not as a species-level identifier.

By shifting the excitation wavelength from 266 to 350 nm, the “NADH peak” will grow while the tryptophan peak will diminish. Hence we can perceive the power of dual wavelengths excitation and the advantage of 2-band monitoring. From analyzing the difference and ratio of the tryptophan and NADH fluorescence peaks, one can decide that some molecules in the particle are biological. Currently the most advanced fluorescence-based aerosol diagnostic techniques use dual-wavelengths excitation for the tryptophan and NADH absorption bands and multiple-wavelength detection bands or entire UV–visible detection spectra. Using current techniques, with fluorescence spectra as a cue, aerosols can be interrogated at rates up to 20,000 per second using a 32-anode PMT for spectral detection [63,64]. The suspect bioaerosols can be sorted (deflected aerodynamically or electronically) from the dominant population of innocuous background particles at rates up to a few hundred per second [66,96]. The bio-enriched aerosols can be deposited onto the surface of a substrate or into a liquid in a microfluidic-reservoir for further analyses. The bio-enriched particles on a substrate can be identified by optical techniques such as FTIR or Raman scattering. Bio-enriched particles in the microfluidic-reservoir well can be identified by specific binding between antigens and fluorescent-tagged antibodies, or possibly by DNA/RNA sequencing (e.g., [35]).

The minimum detectable background of particular bioaerosol particles (e.g., biothreat agent) depends on the highly variable site and atmospheric background of OC aerosols that act as interferents to detection, even without considering the atmospheric aging and processing as discussed on Section 5. These interferent particles may be PAH, humic and fulvic acids, HULIS, or bacteria that have fluorescence emission similar to the target agents, and can cause positive false alarms. Not only must we decrease the false alarm rate, we must be able to detect one threat aerosol in the ambient atmospheric background like “finding a needle in a haystack.” This can be best accomplished with continuous monitoring and providing data in quasi real time. With the highest quantum efficiency, elastic scattering and fluorescence provide the first choice for the instrumentation of bio-aerosol detection

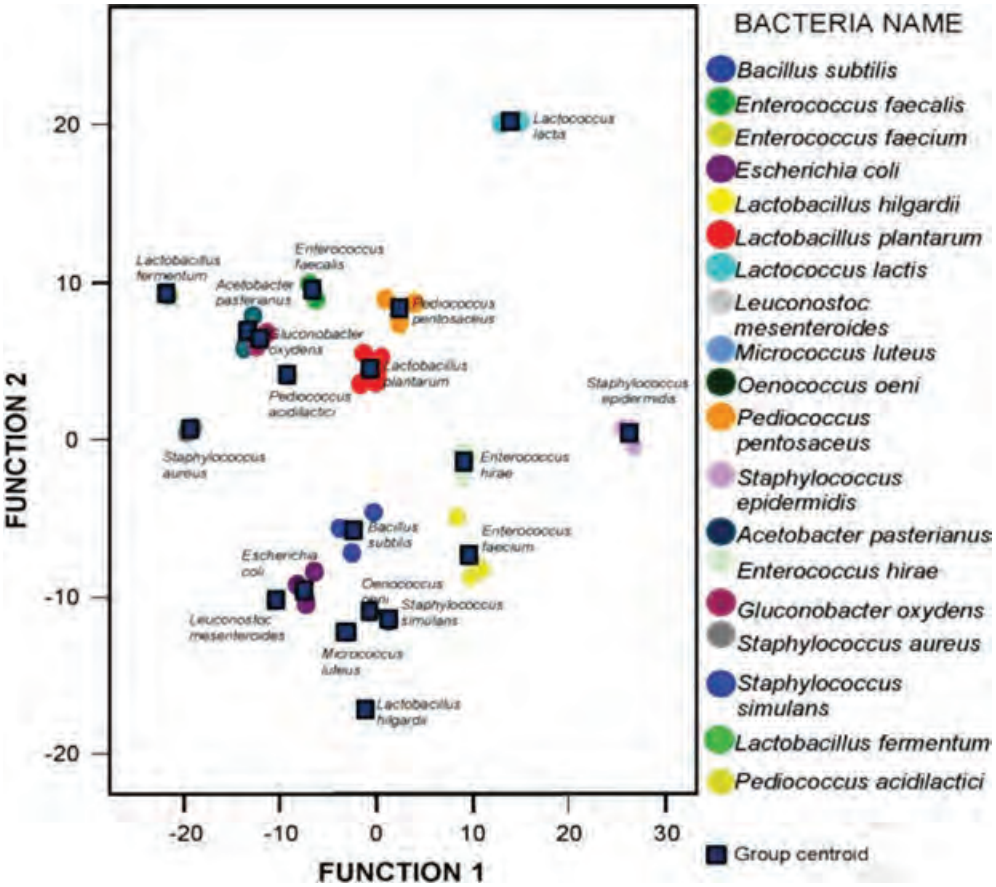

Fig. 17. Plot of the samples on the plane defined by the two first canonical discriminant functions according to the name of the bacteria (Fig. 2 from [8]).

and characterization. Besides satisfying all the requirements, the instrument should be inexpensive, maintenance free, sensitive to one ACPLA, and have low power consumption and low false alarm rates. That will be a real challenge!

The fluorescence and elastic scattering based detection and characterization systems supply a complementary on-line method for studying atmospheric aerosol particles, and can also be used as a fast classifier to a certain level for fluorescent organic-carbon (including biological) aerosol particles. However, even using the information obtained from multi-wavelength excited spectrally resolved fluorescence and elastic scattering, it is still a big challenge to discriminate different bacteria, and even harder to differentiate the species from the same bacteria, except the aerosol particles are grown in the same conditions, prepared and dispersed in the same methods, and exposed to the same atmospheric environments within the same time elapsed.

In order to develop the single-particle laser-induced-fluorescence techniques into a more powerful analytical tool, the compositions of atmospheric aerosol particles in each fluorescence clusters should be identified using biochemical identification processes, at least to a more accurate level of classification than the present speculations that were deduced from the well-known UV-LIF spectra (Section 6). After building such a database by the biochemical identification processes (e.g., [76]), any atmospheric aerosol particle detected by fluorescence can be easily assign to a corresponding cluster with higher confidence. This then will greatly improve the precision of aerosol determination from their fluorescence properties, which have been identified by applying the advanced and standardized biochemical methodologies to include all the abundance and diversity of atmospheric OC aerosol and bioaerosol particles. Therefore, sorted aerosol particles based on the variety of fluorescence properties need to be collected and analyzed to build such a database. More long-term measurements and observations at different sites and seasons are also needed to better understand atmospheric aerosol particles. Meanwhile, more extensive studies based on laboratory experiments and field observations are definitively required for understanding the complicated evolution process of OC and bioaerosol particles under various atmospheric conditions. It is very important to isolate the key effective OAFs, to figure out the correlation between the changes and their corresponding OAFs, then build the consequential model that can apply atmospheric aging, transforming, and transporting, then provide the fluorescence aerosol effects on climate and health.

Acknowledgment

Thank for the U.S. Army Research Laboratory mission funds. Thank Carol Johnson and Water Bailey for assisting editing this article.

References

[1] Atkins J, Thomas ME, Joseph RI. Spectrally resolved fluorescence cross sections of BG and BT with a 266-nm pump wavelength. In: Augustus W, Fountain III, editors. Chemical and Biological Sensing VIII, vol. 6554. Proceedings of SPIE; 2007 (65540T1-8).

[2] Bailey R, Fielding L, Young A, Griffith C. Effect of ozone and open air factor against aerosolized *Micrococcus luteus*. J Food Prot 2007;70 (12):2769–73.

[3] Bauer H, Schueller E, Weinke G, Berger A, Hitzenberger R, Marr IL, et al. Significant contributions of fungal spores to the organic carbon and to the aerosol mass balance of the urban atmospheric aerosol. Atmos Environ 2008;42:5542–9.

[4] Berlett BS, Levine RL, Stadtman ER. Comparison of the effects of ozone on the modification of amino acid residues in glutamine synthetase and bovine serum albumin. J Biol Chem 1996;271(8):4177–82.

[5] Bones DL, Henricksen DK, Mang SA, Gonsior M, Bateman AP, Nguyen TB, et al. Appearance of strong absorbers and fluorophores in limonene-O3 secondary organic aerosol due to NH+4-mediated chemical aging over long time scales. J Geophys Res 2010;115: D05203.

[6] Boutou V, Favre C, Hill SC, Pan YL, Chang RK, Wolf JP. Backward enhanced emission from multiphoton processes in aerosols. App Phys B 2002;755(2–):145–53.

[7] Buteau S, Simard JR, Nadeau D. Characterization of laser induced fluorescence from background aerosols in a maritime environment. Proc SPIE 2011;8018 (801803-1-11).

[8] Cabredo S, Parra A, Sáenz C, Anzano J. Bioaerosols chemometric characterization by laser-induced fluorescence: air sample analysis. Talanta 2009;77:1837–42.

[9] Carrera M, Zandomeni RO, Fitzgibbon J, Sagripanti JL. Difference between the spore osizes of *Bacillus anthracis* and other Bacillus species. J Appl Microbiol 2006;102:303–12.

[10] Cheng YS, Barr EB, Fan BJ, Hargis PJ, Rader DJ, O'Hern TJ, et al. Detection of bioaerosols using multiwavelength UV fluorescence spectroscopy. Aerosol Sci Technol 1999;30:186–201.

[11] Courvoisier F, Boutou V, Wood V, Bartelt A, Roth M, Rabitz H, et al. Bacteria from background urban aerosols. Appl Phys Lett 2005;87 (5):063901–3.

[12] Courvoisier F, Boutou V, Guyon L, Roth M, Rabitz H, Wolf J-P. Discriminating bacteria from other atmospheric particles using femtosecond molecular dynamics. J Photochem Photobiol A: Chem 2006;180(3):300–6.

[13] Courvoisier F, Bonacina L, Boutou V, Guyon L, Bonnet C, Thuillier B, et al. Identification of biological microparticles using ultrafast depletion spectroscopy. Faraday Discuss 2008;137:37–49.

[14] Deguillaume L, Leriche M, Amato P, Ariya PA, Delort A-M, Pöschl U, et al. Microbiology and atmospheric processes: chemical interactions of primary biological aerosols. Biogeosciences 2008;5:1073–84.

[15] Dery B, Buteau S, Simard J-R, Bouchard J-P, Vallee R. Spectroscopic calibration correlation of field and lab-sized fluorescence lidar systems. IEEE Trans Geosci Remote Sens 2010;48:3580–6.

[16] Després VR, Huffman JA, Burrows SM, Hoose C, Safatov AS, Buryak G, et al. Primary biological aerosol particles in the atmosphere: a review. Tellus B 2012;64:15598.

[17] Duarte RMBO, Pio CA, Duarte AC. Spectroscopic study of the water-soluble organic matter isolated from atmospheric aerosols collected under different atmospheric conditions. Anal Chim Acta 2005;530: 7–14.

[18] Dungan RS. Fate and transport of bioaerosols associated with livestock operations and manures. J Anim Sci 2010;88:3693–706.

[19] Eversole JD, Hardgrove JJ, Cary WK, Choulas DP, Seaver M. Continuous, rapid biological aerosol detection with the use of UV fluorescence: outdoor test results. Field Anal Chem Technol 1999;3:249–59.

[20] Faris GW, Williams A, Carlisle CB, Bronk BV. Spectrally resolved absolute fluorescence cross sections of *B. Globigii* and *B. Cereus*, SRI technical note. SRI project 2913; 1992.

[21] Faris GW, Copeland RA, Mortelmans K, Bronk BV. Spectrally resolved absolute fluorescence cross sections for bacillus spores. Appl Opt 1997;36(4):958–67.

[22] Farsund O, Rustad G, Kasen I, Haavardsholm TV. Required spectral resolution for bioaerosol detection algorithms using standoff laser-induced fluorescence measurements. IEEE Sens J 2010;10:655–61.

[23] Fujimori E. Changes induced by ozone and ultraviolet light in type I collagen *Bovine Achilles* tendon collagen versus rat tail tendon collagen. Eur J Biochem 1985;152(2):299–306.

[24] Gabey AM, Gallagher MW, Whitehead J, Dorsey JR, Kaye PH, Stanley WR. Measurements and comparison of primary biological aerosol above and below a tropical forest canopy using a dual channel fluorescence spectrometer. Atmos Chem & Phys 2010;10: 4453–66.

[25] Gabey AM, Stanley WR, Gallagher MW, Kaye PH. The fluorescence properties of aerosol larger than 0.8 mu m in urban and tropical rainforest locations. Atmos Chem & Phys 2011;11(11):5491–504.

[26] Gabey AM, Vaitilingom M, Freney E, Boulon J, Sellegri K, Gallagher MW, et al. Observations of fluorescent and biological aerosol at a high-altitude site in central France. Atmos Chem Phys 2013;13(15):7415–28.

[27] Hairston PP, Ho J, Quant FR. Design of an instrument for real-time detection of bioaerosols using simultaneous measurement of particle aerodynamic size and intrinsic fluorescence. J Aerosol Sci 1997;28:471–82.

[28] Healy DA, O'Connor DJ, Burke AM, Sodeau JR. A laboratory assessment of the Waveband Integrated Bioaerosol Sensor (WIBS-4) using individual samples of pollen and fungal spore material. Atmos Environ 2012;60:534–43.

[29] Hill SC, Pinnick RG, Pan YL, Holler S, Chang RK, Bottiger JR, et al. Real-time measurement of fluorescence spectra from single air-borne biological particles. Field Anal Chem Technol 1999;3:221–39.

[30] Hill SC, Boutou V, Yu J, Ramstein S, Wolf JP, Pan YL, et al. Enhanced backward-directed multi-photon-excited fluorescence from dielectric microcavity. Phys Rev Lett 2000;85(1):54–7.

[31] Hill SC, Pinnick RG, Niles S, Fell NF, Pan YL, Bottiger J, et al. Fluorescence from air-borne microparticles: dependence on size, concentration of fluorophores, and illumination intensity. Appl Opt 2001;40:3005–13.

[32] Hill SC, Mayo MW, Chang RK., Fluorescence of bacteria, pollens, and naturally occurring airborne particles: excitation/emission spectra. ARL-TR-4722; 2009.

[33] Hill SC, Pan YL, Williamson C, Santarpia JL, Hill HH. Fluorescence of bioaerosols: mathematical model including primary fluorescing and absorbing molecules in bacteria. Opt Express 2013;21(19): 22285.

[34] Huffman JA, Treutlein B, Poschl U. Fluorescent biological aerosol particle concentrations and size distributions measured with an Ultraviolet Aerodynamic Particle Sizer (UV-APS) in Central Europe. Atmos Chem Phys 2010;10:3215–33.

[35] Hermes H, Pan YL, Hill SC, Chang RK, Deposition of selected airborne particles into a microfluidic flow cytometer for bioanalysis. ARL-TR-4446; 2008.

[36] Ignatenko AV, Tatarino BA, Khovratovich NN, Khrapovitskii VP, Cherenkevich SN. Spectral-fluorescent investigation of the action of ozone on aromatic amino acids. J Appl Spectrosc 1982;37(1):781–4.

[37] Ignatenko AV. Use of the method of tryptophan fluorescence to characterize disruptions of the structure of ozonized proteins. J Appl Spectrosc 1988;49(1):691–5.

[38] Jung JH, Lee JE. Variation in the fluorescence intensity of thermally-exposed bacterial bioaerosols. J Aerosol Sci 2013;65:101–10.

[39] Kananga H, Hargreavesa M, Ristovskia Z, Morawskaa L. Performance assessment of UVAPS: influence of fungal spore age and air exposure. J Aerosol Sci 2007;38:83–96.

[40] Kasparian J, Boutou V, Wolf JP, Pan YL, Chang RK. Angular distribution of non-linear optical emission from spheroidal microparticles. Appl Phys B 2008;91(1):167–71.

[41] Kaye PH, Barton JE, Hirst E, Clark JM. Simultaneous light scattering and intrinsic fluorescence measurement for the classification of airborne particles. Appl Opt 2000;39:3738–45.

[42] Kaye, P. H. PH, Stanley WR, Hirst E, Foot EV, Baxter KL, Barrington SJ. Single particle multichannel bio-aerosol fluorescence sensor. Opt Express 2005;13:3583–93.

[43] Killinger DK, Menyuk N. laser remote-sensing of the atmosphere. Science 1987;235(4784):37–45.

[44] Kiselev D, Bonacina L, Wolf J-P. Individual bioaerosol particle discrimination by multi-photon excited fluorescence. Opt Express 2011;19(24):24516–21.

[45] Kiselev D, Bonacina L, Wolf J-P. A flash-lamp based device for fluorescence detection and identification of individual pollen grains. Rev Sci Instrum 2013;84(3):033302.

[46] Klapper L, Mcknight D, Robinfolton J, Blunt-Harris EL, Nevin KP, Lovley DR, et al. Fulvic acid oxidation state detection using fluorescence spectroscopy. Environ Sci Technol 2002;36:3170–5.

[47] Kochelaev EA, Volchek AO, Elizarov BA, Pribor NPO, Petersburg St, Sidorenko VM. Study of the angular fluorescence distribution of bioaerosol particles: modeling and experiment. J Opt Technol 2012;79(6):1070–7.

[48] Kotiaho T, Eberlin MN, Vainiotalo P, Kostiainen R. Electrospray mass and tandem mass spectrometry identification of ozone oxidation products of amino acids and small peptides. J Am Soc Mass Spectrom 2000;11:526–35.

[49] Krivacsy Z, Kiss G, Ceburnis D, Jennings G, Maenhaut W, Salma I, et al. Study of water-soluble atmospheric humic matter in urban andmarine environments. Atmos Res 2008;87:1–12.
[50] Kunnil J, Sarasanandarajah S, Chacko E, Reinisch L. Fluorescence quantum efficiency of dry *Bacillus globigii* spores. Opt Express 2005;13(22):8969–79.
[51] Laflamme C, Simard J-R, Buteau S, Lahaie P, Nadeau D, Déry B, et al. Effect of growth media and washing on the spectral signatures of aerosolized biological stimulants. Appl Opt 2011;50(6):788–96.
[52] Lakowicz JR. Principles of fluorescence spectroscopy. New York: Plenum; 341–3.
[53] Manninen A, Putkiranta M, Saarela J, Rostedt A, Sorvajärvi T, Toivonen J, et al. Fluorescence cross sections of bioaerosols and suspended biological agents. Appl Opt 2009;48(22):4320–8.
[54] Lee HJ, Laskin A, Laskin J, Nizkorodov SA. Excitation – emission spectra and fluorescence quantum yields for fresh and aged biogenic secondary organic aerosols. Environ Sci Technol 2013;47:5763–70.
[55] Matthews BJ H, Jones AC, Theodorou NK, Tudhope AW. Excitation-emission-matrix fluorescence spectroscopy applied to humic acid bands in coral reefs. Mar Chem 1996;55:317–32.
[56] Measures RM. Laser remote sensing – fundamentals and applications. Malabar, Florida: Krieger Publishing Company; 1992.
[57] Mejean G, Kasparian J, Yu J, Frey S, Salmon E, Wolf J-P. Remote detection and identification of biological aerosols using a femtosecond terawatt lidar system. Appl Phys B 2004;78:535–7.
[58] Mitsumoto K, Yabusaki K, Kobayashi K, Aoyagi H. Development of a novel real-time pollen-sorting counter using species-specific pollen autofluorescence. Aerobiologia 2010;26:99–111.
[59] Mudd JB, Dawson PJ, Tseng S, Liu FP. Reaction of ozone with protein tryptophans: band III, serum albumin, and cytochrome C. Arch Biochem Biophys 1997;388:143–9.
[60] Muller CL, Baker A, Hutchinson R, Fairchild IJ, Kidd C. Analysis of rainwater dissolved organic carbon compounds using fluorescence spectrophotometry. Atmos Environ 2008;42:8036–45.
[61] Nisimoto Y, Shibata Y. Studies on FAD- and FMN-binding domains in NADPH-cytochrome P-450 reductase from rabbit liver microsomes. J Biol Chem 1982;257(21):12532–9.
[62] Pan YL, Holler S, Chang RK, Hill SC, Pinnick RG, Niles S, et al. Single-shot fluorescence spectra of individual micrometersized bioaerosols illuminated by a 351- or a 266-nm ultraviolet laser. Opt Lett 1999;24:116–8.
[63] Pan YL, Cobler P, Rhodes S, Potter A, Chou T, Holler S, et al. High-speed, high-sensitivity aerosol fluorescence spectrum detection using a 32-anode photomultiplier tube detector. Rev Sci Instrum 2001;72:1831–6.
[64] Pan YL, Pinnick RG, Hill SC, Niles S, Holler S, Bottiger JR, et al. Dynamics of photon-induced degradation and fluorescence in riboflavin microparticles. Appl Phys B 2001;72(4):449–54.
[65] Pan YL, Hartings J, Pinnick RG, Hill SC, Halvorson J, Chang RK. Single-particle fluorescence spectrometer for ambient aerosols. Aerosol Sci Technol 2003;37:628–39.
[66] Pan YL, Boutou VE, Bottiger JR, Zhang SS, Wolf JP, Chang RK. A puff of air sorts bioaerosols for pathogen identification. Aerosol Sci Technol 2004;38(6):598–602.
[67] Pan YL, Eversole JD, Kaye P, Foote V, Pinnick RG, Hill SC, et al. Bioaerosol Fluorescence. In: Hoekstra A, Maltsev V, Videen G, editors. Optics of Biological Particles (NATO Science Series II: Mathematics Physics and Chemistry). Springer; 2006. p. 63–164.
[68] Pan YL, Pinnick RG, Hill SC, Rosen JM, Chang RK. Single-particle laser-induced-fluorescence spectra of biological and other organic-carbon aerosols in the atmosphere: measurements at New Haven, CT and Las Cruces, NM, USA. J Geophys Res 2007;112:D24S19.
[69] Pan YL, Pinnick RG, Hill SC, Chang RK. Particle-fluorescence spectrometer for real-time measurements of atmospheric organic carbon and biological aerosol. Environ Sci Technol 2009;43:429–34.
[70] Pan YL, Hill SC, Pinnick RG, Huang H, Bottiger JR, Chang RK. Fluorescence spectra of atmospheric aerosol particles measured using one or two excitation wavelengths: comparison of classification schemes employing different emission and scattering results. Opt Express 2010;18(12):12436–57.
[71] Pan YL, Hill SC, Pinnick RG, House JM, Flagan RC, Chang RK. Dual-excitation-wavelength fluorescence spectra and elastic scattering for differentiation of single airborne pollen and fungal particles. Atmos Environ 2011;45:1555–63.
[72] Pan YL, Huang H, Chang RK. Clustered and integrated fluorescence spectra from single atmospheric aerosol particles excited by 263 nm and 351 nm laser at New Haven, Connecticut and Adelphi, Maryland. J Quant Spectrosc Radiat Transf 2012;113(17):2213–21.
[73] Pan YL, Houck JDT, Clark PA, Pinnick RG. Single particle size and fluorescence spectrum from emission of burning materials in a tube furnace to simulate burn pit. Appl Phys B: Lasers Opt 2013;112(1):89–98.
[74] Pan YL, Hill SC, Santarpia JL, Brinkley K, Sickler T, Coleman M, et al. Spectrally-resolved fluorescence cross sections of aerosolized biological live agents and simulants using five excitation wavelengths in a BSL-3 laboratory. Opt Express 2014;22:8165–89.
[75] Pan YL, Santarpia JL, Ratnesar-Shumate S, Corson E, Eshbaugh J, Hill SC, et al. Effects of ozone and relative humidity on fluorescence spectra of octapeptide bioaerosol particles. J Quant Spectrosc Radiat Transf 2014;133:538–50.
[76] Pecciaa J, Hernandez M. Incorporating polymerase chain reaction-based identification, population characterization, and quantification of microorganisms into aerosol science: a review. Atmos Environ 2006;40:3941–61.
[77] Pinnick RG, Hill SC, Nachman P, Pendleton JD, Fernandez GL, Mayo MW, et al. Fluorescence Particle Counter for Detecting Airborne Bacteria and Other Biological Particles. Aerosol Sci Technol 1995;23:653–64.
[78] Pinnick RG, Hill SC, Pan YL, Chang RK. Fluorescence spectra of atmospheric aerosol at Adelphi, Maryland, USA; measurement and classification of single particles containing organic carbon. Atmos Environ 2004;38:1657–72.
[79] Pinnick RG, Fernandez E, Rosen J M, Hill S C, Wang Y, Pan YL. Fluorescence spectra and elastic scattering characteristics of atmospheric aerosol particles in Las Cruces, New Mexico, USA: time series of particle concentrations in various spectral clusters. Atmos Environ 2013;65:195–204.
[80] Pohlker C, Huffman JA, Poschl U. Autofluorescence of atmospheric bioaerosols – fluoresct biomolecules and potential inferences. Atmos Meas Technol 2012;5:37–71.
[81] Poschl U. Atmospheric aerosols: composition, transformation, climate and health effects. Angew Chem-Int Ed 2005;44(46):7520–40.
[82] Ratnesar-Shumate S, Wagner ML, Kerechanin C, House G, Brinkley KM, Bare C, et al. Improved method for the evaluation of real-time biological aerosol detection technologies. Aerosol Sci Technol 2011;45(5):635–44.
[83] Reyes FL, Jeys TH, Newbury NR, Primmerman CA, Rowe GS, Sanchez A. Bio-aerosol fluorescence sensor. Field Anal Chem Technol 1999;3:240–8.
[84] Robinson NH, Allan JD, Huffman JA, Kaye PH, Foot VE, Gallagher M. Cluster analysis of WIBS single-particle bioaerosol data. Atmos Meas Technol 2013;6:337–47.
[85] Roshchina VV, Melnikova EV. Pollen chemosensitivity to ozone and peroxides. Russ J Plant Physiol 2001;48(1):74–83.
[86] Roshchina VV. Autofluorescence of plant secreting cells as a biosensor and bioindicator reaction. J Fluorescence 2003;13(5):403–20.
[87] Rudich Y, Donahue NM, Mentel TF. Aging of organic aerosol: bridging the gap between laboratory and field studies. Ann Rev Phys Chem 2007;58:321–52.
[88] Saari SE, Putkiranta MJ, Keskinen J. Fluorescence spectroscopy of atmospherically relevant bacterial and fungal spores and potential interferences. Atmos Environ 2013;71:202–9.
[89] Saari SE, Reponen T, Keskinen J. Performance of two fluorescence-based real-time bioaerosol detectors: BioScout vs. UVAPS. Aerosol Sci Technol 2014;48(4):371–8.
[90] Santos PS M, Duarte RM BO, Duarte AC. Absorption and fluorescence properties of rainwater during the cold season at a town in Western Portugal. J Atmos Chem 2009;62:45–57.
[91] Santarpia JL, Pan YL, Hill SC, Baker N, Cottrell B, McKee L, et al. Changes in fluorescence spectra of bioaerosols exposed to ozone in a laboratory reaction chamber to simulate atmospheric aging. Opt Express 2012;20(28):29867–81.
[92] Satterwhite MB. Luminescence of some airborne plant materials. ⟨http://oai.dtic.mil/oai/oai?verb=getRecord&metadataPrefix=html&identifier=ADA355121⟩; 1995.
[93] Seaver M, Eversole JD, Hardgrove JJ, Cary Jr. WK, Roselle DC. Size and fluorescence measurements for field detection of biological aerosols. Aerosol Sci Technol 1999;30:174–85.
[94] Simard JR, Roy G, Mathieu P, Larochelle V, McFee J, Ho J. Standoff sensing of bioaerosols using intensified range-gated spectral analysis of laser-induced fluorescence. IEEE Trans Geosci Remote Sens 2004;42(4):865–74.
[95] Sivaprakasam V, Huston A, Scotto C, Eversole J. Multiple UV wavelength excitation and fluorescence of bioaerosols. Opt Express 2004;12(19):4457–66.

[96] Sivaprakasam V, Pletcher T, Tucker JE, Huston AL, McGinn J, Keller D, et al. Classification and selective collection of individual aerosol particles using laser-induced fluorescence. Appl Opt 2009;48(4): B126–36.
[97] Sivaprakasam V, Lin HB, Huston AL, Eversole JD. Spectral characterization of biological aerosol particles using two-wavelength excited laser-induced fluorescence and elastic scattering measurements. Opt Express 2011;19(7):6191–208.
[98] Stephens JR. Measurements of the ultraviolet fluorescence cross sections and spectra of bacillus anthracis simulants. Los Alamos National Lab Report, LAUR-98-4173; May 1999.
[99] Sugimoto N, Huang ZW, Nishizawa T, Matsui I, Tatarov B. Fluorescence from atmospheric aerosols observed with a multi-channel lidar spectrometer. Opt Express 2012;20(19):20800–7.
[100] Taketani F, Kanaya Y, Nakamura T, Koizumi K, Moteki N, Takegawa NJ. Measurement of fluorescence spectra from atmospheric single submicron particle using laser-induced fluorescence technique. Aerosol Sci 2013;58:1–8.
[101] Toprak E, Schnaiter M. Fluorescent biological aerosol particles measured with the Waveband Integrated Bioaerosol Sensor WIBS-4: laboratory tests combined with a one year field study. Atmos Chem Phys 2013;13:225–43.
[102] Vanderbeek R, Castle M. et al.. Laser based stand-off detection of biological agents. RTO technical report (TR-SET-098); 2010.
[103] Weichert R, Klemm W, Legenhausen K, Pawellek C. Determination of fluorescence cross-sections of biological aerosols part. Syst Charact 2002;19:216–22.
[104] Winiwarter W, Bauer H, Caseiro A, Puxbaum H. Quantifying emissions of primary biological aerosol particle mass in Europe. Atmos Environ 2009;43:1403–9.
[105] Adhikari A, Reponen T, Grinshpun SA, Martuzevicius D, LeMasters G. Correlation of ambient inhalable bioaerosols with particulate matter and ozone: a two-year study. Environ Pollut 2006;104: 16–28.

Influence of Molecular Structure on the Laser-Induced Plasma Emission of the Explosive RDX and Organic Polymers

Frank C. De Lucia, Jr. and Jennifer L. Gottfried

The Journal of Physical Chemistry A, 117 (2013)

Influence of Molecular Structure on the Laser-Induced Plasma Emission of the Explosive RDX and Organic Polymers

Frank C. De Lucia, Jr.* and Jennifer L. Gottfried

U.S. Army Research Laboratory, Aberdeen Proving Ground, Maryland 21005, United States

ABSTRACT: A series of organic polymers and the military explosive cyclotrimethylenetrinitramine (RDX) were studied using the light emission from a femtosecond laser-induced plasma under an argon atmosphere. The relationship between the molecular structure and plasma emission was established by using the percentages of the atomic species (C, H, N, O) and bond types (C—C, C═C, C—N, and C≡N) in combination with the atomic/molecular emission intensities and decay rates. In contrast to previous studies of organic explosives in which C_2 was primarily formed by recombination, for the organic materials in this study the percentage of C—C (and C═C) bonds was strongly correlated to the molecular C_2 emission. Time-resolved emission spectra were collected to determine the lifetimes of the atomic and molecular species in the plasma. Observed differences in decay rates were attributed to the differences in both the molecular structure of the organic polymers or RDX and the chemical reactions that occur within the plasma. These differences could potentially be exploited to improve the discrimination of explosive residues on organic substrates with laser-induced breakdown spectroscopy.

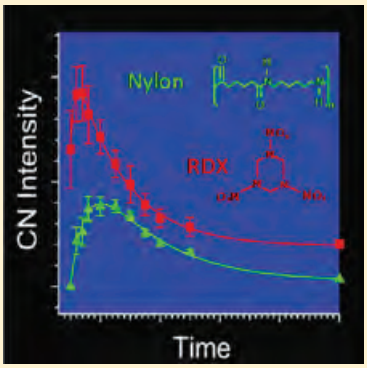

INTRODUCTION

At the US Army Research Laboratory (ARL), laser-induced breakdown spectroscopy (LIBS) has been used to classify a variety of materials, including biomaterials and chemical warfare simulants,[1] geological materials,[2] and organic materials such as high-energy explosives[3] and plastic landmines.[4] LIBS is an optical spectroscopic technique that uses the emission generated from a laser-induced microplasma to determine the composition of a material.[5−7] Light from the microplasma is collected by a spectrometer and detector to spectrally and temporally resolve the emission from the excited material. Classification is based on the relative intensities of the emission from the various excited atomic, ionic, and molecular fragments originating from the ablated sample. In recent years the application of chemometric techniques to the analysis of LIBS data has resulted in the ability to discriminate complex molecular species, including molecular explosives.[8]

Recently, we have been investigating the potential of LIBS to correctly classify organic explosive residues on organic surfaces for security applications.[9,10] One of the main challenges is that the organic substrate contributes to the atomic and molecular emission from key species necessary for the discrimination of explosive residues from other nonexplosive organic residues. Although classification of explosive residues on organic substrates with LIBS has been successfully demonstrated with the aid of advanced chemometrics,[10] a better understanding of the influences on C, H, N, O, C_2, and CN emission generated from the plasma is needed to exploit any differences in emission that may occur between the organic explosive and the organic surface for improved classification results.

Several groups have investigated the formation of C_2 and CN following the laser ablation of graphite under a nitrogen atmosphere,[11−14] The connection between the molecular structure of an organic molecule and the LIBS emission has been also shown previously. Locke et al. surveyed carbon-containing vapors in a He flow and observed the most intense C_2 emission from molecules containing benzene rings.[15] A later study by St-Onge et al. on solid graphite and organic samples determined that the C_2 was ablated directly from samples with aromatic rings, whereas CN was formed from graphite by recombination with atmospheric nitrogen.[16] In addition to direct fragmentation from aromatic rings, C_2 can be formed through recombination reactions in the plasma, as shown conclusively by the isotopic study of Dong et al.[17] Both Portnov et al.[18,19] and Grégoire et al.[20] were also able to show correlations between the spectral emission from organic compounds and the molecular structure. Along with the work by St-Onge et al., however, their studies were performed in ambient air, which complicates the chemistry due to the presence of atmospheric oxygen, nitrogen, and hydrogen (depending on humidity levels).

Though most previous studies utilized nanosecond-pulsed lasers for the material ablation, the plasma chemistry is significantly altered with the use of femtosecond lasers. Fuge et al. found that the nanosecond-laser ablation of graphite in the presence of N_2 resulted in strong CN and weak N_2^+ emissions, whereas femtosecond-laser ablation produced spectra dominated by N_2^+.[13] In addition, Baudelet et al. demonstrated distinct differences in the plasma chemistry of bacterial samples subjected to femtosecond laser pulses.[21] In particular, the lower temperatures

Special Issue: Oka Festschrift: Celebrating 45 Years of Astrochemistry

Received: December 12, 2012
Revised: July 10, 2013
Published: July 10, 2013

of a femtosecond laser-induced plasma were found to favor the formation of molecular species such as C_2 and CN, which is potentially more useful for the analysis of organic samples.

Several kinetic models have been developed in an effort to understand the complex chemistry that occurs in laser-induced plasmas of cyclotrimethylenetrinitramine (RDX)[22] and other organic compounds in air.[23,24] LIBS spectra from nanosecond-pulsed lasers were used to constrain the plasma temperature and electron density in the most recent models,[23,24] which significantly underpredict the ratio of molecular to atomic emissions for certain compounds even at the higher temperatures associated with nanosecond laser-induced plasmas.[24] To gain a better understanding of the emission process for laser-ablated explosives, we have been investigating how the chemistry occurring within the plasma influences the spectral emission. Using a series of novel high-nitrogen explosive molecules, we have demonstrated that emission from the molecular species CN and C_2 was influenced by not only the molecular structure but also the chemical composition of the molecule.[25] Furthermore, Gottfried demonstrated that the presence of aluminum nanoparticles in the plasma increased the C_2 emission from the laser ablation of RDX residue on aluminum, indicating that the substrate composition also strongly affects the plasma chemistry and resulting spectra.[26]

For this paper, we have used femtosecond LIBS under an argon atmosphere to investigate the laser-induced plasma emission from the organic explosive RDX and a series of organic polymers shown in Figure 1: acrylonitrile butadiene styrene (ABS), nylon 6,6 (NYL), polyoxymethylene (POM), polyethylene terephthalate (PET), and ultrahigh molecular weight polyethylene (UHMW). These polymers contain different amounts of C, C−C bonds, O, and N. Previous LIBS studies of polymers have focused on using the emission to classify or identify the polymers.[27−31] In this study, we have demonstrated how organic molecular structure and composition influences atomic and molecular emission from the LIBS plasma, with the goal of eventually exploiting these differences for the classification of explosive residues on polymer substrates.

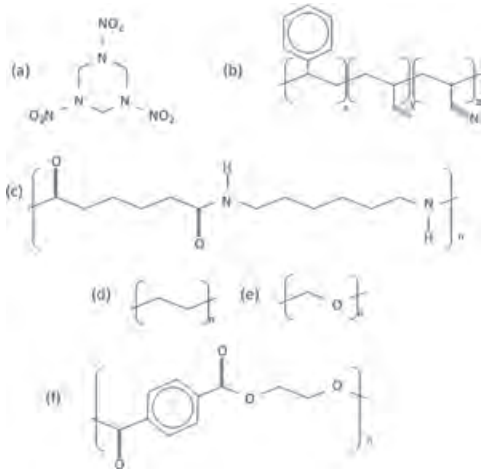

Figure 1. Structures of (a) RDX, $C_3H_6N_6O_6$, (b) acrylonitrile butadiene styrene, $(C_8H_8)_x(C_4H_6)_y(C_3H_3N)_z$ (ABS), (c) nylon 6,6, $(C_{12}H_{22}N_2O_2)_n$, (NYL), (d) ultrahigh molecular weight polyethylene $(C_2H_4)_n$ (UHMW), (e) polyoxymethylene, $(CH_2O)_n$ (POM), and (f) polyethylene terephthalate $(C_{10}H_8O_4)_n$ (PET).

Femtosecond-laser pulses have previously been shown to provide optimal laser ablation conditions for organic material analysis.[32] Here we compare the relative emission intensities and decay rates from the various polymers and RDX excited by a femtosecond-laser pulse.

■ EXPERIMENT

RDX was obtained from colleagues at ARL. The RDX powder was spread in a thick layer across double-sided sticky tape. After each laser shot, the sample was moved to interrogate a fresh surface to ensure that only RDX was sampled by the laser. Because the shock from each laser shot dispersed the RDX powder from a relatively large area (at least 5−10 times the diameter of the focused laser pulse), we were only able to obtain 20 laser shots. The five 6 in. × 6 in. industrial polymer samples were obtained from McMaster-Carr (thermoplastic material selector pack, #5331K1); these materials contain trace organic additives, but the only metal impurity was trace amounts of Mg in the ABS, PET, and POM (as well as the RDX).

The ultrafast laser used for generating LIBS spectra was a Ti:sapphire amplifier (Coherent Hidra-25) seeded by a femtosecond-pulsed oscillator (Coherent Vitesse, centered at 790 nm, 100 fs pulse duration). A Nd:YLF pump laser (Coherent Evolution-15) amplified the output energy of the femtosecond laser to 1 mJ, and an additional Nd:YAG pump laser (Continuum Powerlite Precision II 8000) amplified the femtosecond pulse energy up to 25 mJ. The polymer samples and RDX were interrogated by 12 mJ pulses from the femtosecond laser focused just below the material surface with a 10 cm lens. The laser irradiance was estimated to be 1.2×10^{14} W/cm^2. Each laser pulse (fired at a 2 Hz repetition rate) ablated a small amount of material from the sample surface (picograms to nanograms), resulting in the formation of a laser-induced plasma consisting of excited atoms, ions, and neutral species. An argon gas flow was directed over the sample surface near the point of laser impact. The Ar flow prevents entrainment of O and N from air in the laser-induced plasma. The subsequent light emission from the microplasma lasted ∼1 μs after the 100 fs laser pulse, depending on the target material properties. The light emission was back-collected by a parabolic mirror and focused onto three fibers that delivered the plasma emission to three Czerny-Turner spectrographs (Andor, Shamrock 163), each with an intensified charge-coupled device (ICCD) detector (Andor, iStar). The three spectrometer channels consisted of a channel sensitive to ultraviolet (UV) emission from 240 to 405 nm (Andor grating, 600 lines/mm, 300 nm blaze), a channel sensitive to visible (VIS) emission from 475 to 705 nm (Andor grating, 600 lines/mm, 500 nm blaze), and a channel sensitive to near-infrared (NIR) emission from 710 to 865 nm (Andor grating, 600 lines/mm, 750 nm blaze grating). The UV spectrometer had a spectral resolution of 0.3 nm, whereas the VIS and NIR spectrometers had spectral resolutions of 0.6 nm. The spectra from the three spectrometers were acquired simultaneously, and the gate delay and gate widths were varied to obtain information about the time-resolved behavior of the emissive species.

Integrated emission spectra with optimized values for the gate delay and width (140 and 380 ns, respectively) were acquired for 100 laser shots on each polymer (50 shots at two different locations) and 20 laser shots at different locations for RDX; the ICCD gains were set to 100, 50, and 50 for the UV, VIS, and NIR channels, respectively. In addition, spectra were acquired with a 20 ns gate width for time delays of 140, 160, 200, 250, 300, 350, 400, and 500 ns. Additional delay times (80, 100, 120, and 1000 ns)

were collected for the RDX, ABS, and NYL samples to track molecular CN formation. For the time-resolved data the ICCD gains were increased to 200, 100, and 100 for the UV, VIS, and NIR channels, respectively. At earlier delays, the scattered light from the laser saturated the NIR spectrometer and continuum emission from the plasma (due to bremsstrahlung processes) began to saturate the UV and VIS spectrometers. Prior to obtaining the LIBS spectra, the polymer surfaces were cleaned at each new location with ten laser shots to remove surface impurities. The spectra from a total of 300 laser shots (20 laser shots for RDX) on each polymer (50 shots at 6 different locations) were acquired at each time delay. Atomic and molecular emission lines of C, H, O, N, C_2, and CN were measured at 248, 656, 777, 822, 516, and 388 nm, respectively. The N emission line at 822 nm was selected because of spectral interferences by Ar lines near the stronger nitrogen triplet peaks at 742, 744, and 746 nm. The maximum peak emission intensity was background-subtracted for each atomic and molecular species. The percentage of C, H, N, and O and the different C- and N-containing bond types in each sample were calculated and are displayed in Table 1.

■ RESULTS AND DISCUSSION

The average LIBS emission spectrum of each polymer and RDX is displayed in Figure 2. The majority of the atomic emission peaks observed in the third spectrometer spectral range (710−860 nm) are due to argon. Atomic oxygen emission was observed at 777 nm in the RDX, NYL, PET, and POM spectra. Atomic carbon and hydrogen emission is present at 248 and 656 nm for each of the six samples, respectively. Although weak nitrogen emission at 822 nm was observed in the integrated emission spectra of RDX, no nitrogen emission was observed in the time-resolved spectra of RDX, NYL or ABS due to the weaker signal with a 20 ns gate width. Evidence for the presence of nitrogen was primarily indicated by the (0,0) band head region of the CN $B^2\Sigma^+-X^2\Sigma^+$ transition at 388 nm. Because the samples were bathed in argon, the nitrogen must have originated from the sample; CN was only observed in the samples containing nitrogen. Molecular emission from the (0,0) band head region of the C_2 $d^3\Pi_g-a^3\Pi_u$ (Swan system) transition was observed at 516 nm for all of the polymers. Consistent with earlier studies, the polymers with C═C bonds (ABS and PET) produced spectra with the strongest C_2 emission; despite a high percentage of C—C bonds, the C_2 emission from NYL and UHMW was not as strong. Atomic emission from trace impurities such as magnesium at 279 nm in POM, PET, RDX, and ABS and calcium at 393 and 396 nm in RDX and UHMW was also observed in the spectra. Finally, in addition to the numerous atomic Ar emission lines at 697 nm and from 710 to 860 nm, ionic argon emission (Ar II) was also observed at 358, 373, 385, 481, and 488 nm in the more emissive polymer spectra such as PET and ABS.

Atomic Emission. The atomic emission intensities of carbon (248 nm), hydrogen (656 nm), and oxygen (777 nm) versus the percent carbon, hydrogen, and oxygen in each sample are shown in Figure 3a−c. There is a general trend of increasing carbon and oxygen intensity with increasing carbon and oxygen content, but they do not correlate very well (r^2 = 0.66 and 0.55). There is no correlation between the hydrogen intensity and %H (r^2 = 0.006). Ideally, one would normalize the atomic emission lines of interest to another atomic emission line that is constant, such as an

Table 1. Percentages of atoms, C—C, C═C, and C—N bonds for polymers and RDX

	%C	%H	%N	%O	%C—C bonds	%C═C bonds	%C—N bonds	%C≡N bonds
ABS	45	50	5	0	35	12	0	3
POM	25	50	0	25	0	0	0	0
NYL	27	58	5	9	26	0	8	0
PET	45	36	0	18	26	13	0	0
UHMW	33	66	0	0	33	0	0	0
RDX	14	29	29	29	0	0	29	0

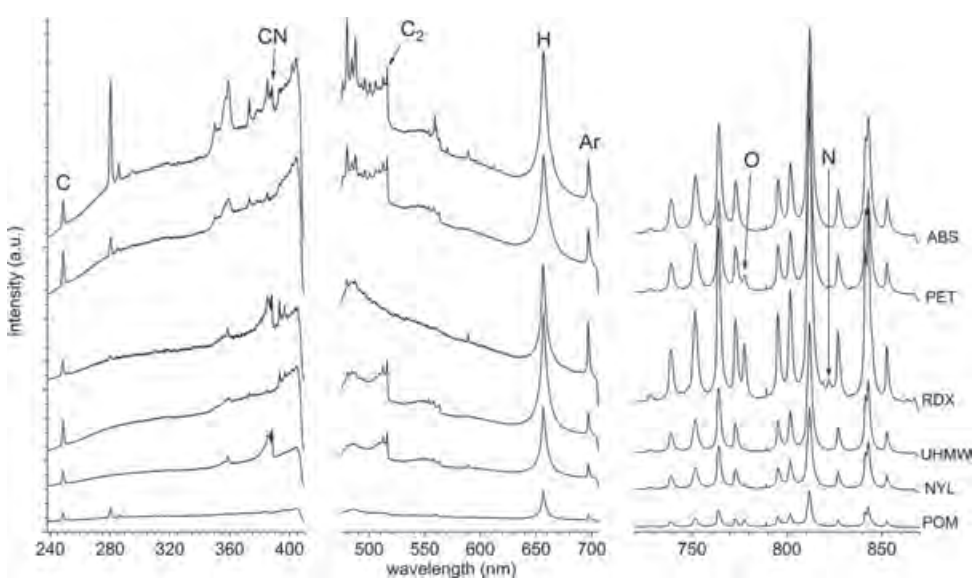

Figure 2. LIBS spectra of the polymer and RDX samples from three spectrometer channels (spectra offset for clarity).

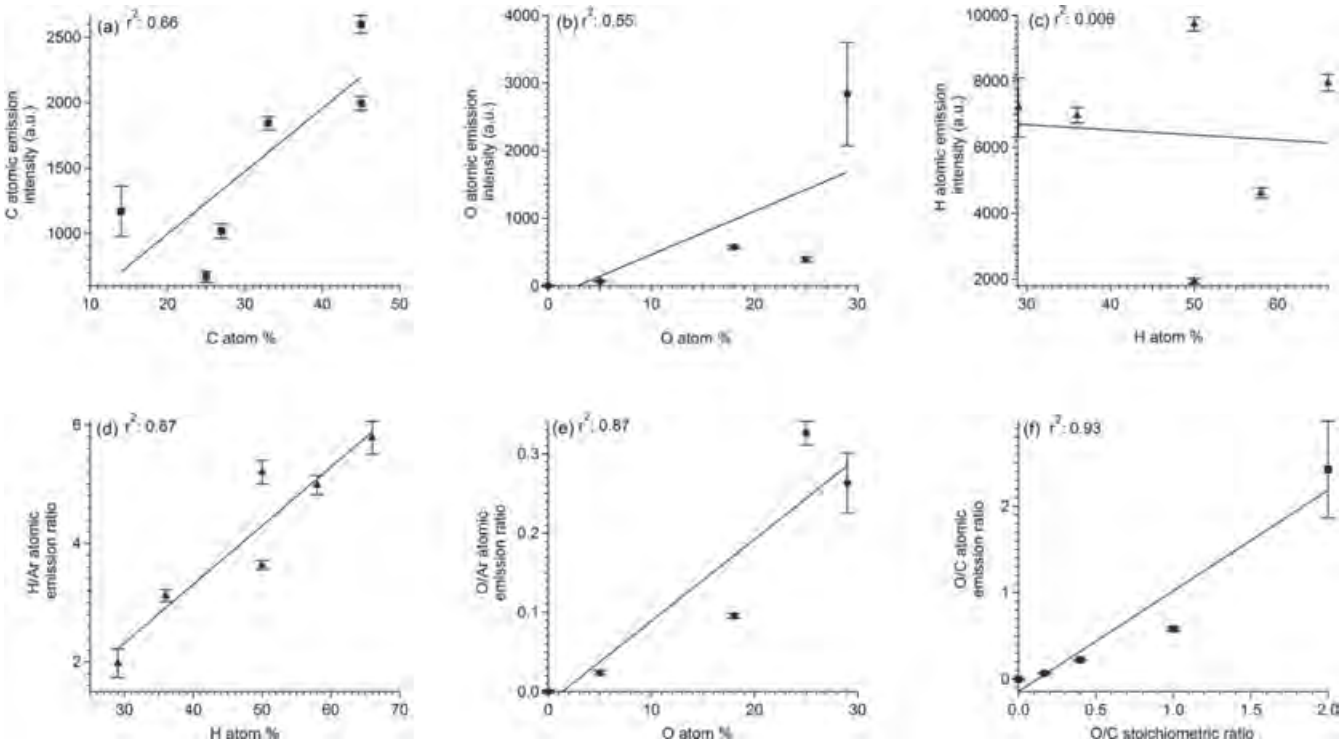

Figure 3. Correlation between (a) carbon, (b) hydrogen, (c) oxygen, (d) normalized hydrogen, and (e) normalized oxygen emission intensities and their respective relative abundance for each polymer and RDX. Correlation between the (f) O/C atomic ratio and the O/C stoichiometric ratio for each polymer and RDX.

internal standard or in this case the argon gas, to minimize laser material interaction differences. In addition, the atomic emission lines should also have similar upper energy levels and closely located emission wavelengths for optimal normalization. Normalizing the hydrogen atomic emission line to the argon atomic emission line at 696 nm meets these criteria. They are in close proximity to one another on the spectra, and the upper energy levels of the hydrogen and argon atomic emission lines are 97 500 and 107 500 cm^{-1}, respectively. As shown in Figure 3d, the correlation between the normalized H emission intensity and %H is much improved (r^2 = 0.87). The oxygen line can be normalized to the argon line at 763.5 nm. The upper energy levels are not as similar, 86 600 cm^{-1} for oxygen at 777 nm compared to 106 200 cm^{-1} for the argon emission line, but an improvement in the oxygen correlation is observed (r^2 = 0.87) in Figure 3e. Unfortunately, there is no argon emission line to normalize to the carbon atomic emission line. Carbon is not in close proximity to any atomic argon emission lines of significant intensity and the upper energy levels for the ionic argon lines are much different, 61 990 cm^{-1} for C compared to the 185 100 cm^{-1} for Ar II at 358 nm.[33] Normalizing the carbon line at 247 nm with the atomic argon line at 696 nm (upper energy level 106 200 cm^{-1}) makes the correlation worse (e.g., r^2 = 0.032).

Alternatively, the stoichiometric ratio of the oxygen to carbon can be correlated to the oxygen and carbon atomic emission ratio for each material. By comparing ratios rather than emission intensities, we can both reduce the effects of laser material interaction and determine if the emission intensities are indicative of the molecular structure. We have previously demonstrated high correlation between stoichiometry and emission intensity ratios using chemical warfare simulants[34] and high-nitrogen molecules.[25] In Figure 3f, the correlation between the atomic emission intensity ratio of oxygen to carbon and the stoichiometric ratios of each sample is shown. The degree of correlation (r^2 = 0.93) for the ratio is much improved compared to the individual oxygen and carbon intensities. The above results indicate that the carbon, hydrogen, and oxygen atomic emission intensities are correlated to the molecular structure of the polymers and RDX, which will significantly aid in the discrimination of the organic materials.

Molecular Emission. The two molecular species that are observed in some of the polymers and RDX are CN and C_2. In the present study, we wanted to determine the extent that the molecular composition or structure influences the CN and C_2 emission, because both are important for the classification of explosive residues.[8] CN can form through fragmentation or recombination. Previously, Baudelet et al. showed that CN originated from fragmentation of biological samples using time-resolved femtosecond LIBS.[21] In this case, we acquired time-resolved spectra at various time delays for the nitrogen-containing organic samples ABS, RDX, and NYL. The ABS spectra at various time delays are shown in Figure 4. Emission intensity decays of particular species in the plasma emission were constructed from the time-resolved spectra by calculating the background-corrected emission intensity of the particular species at each time delay. In Figure 5, the CN emission intensity as a function of time for ABS, NYL, and RDX is shown. We collected additional early delay times (before 140 ns) to capture the CN rise; at very early times no CN emission intensity could be observed due to the strong continuum emission which saturated the detector. From the time-resolved emission spectra, it is apparent that the CN grew in after 80 ns, indicating recombination has occurred due to one of the following reactions:[22]

$$C + N \rightarrow CN \quad (1)$$

$$C_2 + N_2 \rightarrow 2CN \quad (2)$$

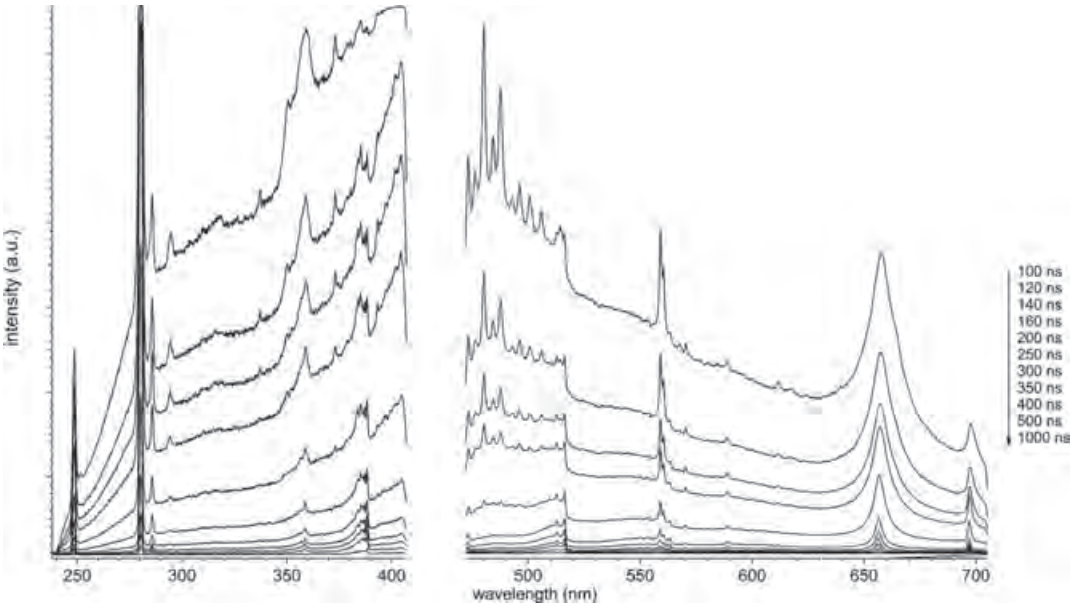

Figure 4. Time-resolved spectra of ABS collected from the UV and VIS spectrometers at various time delays with a 20 ns gate. The most intense spectrum is at 100 ns and the intensity decreases as the time delay is increased to 1000 ns.

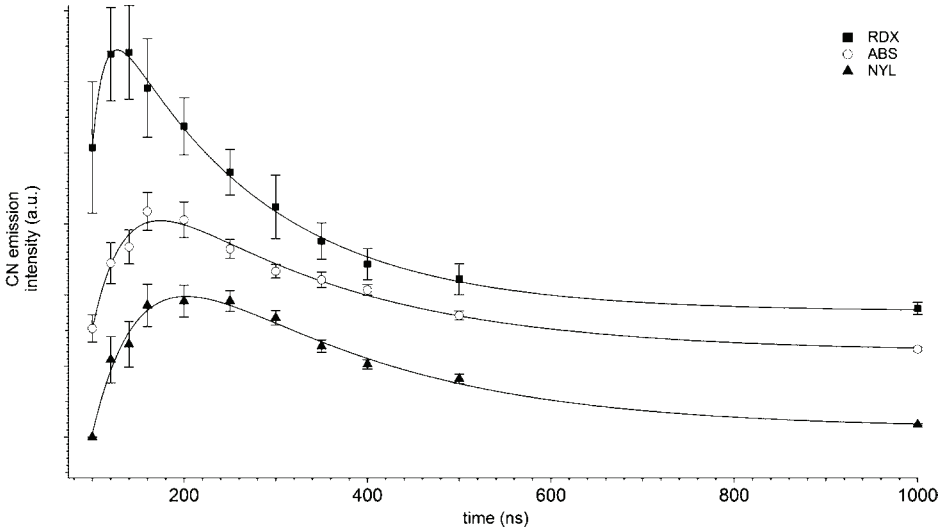

Figure 5. CN (388 nm) time-resolved emission decays of RDX (■), ABS (○), and NYL (▲) (offset for clarity). The curve fit (solid line) was used to determine the rise time and decay of each sample.

Across all six samples, the CN intensity does not correlate to the %C ($r^2 = 0.27$) and the fit only slightly improves when correlated with the %N ($r^2 = 0.72$). This is not an unexpected result because the formation of CN is dependent on both the presence and the amounts of nitrogen and carbon. Figure 6 shows a contour plot using the %C, %N, and CN intensity of each polymer and RDX. The contour plot tracks the relationship between the CN emission intensity and the relative amount of carbon and nitrogen simultaneously. As the %C and %N increase, so does the CN intensity, behavior also observed in previous work.[25]

C_2 emission can also originate from recombination or fragmentation. In our previous work with high-nitrogen samples, we observed C_2 emission from organic molecules containing zero C—C or C═C bonds.[25] Thus, the C_2 originated from recombination in the plasma. In addition, the presence of oxygen

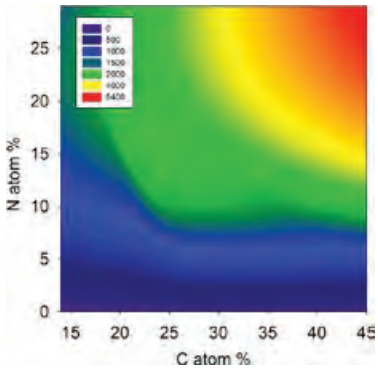

Figure 6. Contour plot of the CN emission intensity (arbitrary units as indicated in the color gradient legend) as a function of the relative abundance of carbon and nitrogen.

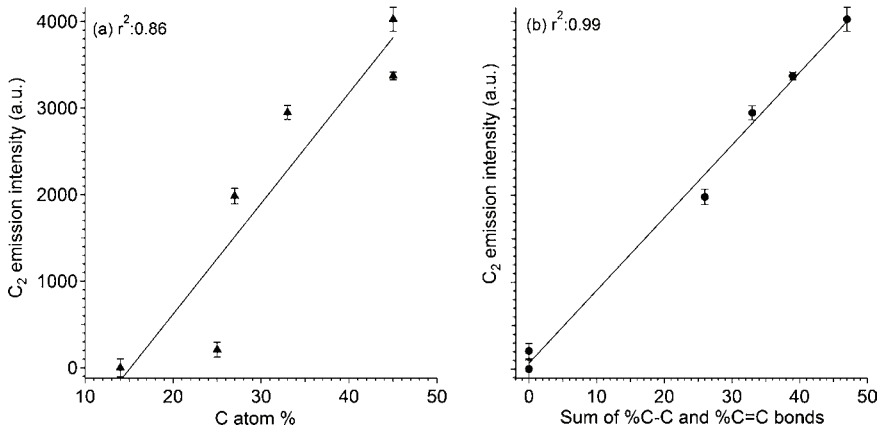

Figure 7. C_2 emission intensity as a function of (a) %C and (b) sum of %C—C and %C═C bonds.

could potentially diminish C_2 emission by one or more of the following reactions:[25,26]

$$C + O \rightarrow CO \tag{3}$$

$$C_2 + O \rightarrow CO + C \tag{4}$$

$$C_2 + O_2 \rightarrow 2CO \tag{5}$$

However, oxygen-containing molecules with C—C bonds such as trinitrotoluene (TNT) or L-glutamine did display C_2 emission,[25] indicating C—C fragmentation as the source of C_2 emission. In the present study, only two samples have zero C—C bonds, RDX and POM. As in the earlier studies, we did not observe C_2 emission in pure RDX because of the high oxygen content compared to carbon and lack of C—C bonds. POM does have C_2 emission even though it contains oxygen, but the C_2 emission intensity is much less than nylon despite having comparable amounts of carbon, 25% versus 27%. In Figure 7, the C_2 emission of each polymer and RDX increases as the %C increases with good correlation (r^2 = 0.86). More importantly, we observe that the C_2 intensity as a function of the sum of the %C—C and %C═C bonds correlates very strongly (r^2 = 0.99). This strong correlation suggests that the number of C—C and C═C bonds is far more influential on the C_2 emission than any other factor, including any chemical reactions in the plasma (e.g., eqs 3−5). It also indicates that fragmentation is a bigger influence on C_2 production and subsequent emission than recombination. Previously, we observed that where recombination is the primary source of C_2 formation, the %C—C and %C═C bonds do not correlate with C_2 emission (r^2 = 0.11). In that study, the C_2 emission was strongly dependent on the amount of carbon and oxygen in a particular molecular structure.[25] As the carbon content increased, so did the C_2 emission. However, as the oxygen content increased, the C_2 emission decreased. Our present study indicates this behavior is true only for molecules where recombination is the primary pathway for C_2 formation. The compounds in the present study have a higher carbon content and %C—C and C═C bonds. The contour plot in Figure 8 shows how these compounds are not as influenced by oxygen content. As the sum of the %C—C and C═C bonds increases, the C_2 intensity increases, as expected. In contrast to the previous study, the amount of oxygen content does not influence the C_2 emission intensity. Further evidence of fragmentation can be observed in Figure 9 where the time-resolved decays of the polymers that have prominent C_2 emission are shown. The emission decreases from the initial time delay,

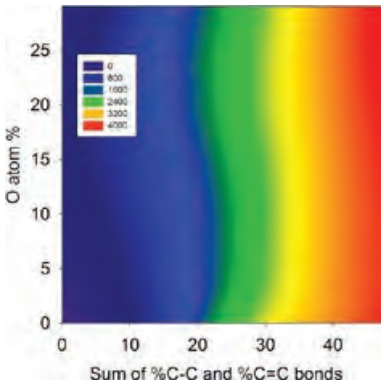

Figure 8. Contour plot of C_2 emission intensity (arbitrary units as indicated in the color gradient legend) as a function of relative abundance of oxygen and sum of %C—C and %C═C bonds.

unlike the CN emission, indicative of fragmentation as being the primary source of C_2. By comparing the results from the earlier study and the results from the current samples, we can see that as the amount of carbon and C−C bonds increases, the influence of oxygen content on preventing C_2 recombination and emission is diminished. Even bis(2,2,2-trinitroethyl)hydrazodicarboxylate (BTHC), a molecule that contains 44% oxygen and only 5% C—C bonds, had some C_2 emission.[25] The primary influence on C_2 emission is due to the total amount of C—C and C═C bonds in a molecular structure.

Decays. Time-resolved decays were constructed from the spectra collected at various time delays for each polymer sample and RDX. In Figure 10, the time-resolved decays of atomic carbon emission for each polymer and RDX are shown. Each time-resolved decay is fit to a weighted single exponential calculate the decay rate. The fit curve is shown for the time decay for each sample. In Figures 5 and 9 the curve fits are shown for CN rise time, CN decay, and C_2 decay. The CN rise and decay times were calculated using the following function:

$$f(t) = y + Ae^{-(t-t_0)/\tau_{decay}}(1 - e^{-(t-t_0)/\tau_{rise}}) \tag{6}$$

where τ_{rise} and τ_{decay} are the rise and decay times, respectively, t is the time at each data point, and t_0, A, and y are fit parameters. The C_2 decays were fitted to a weighted single exponential decay. In Table 2, the decay rates of each sample are displayed for carbon emission as well as C_2 and CN molecular emission if present in the spectra.

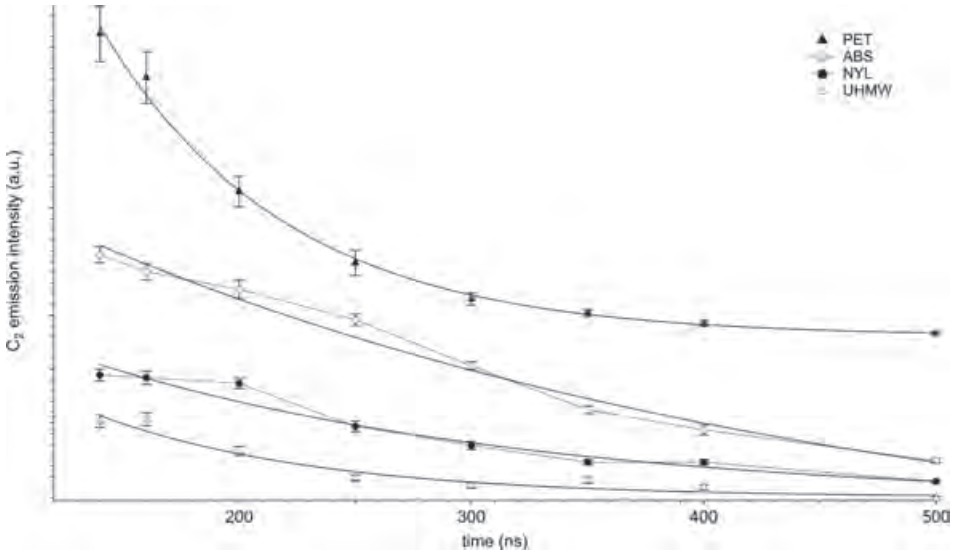

Figure 9. C_2 (516 nm) time-resolved emission decays of PET (▲), ABS (○), NYL (●), and UHMW (Δ) (offset for clarity). Curve fits (solid line) are shown for decay of each sample; the dashed lines for ABS and NYL connect the data points.

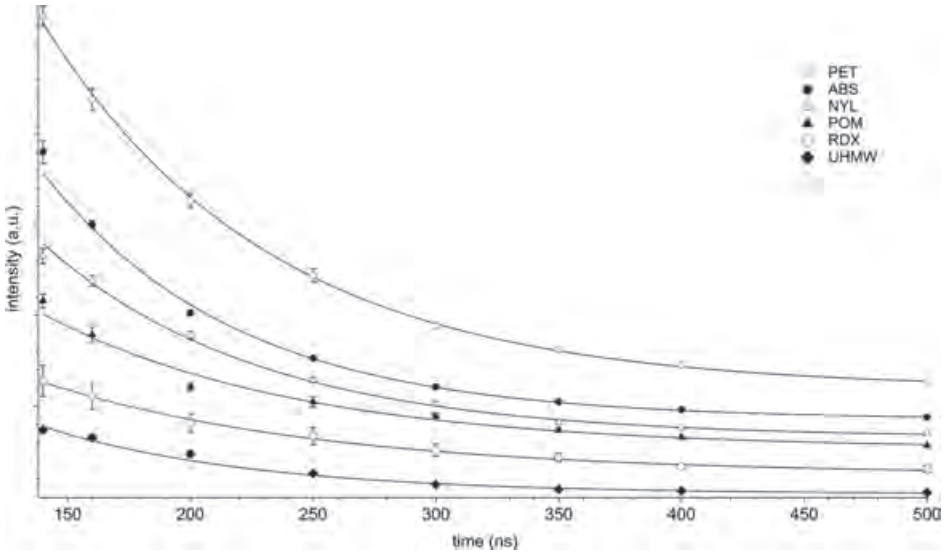

Figure 10. C (247 nm) time-resolved emission decays of PET (○), ABS (●), NYL (Δ), POM (▲), RDX (◇), and UHMW (◆) (offset for clarity). Curve fits (solid line) are shown for decay of each sample.

Table 2. Decay Rates (ns) of Atomic and Molecular Species of Each Polymer and RDX

	C	C_2	CN rise	CN decay
ABS	77 ± 6	338 ± 136	44 ± 15	221 ± 56
POM	104 ± 20			
NYL	88 ± 8	190 ± 60	73 ± 13	219 ± 73
PET	93 ± 8	79 ± 16		
UHMW	86 ± 13	95 ± 31		
RDX	115 ± 30		15 ± 4	165 ± 11

There are obvious differences in the decay rates from each of the emitting species. Although the data ranges for the atomic carbon emission decay rates overlap, the materials without oxygen (ABS, UHMW) have the shortest average carbon decay rates and RDX, with the largest %O, has the longest decay rate. The decay rate for C_2 emission may be faster for the PET compared to the UHMW due to the presence of oxygen (reaction 4). The single exponential decay does not fit the C_2 decay well for the two nitrogen containing materials (ABS and NYL) that have C_2 emission. The lifetime of the C_2 is much longer in these two materials. One possible explanation is that C_2 is being formed via the following reaction:[22]

$$CN + C \rightarrow C_2 + N \tag{7}$$

Because ABS has a higher carbon content, more C_2 could be formed relative to nylon. In addition the oxygen present in nylon could be preventing some C_2 formation or emission via reactions 3 and 4; thus the decay rate is faster in NYL. Furthermore, there is no C_2 emission in RDX even though reaction 7 is a possible C_2 formation route. This is probably due to the fact that RDX has lower carbon content and higher oxygen content than both ABS and NYL. The CN rise time is the fastest for RDX, which contains the highest percentage of single C−N bonds. RDX also has the fastest CN decay rate, which could be explained by the following reaction:[26]

$$CN + O \rightarrow CO + N \tag{8}$$

The chemical reactions mentioned in this paper (1−5, 7, and 8) are only a few in a myriad of reactions that are likely occurring. Previous kinetic modeling of the RDX plasma used 137 species with 577 reactions.[22] A similar modeling effort would be necessary to obtain a better understanding of the reactions in the plasma plume of each of the polymers. Experimental results such as the lifetimes of particular atomic and molecular species obtained in this study could be used to develop and validate models of the different plasmas.

CONCLUSION

In this study, we collected time-resolved LIBS spectra from several polymers and RDX. The atomic emission intensities of interest were compared between each sample. The trends observed from the emission intensities indicate that atomic emission intensities can be related to the chemical composition (i.e., relative abundance of the atomic constituents) of the sample. The connection between emission intensity and molecular structure is an important factor for the ability to discriminate between different types of organic materials using LIBS. The emission from molecular species was also compared among the various polymers. For the samples studied in this paper, we determined that the formation of CN and C_2 is primarily due to recombination and fragmentation, respectively; however, some C_2 formation through recombination was observed in polymers containing nitrogen. We observed the formation of CN using time-resolved spectra collected at various time delays >80 ns, although we could not rule out fragmentation of CN at earlier times. The C_2 emission decay did not have any rise time, indicating it was initially formed via fragmentation. The C_2 emission intensity of each sample correlates more with the sum of the %C—C and %C═C bonds of each sample than the %C, indicating that fragmentation is the main source of C_2 formation. In our previous study with a series of high-nitrogen molecules, recombination was the only method for C_2 formation in a majority of the samples.[25] If these samples contained enough oxygen (>10%), then there was no C_2 emission; reactions 3−5 are possible pathways for the emission reduction. The presence of oxygen in the sample can completely suppress the C_2 emission intensity only in cases where carbon is present in a molecule but there are no C—C bonds, i.e., when the primary mechanism for C_2 emission is recombination. Although the %O in samples containing C—C bonds may increase the C_2 decay rate, competing reactions such as the formation of C_2 from CN (7) complicate the chemistry. Although a full understanding of the lifetimes obtained in this study is not possible without further investigation and/or modeling, it is worth noting the differences that are present between the decay rates of the samples. In particular it is interesting to note the faster decay rate of the CN molecular emission in RDX relative to the other two compounds that produce CN. The effect of oxygen and nitrogen on the plasma chemistry and subsequent LIBS emission (intensities and decay rates) can be used to help discriminate explosives from other organic materials, because explosives have significantly more oxygen and nitrogen relative to their carbon content.

AUTHOR INFORMATION

Corresponding Author

*Tel: (410) 306-0884. Fax: (410) 278-1365. E-mail: frank.c.delucia.civ@mail.mil.

Notes

The authors declare no competing financial interest.

ACKNOWLEDGMENTS

The authors thank Rose Pesce-Rodriguez for her assistance analyzing the purity of the polymer samples.

REFERENCES

(1) Gottfried, J. L. Discrimination of Biological and Chemical Threats in Residue Mixtures on Multiple Surfaces. *Anal. Bioanal. Chem.* **2011**, *400*, 3289−3301.

(2) Gottfried, J. L.; Harmon, R. S.; De Lucia, F. C., Jr.; Miziolek, A. W. Multivariate Analysis of Laser-Induced Breakdown Spectroscopy Chemical Signatures for Geomaterial Classification. *Spectrochim. Acta, Part B* **2009**, *64*, 1009−1019.

(3) De Lucia, F. C., Jr.; Harmon, R. S.; McNesby, K. L.; Winkel, R. J., Jr.; Miziolek, A. W. Laser-Induced Breakdown Spectroscopy Analysis of Energetic Materials. *Appl. Opt.* **2003**, *42*, 6148−6152.

(4) Harmon, R. S.; De Lucia, F. C., Jr.; LaPointe, A.; Winkel, R. J., Jr.; Miziolek, A. W. LIBS for Landmine Detection and Discrimination. *Anal. Bioanal. Chem.* **2006**, *385*, 1140−1148.

(5) Cremers, D. A.; Radziemski, L. J. *Handbook of Laser-Induced Breakdown Spectroscopy*; John Wiley & Sons, Ltd.: West Sussex, England, 2006.

(6) Hahn, D. W.; Omenetto, N. Laser-Induced Breakdown Spectroscopy (LIBS), Part I: Review of Basic Diagnostics and Plasma-Particle Interactions: Still-Challenging Issues within the Analytical Plasma Community. *Appl. Spectrosc.* **2010**, *64*, 335A−366A.

(7) Hahn, D. W.; Omenetto, N. Laser-Induced Breakdown Spectroscopy (LIBS), Part II: Review of Instrumental and Methodological Approaches to Material Analysis and Applications to Different Fields. *Appl. Spectrosc.* **2012**, *66*, 347−419.

(8) Gottfried, J. L.; De Lucia, F. C., Jr.; Munson, C. A.; Miziolek, A. W. Laser-Induced Breakdown Spectroscopy for Detection of Explosives Residues: A Review of Recent Advances, Challenges, and Future Prospects. *Anal. Bioanal. Chem.* **2009**, *395*, 283−300.

(9) Gottfried, J. L.; De Lucia, F. C., Jr.; Miziolek, A. W. Discrimination of Explosive Residues on Organic and Inorganic Substrates Using Laser-Induced Breakdown Spectroscopy. *J. Anal. At. Spectrom.* **2009**, *24*, 288−296.

(10) De Lucia, F. C., Jr.; Gottfried, J. L. Classification of Explosive Residues on Organic Substrates Using Laser Induced Breakdown Spectroscopy. *Appl. Opt.* **2012**, *51*, B83−B92.

(11) Vivien, C.; Hermann, J.; Perrone, A.; Boulmer-Leborgne, C.; Luches, A. A Study of Molecule Formation During Laser Ablation of Graphite in Low-Pressure Nitrogen. *J. Phys. D* **1998**, *31*, 1263.

(12) Zelinger, Z.; Novotný, M.; Bulíř, J.; Lančok, J.; Kubát, P.; Jelínek, M. Laser Plasma Plume Kinetic Spectroscopy of the Nitrogen and Carbon Species. *Plasma Phys.* **2003**, *43*, 426−432.

(13) Fuge, G. M.; Ashfold, M. N. R.; Henley, S. J. Studies of the Plume Emission During the Femtosecond and Nanosecond Ablation of Graphite in Nitrogen. *J. Appl. Phys.* **2006**, *99*, 014309−014312.

(14) Kushwaha, A.; Thareja, R. K. Dynamics of Laser-Ablated Carbon Plasma: Formation of C2 and Cn. *Appl. Opt.* **2008**, *47*, G65−G71.

(15) Locke, R. J.; Morris, J. B.; Forch, B. E.; Miziolek, A. W. Ultraviolet-Laser Microplasma Gas-Chromatography Detector - Detection of Species-Specific Fragment Emission. *Appl. Opt.* **1990**, *29*, 4987−4992.

(16) St-Onge, L.; Sing, R.; Béchard, S.; Sabsabi, M. Carbon Emissions Following 1.064 μm Laser Ablation of Graphite and Organic Samples in Ambient Air. *Appl. Phys. A: Mater. Sci. Process.* **1999**, *69*, S913−S916.

(17) Dong, M.; Mao, X.; Gonzalez, J. J.; Lu, J.; Russo, R. E. Carbon Isotope Separation and Molecular Formation in Laser-Induced Plasmas by Laser Ablation Molecular Isotopic Spectrometry. *Anal. Chem.* **2013**, *85*, 2899−2906.

(18) Portnov, A.; Rosenwaks, S.; Bar, I. Identification of Organic Compounds in Ambient Air Via Characteristic Emission Following Laser Ablation. *J. Lumin.* **2003**, *102−103*, 408−413.

(19) Portnov, A.; Rosenwaks, S.; Bar, I. Emission Following Laser-Induced Breakdown Spectroscopy of Organic Compounds in Ambient Air. *Appl. Opt.* **2003**, *42*, 2835−2842.

(20) Grégoire, S.; Boudinet, M.; Pelascini, F.; Surma, F.; Detalle, V.; Holl, Y. Laser-Induced Breakdown Spectroscopy for Polymer Identification. *Anal. Bioanal. Chem.* **2011**, *400*, 3331–3340.
(21) Baudelet, M.; Guyon, L.; Yu, J.; Wolf, J. P.; Amodeo, T.; Frejafon, E.; Laloi, P. Femtosecond Time-Resolved Laser-Induced Breakdown Spectroscopy for Detection and Identification of Bacteria: A Comparison to the Nanosecond Regime. *J. Appl. Phys.* **2006**, *99*, 84701.
(22) Babushok, V. I.; De Lucia, F. C., Jr.; Dagdigian, P. J.; Gottfried, J. L.; Munson, C. A.; Nusca, M. J.; Miziolek, A. W. Kinetic Modeling Study of the Laser-Induced Plasma Plume of Cyclotrimethylenetrinitramine (RDX). *Spectrochim. Acta, Part B* **2007**, *62*, 1321–1328.
(23) Dagdigian, P. J.; Khachatrian, A.; Babushok, V. I. Kinetic Model of C/H/N/O Emissions in Laser-Induced Breakdown Spectroscopy of Organic Compounds. *Appl. Opt.* **2010**, *49*, C58–C66.
(24) Ma, Q.; Dagdigian, P. Kinetic Model of Atomic and Molecular Emissions in Laser-Induced Breakdown Spectroscopy of Organic Compounds. *Anal. Bioanal. Chem.* **2011**, *400*, 3193–3205.
(25) De Lucia, F. C., Jr.; Gottfried, J. L. Characterization of a Series of Nitrogen-Rich Molecules Using Laser-Induced Breakdown Spectroscopy. *Propellants, Explos., Pyrotech.* **2010**, *35*, 268–277.
(26) Gottfried, J. L. Laser-Induced Plasma Chemistry of the Explosive RDX with Various Metallic Nanoparticles. *Appl. Opt.* **2012**, *51*, B13–B21.
(27) Anzano, J. M.; Gornushkin, I. B.; Smith, B. W.; Winefordner, J. D. Laser-Induced Plasma Spectroscopy for Plastic Identification. *Polym. Eng. Sci.* **2000**, *40*, 2423–2429.
(28) Anzano, J.; Lasheras, R. J.; Bonilla, B.; Casas, J. Classification of Polymers by Determining of C-1: C-2: Cn: H: N: O Ratios by Laser-Induced Plasma Spectroscopy (LIPS). *Polym. Test* **2008**, *27*, 705–710.
(29) Anzano, J.; Bonilla, B.; Montull-Ibor, B.; Casas-Gonzalez, J. Plastic Identification and Comparison by Multivariate Techniques with Laser-Induced Breakdown Spectroscopy. *J. Appl. Polym. Sci.* **2011**, *121*, 2710–2716.
(30) Boueri, M.; Motto-Ros, V.; Lei, W.-Q.; Ma, Q.-L.; Zheng, L.-J.; Zeng, H.-P.; Yu, J. Identification of Polymer Materials Using Laser-Induced Breakdown Spectroscopy Combined with Artificial Neural Networks. *Appl. Spectrosc.* **2011**, *65*, 307–314.
(31) Gregoire, S.; Motto-Ros, V.; Ma, Q. L.; Lei, W. Q.; Wang, X. C.; Pelascini, F.; Surma, F.; Detalle, V.; Yu, J. Correlation between Native Bonds in a Polymeric Material and Molecular Emissions from the Laser-Induced Plasma Observed with Space and Time Resolved Imaging. *Spectrochim. Acta, Part B* **2012**, *74–75*, 31–37.
(32) Boueri, M.; Baudelet, M.; Yu, J.; Mao, X. L.; Mao, S. S.; Russo, R. Early Stage Expansion and Time-Resolved Spectral Emission of Laser-Induced Plasma from Polymer. *Appl. Surf. Sci.* **2009**, *255*, 9566–9571.
(33) Ralchenko, Y.; Kramida, A. E.; Reader, J.; Team, N. A. *NIST Atomic Spectra Database* (Version 4.1); National Institute of Standards and Technology: Gaithersburg, MD, 2010.
(34) De Lucia, F. C., Jr.; Samuels, A. C.; Harmon, R. S.; Walters, R. A.; McNesby, K. L.; LaPointe, A.; Winkel, R. J., Jr.; Miziolek, A. W. Laser-Induced Breakdown Spectroscopy (LIBS): A Promising Versatile Chemical Sensor Technology for Hazardous Material Detection. *IEEE Sens. J.* **2005**, *5*, 681–689.

A Nanosensor for TNT Detection Based on Molecularly Imprinted Polymers and Surface Enhanced Raman Scattering

Ellen L. Holthoff, Dimitra N. Stratis-Cullum and Mikella E. Farrell

Sensors, 11 (2011)

OPEN ACCESS
sensors
ISSN 1424-8220
www.mdpi.com/journal/sensors

Article

A Nanosensor for TNT Detection Based on Molecularly Imprinted Polymers and Surface Enhanced Raman Scattering

Ellen L. Holthoff *, Dimitra N. Stratis-Cullum and Mikella E. Hankus

United States Army Research Laboratory, RDRL-SEE-O, 2800 Powder Mill Road, Adelphi, MD 20783, USA; E-Mails: dimitra.stratiscullum1@us.army.mil (D.N.S.-C.); mikella.hankus@us.army.mil (M.E.H.)

* Author to whom correspondence should be addressed; E-Mail: ellen.holthoff@us.army.mil; Tel.: +1-301-394-0939; Fax: +1-301-394-0310.

Received: 11 January 2011; in revised form: 8 February 2011 / Accepted: 22 February 2011 / Published: 1 March 2011

Abstract: We report on a new sensor strategy that integrates molecularly imprinted polymers (MIPs) with surface enhanced Raman scattering (SERS). The sensor was developed to detect the explosive, 2,4,6-trinitrotoluene (TNT). Micron thick films of sol gel-derived xerogels were deposited on a SERS-active surface as the sensing layer. Xerogels were molecularly imprinted for TNT using non-covalent interactions with the polymer matrix. Binding of the TNT within the polymer matrix results in unique SERS bands, which allow for detection and identification of the molecule in the MIP. This MIP-SERS sensor exhibits an apparent dissociation constant of $(2.3 \pm 0.3) \times 10^{-5}$ M for TNT and a 3 μM detection limit. The response to TNT is reversible and the sensor is stable for at least 6 months. Key challenges, including developing a MIP formulation that is stable and integrated with the SERS substrate, and ensuring the MIP does not mask the spectral features of the target analyte through SERS polymer background, were successfully met. The results also suggest the MIP-SERS protocol can be extended to other target analytes of interest.

Keywords: molecular imprinting; surface enhanced Raman scattering; sensor; explosives detection

---

1. Introduction

Rapid detection and identification of energetic materials is a priority for military and homeland defense applications with the increased need to avoid potential harm caused by explosive hazards. An analyte of particular interest is 2,4,6-trinitrotolune (TNT), a commonly used explosive in the preparation of landmines for military and terrorist activities. Several methodologies for TNT detection have been reported, including fluorescent polymers [1-3], microcantilevers [4-6], ion mobility spectrometry [7-9], and Raman spectroscopy [10-12]. Although successfully employed, current capabilities have limitations. For example, these technologies may not always be specific or extendable to other chemical systems, and may only allow for bulk material assessment.

In the current work, we report on a spectroscopic method that aims to address many of the above limitations using molecularly imprinted sol-gel derived xerogels in combination with surface enhanced Raman scattering (SERS). Molecular imprinting involves arranging polymerizable functional monomers around a template, followed by polymerization and template removal [13]. Molecularly imprinted polymers (MIPs) can be utilized as artificial recognition elements for target chemical analytes of interest and there are numerous reports detailing the use of this technique for the preparation of polymers which have the ability to bind a specific chemical target [14-18]. Here, molecular imprinting of TNT in xerogels was achieved using a non-covalent imprinting approach [19]. Polymerizable monomers (*i.e.*, precursors) were chosen based on potential non-covalent interactions with the TNT molecules, allowing for increased target recognition [20]. The xerogel matrix included 3-aminopropyltriethoxysilane (APTES), which has been shown to engage in strong non-covalent interactions with TNT molecules [21] via the formation of a charge-transfer complex between the electron-deficient aromatic ring of the nitro-aromatic species and the electron-rich amino group of the precursor [3,22]. This interaction significantly improves polymer selectivity and affinity for TNT [23].

In chemical sensing applications, a MIP alone does not meet the requirements for a sensor without some form of a transducer to convert the analyte interaction into a measureable signal. There is increasing evidence in the literature of a variety of electrochemical and optical transduction techniques applied to convert a MIP into a sensor for TNT detection [23-27]. In this work, SERS [28] was used as the transduction method to achieve a high level of selectivity. This technique provides vibrational spectra with unique chemical and structural information for a given species. SERS is an extremely sensitive and selective technique that involves enhancements in the Raman scattering intensities of analytes adsorbed on a roughened metal surface (typically, gold or silver) [29,30]. These enhancements (up to 14 orders of magnitude as compared to spontaneous Raman) are due to chemical and electromagnetic enhancement, which results when the incident light in the experiment strikes the metal surface and excites localized surface plasmons. The detection capabilities of SERS make it an excellent transduction method for selective, full compound identification, a capability that is not currently possible with existing MIP sensors. Compared to other, more conventional spectroscopic techniques employed with MIPs, SERS should be less affected by cross-selectivity resulting from non-specific adsorption to the polymer. The basic MIP-SERS detection concept is illustrated in Figure 1. It is important to note that SERS-based techniques alone have not typically proven to be useful for explosives detection. The primary concern is that any chemical components that enter the enhancing field can potentially contribute to the resulting spectra, making real-world samples difficult

to differentiate, even with advanced chemometric analysis tools. However, by employing the developed approach presented here, the MIP will concentrate the target to the SERS-active surface, thereby making the combined approach more highly selective than a SERS-only detection platform and free from errors related to background interference.

Figure 1. MIP-SERS detection concept.

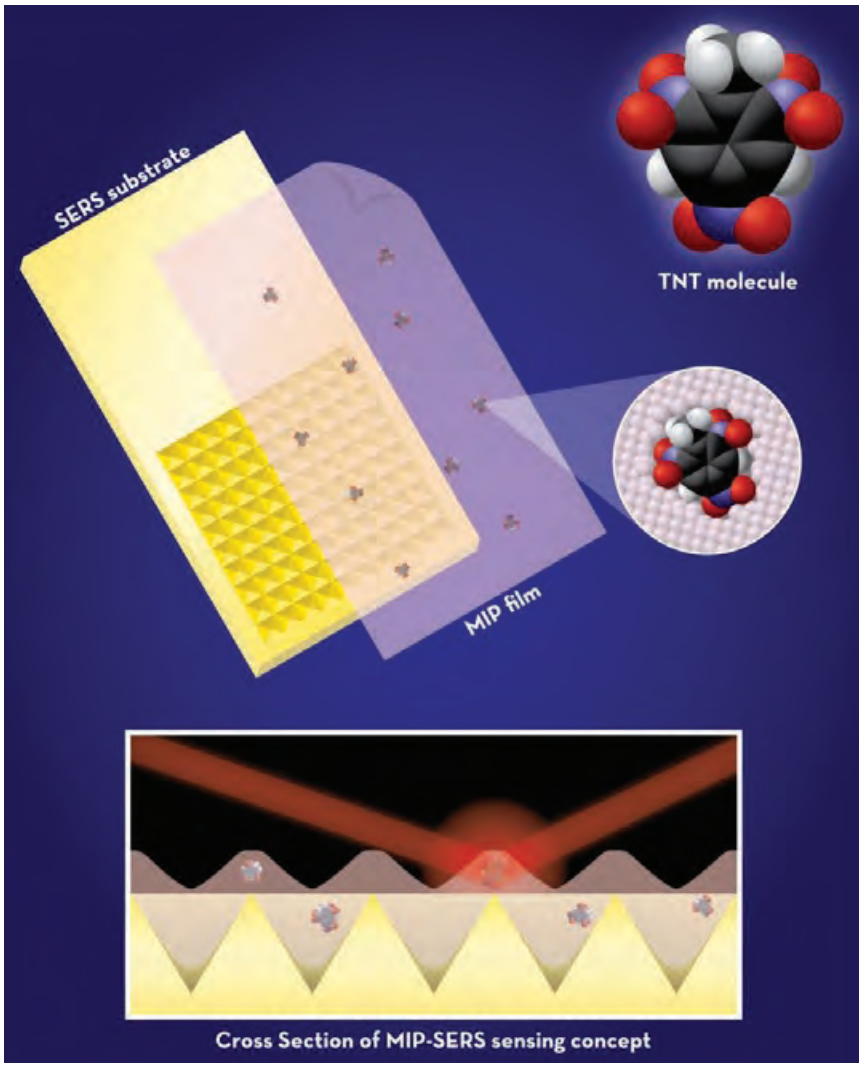

This integrated MIPs and SERS concept is a novel approach to chemical sensing; however reported investigations of this pairing are scarce [31,32]. The Kantarovich group used a nano fountain pen to print MIP droplets on SERS-active surfaces and directly monitor the uptake and release of the β-blocking drug propranolol by SERS [31]. Kostrewa *et al.* prepared MIPs on SERS-active surfaces to directly monitor the uptake and release of either (2S,3S)-(+)-di-O-benzoyl-tartaric acid or N-benzyloxycarbonyl-(L)-aspartic acid to the polymer by SERS [32]. In this instance, adhesion of the MIP to the SERS-active substrates was unsatisfactory for practical application as the MIP was not truly integrated with the substrate. Herein, we consider adhesion of the polymer to the SERS substrate. Xerogel precursors were chosen based on potential interactions with the metallic under layer of the substrate. The xerogel matrix included 3-mercaptopropyltrimethoxysilane (MPTMS), which contains a thiol group and results in chemisorption of the polymer to the metal surface of the SERS substrate.

Films of molecularly imprinted xerogels were deposited on SERS substrates to create a sensor for TNT. Sensitivity is determined by the SERS substrate used in this study, while selectivity is provided by both the specific binding interaction of the TNT with the MIP and the unique molecular "fingerprint" provided by the SERS measurement.

2. Experimental Section

2.1. Reagents and Materials

APTES, methyltriethoxysilane (C1-TriEOS), and MPTMS were obtained from Gelest. TNT, 2,4-dinitrotoluene (2,4-DNT), 2,6-dinitrotoluene (2,6-DNT), and 1,3-dinitrobenzene (1,3-DNB) were purchased from Cerilliant. Ethanol, acetonitrile, acetic acid, and HCl were obtained from Sigma-Aldrich.

Klarite® substrates were purchased from Renishaw Diagnostics. These substrates consist of a smooth border and a SERS-active patterned grid area. Both surfaces are gold-coated. To protect against environmental and shipping hazards, each substrate is placed in a separate microscope slide holder enclosed within an opaque vacuum-sealed pouch before shipping. Just prior to use, each substrate was removed from the vacuum-sealed pouch and slide holder. The substrates were used as received.

All solvents were HPLC grade. All chemicals were used as received unless otherwise noted.

2.2. Instrumentation

SERS data was recorded using a Renishaw inVia Reflex Raman microscope equipped with a near-infrared diode laser excitation source (λ = 785 nm). The light from the diode was focused onto the samples at the microscope stage through a 20× objective. Prior to coupling into the microscope, the diode laser beam was circularized by inserting a pinhole into the optical beam path and neutral density filters were used resulting in reduction of the maximum available laser power to 17 mW. Samples at the microscope stage were positioned remotely with a joystick using an encoded, motorized *XYZ* translation stage (0.1 μm step size) controlled by a Prior Scientific ProScan II controller. WiRE 2.0 software, operating on a bench top computer, was used for instrument control and data collection. Before all measurements, the instrument was wavelength calibrated using an internal silicon standard.

Films were produced by spin casting with a spin coater (Laurell Technologies, model WS-400B-6NPP/LITE).

2.3. SERS Measurements

A stock solution of TNT was prepared at 4.0×10^{-4} M, in acetonitrile. All xerogel films were incubated in this solution at room temperature for 24 h. The xerogels were subsequently rinsed with acetonitrile (200 μL) to remove residual TNT from the surface. Stock solutions of TNT, 2,4-DNT, 2,6-DNT, and 1,3-DNB were prepared at 7.5×10^{-5} M, in acetonitrile, and incubated with the xerogel films in the same manner.

All SERS spectra were acquired using Klarite® substrates. Duplicate samples were prepared for each study and five separate spectral acquisitions were obtained for each sample. Each SERS spectrum was collected over a range from 700 cm^{-1} to 1,500 cm^{-1} with a 10.00 s exposure time and a spectral

resolution better than 1 cm^{-1} and is the result of three accumulations. All data are presented as the average (10 measurements) from duplicate samples and corresponding variance represents 1σ.

2.4. Overall MIP Fabrication

The overall MIP production and SERS integration protocol is illustrated in Figure 2 for the template/target molecule, TNT (**1**). Briefly, the TNT-doped sol, comprised of APTES (**2**), MPTMS (**3**), and C1-TriEOS is spun cast onto a Klarite® substrate and allowed to gel, and the xerogel formed. The non-covalent interaction between APTES and TNT is illustrated, as well as chemisorption of the MPTMS to the gold metal layer of the Klarite® substrate. The TNT is removed from the xerogel with a solution containing ethanol, acetonitrile, and acetic acid. The xerogel is then immersed in a target analyte (TNT) solution, filling all the analyte accessible template sites.

Figure 2. Reaction protocol for producing an integrated MIP-SERS sensor.

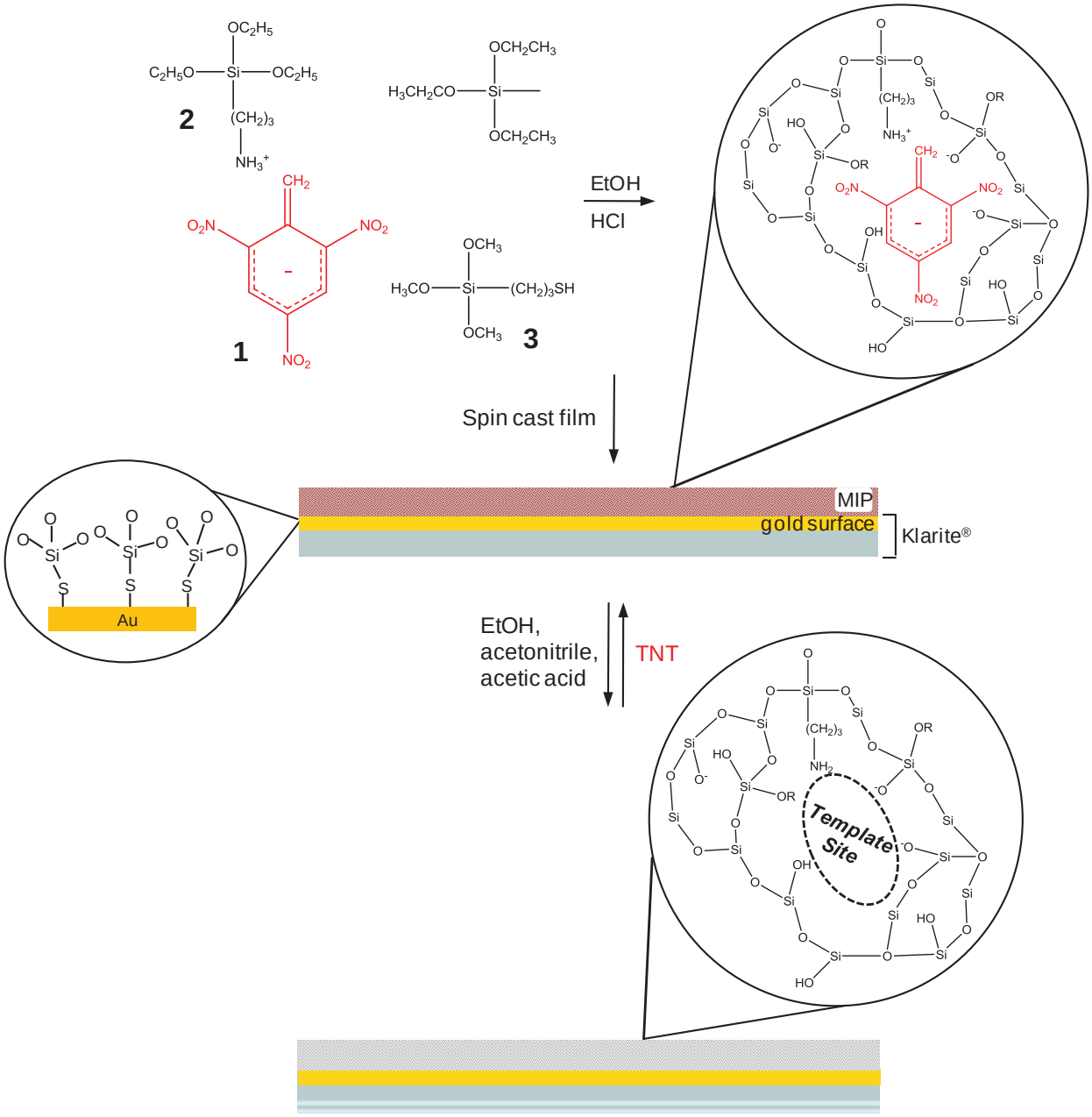

2.5. TNT-Doped Xerogel Preparation

A TNT stock solution was prepared at 9.85×10^{-3} M, in acetonitrile. Sol solutions were prepared by mixing C1-TriEOS (110 μL, 0.552 mmol), MPTMS (2.813 μL, 1.51×10^{-2} mmol), APTES (3.50 μL, 1.51×10^{-2} mmol), ethanol (1.25 mL, 21.4 mmol), and HCl (6.25 μL of 1 M, 6.25×10^{-3} mmol). The C1-TriEOS, MPTMS, APTES, and HCl were added to the ethanol at room temperature and then stirred for 30 min to ensure a visually homogeneous sol solution.

The TNT-doped sol solution was prepared by adding 150 μL of the TNT stock solution to the prehydrolyzed C1-TriEOS/MPTMS/APTES/HCl/ethanol sol solution. This sol solution was then vigorously mixed for 30 s with a touch mixer (Scientific Industries, Vortex-Genie 2).

Xerogel films (7 μm to 10 μm thickness) were formed by spin casting (4,000 rpm, 2 min) a 50 μL aliquot of the final sol mixture onto a Klarite® substrate. The films were aged at room temperature for 2–3 days and were transparent to the eye.

2.6. TNT Removal from the Xerogel

TNT was extracted from the xerogel films with an ethanol/acetonitrile/acetic acid (v/v/v 8:2:1) solution. The xerogels were allowed to react with this solution at room temperature for 24 h. All xerogel films were subsequently rinsed with ethanol to remove the residual acidic solvent.

2.7. Control Xerogels

A series of control xerogel films were prepared to ensure that the observed sensor response did not arise from artifacts. The controls were prepared by following the exact reaction sequence described above except as noted below. Control A is formed by eliminating TNT. Control B is formed by eliminating TNT and APTES.

3. Results and Discussion

There are several key challenges to overcome in the development of a hybrid MIP-SERS sensing platform including: (i) developing a MIP that does not completely mask the spectral features of the target analyte through SERS polymer background; (ii) developing a strategy for MIP integration that enables target interaction within the surface enhanced plasmon field responsible for SERS signal enhancement; (iii) developing a MIP formulation that is stable and truly integrated with the SERS substrate to allow for practical application in the field; and (iv) ensuring that the developed MIP allows for template removal, analyte reintroduction, and also provides selectivity for the target analyte components.

3.1. Molecularly Imprinted Xerogels

Different formulations of molecularly imprinted xerogel films were tested where the amino-containing precursor was varied to determine the effect on TNT binding (data not shown). These precursors included 3-(N-allylamino)propyltrimethoxysilane, 4-aminobutyltriethoxysilane, n-butylaminopropyltrimethoxysilane, and APTES. Xerogels containing the APTES precursor exhibited the most effective TNT binding when templated. Therefore the discussion is limited to the results observed for this xerogel formulation.

3.2. SERS Integration

In order to verify molecule templating with SERS, spectra of the chemical analytes and interferents were acquired. Shown in Figure 3(a–d) are intensity-normalized spectra of the analytes investigated during this study. Specifically, the SERS spectra for (a) TNT, (b) 2,4-DNT, (c) 1,3-DNB, and (d) 2,6-DNT (all 1,000 μg/mL, in acetonitrile), over the Raman shift range from 700 cm^{-1} to 1,500 cm^{-1} are presented. As illustrated, this spectral region is interesting since it contains features representative of Raman-active components present in these analytes. In general, the spectra are dominated by SERS-enhanced features centered near 830 cm^{-1} and 1,350 cm^{-1}. These bands are a result of NO_2 out-of-plane bending modes and NO_2 stretching modes, respectively [33]. These peaks can be used as a "fingerprint" for the detection of these nitro-aromatic compounds by their SERS spectra. Although the key spectral features are comparable, there are minor frequency differences between each nitro-aromatic species. The SERS nitrate stretching modes are observed at 1,356 cm^{-1}, 1,350 cm^{-1}, 1,366 cm^{-1}, and 1,350 cm^{-1} for TNT, 2,4-DNT, 2,6-DNT, and 1,3-DNB, respectively. The absence of the toluene group in 1,3-DNB allows the benzene ring to adsorb more strongly to the substrate surface, leading to a unique feature centered near 1,000 cm^{-1} when compared to the other compounds [34]. These data suggest that it is possible to distinguish these nitro-aromatic species based on their molecular composition, and therefore SERS spectral signatures.

Figure 3. SERS spectral signature of **(a)** TNT, **(b)** 2,4-DNT, **(c)** 1,3-DNB, and **(d)** 2,6-DNT on Klarite®. Spectra are offset for clarity. The vertical dashed lines are aligned with the characteristic NO_2 out-of-plane bending and stretching modes of TNT.

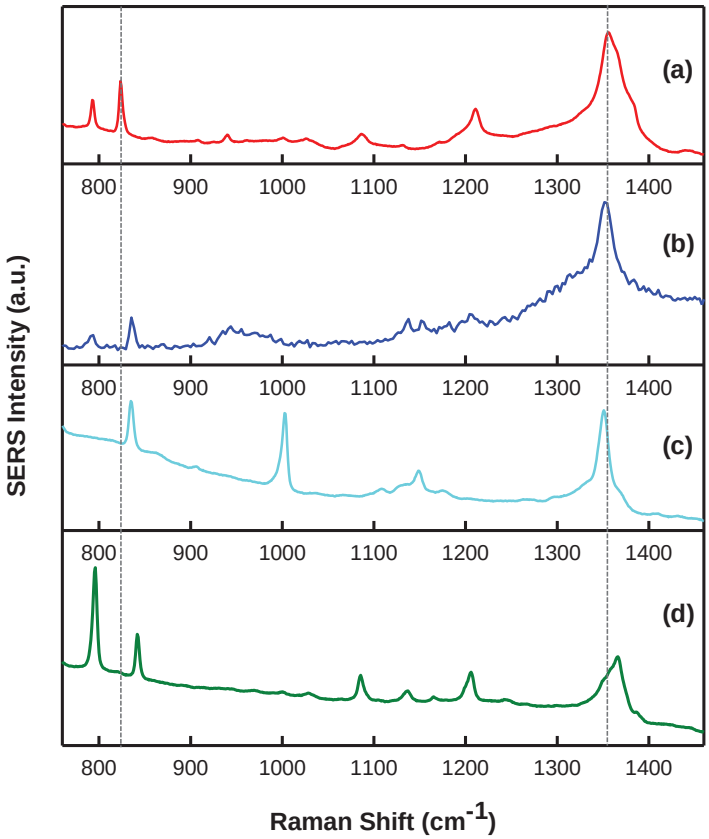

The integration of MIPs with SERS is not straightforward and poses a unique set of challenges. A major technical challenge is ensuring that the polymer layer is thin and porous enough to concentrate the target analyte within the surface plasmon field responsible for the Raman enhancement, which drops off exponentially with distance from the nanostructured surface. In order to demonstrate SERS enhancement of TNT templated within the polymer matrix, a film was spun cast over both the smooth border (inactive) and SERS-active region of the Klarite® substrate. Figure 4 shows the corresponding Raman and SERS spectra illustrating successful SERS enhancement for TNT (b). The signal from the inactive region (c) does not exhibit TNT and is indicative of Klarite substrate background [30,35]. When incorporated into the polymer, the SERS nitrate stretching mode is shifted to 1,352 cm^{-1}. The exact origin of this shift is unclear; however changes in the shifts can be expected if minor structural changes occur when the molecule is encapsulated in a polymer matrix. Kantarovich *et al.* noted a similar observation in the SERS spectra of a MIP that was prepared using (S)-propranolol as a template [31]. Despite these subtle spectral shifts, it is clear from Figure 4 that the polymer background does not prohibit TNT detection. Furthermore, the successful measurement of the TNT template within the MIP shows it is possible to develop a thin and porous MIP film which allows analyte measurement within the critical surface enhancing field distance from the underlying substrate.

Figure 4. (a) SEM image of a Klarite® substrate showing the smooth inactive border and the SERS-active patterned grid area. The black and red arrows illustrate the measurement areas for the Raman and SERS spectra, respectively. SERS **(b)** and Raman **(c)** spectra recorded for a TNT-doped xerogel film. The vertical lines indicate the peaks related to TNT, which are not evident in the Raman spectra.

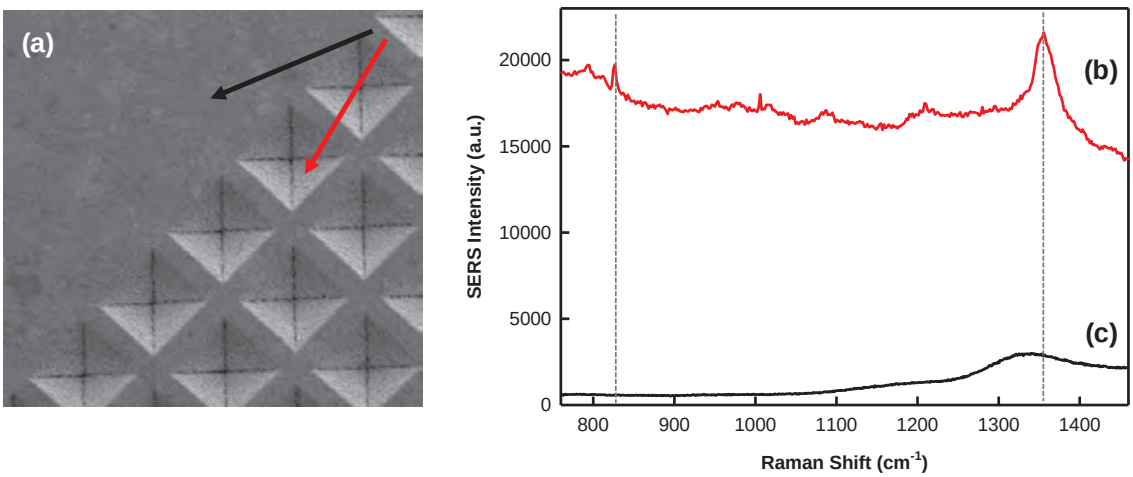

Figure 5(a–d) presents the SERS spectra for both a TNT-doped xerogel film (b) and control (A and B) xerogel films (c) and (d) spun cast on a Klarite® substrate. Spectrum (b) has been blank corrected by subtracting spectrum (c). A representative SERS spectrum of free TNT on a Klarite® substrate (a) is also provided for reference.

Figure 5. SERS spectra recorded for **(a)** free template TNT, **(b)** TNT-doped xerogel film (MIP), **(c)** control A, and **(d)** control B. Spectra are offset for clarity. The vertical dashed lines indicate the peaks related to TNT, which are not evident in the control spectra.

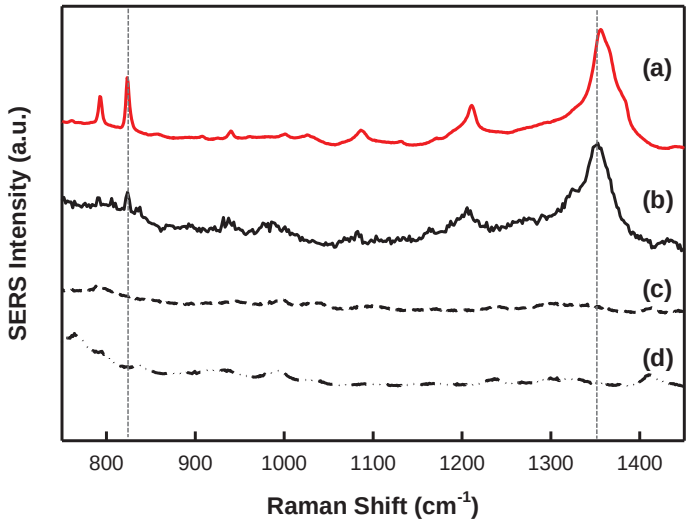

3.3. Efficiency of TNT Removal

Figure 6 presents the SERS spectra for a TNT-doped xerogel film spun cast on a Klarite® substrate measured before (—) and after (– ··–) treatment with the ethanol/acetonitrile/acetic acid extraction solution. Both spectra have been blank corrected by subtracting control A (Figure 5(c)). In the spectrum measured following treatment with the extraction solution, the nitrate stretching mode (1,352 cm^{-1}) was reduced extensively and the nitrate bending mode (~830 cm^{-1}) disappeared.

Figure 6. SERS spectra recorded for a TNT-doped xerogel film before (—) and after (– ··–) TNT extraction. Spectra are offset for clarity. The vertical dashed lines indicate the peaks related to TNT, which decreased after template extraction.

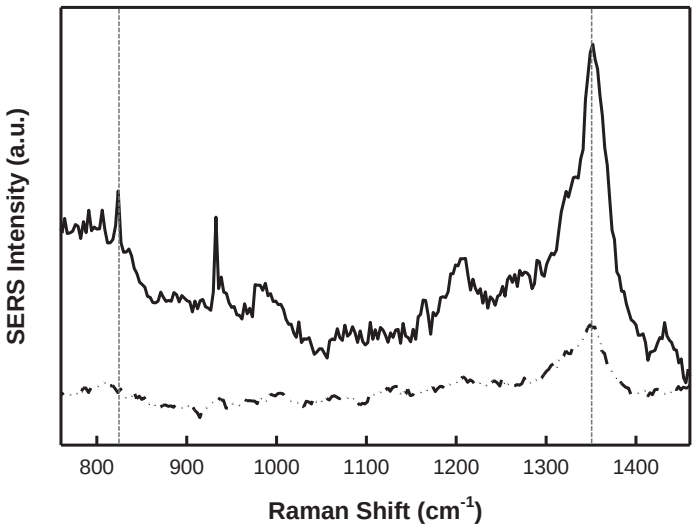

3.4. Sensor Response to TNT

Sensors based on TNT-imprinted xerogel films integrated with Klarite® substrates were tested by exposure to TNT. Specifically, SERS data for both MIP and control (A and B) xerogel films was recorded after incubation in a solution of TNT (4.0×10^{-4} M, in acetonitrile). The response is completely reversible after more than 10 cycles with no evidence of signal intensity degradation. These results are summarized in Figure 7(a–c). The SERS TNT fingerprint is apparent in the spectra recorded for the MIP (a) and control A (b). There is no visible TNT fingerprint present in the spectra collected for control B (c). Spectra (a) and (b) have been blank corrected by subtracting control A (Figure 5(c)). Spectrum (c) has been blank corrected by subtracting control B (Figure 5(d)). Due to the presence of APTES in control A and the resulting free amine moieties in the polymer matrix and at the surface, it was expected that TNT would react with this polymer; however it is evident from the recorded SERS spectra that there is preferential binding of TNT to the MIP.

Figure 7. SERS spectra recorded for **(a)** MIP, **(b)** control A, and **(c)** control B after incubation in a 4.0×10^{-4} M solution of TNT. Spectra are offset for clarity. The vertical dashed lines indicate the peaks related to TNT, which increased after incubation.

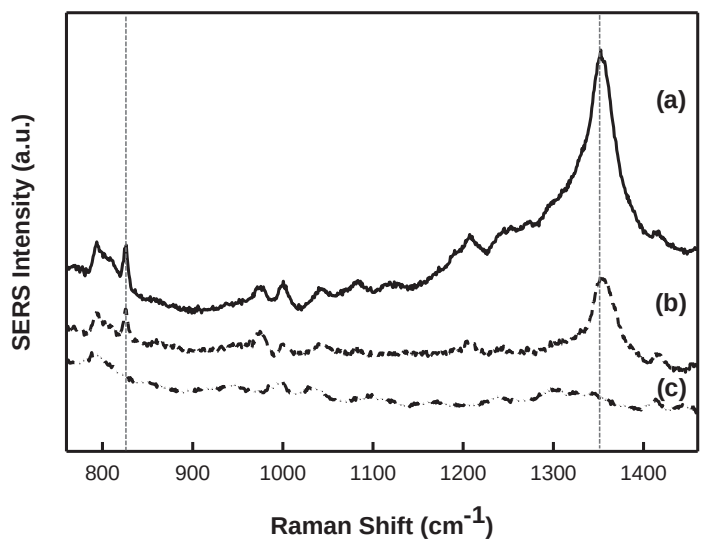

Figure 8 illustrates the response profile form TNT-responsive and control (A and B) xerogel films integrated with Klarite® substrates to increasing concentrations of TNT. These curves were determined using the height of the spectral band (peak height) resulting from the nitrate stretching mode (1,352 cm^{-1}) for both the MIP and controls. Peak heights for the SERS spectral bands associated with the nitrate stretching modes were determined by taking the difference between the peak intensity maximum and an average baseline for each spectrum. This calculation was done after the spectra had been blank corrected. In the MIP, the SERS signal increases as the TNT concentration increases. A single-site saturation ligand binding model (—) yields a dissociation constant of $(2.3 \pm 0.3) \times 10^{-5}$ M for this molecularly imprinted xerogel for TNT. No significant response is seen from control B when challenged by TNT; however non-specific binding is evident in the results from control A (– –). In this case, the dissociation constant was determined to be $(6.7 \pm 1.1) \times 10^{-5}$ M. Based on these results, the binding strength of TNT to the MIP is about three times that of control A.

Figure 8. Response profiles for a MIP and control A and B films integrated with a Klarite® substrate.

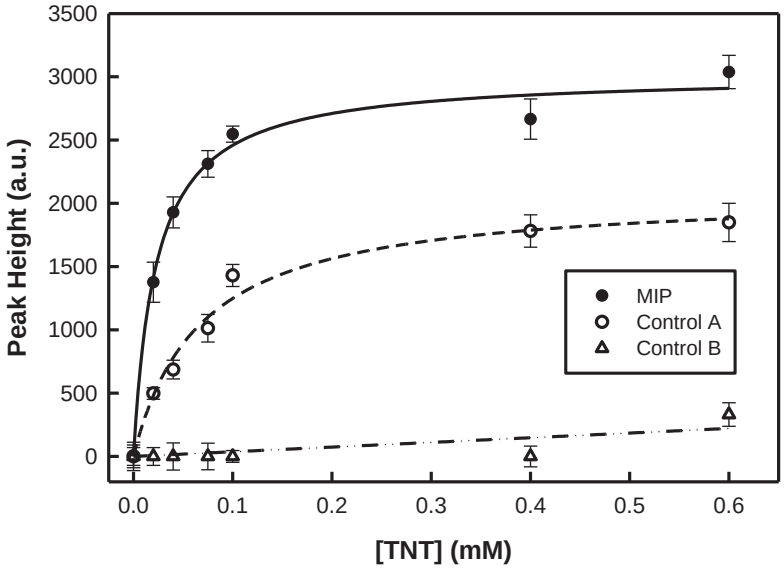

The 3σ limit of detection was determined to be 3.0 μM for this first-generation MIP-SERS sensor for TNT. The achievable sensitivity is limited by the Klarite® SERS substrate. This commercially available substrate was a convenient choice for these seminal studies as it offers reproducibility; however the sensitivity is lacking [35].

3.5. Sensor Stability

Adhesion of the MIP to the SERS substrate was assessed by soaking the xerogel films integrated with Klarite® substrates in various aqueous environments (duration ≥ 1 h), including water, 6 M HCl, 0.1 M pH 7.4 phosphate buffer, toluene, and the ethanol/acetonitrile/acetic acid extraction solution. The polymer showed excellent adhesion and stability, with no apparent degradation in sensing performance, which is necessary for practical field use.

We tested the sensor response over a six-month period. The aforementioned analytical figures of merit are reproducible to within <7% relative standard deviation.

3.6. Sensor Selectivity

To assess the selectivity of the integrated MIP-SERS sensor for the target analyte (*i.e.*, TNT) the sensor was challenged by a series of molecules that are structurally similar to the target molecule. Figure 9(a–d) presents the intensity-normalized SERS spectra for a molecularly imprinted xerogel film (solid lines) and a control A film (dashed lines) integrated with Klarite® substrates recorded after incubation in stock solutions (7.5×10^{-5} M, in acetonitrile) of (a) TNT (included for comparison), (b) 2,4-DNT, (c) 1,3-DNB, and (d) 2,6-DNT. All spectra have been blank corrected by subtracting control A (Figure 5(c)). The SERS fingerprints for these compounds are apparent in the spectra recorded for the MIP and are also evident in control A to some extent. There is no visible SERS fingerprint present for any of these analytes in the data collected for control B (data not shown). Due to the presence of APTES in the MIP and control A, it was expected that these nitro-aromatic compounds

would react with the polymer; however it is apparent from these spectra that there is preferential binding of TNT to the MIP compared to the other structurally similar molecules. For further comparison, the MIP and control A peak heights of the SERS spectral bands associated with the nitrate stretching modes (~1,350 cm^{-1}) are provided in Table 1. Peak heights were determined by taking the difference between the peak intensity maximum and an average baseline for each spectrum. This calculation was done after the spectra had been blank corrected. The results presented in Figure 9 and Table 1 suggest the MIP has preferential affinity for TNT. The integrated MIP-SERS sensor yields a selectivity factor [18] of 1.63 for TNT over 2,4-DNT, 1.72 for TNT over 1,3-DNB, and 2.12 for TNT over 2,6-DNT.

Table 1. Peak heights of SERS spectral bands associated with the nitrate stretching modes of various nitro-aromatic compounds.

Analyte	**Peak Height**		
	MIP	Control A	Control B
TNT	12,145.05 ± 160.22	5,560.28 ± 226.25	no response
1,4-DNT	7,425.98 ± 274.55	5,581.05 ± 250.54	no response
1,3-DNB	7,038.34 ± 190.38	2,131.46 ± 327.40	no response
2,6-DNT	5,702.42 ± 288.15	1,898.60 ± 267.94	no response

Figure 9. SERS spectra recorded for a MIP after incubation in a 7.5×10^{-5} M solution of **(a)** TNT, **(b)** 2,4-DNT, **(c)** 1,3-DNB, and **(d)** 2,6-DNT. The vertical dashed lines are aligned with the characteristic NO_2 out-of-plane bending and stretching modes of TNT. Spectra are offset for clarity.

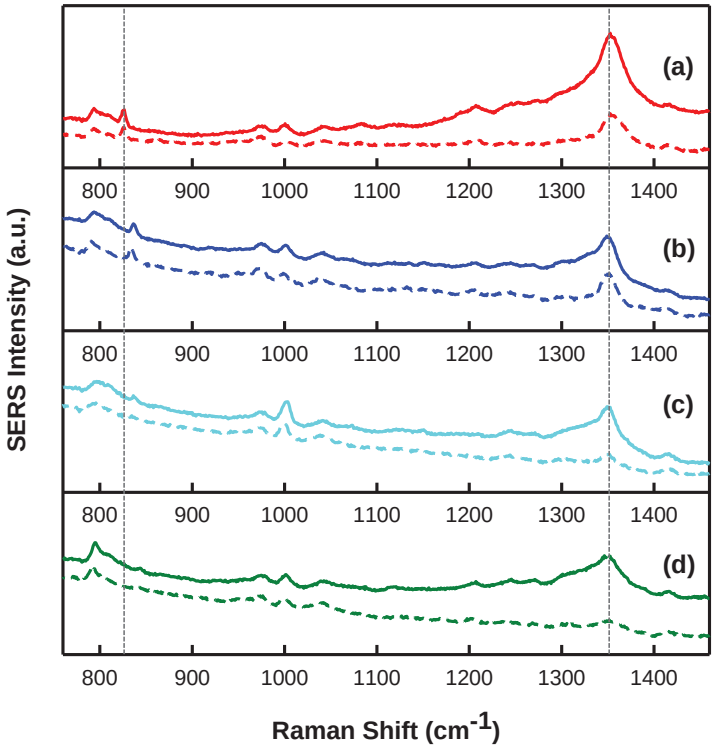

Additionally, the selectivity can be optimized by considering the unique SERS spectral features associated with these structurally similar compounds. For example, the feature located at 1,000 cm^{-1} is more distinct in Figure 9(c), which suggests the presence of 1,3-DNB. Additionally, comparison of the Raman shifts associated with the NO_2 out-of-plane bending and stretching modes (~830 cm^{-1} and ~1,350 cm^{-1}, respectively) for each of these molecules allows for further differentiation. This is evidenced by the differences in the Raman shifts for these NO_2 modes in Figure 9(a,b). Finally, it is important to note that some selectivity for these structurally similar molecules may be advantageous as 2,4-DNT and 1,3-DNB are manufacturing impurities found in TNT [33] and the detection of these species would be beneficial in recognizing the presence of TNT in the field.

4. Conclusions

We have successfully demonstrated a hybrid MIP and SERS sensing concept for the detection of TNT. The first-generation integrated MIP-SERS sensor exhibits a reversible response to the target analyte and is stable in a variety of environments. The results suggest that the MIP-SERS combination is an effective and robust chemical nanosensing scheme. We anticipate the MIP-SERS protocol being extended to include other explosives and chemical warfare agents of interest to the Army. Future work will include incorporation of next generation Klarite® substrates for enhanced sensitivity, additional film optimization for template removal and temporal response studies. A successful MIP-SERS sensing format could reduce sensor cost and size, while maintaining the high sensitivity, selectivity, and portability needed for military applications.

Acknowledgements

This research was supported by the Army Research Laboratory Director's Research Initiative (DRI FY09-SED-13).

References

1. Narayanan, A.; Varnavski, O.P.; Swager, T.M.; Goodson, T. Multiphoton fluorescence quenching of conjugated polymers for TNT detection. *J. Phys. Chem. C* **2008**, *112*, 881-884.
2. Yang, J.S.; Swager, T.M. Fluorescent porous polymer films as TNT chemosensors: Electronic and structural effects. *J. Am. Chem. Soc.* **1998**, *120*, 11864-11873.
3. Yang, J.S.; Swager, T.M. Porous shape persistent fluorescent polymer films: An approach to TNT sensory materials. *J. Am. Chem. Soc.* **1998**, *120*, 5321-5322.
4. Pinnaduwage, L.A.; Yi, D.; Tian, F.; Thundat, T.; Lareau, R.T. Adsorption of trinitrotoluene on uncoated silicon microcantilever surfaces. *Langmuir* **2004**, *20*, 2690-2694.
5. Pinnaduwage, L.A.; Wig, A.; Hedden, D.L.; Gehl, A.; Yi, D.; Thundat, T.; Lareau, R.T. Detection of trinitrotoluene via deflagration on a microcantilever. *J. Appl. Phys.* **2004**, *95*, 5871-5875.
6. Guomin, Z.; Xinxin, L.; Peng, L.; Yuelin, W.; Zhenxing, C.; Songlin, F. In trace TNT vapor detection with an SAM-functionalized piezoresistive SiO_2 microcantilever. In *Proceedings of IEEE Sensors* 2006, Daegu, Korea, 22–25 October 2006; IEEE: Daegu, Korea, 2007; pp. 749-752.

7. Ewing, R.G.; Atkinson, D.A.; Eiceman, G.A.; Ewing, G.J. A critical review of ion mobility spectrometry for the detection of explosives and explosive related compounds. *Talanta* **2001**, *54*, 515-529.
8. Asbury, G.R.; Klasmeier, J.; Hill, H.H.J. Analysis of explosives using electrospray ionization/ion mobility spectrometry (ESI/IMS). *Talanta* **2000**, *50*, 1291-1298.
9. Smiths Detection IONSCAN, SABRE. Available online: www.smithsdetection.com (accessed on 22 December 2010).
10. Ali, E.M.A.; Edwards, H.G.M.; Scowen, I.J. Raman spectroscopy and security applications: The detection of explosives and precursors on clothing. *J. Raman Spectrosc.* **2009**, *40*, 2009-2014.
11. Pacheco-Londono, L.C.; Ortiz-Rivera, W.; Primera-Pedrozo, O.M.; Hernandez-Rivera, S.P. Vibrational spectroscopy standoff detection of explosives. *Anal. Bioanal. Chem.* **2009**, *395*, 323-335.
12. Thermo Scientific AhuraFD. Available online: www.ahurascientific.com (accessed on 22 December 2010).
13. Yan, M.; Ramström, O. *Molecularly Imprinted Materials: Science and Technology*; Marcel Dekker: New York, NY, USA, 2005.
14. Holthoff, E.L.; Bright, F.V. Molecularly templated materials in chemical sensing. *Anal. Chim. Acta* **2007**, *594*, 147-161.
15. Li, W.; Li, S.J. Molecular imprinting: A versatile tool for separation, sensors and catalysis. In *Oligomers Polymer Composites Molecular Imprinting*; Springer-Verlag Berlin: Berlin, Germany, 2007; Volume 206, pp. 191-210.
16. Piletsky, S.A.; Turner, A.P.F. *Molecular Imprinting of Polymers*; Landes Bioscience: Georgetown, TX, USA, 2006.
17. Holthoff, E.L.; Bright, F.V. Molecularly imprinted xerogels as platforms for sensing. *Acc. Chem. Res.* **2007**, *40*, 756-767.
18. Shughart, E.L.; Ahsan, K.; Detty, M.R.; Bright, F.V. Site selectively templated and tagged xerogels for chemical sensors. *Anal. Chem.* **2006**, *78*, 3165-3170.
19. Mosbach, K. Molecular imprinting. *Trends Biochem. Sci.* **1994**, *19*, 9-14.
20. Saloni, J.; Dasary, S.S.R.; Anjaneyulu, Y.; Yu, H.T.; Hill, G. Molecularly imprinted polymers for detection of explosives: Computational study on molecular interactions of 2,6-dinitrotoluene and methacrylic acid complex. *Struct. Chem.* **2010**, *21*, 1171-1184.
21. Xie, C.; Zhang, Z.; Wang, D.; Guan, G.; Gao, D.; Liu, J. Surface molecular self-assembly strategy for TNT imprinting of polymer nanowire/nanotube arrays. *Anal. Chem.* **2006**, *78*, 8339-8346.
22. Rose, A.; Zhu, Z.; Madigan, C.F.; Swager, T.M.; Bulovic, V. Sensitivity gains in chemosensing by lasing action in organic polymers. *Nature* **2005**, *434*, 876-879.
23. Walker, N.R.; Linman, M.J.; Timmers, M.M.; Dean, S.L.; Burkett, C.M.; Lloyd, J.A.; Keelor, J.D.; Baughman, B.M.; Edmiston, P.L. Selective detection of gas-phase TNT by integrated optical waveguide spectrometry using molecularly imprinted sol-gel sensing films. *Anal. Chim. Acta* **2007**, *593*, 82-91.
24. Trammell, S.A.; Zeinali, M.; Melde, B.J.; Charles, P.T.; Velez, F.L.; Dinderman, M.A.; Kusterbeck, A.; Markowitz, M.A. Nanoporous organosilicas as preconcentration materials for the electrochemical detection of trinitrotoluene. *Anal. Chem.* **2008**, *80*, 4627-4633.

25. Xie, C.; Liu, B.; Wang, Z.; Gao, D.; Guan, G.; Zhang, Z. Molecular imprinting at walls of silica nanotubes for TNT recognition. *Anal. Chem.* **2008**, *80*, 437-443.
26. Henry, O.Y.F.; Cullen, D.C.; Piletsky, S.A. Optical integration of molecularly imprinted polymers and development of MIP sensors: A review. *Anal. Bioanal. Chem.* **2005**, *382*, 947-956.
27. Piletsky, S.A.; Turner, A.P.F. Electrochemical sensors based on molecularly imprinted polymers. *Electroanalysis* **2002**, *14*, 317-323.
28. Fleischmann, M.; Hendra, P.J.; Quillan, A.J.M. Raman spectra of pyridine adsorbed at a silver electrode. *Chem. Phys. Lett.* **1974**, *26*, 163-166.
29. Hankus, M.E.; Li, H.G.; Gibson, G.J.; Cullum, B.M. Surface-enhanced Raman scattering-based nanoprobe for high-resolution, non-scanning chemical imaging. *Anal. Chem.* **2006**, *78*, 7535-7546.
30. Hankus, M.E.; Stratis-Cullum, D.N.; Pellegrino, P.M. Enabling technologies for point and remote sensing of chemical and biological agents using surface enhanced Raman scattering (SERS) techniques. Available online: http://handle.dtic.mil/100.2/ADA506582 (accessed 5 January 2011).
31. Kantarovich, K.; Tsarfati, I.; Gheber, L.; Haupt, K.; Bar, I. Writing droplets of molecularly imprinted polymers by nano fountain pen and detecting their molecular interactions by surface-enhanced raman scattering. *Anal. Chem.* **2009**, *81*, 5686-5690.
32. Kostrewa, S.; Emgenbroich, M.; Klockow, D.; Wulff, G. Surface-enhanced Raman scattering on molecularly imprinted polymers in water. *Macromol. Chem. Phys.* **2003**, *204*, 481-487.
33. Sylvia, J.M.; Janni, J.A.; Klein, J.D.; Spencer, K.M. Surface-enhanced Raman detection of 2,4-dinitrotoluene impurity vapor as a marker to detect landmines. *Anal. Chem.* **2000**, *72*, 5834-5840.
34. Spencer, K.M.; Sylvia, J.M.; Janni, J.A.; Klein, J.D. Advances in land mine detection using surface-enhanced Raman spectroscopy. *Proc. SPIE* **1999**, *3710*, 373-379.
35. Hankus, M.E.; Stratis-Cullum, D.N.; Pellegrino, P.M. Towards advanced biological detection using surface enhanced Raman scattering (SERS)-based sensors. *Proc. SPIE* **2010**, *7759*, 77590G-1-77590G-13.

© 2011 by the authors; licensee MDPI, Basel, Switzerland. This article is an open access article distributed under the terms and conditions of the Creative Commons Attribution license (http://creativecommons.org/licenses/by/3.0/).

Constellation Design for Channel Precompensation in Multi-Wavelength Visible Light Communications

Robert J. Drost, and Brian M. Sadler

IEEE Transactions on Communications, 62 (2014)

Constellation Design for Channel Precompensation in Multi-Wavelength Visible Light Communications

Robert J. Drost, *Member, IEEE*, and Brian M. Sadler, *Fellow, IEEE*

***Abstract*—The predicted ubiquity of light-emitting diodes (LEDs) suggests great potential for dual-use systems with visible light communications (VLC) capabilities. One class of LEDs employs multiple emitters at different wavelengths, making them appropriate for applications requiring colored output and providing multiple channels for communication. We present a design framework for optimizing the signaling constellation of VLC systems employing an arbitrary number of such LEDs, each with an arbitrary number of emitters. In particular, by considering the design of constellation-symbol locations jointly across LED emitters, the framework provides for the precompensation of linear channel distortions arising from, for example, cross-channel leakage, noise correlation, or wavelength-dependent received-signal and/or noise power, as well as the incorporation of design constraints for color-shift keying, dimming, and/or perceived color. Simulation results demonstrate the design approach and the potential performance enhancement that can be achieved for particular system scenarios. Experimental measurements using a prototype VLC system confirm such performance enhancements, providing real-world evidence of the benefit of applying the proposed framework to VLC channel precompensation.**

***Index Terms*—Channel precompensation, constellation design, modulation, visible-light communications (VLC).**

I. Introduction

THE efficiency, durability, and lifetime of light-emitting diodes (LEDs) have led to their use in a variety of applications, including general illumination, vehicle lights, signage, and displays [1]. In fact, it is often predicted that LED bulbs will soon replace all traditional incandescent bulbs, as well as compact fluorescent alternatives, in general lighting applications [2]. It has long been recognized that LEDs used in such systems can be simultaneously modulated to provide a dual function of communications. Proposed applications for visible light communications (VLC) include indoor local area networks through room lighting [3], in-flight data downlinks through airplane reading lamps [4], intelligent transportation [5], positioning in wireless sensor networks [6], and underwater communications [7].

The continued progress in the development of LED devices (e.g., [8]–[10]) has led to an explosion in research on how to effectively use LEDs in VLC systems. Fundamental analysis of indoor VLC performance was provided in [11], with subsequent work examining complicating factors such as nonlinear LED response [12] and clock jitter [13]. The effectiveness of various system design choices have been extensively studied, including modulation formats such as orthogonal frequency-division multiplexing (OFDM) [14]–[16] and multiple-input multiple-output (MIMO) transmission [17], adaptive equalization algorithms [18], and forward error correction [19], [20]. Implications of design constraints, such as uniformity of illumination [21] and LED dimming capabilities [22], [23], arising from the dual-use nature of VLC in many applications, have also been examined. Experimental systems have been produced as well, often with the goal of demonstrating communications at increasingly higher bit rates, albeit typically over very short distances. For example, [24]–[26] report on, respectively, a 200 Mbs discrete multitone (DMT) system, a 1.1 Gbs system employing carrierless modulation, and a 1 Gbs MIMO-OFDM system.

Due primarily to lower manufacturing cost and complexity, white-light LEDs comprising a single blue emitter along with a yellow phosphorescent coating are the leading technology for many VLC applications, and, as such, much of the prior VLC research has focused on these devices. However, white light can also be produced by multi-wavelength LEDs (most notably red-green-blue, or RGB, LEDs), which comprise three or more emitters in a single package. Furthermore, by varying the relative intensity output by each emitter, a multi-wavelength LED can generate a range of perceived colors, including white. Hence, these LEDs, which are the focus of this paper, can be used in a broader set of applications where colored light might be required, such as mood lighting, effects lighting, signage, and displays.

Although many of the approaches for communicating with a single-emitter LED can be applied to a multi-wavelength LED (e.g., DMT [27]), application requirements on the perceived output of the LED can further constrain the VLC system. For example, effects lighting may require the ability to adjust the perceived color of the modulated LED, while the modulation of the multiple LEDs in a sign or display may need to be designed jointly so as to ensure constructive operation. On the other hand, the ability to control each of the emitters in a multi-wavelength LED provides additional design freedom. For example, color-shift keying (CSK), supported by IEEE 802.15.7 [28], is a modulation method in which the combined intensity of the emitters of a multi-wavelength LED is held constant to, e.g., avoid intensity flicker and reduce inrush current design requirements, while information is transmitted by the instantaneous color (i.e., relative emitter intensities) of the LED.

Manuscript received October 15, 2013; revised March 5, 2014; accepted April 27, 2014. Date of publication May 1, 2014; date of current version June 18, 2014. The editor coordinating the review of this paper and approving it for publication was H. Haas.

The authors are with the U.S. Army Research Laboratory, Adelphi, MD 20783 USA (e-mail: robert.j.drost6.civ@mail.mil; brian.m.sadler6.civ@mail.mil).

Digital Object Identifier 10.1109/TCOMM.2014.2321402

U.S. Government work not protected by U.S. copyright.

IEEE 802.15.7 defines static sets of colors to be used in 4-CSK, 8-CSK, and 16-CSK, where N-CSK employs N distinct instantaneous colors. However, alternative sets of colors may be useful to satisfy color constraints imposed on the VLC system or to improve performance by adapting to particular channel conditions. For example, a CSK design algorithm was described in [29] that approximately optimizes the symbol-error rate (SER) of a VLC system employing an RGB LED, possibly with a perceived-color constraint (e.g., appearing to output white light). Whereas a billiards algorithm [30] is employed in [29] for SER optimization, an alternative approach using interior-point methods is described in [31]. In either case, the perceived color constraint is transformed into an equivalent constraint on the average intensity of each emitter, where the average is taken over the symbols in the designed constellation and it is assumed that symbols are output with equal frequency over a time scale that is much shorter than the response time of the human eye. This last assumption can be justified probabilistically or with the use of a suitable line code.

In this paper, we examine VLC systems comprising one or more multi-wavelength LEDs and develop a framework for the (possibly constrained) design of transmitter symbol constellations to precompensate for channel conditions, optimizing the symbol error rate while satisfying various design constraints, if present, on the modulation format. Building off of [29] and [31], we consider an arbitrary number of emitters per LED and the possibility of modulating both the combined intensity and relative intensity of the LED emitters (i.e., the LED brightness and color, respectively). We also allow for the possibility of different perceived color and total-intensity constraints on the multiple LEDs in a VLC system (as might be encountered in, e.g., displays). By designing the location of constellation symbols jointly across LED emitters, the framework provides for the precompensation of such channel impairments as crosstalk and noise correlation between subchannels, even while satisfying constellation constraints imposed by a given application or the designer.

In Section II, we develop the VLC system model considered here and formulate the constrained signal-constellation optimization problem. While either the billiards optimization of [29] or the interior-point optimization of [31] could be adapted for many versions of the optimization problem addressed here, we more closely follow the latter approach as it provides for a more concise description and unified framework, as described in Section III. Simulation results are presented in Section IV that predict performance improvements achievable with optimized constellations versus several competing constellations (e.g., CSK-8 and CSK-16 defined in IEEE 802.15.7) in representative communication scenarios. In addition, we present data collected using a prototype RGB VLC system in Section V to experimentally validate our approach. Finally, Section VI offers some concluding remarks.

II. Problem Formulation

A. System Description

Table I summarizes selected notation that will be defined in the following problem formulation. We consider an equivalent discrete-time model of a VLC system comprising a set of $L \geq 1$ identical LEDs with $P \geq 1$ emitters per LED, each at an arbitrary but fixed wavelength. The number of LEDs and emitters may be communication system design choices (e.g., the use of an array of LEDs for increased output power) or may be dictated by the primary function of the system (e.g., illumination, effects lighting, image display, etc.) Although the case of $P = 3$ (e.g., an RGB LED) is most common, LEDs with more emitters can be used to extend the color gamut of the device.

TABLE I
SELECTED NOTATION

Symbol	Definition
L	Number of LEDs
M	Number of LED groups
L_m	Number of LEDs in the mth LED group
P	Number of emitters per LED
N	Number of constellation points
Q	Number of receiver photodetectors
$\mathbf{s}_{m,n}$	nth constellation point for mth LED group
$\mathbf{s}_m^{\text{avg}}$	Average color constraint for mth LED group
c_m	CSK total intensity for mth LED group
$\check{\mathbf{r}}_n$	nth receiver constellation symbol

The primary function of the system (e.g., signage) may dictate that each LED outputs a particular color (hue, saturation, and lightness [32]), and hence, a particular average intensity for each emitter, over a given period of time. Some applications, such as video displays, might require that the output colors be updated at relatively fast intervals (e.g., at the limits of human perception), whereas other applications, such as illumination, might require relatively static output (such as white light). Regardless, we consider the operation of the system over an interval during which any such required perceived color constraints are constant. We also note that many LEDs may be required to output an identical color. As such, we partition the L LEDs into $M \geq 1$ sets, such that the mth set of LEDs $(m \leq M)$ comprises $L_m \geq 1$ individual LEDs with the same color constraint. If applicable, the color constraint for the mth set of LEDs is assumed to be provided as

$$\mathbf{s}_m^{\text{avg}} = \left[s_{m,1}^{\text{avg}} \; s_{m,2}^{\text{avg}} \; \ldots \; s_{m,P}^{\text{avg}} \right]^T, \tag{1}$$

where $s_{m,p}^{\text{avg}}$ is the required average intensity level of the pth emitter of each of the LEDs in the mth set. (If the colors of the LEDs are to be unconstrained, we can assume $M = 1$, $L_1 = L$, and that $\mathbf{s}_1^{\text{avg}}$ is undefined.)

Information is to be transmitted to a receiver by signaling a sequence of data symbols from a size-N alphabet, where $N \geq 2$. Each data symbol is mapped to an average intensity level for each emitter that is to be output during a symbol period when communicating the given data symbol. The combination of these average intensity levels for all emitters and all data symbols is called the signaling constellation, and our goal is to design the signaling constellation to optimize communication performance while satisfying various system constraints.

There is freedom in designing the precise waveforms used to implement particular average intensity levels. Perhaps the most conceptually straightforward approach is to output a constant intensity equal to the desired average intensity level. An "integrate-and-dump" operation at the receiver, for example, can then output a discrete-time sequence of estimates of average intensity levels. However, the nonlinear dependence of LED output power on driving current [12], as well as chromaticity shifts with driving current [33], can complicate such a design. An alternative approach employs pulse-width modulation (PWM) at the transmitter, such that a particular average symbol intensity level is implemented by driving an emitter at full power for an appropriate fraction of the symbol period. An "integrate-and-dump" operation at the receiver could again recover the corresponding average intensity levels.

Finally, we note that the modulation format described above is quite general and subsumes many standard approaches. For example, CSK constellations considered in [28] are of the above form with $L = 1$, $M = 3$, and a constant constraint on the combined emitter intensities for each constellation point. Similarly, a class of wavelength division multiplexing (WDM) modulation formats can be described as a subset of the constellation design space obtained as the Cartesian product of individual signaling constellations on each emitter. For example, the use of OOK independently (though synchronously) on each of three emitters can be expressed (with a suitable mapping from bits to symbols) by the 3-D constellation $\{0,1\} \times \{0,1\} \times \{0,1\}$. Although this WDM constellation may be optimal (with respect to all 8-point constellations) on an ideal channel when constellation-design constraints are not imposed, it might be suboptimal on impaired channels (with, e.g., cross-channel leakage) or not an option when design constraints are considered for a particular application. In any case, an optimized constellation (under whatever constraints that are imposed by the application and/or designer) will theoretically perform at least as well as any such modulation subclass (subject to those same constraints).

B. Channel Model

Let $S_m = \{\mathbf{s}_{m,1}, \mathbf{s}_{m,2}, \ldots, \mathbf{s}_{m,N}\}$, $1 \le m \le M$, denote the signaling constellation for the mth set of LEDs, where $\mathbf{s}_{m,n} \triangleq [s_{m,n,1}\ s_{m,n,2}\ \ldots\ s_{m,n,P}]^T$ is the nth symbol employed by the mth LED group and $s_{m,n,p}$ is the average intensity level output by the pth emitter for that data symbol. The overall signaling constellation is then the collection $S = (S_1, S_2, \ldots, S_M)$ of the constellations of the LED sets. Since the $s_{m,n,p}$ are intensities, we require $s_{m,n,p} \ge 0$. Similarly, there is a maximum intensity $s_p^{\max} > 0$ that can be output by each emitter, and, therefore, we require $s_{m,n,p} \le s_p^{\max}$ for all m, n, and p. Next, an average color constraint for the mth LED group, if applicable, implies that

$$\mathbf{s}_m^{\text{avg}} = \frac{1}{N} \sum_{n=1}^{N} \mathbf{s}_{m,n}, \tag{2}$$

where we have assumed equally likely data symbols, either from probabilistic arguments or through deterministic enforcement with a suitable line code. Note that the use of N-CSK for each LED set is just one particular case of the above signaling format in which the constant intensity property of CSK is expressed by the additional requirement that, for each m and n,

$$\frac{1}{P} \sum_{p=1}^{P} s_{m,n,p} = c_m, \tag{3}$$

where the c_m are given nonnegative CSK intensity levels.

A receiver comprising $Q \ge 1$ photodetectors measures the combined average intensity of the LEDs during each symbol period, where each photodetector is designed to respond to a particular range of wavelengths of incident light. This can be accomplished in practice with a light-separating mechanism (e.g., a prism or diffraction grating [34]) or a series of optical filters; our discussion will assume the latter for brevity, although our results apply in either case. The choice of $Q = P$ is common, but increasing Q can allow for enhanced interoperability with differing transmitter designs and improved robustness with respect to channel and noise conditions. Each of the Q receiver channels outputs a weighted superposition of the average transmitted LED intensities, where the weighting is determined by the matching between the emission spectra of the transmitter LEDs and the receiver optical filter and photodetector responses. Even in the case where the receiver channels are designed to be nominally in a one-to-one correspondence with the P emitters (e.g., an RGB system with $Q = 3$), the nonzero bandwidth and out-of-band transmission of LEDs and nonideal filters can result in cross-channel leakage.

Based on the above receiver structure, we model a received symbol $\mathbf{r}_n \in \mathbb{R}^Q$ when the nth transmitter symbol is sent as

$$\mathbf{r}_n = \sum_{m=1}^{M} w_m \mathbf{H} \mathbf{s}_{m,n} + \mathbf{v}, \tag{4}$$

where $\mathbf{H}$ is a $Q \times P$ channel matrix, $w_m \ge 0$ is a weighting factor, $\mathbf{v}$ is a length-Q vector of zero-mean Gaussian random noise with covariance $\mathbf{\Sigma} \triangleq E\{\mathbf{v}\mathbf{v}^T\}$, and $E\{\cdot\}$ denotes expectation. (Noise with nonzero mean can be accommodated in a straightforward manner.) The channel matrix $\mathbf{H}$ can model the previously described cross-channel leakage, as well as the possibility of different subchannel gains due to, e.g., variation with wavelength in filter attenuation and detector responsivity. The w_m may simply account for the number of LEDs in each group (i.e., $w_m = L_m/L$), or they may model other effects (e.g., the varying orientation of LEDs with respect to the receiver) that can cause unequal detection of the output of different LED groups.

Meanwhile, $\mathbf{v}$ models the contribution to the received signal from all noise sources, such as ambient shot noise and thermal noise (which are well-modeled as Gaussian), as well as noise resulting from random or nonrandom fluctuations of optical noise sources, including incandescent, fluorescent, and LED lighting and LEDs in displays or other VLC systems. While the effects of some of these sources may be mitigated through, e.g., filtering, the sheer number and variety of sources challenge the design of systems that are fully robust to *a priori* unknown operating conditions. While the Gaussian model for many of these

noise sources is only an approximation, it can be shown that the constellation design problem discussed in the next section is more-generally applicable to noise distributions that (possibly after a linear transformation of the noise) can be approximated as circularly symmetric and unimodal. Furthermore, the Gaussian noise model can be considered as a conservative choice when a precise characterization of the noise is unavailable or as a simplifying approximation when the known distribution of noise is unmanageable, in either case producing reasonable (albeit, potentially suboptimal) results.

Although the above model does not address intersymbol interference (ISI), we note that many approaches to mitigating ISI, such as equalization, yield an equivalent channel that can be approximated by (4), and so the framework developed here appears directly applicable. Being quite specific to the particular ISI compensation technique at hand, however, the study of such an approach is beyond the scope of this paper, though we consider it an important avenue of future research.

Now, one receiver approach involves estimating $\mathbf{\Sigma}$, either blindly or from training data. (Since we treat the Gaussian noise in general, we do not assume any particular form for $\mathbf{\Sigma}$; however, additional *a priori* information regarding $\mathbf{\Sigma}$ could certainly be used if available in a particular application.) With $\mathbf{\Sigma}$, the receiver can premultiply a received symbol by $\mathbf{\Sigma}^{-1/2}$ to orthonormalize the noise $\mathbf{v}$ (i.e., the covariance of $\mathbf{\Sigma}^{-1/2}\mathbf{v}$ is identity). From (4), premultiplication by $\mathbf{\Sigma}^{-1/2}$ results in a receiver constellation (i.e., the set of possible received symbols in the absence of noise) given by

$$R = \left\{ \sum_{m=1}^{M} w_m \mathbf{\Sigma}^{-1/2} \mathbf{H} \mathbf{s} : \mathbf{s} \in S \right\}. \tag{5}$$

A received symbol, expressible as an element of R in orthonormal additive white Gaussian noise (AWGN), can be optimally decoded to the receiver constellation symbol that is nearest in Euclidean distance, with the corresponding transmitted constellation point taken as the estimate of the transmitted symbol. Note that this procedure requires that the receiver determines R, either by estimating $\mathbf{H}$ and the w_m (using, e.g., training data) and applying (5) if the transmitter constellation points are known or by direct estimation of the location of the constellation points (using, e.g., clustering).

C. Constellation Design Problem

The transmitter is to design a signaling constellation that satisfies given design constraints and that optimizes communication performance for the channel and receiver structure described in Section II-B. The specific optimization problem to be addressed depends on the channel information that is available to the transmitter. Let

$$\tilde{\mathbf{H}} \triangleq \hat{\mathbf{\Sigma}}^{-1/2} \hat{\mathbf{H}} \tag{6}$$

be the composite channel matrix (including noise decorrelation) that is assumed by the transmitter, where $\hat{\mathbf{H}}$ and $\hat{\mathbf{\Sigma}}$ are estimates of $\mathbf{H}$ and $\mathbf{\Sigma}$, respectively. If feedback from the receiver is available, then the receiver can provide the transmitter with the estimates of $\mathbf{H}$ and $\mathbf{\Sigma}$ (or simply $\tilde{\mathbf{H}}$). Even if feedback is not available, the transmitter may still be able to compensate for certain channel impairments (e.g., mismatch between LED transmission spectra and filter responses) by considering nominal device specifications, possibly taking $\hat{\mathbf{\Sigma}} = \mathbf{I}_Q$ in the absence of *a priori* knowledge of the noise statistics (where, for $k \in \mathbb{N}$, $\mathbf{I}_k$ is the $k \times k$ identity matrix). Finally, if nominal device specifications are not available or if the transmitter is broadcasting to multiple receivers with different (or unknown) specifications, it can still be useful to consider an optimization problem with $\hat{\mathbf{H}} = \hat{\mathbf{\Sigma}} = \mathbf{I}_P$ so as to obtain a generic constellation that satisfies the design constraints and that is approximately optimal on a low-distortion channel. It should be clear, however, that the performance of the resulting design will depend on the quality of the channel estimation; performance results presented in this paper assume that $\tilde{\mathbf{H}} = \mathbf{\Sigma}^{-1/2}\mathbf{H}$.

Given $\tilde{\mathbf{H}}$ and a signaling constellation, the transmitter can estimate the associated receiver constellation R in (5) using

$$\check{\mathbf{r}}_n = \sum_{m=1}^{M} w_m \tilde{\mathbf{H}} \mathbf{s}_{m,n}, \tag{7}$$

where $\check{\mathbf{r}}_n$ is the estimated receiver constellation symbol corresponding to the nth transmitter constellation symbol of all the LED groups. Recall that, according to the assumed channel model, a received observation can be expressed as a receiver constellation symbol in orthonormalized AWGN. As such, we wish to maximize the minimum Euclidean distance between any two symbols of the receiver constellation, since, at least at high signal-to-noise ratio (SNR), the symbol-error rate (SER) of an orthonormal-AWGN channel is dominated by errors between receiver constellation points that are at minimum Euclidean distance. Hence, we seek

$$S^* = \arg\max_{S \in \mathbb{S}} \min_{n_1 \neq n_2} \left\| \check{\mathbf{r}}_{n_1} - \check{\mathbf{r}}_{n_2} \right\|^2, \tag{8}$$

where $\mathbb{S}$ is the set of signaling constellations satisfying a given set of design constraints.

III. Constellation Design Algorithm

We consider an optimization problem that is approximately equivalent to (8) involving a continuously differentiable objective function with affine constraints. We provide a compact description of the affine constraints to facilitate their incorporation into an optimization routine. We then describe the objective function that is amenable to solution by a standard nonlinear optimization method.

Let $\mathbf{x}$ be the optimization decision variable formed by stacking the vectors $[\mathbf{s}_{m,1}^T \ \mathbf{s}_{m,2}^T \ \ldots \ \mathbf{s}_{m,N}^T]^T$ from $m = 1$ to M. Also, let $\mathbf{x}^{\max} = \mathbf{1}_{MN} \otimes [s_1^{\max} \ s_2^{\max} \ \ldots \ s_P^{\max}]^T$, where, for $k \in \mathbb{N}$, $\mathbf{1}_k$ denotes a the length-k vector whose elements are all 1 and $\otimes$ denotes the Kronecker product. Then the nonnegativity and upper bound constraints on the symbol intensities can be expressed as

$$\begin{bmatrix} -\mathbf{I}_{MNP} \\ \mathbf{I}_{MNP} \end{bmatrix} \mathbf{x} \leq \begin{bmatrix} \mathbf{0}_{MNP} \\ \mathbf{x}^{\max} \end{bmatrix}, \tag{9}$$

where, for $k \in \mathbb{N}$, $\mathbf{0}_k$ is the length-k all-zero vector. Next, if average color constraints are to be imposed on the constellation

design as in (2), we require

$$\frac{1}{N}\left(\mathbf{I}_M \otimes \mathbf{1}_N^T \otimes \mathbf{I}_P\right)\mathbf{x} = [\mathbf{s}_1^{\text{avg}}\ \mathbf{s}_2^{\text{avg}}\ \ldots\ \mathbf{s}_M^{\text{avg}}]^T. \tag{10}$$

Similarly, if employed, the constant intensity constraint of CSK in (3) can be expressed as

$$\left(\mathbf{I}_{MN} \otimes \mathbf{1}_P^T\right)\mathbf{x} = [c_1\ c_2\ \ldots\ c_M]^T \otimes \mathbf{1}_N. \tag{11}$$

Now, analogous to [31], we substitute a summation for the minimization function in (8) to obtain a continuously differentiable objective function f. First, note that we can express $\check{\mathbf{r}}_n$ in terms of $\mathbf{x}$ as

$$\check{\mathbf{r}}_n(\mathbf{x}) = \sum_{m=1}^{M} w_m \tilde{\mathbf{H}} \mathbf{x}_{NP(m-1)+P(n-1)+1}^{NP(m-1)+Pn} \tag{12}$$

where, for a vector $\mathbf{z}$ and for k, $l \in \mathbb{N}$, we define $\mathbf{z}_k^l = [z_k\ z_{k+1}\ \ldots\ z_l]^T$. Then we let

$$f(\mathbf{x}) = \frac{1}{\beta}\ln \sum_{n_1 \neq n_2} \exp\left\{-\beta\left\|\check{\mathbf{r}}_{n_1}(\mathbf{x}) - \check{\mathbf{r}}_{n_2}(\mathbf{x})\right\|^2\right\}. \tag{13}$$

It is straightforward to show that [35]

$$\lim_{\beta\to\infty} f(\mathbf{x}) = -\min_{n_1 \neq n_2}\left\|\check{\mathbf{r}}_{n_1}(\mathbf{x}) - \check{\mathbf{r}}_{n_2}(\mathbf{x})\right\|^2. \tag{14}$$

So, we have obtained our approximately equivalent optimization problem of minimizing (13) for finite β subject to the applicable constraints of (9)–(11), which can be solved using a conventional nonlinear optimization method. In particular, we employ sequential quadratic programming (SQP) throughout [36].

Because (13) is nonconvex, the result of an optimization attempt might not be a global optimum [36], and so it is advisable, if possible, to select the best result from multiple optimization attempts with different (e.g., randomized) initial conditions. Also, since β is a parameter that inversely affects the rate of convergence and the quality of the objective function approximation, an iterative procedure has been suggested in which the optimization is performed with (e.g., exponentially) increasing values of β, where the solution for one value of β is used as the initial condition for the optimization with the next value of β [31], [35]. Since large values of β may be necessary to achieve a solution with a desired level of precision, the following equivalent expression can be useful to avoid underflow when evaluating $f(\mathbf{x})$:

$$f(\mathbf{x}) = -d_{\min}^2(\mathbf{x}) + \frac{1}{\beta}\ln \sum_{n_1 \neq n_2} \exp\left\{-\beta\left[\left\|\check{\mathbf{r}}_{n_1}(\mathbf{x}) - \check{\mathbf{r}}_{n_2}(\mathbf{x})\right\|^2 - d_{\min}^2(\mathbf{x})\right]\right\}, \tag{15}$$

where $d_{\min}^2(\mathbf{x}) = \min_{n_1 \neq n_2}\left\|\check{\mathbf{r}}_{n_1}(\mathbf{x}) - \check{\mathbf{r}}_{n_2}(\mathbf{x})\right\|^2$.

An efficient implementation of the optimization algorithm should incorporate the specific structure inherent in the general constellation design problem. Furthermore, a particular application may present the opportunity for additional algorithmic simplifications. For example, both [29] and [31] consider CSK design with $M = 1$ and an invertible channel matrix $\tilde{\mathbf{H}}$, allowing for the direct design of the receiver constellation, from which the transmitter constellation can be obtained via $\mathbf{s}_n = \tilde{\mathbf{H}}^{-1}\mathbf{r}_n$ for each n. This avoids N matrix-vector multiplications for each objective function evaluation.

Specific computational limits on the optimization routine can vary dramatically between potential applications. For example, one can employ the proposed design framework offline to improve the minimum distance of constellations prescribed by IEEE 802.15.7, thus incurring no direct added complexity during the operation of the communication system. At the other extreme, a real-time constellation design problem for a moving image display would likely involve a large value of M and a short run-time constraint on the optimization algorithm, and, as such, reduced complexity approximations could be required for tractability. (Note that the added complexity results primarily from the implementation of the optimization routine itself, which is most likely performed at the transmitter. The receiver design is not expected to be significantly affected.) An approximate approach in this case might involve clustering the M LED groups based on similar colors, performing an optimization based on the clusters, and then, for each LED group, translating and scaling the corresponding cluster constellation.

While such algorithmic simplifications and approximations can be addressed within the proposed framework, they can be highly dependent on the particular application at hand. Here, we focus on general aspects of the design framework and the potential communication performance that may be obtained through its application.

IV. Simulation Results

In this section, we illustrate several simulated examples of the proposed constellation design framework. We focus on relatively simple cases (e.g., ideal channels) so that the design results can be visually interpreted. Even in such simple cases, the resulting constellation designs can be unexpected and/or difficult to derive outside of the optimization framework, and this serves to emphasize the usefulness of the framework. Furthermore, we show that the resulting constellations can exhibit a significant performance enhancement over certain other competing approaches.

A. Constellation Design of 16-CSK

We begin by considering the design of 16-CSK ($N = 16$) constellations for a single RGB group ($M = 1$ and $P = 3$). In particular, we assume that $c_1 = 1$ and $s_p^{\max} = 1$ for all p. For this case, the design region is a 2-simplex, as illustrated in Fig. 1. The 16-CSK constellation design proposed by IEEE 802.15.7 [28] is shown in Fig. 2(a), which depicts the constraint region, the location of the constellation points (small filled circles), and larger unfilled circles with diameter

$$d = \min_{n_1 \neq n_2}\left\|\mathbf{s}_{1,n_1} - \mathbf{s}_{1,n_2}\right\| \tag{16}$$

around each constellation point. Note that the coordinate system represents a distance-preserving affine transformation of the 3-D RGB intensities such that, e.g., $\mathbf{s}_{1,n} = [1/3\ 1/3\ 1/3]^T$ corresponds to (0, 0).

Since the IEEE 16-CSK constellation does not incorporate channel precompensation, we consider $\tilde{\mathbf{H}} = \mathbf{I}_3$ to construct

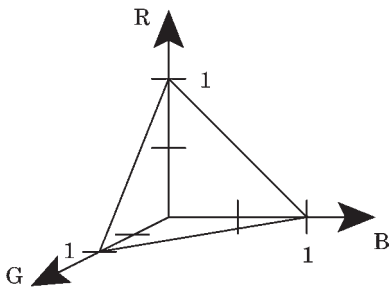

Fig. 1. Constraint region (2-simplex) for the CSK constellation designs of Section IV-A.

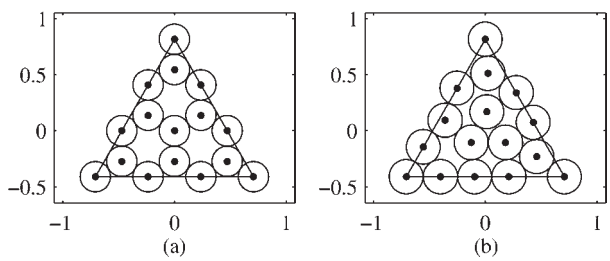

Fig. 2. Constellation designs for 16-CSK: (a) IEEE design and (b) optimized design.

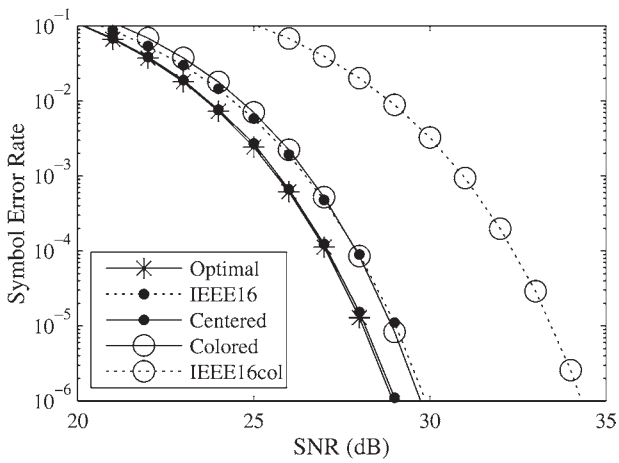

Fig. 3. Performance comparisons of 16-CSK constellation designs. Legend terminology is defined in the text.

a reasonably fair comparison with our design approach. The constellation design resulting from an unconstrained (i.e., $\mathbf{s}_1^{\text{avg}}$ undefined) optimization is shown Fig. 2(b). The improved minimum distance (0.3058 vs. 0.2722) is evident from the increased diameter of the unfilled circles around the constellation points.

Fig. 3 depicts the SER, obtained through Monte Carlo simulation, for several 16-CSK designs to be presented, including the previously discussed IEEE design ("IEEE16") and the optimized design ("Optimal"). The signal-to-noise ratio (SNR) is defined throughout as

$$\text{SNR} = \left\| \tilde{\mathbf{H}} \, [s_1^{\max} \; s_2^{\max} \; \ldots \; s_P^{\max}]^T \right\|^2 / (4\sigma^2), \tag{17}$$

where σ^2 is the variance of each component of the AWGN vector (after orthnormalization by $\hat{\Sigma}^{-1/2}$). We choose this SNR definition because it is does not depend on a particular constellation being studied (thus allowing for the comparison of different designs) and because it has the following property. If one interprets the (one LED group) signaling constellation of $\{\mathbf{0}_P, [s_1^{\max} \; s_2^{\max} \ldots s_P^{\max}]^T\}$ as a form of on-off keying (OOK), the above SNR definition yields the standard theoretical OOK performance result

$$\text{SER} = Q\left(\frac{d_{\text{OOK}}/2}{\sigma}\right) = Q\left(\sqrt{\frac{d_{\text{OOK}}^2}{4\sigma^2}}\right) = Q\left(\sqrt{\text{SNR}}\right), \tag{18}$$

where $d_{\text{OOK}} \triangleq \|\tilde{\mathbf{H}}[s_1^{\max} \; s_2^{\max} \; \ldots \; s_P^{\max}]^T\|$ is the distance between OOK constellation points and $Q(\cdot)$ is the tail probability of the standard Gaussian distribution [37].

As shown in Fig. 3, the optimized 16-CSK design performs nearly 1 dB better than the IEEE constellation at an SER of 10^{-4}. However, it should be noted that the average value (and, hence, expected perceived color) of the optimized design is slightly different than that of the IEEE design (which is "balanced" at $[1/3 \; 1/3 \; 1/3]^T$). To ensure a fair comparison, we also considered a constrained optimization with $\mathbf{s}_1^{\text{avg}} = [1/3 \; 1/3 \; 1/3]^T$. With a minimum distance of 0.3023, the optimized constrained constellation (not shown) is similar to the unconstrained design of Fig. 2(b). The associated performance curve labeled "Centered" in Fig. 3 is nearly identical to that of the unconstrained design, yielding a similar performance enhancement over the IEEE constellation.

IEEE 802.15.7 does not address modifications to the prescribed CSK constellation to account for the transmission of specific perceived colors (although it does address the related issue of dimming). A straightforward approach would be to consider an optimal translation and scaling of the unconstrained constellation to meet a given requirement. For a set S of vectors in $\mathbb{R}^P$, $a \in \mathbb{R}$, and $\mathbf{b} \in \mathbb{R}^P$, let $aS + \mathbf{b} = \{a\mathbf{s} + \mathbf{b} : \mathbf{s} \in S\}$. Then, for example, a modification of the IEEE 16-CSK constellation S_{IEEE16} for a perceived color requirement $\mathbf{s}_1^{\text{avg}} = [0.2 \; 0.4 \; 0.4]^T$ is given by $S_{\text{IEEE16col}} \triangleq 0.6 S_{\text{IEEE16}} + [0 \; 0.2 \; 0.2]^T$, where we have arbitrarily chosen the value of $\mathbf{s}_1^{\text{avg}}$ for illustrative purposes. The remaining two curves in Fig. 3 compare the performance of this constellation (labeled "IEEE16col") versus that of an optimized constellation (labeled "Colored") with the same perceived color requirement. The optimized design performs nearly 5 dB better at an SER of 10^{-4} than the "translate-and-scale" approach, demonstrating the value of using a more sophisticated design method.

B. Constellation Design of 8-ASK

We next consider constellation design without the CSK constraint. [We refer to the resulting modulation format as amplitude-shift keying (ASK) to emphasize that the combined intensity of the LED emitters over each symbol period is allowed to vary, but we reiterate that there is flexibility in implementation, such as by using PWM.] Suppose $M = 1$, $N = 8$, $P = 3$, $\tilde{\mathbf{H}} = \mathbf{I}_3$, and $s_p^{\max} = 1$ for all p, so that, in particular, the design region is the unit cube. It is straightforward to show that, in the absence of a perceived color constraint, the optimal constellation S_8 comprises the corners of the unit cube. Constraining the perceived color to $\mathbf{s}_1^{\text{avg}} = [s_{\text{avg}} \; s_{\text{avg}} \; s_{\text{avg}}]^T$ for some $0 < s_{\text{avg}} < 0.5$, it might seem reasonable to simply

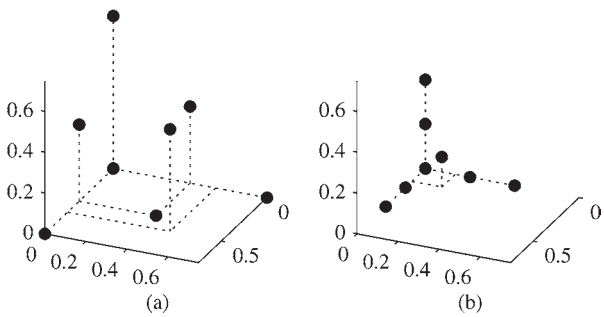

Fig. 4. Optimized 8-ASK constellations with average intensity constraints of (a) $[0.25\ 0.25\ 0.25]^T$ and (b) $[0.1\ 0.1\ 0.1]^T$.

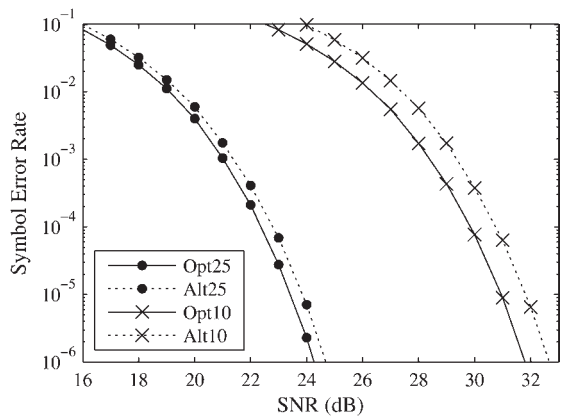

Fig. 5. Performance comparison of 8-ASK constellation designs with average-intensity constraints. Legend terminology is defined in the text.

choose the constellation $2s_{\text{avg}}S_8$, for which the minimum distance is simply $2s_{\text{avg}}$. However, the optimization approach yields alternative arrangements of the constellation points depending on the value of s_{avg}.

For example, Fig. 4(a) and (b) depict optimized ASK constellations for $s_{\text{avg}} = 0.25$ and $s_{\text{avg}} = 0.10$, respectively, with minimum distances of 0.5303 and 0.2182. We see again that even when considering a relatively simple scenario, there can be surprising complexity in the optimal constellation design. A performance comparison of the designs is shown in Fig. 5, where "Opt25" and "Opt10" refer respectively to the optimized designs with $s_{\text{avg}} = 0.25$ and $s_{\text{avg}} = 0.10$, and "Alt25" and "Alt10" refer respectively to constellations $2(0.25)S_8$ and $2(0.10)S_8$ (the corners of scaled unit cubes). At an SER of 10^{-4}, we see a performance improvement of over 0.4 dB for $s_{\text{avg}} = 0.25$ and nearly 0.9 dB for $s_{\text{avg}} = 0.10$.

C. Constellation Design for Two LED Groups

To demonstrate the challenge of constellation design as the complexity of a given scenario is increased slightly, we consider the 4-CSK $(N = 4)$ design of two LED groups $(M = 2)$. We suppose that each LED has three emitters $(P = 3)$, $\mathbf{w} = [1/3\ 2/3]^T$, and

$$\tilde{\mathbf{H}} = \begin{bmatrix} 1.0 & 0.1 & 0.0 \\ 0.3 & 0.6 & 0.2 \\ 0.1 & 0.8 & 0.2 \\ 0.0 & 0.2 & 1.0 \end{bmatrix}. \tag{19}$$

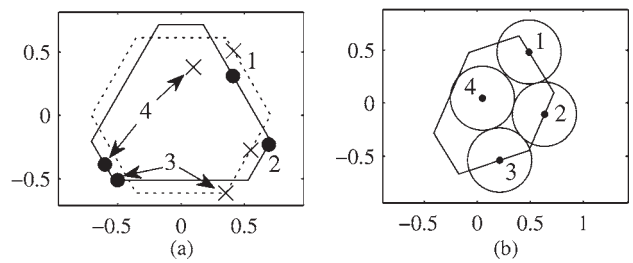

Fig. 6. Optimized constellation design for a scenario with two LED groups: (a) transmitter constellations for both groups and (b) the receiver constellation.

The matrix $\tilde{\mathbf{H}}$ captures the channel and noise features between the LED transmitters and the receiver, and with this information the constellation designs for the two LED groups can be jointly optimized. Finally, we assume that perceived color constraints are given by $\mathbf{s}_1^{\text{avg}} = [0.50\ 0.50\ 0.25]^T$ and $\mathbf{s}_2^{\text{avg}} = [0.25\ 0.75\ 0.50]^T$, implying that $c_1 = 1.25$ and $c_2 = 1.50$.

Fig. 6(a) depicts the transmitter constellations for both LED groups after performing distance-preserving affine transformations of each constellation to the same plane. The constellation for the first group of LEDs is shown with filled-in circles and the polygonal region satisfying the design constraints for the first group is bounded by a solid line. The corresponding elements for the second constellation are depicted with $\times$'s and a dashed line. (Note that the two design regions differ because $c_1 \neq c_2$ and that neither is a triangle because $s_p^{\max} = 1 < c_m$ for all m and p). Finally, the pair of constellation points (one from each group) corresponding to each transmitted symbol is indicated by a numbering of the associated pairs.

By inspection, it can be seen that neither constellation attempts to maximize its own minimum distance. In fact, we observe that $\mathbf{s}_{1,3} \approx \mathbf{s}_{1,4}$ [the constellation points near $(-0.5, -0.5)$]. However, the wide horizontal spacing between pairs of constellation points in the first LED group and the wide vertical spacing between different pairs of constellation points in the second LED group can combine in a superposition at the receiver to yield a good minimum distance in the receiver constellation, as depicted in Fig. 6(b). In this figure, we see the effect of the weighted superposition and the nonideal channel (i.e., $\tilde{\mathbf{H}} \neq \mathbf{I}_{\text{P}}$) on the constraint region (which is a polygon in $\mathbb{R}^4$). While it is difficult to evaluate the optimality of the receiver constellation even heuristically, the adjacency of the disks around each constellation point and the location of three of the constellation points on the constraint boundary provide some evidence of the quality of the design.

To evaluate the performance of this design, we compare it to the following alternative, which is based on the "translate-and-scale" approach of Section IV-A for modifying an existing constellation to satisfy a desired perceived color constraint. Let

$$S_{\text{IEEE4}} = \left\{[1\ 0\ 0]^T, [0\ 1\ 0]^T, [0\ 0\ 1]^T, [1/3\ 1/3\ 1/3]^T\right\} \tag{20}$$

denote the optimal 4-CSK constellation defined by IEEE 802.15.7. Then an alternative constellation design for the scenario at hand is given by

$$S_1 = 0.75 S_{\text{IEEE4}} + [0.25\ 0.25\ 0]^T \tag{21}$$

and

$$S_2 = 0.375 S_{\text{IEEE4}} + [0.125\ 0.625\ 0.375]^T. \qquad (22)$$

The minimum distance of the receiver constellation for this alternative design is 0.2972, whereas the corresponding minimum distance for the optimized design is 0.6052. This translates to greater than a 5-dB performance difference at an SER of 10^{-4}.

V. Experimental Results

A. System Description

To provide experimental validation of the performance benefits of using the proposed constellation-design framework, a VLC system was developed with constellation reprogrammability. The transmitter employed an RGB LED ($M = 1$ and $P = 3$) with nominal output of 69 lm, 109 lm, and 29 lm; nominal center wavelengths of 625 nm, 525 nm, and 465 nm; and nominal full-width half-maximum (FWHM) linewidths of 16 nm, 35 nm, and 24 nm, respectively. The emitters were modulated using PWM at a maximum chip rate f_c of approximately 4 MHz, where the chip rate is defined such that the pulse widths employed by the system are constrained to be multiples of $1/f_c$. A variable optical attenuator comprising a pair of crossed polarizers was placed directly in front of the LED to provide SNR control.

At the receiver, which was positioned about one meter from the transmitter, the red, green, and blue signals were separated by three optical bandpass filters with nominal center wavelengths of 620 nm, 530 nm, and 467 nm, all with a nominal FWHM bandwidth of 10 nm. The filtered signals were received by three photodetectors with nominal relative spectral sensitivities of 1.00, 0.65, and 0.43 at 625 nm, 525 nm, and 465 nm, respectively. Integrators performed PWM to ASK conversion on each channel, and the results were sampled by a 16-bit analog-to-digital converter at a maximum symbol rate of 1 MHz. The analog-to-digital conversion was performed by a National Instruments data acquisition device, which was also responsible for synchronization of the transmitter and receiver and for controlling data transfer between a personal computer (PC) and the VLC system components.

Desired signaling constellations were implemented through preprocessing of the transmitted data by the PC, which was also responsible for decoding received signals and computing SERs. In particular, respective estimates $\hat{\mathbf{H}}$ and $\hat{\mathbf{\Sigma}}$ of the channel matrix $\mathbf{H}$ and the noise covariance $\mathbf{\Sigma}$ were obtained using training data. The optimization of the transmitter constellation and the estimation of the SNR were based on the estimated composite channel $\tilde{\mathbf{H}} = \hat{\mathbf{\Sigma}}^{-1/2}\hat{\mathbf{H}}$. The designed constellations were quantized to 30 equally-spaced PWM levels per emitter and mapped to corresponding pulse widths. (It was found empirically that the choice of 30 levels resulted in a negligible effect on measured SERs.) To demodulate unknown data, received symbols were premultiplied by the decorrelation matrix $\hat{\mathbf{\Sigma}}^{-1/2}$ and the resulting noise-compensated symbols were decoded to the nearest (in Euclidean distance) receiver constellation point. The receiver constellation points themselves were estimated from the training data, but these estimates were also continually adapted during SER measurements based on decision feedback.

To verify the operation of the system, we measured the SER as a function of SNR when using the OOK signaling constellation $\{\mathbf{0}_3, \mathbf{1}_3\}$. The measured curve was in reasonable agreement with the theoretical prediction SER $= Q(\sqrt{\text{SNR}})$ [37]. For example, the measured performance was approximately 1 dB better than predicted at an SER of 10^{-4}. We attribute this relatively minor difference to deviation of the noise from a Gaussian distribution and the adaptation to temporal variations in the channel and noise by the experimental system, which is unaccounted for in the theoretical prediction. That the constellation design algorithm performs well (as will be seen in the following subsections) despite this deviation demonstrates robustness of our approach to model inaccuracies.

B. CSK Measurements

Here, we compare the performance of optimized 16-CSK and 8-CSK constellation designs relative to the corresponding constellations defined by IEEE 802.15.7. Because the LED spectra and the receiver filter responses are well matched and had relatively small bandwidths, we expect virtually no cross-channel leakage (as estimated from the nominal specifications). Indeed, prior to optimizing the 16-CSK constellation, the raw channel matrix was estimated as

$$\hat{\mathbf{H}} = \begin{bmatrix} 1.0000 & 0.0001 & 0.0003 \\ 0.0019 & 0.4583 & 0.0010 \\ 0.0015 & 0.0030 & 0.6300 \end{bmatrix}, \qquad (23)$$

from which we observe small off-diagonal elements. (While the diagonal elements appear reasonable, a precise comparison with estimates based on device specifications is not possible because of independent gain settings for each channel in the receiver.) However, the noise, which was dominated by standard fluorescent office lighting and illumination from a computer monitor (as empirically confirmed by comparing the received signal with each of these sources on and off), had significant channel coupling, as indicated by the following noise-covariance estimate:

$$\hat{\mathbf{\Sigma}} = \begin{bmatrix} 0.0370 & 0.0117 & 0.0131 \\ 0.0117 & 0.0047 & 0.0036 \\ 0.0131 & 0.0036 & 0.0178 \end{bmatrix}. \qquad (24)$$

The resulting composite channel exhibits significant cross-channel leakage:

$$\tilde{\mathbf{H}} = \alpha\hat{\mathbf{\Sigma}}^{-1/2}\hat{\mathbf{H}} = \begin{bmatrix} 0.5949 & -0.2805 & -0.0959 \\ -0.6068 & 1.0000 & -0.0311 \\ -0.1506 & -0.0230 & 0.3844 \end{bmatrix}, \qquad (25)$$

where α is an arbitrary scale factor. As such, we expect that precompensation of this channel has the potential to yield significant performance gains.

Fig. 7(a) illustrates the 16-CSK transmitter constellation designed to precompensate the above composite channel. Without accounting for the channel distortion, the constellation might appear to be suboptimal. However, the resulting receiver

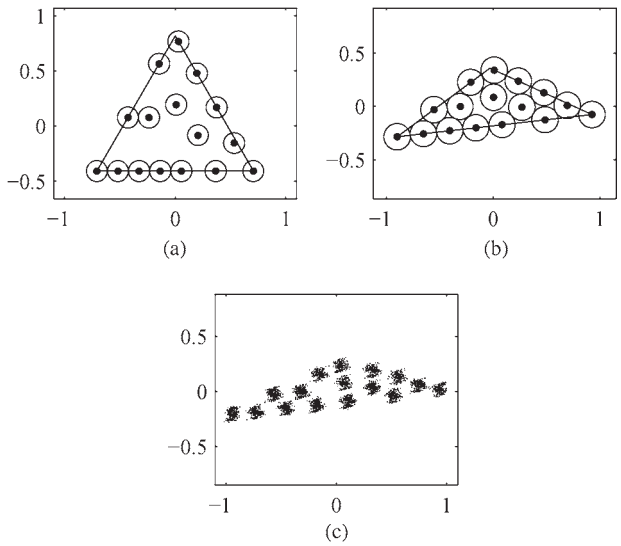

Fig. 7. Optimized 16-CSK constellations for the experimental system: (a) transmitter constellation design, (b) receiver constellation design, and (c) experimentally measured receiver constellation (with noise).

constellation depicted in Fig. 7(b) appears to exhibit a reasonably tight packing and a good minimum distance. Fig. 7(c) depicts experimental data received when transmitting with the proposed constellation design. The experimental data is in reasonable agreement with the theoretically predicted receiver constellation, with differences likely due in part to the projection chosen to visualize the 3-D data as a 2-D constellation.

Fig. 8(a) compares the measured performance of the optimized 16-CSK constellation ("Opt16") versus that of the IEEE 802.15.7 16-CSK constellation ("IEEE16"). Precompensation has yielded about 5.5 dB of performance improvement at an SER of 10^{-4}. Fig. 8(a) also shows an analogous comparison for 8-CSK ("Opt8" vs. "IEEE8"), and in this case we observe nearly a 3-dB performance difference. Such substantial gains motivate the use of precompensation for this experimental channel. Also, for further validation of the experimental system, Fig. 8(b) shows corresponding performance predictions for each constellation using simulated data based on the experimental estimates of the channel and noise statistics. As noted previously, minor variations between experimental and simulated results are observed, but similar conclusions regarding the performance enhancement exhibited by the optimized constellations can be drawn in each case.

C. ASK Measurements

Finally, we revisit the 8-ASK scenario simulated in Section IV-B, but in this case we consider the experimental channel described in Section V-B, optimizing the transmitter constellations accordingly. In particular, we again consider average color constraints of $\mathbf{s}_1^{\text{avg}} = [0.25\ 0.25\ 0.25]^T$ and $\mathbf{s}_1^{\text{avg}} = [0.10\ 0.10\ 0.10]^T$ and implement optimized (for the channel at hand) constellations ("Opt25" and "Opt10", respectively). For comparison, we also implemented the corresponding unoptimized ASK constellations ("ASK25" and "ASK10", respectively) from Section IV-B. Additionally, we considered the average color constraint of $\mathbf{s}_1^{\text{avg}} = [0.50\ 0.50\ 0.50]^T$. In

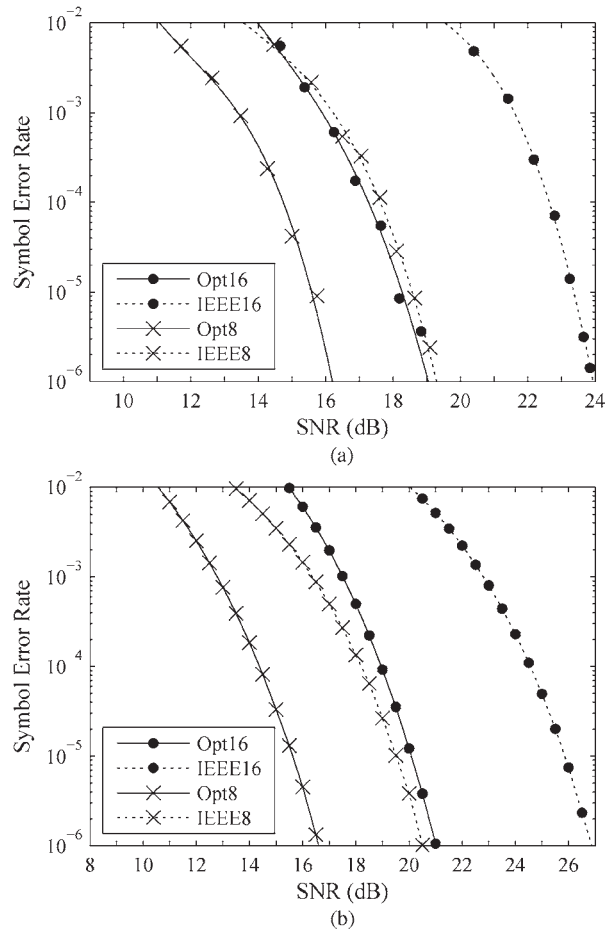

Fig. 8. Performance comparison of 16-CSK and 8-CSK constellation designs for an experimental channel: (a) experimentally measured performance and (b) performance based on corresponding simulated data. Legend terminology is defined in the text.

this last case, the ASK constellation ("ASK50") comprising the corners of the unit cube is optimal for an ideal channel (i.e., $\tilde{\mathbf{H}} = \mathbf{I}_3$), and so any performance improvement by the optimized constellation ("Opt50") is entirely attributable to precompensation of the channel.

Fig. 9 describes the measured performance of the various ASK constellations. For each of the average color constraints, we observe that the optimized constellation outperforms the corresponding unoptimized constellation by at least approximately 2 dB at an SER of 10^{-4}, and by nearly 5 dB in the case of $\mathbf{s}_1^{\text{avg}} = [0.25\ 0.25\ 0.25]^T$.

VI. Conclusion

We have described an optimization framework for the design of multi-wavelength VLC signaling constellations that precompensate for linear channel distortions arising from, e.g., wavelength-dependent signal/noise power, cross-channel signal leakage, and/or cross-channel noise correlation. The constellation design problem was cast in a general setting, allowing for the consideration of CSK constraints, multiple perceived color constraints (on different groups of LEDs), and arbitrary numbers of emitters and detectors. With an appropriate objective

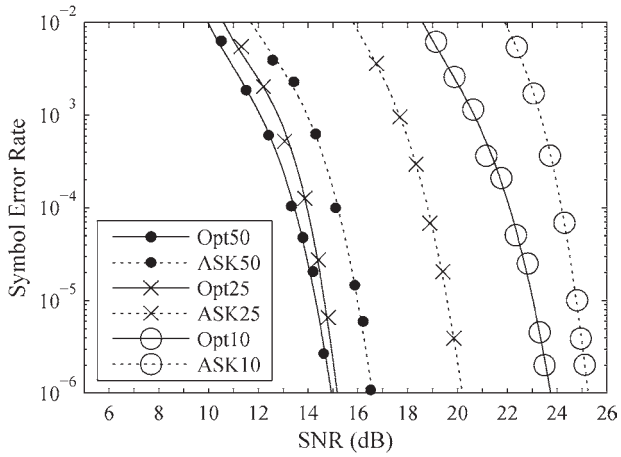

Fig. 9. Experimental performance comparison of constrained-average ASK constellation designs. Legend terminology is defined in the text.

function approximation, the well-known optimization method SQP was proposed to solve the general design problem.

Simulated design examples demonstrated optimized constellations and the performance improvement that they can achieve over competing approaches, even in the absence of channel distortions. Finally, measurements made using an experimental VLC system provide real-world validation of the design framework. Although pertaining to specific channels, the simulation and experimental results provide strong evidence of the potential benefit of constellation optimization. Future research directions include the study of practical SQP implementations (with, e.g., reduced computational complexity or fixed-point arithmetic) for constellation optimization and the incorporation of ISI compensation.

Acknowledgment

The authors thank P. Fisher for designing the VLC system hardware.

References

[1] J. K. Kim and E. F. Schubert, "Transcending the replacement paradigm of solid-state lighting," *Opt. Exp.*, vol. 16, no. 26, pp. 21 835–21 837, Dec. 2008.

[2] L. Hanzo *et al.*, "Wireless myths, realities, futures: From 3G/4G to optical and quantum wireless," *Proc. IEEE*, vol. 100, pp. 1853–1888, May 2012.

[3] J. Grubor, S. Randel, K.-D. Langer, and J. W. Walewski, "Broadband information broadcasting using LED-based interior lighting," *J. Lightw. Technol.*, vol. 26, no. 24, pp. 3883–3892, Dec. 2008.

[4] C. Quintana, V. Guerra, J. Rufo, J. Rabadan, and R. Perez-Jimenez, "Reading lamp-based visible light communication system for in-flight entertainment," *IEEE Trans. Consum. Electron.*, vol. 59, no. 1, pp. 31–37, Feb. 2013.

[5] N. Kumar, D. Terra, N. Lourenço, L. N. Alves, and R. L. Aguiar, "Visible light communication for intelligent transportation in road safety applications," in *Proc. 7th Int. Wireless Commun. Mobile Comput. Conf.*, 2011, pp. 1513–1518.

[6] Z. Jia, "A visible light communication based hybrid positioning method for wireless sensor networks," in *Proc. Int. Conf. Intell. Syst. Design Eng. Appl.*, 2012, pp. 1367–1370.

[7] I. Rust and H. H. Asada, "A dual-use visible light approach to integrated communication and localization of underwater robots with application to non-destructive nuclear reactor inspection," in *Proc. IEEE Int. Conf. Robot. Autom.*, 2012, pp. 2445–2450.

[8] J. Park, "Speedup of dynamic response of organic light-emitting diodes," *J. Lightw. Technol.*, vol. 28, no. 19, pp. 2873–2880, Oct. 2010.

[9] C.-L. Tsai, C.-T. Yen, W.-J. Huang, Z.-F. Xu, and S.-C. Ko, "InGaN-based resonant-cavity light-emitting diodes fabricated with a Ta_2O_5/SiO_2 distributed Bragg reflector and metal reflector for visible light communications," *J. Display Technol.*, vol. 9, no. 5, pp. 365–370, May 2013.

[10] C.-L. Liao, Y.-F. Chang, C.-L. Ho, and M.-C. Wu, "High-speed GaN-based blue light-emitting diodes with gallium-doped ZnO current spreading layer," *IEEE Electron Device Lett.*, vol. 34, no. 5, pp. 611–613, May 2013.

[11] T. Komine and M. Nakagawa, "Fundamental analysis for visible-light communication system using LED lights," *IEEE Trans. Consum. Electron.*, vol. 50, no. 1, pp. 100–107, Feb. 2004.

[12] I. Neokosmidis, T. Kamalakis, J. W. Walewski, B. Inan, and T. Sphicopoulos, "Impact of nonlinear LED transfer function on discrete multitone modulation: Analytical approach," *J. Lightw. Technol.*, vol. 27, no. 22, pp. 4970–4978, Nov. 2009.

[13] S. Arnon, "The effect of clock jitter in visible light communication applications," *J. Lightw. Technol.*, vol. 30, no. 21, pp. 3434–3439, Nov. 2012.

[14] J. Grubor, V. Jungnickel, K.-D. Langer, and C. von Helmolt, "Dynamic data-rate adaptive signal processing method in a wireless infra-red data transfer system," U.S. Patent Appl. 20110110661, May 12, 2011.

[15] O. Gonazález, R. Pérez-Jiménez, S. Rodríguez, J. Rabadán, and A. Ayala, "OFDM over indoor wireless optical channel," *IEE Proc. Optoelectron.*, vol. 152, no. 4, pp. 199–204, Aug. 2005.

[16] M. Z. Afgani, H. Haas, H. Elgala, and D. Knipp, "Visible light communication using OFDM," in *Proc. 2nd Int. Conf. Testbeds Res. Infrastruct. Develop. Netw. Commun.*, 2006.

[17] L. Zeng *et al.*, "High data rate multiple input multiple output (MIMO) optical wireless communications using white LED lighting," *IEEE J. Sel. Areas Commun.*, vol. 27, no. 9, pp. 1654–1662, Dec. 2009.

[18] T. Komine, J. H. Lee, S. Haruyama, and M. Nakagawa, "Adaptive equalization system for visible light wireless communication utilizing multiple white LED lighting equipment," *IEEE Trans. Wireless Commun.*, vol. 8, no. 6, pp. 2892–2900, Jun. 2009.

[19] S. H. Lee and J. K. Kwon, "Turbo code-based error correction scheme for dimmable visible light communication systems," *IEEE Photon. Technol. Lett.*, vol. 24, no. 17, pp. 1463–1465, Sep. 2012.

[20] S. Kim and S.-Y. Jung, "Modified Reed-Muller coding scheme made from the bent function for dimmable visible light communications," *IEEE Photon. Technol. Lett.*, vol. 25, no. 1, pp. 11–13, Jan. 2013.

[21] J. P. Ding and Y. F. Ji, "Evolutionary algorithm-based optimisation of the signal-to-noise ratio for indoor visible-light communication utilising white light-emitting diode," *IET Optoelectron.*, vol. 6, no. 6, pp. 307–317, Dec. 2012.

[22] K. Lee and H. Park, "Modulations for visible light communications with dimming control," *IEEE Photon. Technol. Lett.*, vol. 23, no. 16, pp. 1136–1138, Aug. 2011.

[23] G. Ntogari, T. Kamalakis, J. W. Walewski, and T. Sphicopoulos, "Combining illumination dimming based on pulse-width modulation with visible-light communications based on discrete multitone," *IEEE J. Opt. Commun. Netw.*, vol. 3, no. 1, pp. 56–65, Jan. 2011.

[24] J. Vuĉić *et al.*, "White light wireless transmission at 200+ mb/s net data rate by use of discrete-multitone modulation," *IEEE Photon. Technol. Lett.*, vol. 21, no. 20, pp. 1511–1513, Oct. 2009.

[25] F.-M. Wu *et al.*, "1.1-Gb/s white-LED-based visible light communication employing carrier-less amplitude and phase modulation," *IEEE Photon. Technol. Lett.*, vol. 24, no. 19, pp. 1730–1732, Oct. 2012.

[26] A. H. Azhar, T.-A. Tran, and D. O'Brien, "A gigabit/s indoor wireless transmission using MIMO-OFDM visible-light communications," *IEEE Photon. Technol. Lett.*, vol. 25, no. 2, pp. 171–174, Jan. 2013.

[27] G. Cossu, A. M. Khalid, P. Choudhury, R. Corsini, and E. Ciaramella, "Long distance indoor high speed visible light communication system based on RGB LEDs," in *Proc. Asia Commun. Photon. Conf.*, 2012, pp. 1–3.

[28] S. Rajagopal, R. D. Roberts, and S.-K. Lim, "IEEE 802.15.7 visible light communication: Modulation schemes and dimming support," *IEEE Commun. Mag.*, vol. 50, no. 3, pp. 72–82, Mar. 2012.

[29] R. J. Drost and B. M. Sadler, "Constellation design for color-shift keying using billiards algorithms," in *Proc. IEEE GLOBECOM Workshops*, 2010, pp. 980–984.

[30] R. L. Graham and B. D. Lubachevsky, "Dense packings of equal disks in an equilateral triangle: From 22 to 34 and beyond," *Electron. J. Combinatorics*, vol. 2, no. 1, pp. 1–39, 1995.

[31] E. Monteiro and S. Hranilovic, "Constellation design for color-shift keying using interior point methods," in *Proc. IEEE GLOBECOM Workshops*, 2012, pp. 1224–1228.

[32] E. Reinhard, E. A. Khan, A. O. Akyüz, and G. M. Johnson, *Color Imaging: Fundamentals and Applications*. Wellesley, MA, USA: A K Peters, Ltd., 2008, pp. 439–444.

[33] M. Dyble, N. Narendran, A. Bierman, and T. Klein, "Impact of dimming white LEDs: Chromaticity shifts due to different dimming methods," in *Proc. SPIE*, 2005, pp. 291–299.
[34] R. Shiraki, "Illumination light receiver and illumination light communications system," U.S. Patent 12 403 782, Nov. 1, 2011.
[35] R. Chen, "Solution of minimax problems using equivalent differentiable functions," *Comput. Math. Appl.*, vol. 11, no. 12, pp. 1165–1169, Dec. 1985.
[36] J. Nocedal and S. J. Wright, *Numerical Optimization*, 2nd ed. New York, NY, USA: Springer-Verlag, 2006, pp. 529–562.
[37] R. M. Gagliardi and S. Karp, *Optical Communications*, 2nd ed. New York, NY, USA: Wiley-Interscience, 1995, pp. 181–191.

Robert J. Drost (M'10) received the B.S. degree in electrical engineering from the University of Arkansas, Fayetteville, AR, USA, in 2000 and the M.S. degree in electrical engineering, the M.S. degree in mathematics, and the Ph.D. degree in electrical and computer engineering from the University of Illinois at Urbana-Champaign, Champaign, IL, USA, in 2002, 2005, and 2007, respectively.

From 2007 to 2009, he was a Digital Signal Processing Design Engineer with Finisar Corporation. He joined the Army Research Laboratory (ARL) in 2010 as a Postdoctoral Fellow and, subsequently, an Electronics Engineer. He has authored several journal and conference papers, receiving the 2013 ARL Honorary Award for Publication. He has also authored two patent applications and has participated as a reviewer and panelist for major organizations such as NSF and IEEE. His research interests include optical communications, signal processing, and graphical models.

Brian M. Sadler (S'81–M'81–SM'02–F'07) received the B.S. and M.S. degrees from the University of Maryland, College Park, MD, USA, and the Ph.D. degree from the University of Virginia, Charlottesville, VA, USA, all in electrical engineering.

He is a Fellow of the Army Research Laboratory (ARL) in Adelphi, MD, USA. His research interests include information science, networked and autonomous systems, sensing, and mixed-signal integrated circuit architectures.

Dr. Sadler is an associate editor for IEEE TRANSACTIONS ON SIGNAL PROCESSING and EURASIP Signal Processing, was an associate editor for IEEE SIGNAL PROCESSING LETTERS, and has been a guest editor for several journals including IEEE JSTSP, IEEE JSAC, the IEEE SP Magazine, and the International Journal of Robotics Research. He is a member of the IEEE Signal Processing Society Sensor Array and Multi-channel Technical Committee and Co-Chair of the IEEE Robotics and Automation Society Technical Committee on Networked Robotics. He received Best Paper Awards from the Signal Processing Society in 2006 and 2010. He has received several ARL and Army R&D awards, as well as a 2008 Outstanding Invention of the Year Award from the University of Maryland.

Simple and efficient absorption filter for single photons from a cold atom quantum memory

Daniel T. Stack, Patricia J. Lee, and Qudsia Quraishi

Optics Express, 23 (2015)

Simple and efficient absorption filter for single photons from a cold atom quantum memory

Daniel T. Stack, Patricia J. Lee, and Qudsia Quraishi
Quantum Sciences Group, Army Research Laboratory, Adelphi, Maryland 20783, USA
*qudsia.quraishi.civ@mail.mil

Abstract: The ability to filter unwanted light signals is critical to the operation of quantum memories based on neutral atom ensembles. Here we demonstrate an efficient frequency filter which uses a vapor cell filled with ^{85}Rb and a buffer gas to attenuate both residual laser light and noise photons by nearly two orders of magnitude with little loss to the single photons associated with our cold ^{87}Rb quantum memory. This simple, passive filter provides an additional 18 dB attenuation of our pump laser and erroneous spontaneous emissions for every 1 dB loss of the single photon signal. We show that the addition of a frequency filter increases the non-classical correlations and the retrieval efficiency of our quantum memory by $\approx 35\%$.

© 2015 Optical Society of America

OCIS codes: (270.0270) Quantum optics; (190.4223) Nonlinear wave mixing; (270.5585) Quantum information and processing; (270.5565) Quantum communications.

References and links

1. C. H. Bennet and G. Brassard, "Quantum cryptography: public key distribution, and coin-tossing," Proc. 1984 IEEE International Conference on Computers, Systems, and Signal Processing, 175–179 (1984).
2. N. Gisin, G. Ribordy, W. Tittel, and H. Zbinden, "Quantum cryptography," Rev. Mod. Phys. **74**(1), 145–195 (2002).
3. H. J. Kimble, "The quantum internet," Nature **453**(7198), 1023–1030 (2008).
4. M. A. Nielsen and I. L. Chuang, *Quantum Computation and Quantum Information*, (Cambridge University Press 2013).
5. P. Komar, E. M. Kessler, M. Bishof, L. Jiang, A. S. Srensen, J. Ye, and M. D. Lukin, "A quantum network of clocks," Nat. Phys. **10**(8), 582–587 (2014).
6. H.-J. Briegel, W. Dur, J. I. Cirac, and P. Zoller, "Quantum repeaters: the role of imperfect local operations in quantum communication," Phys. Rev. Lett. **81**(26), 5932–5935 (1998).
7. S. Olmschenk, D. Hayes, D. N. Matsukevich, P. Maunz, D. L. Moehring, and C. Monroe, "Quantum logic between distant trapped ions," Int. J. Quantum Info. **08**(01n02), 337–394 (2010).
8. D. N. Matsukevich and A. Kuzmich. "Quantum state transfer between matter and light," Science **306**(5696), 663–666 (2004).
9. T. Wilk, A. Gatan, C. Evellin, J. Wolters, Y. Miroshnychenko, P. Grangier, and A. Browaeys, "Entanglement of two individual neutral atoms using rydberg blockade," Phys. Rev. Lett. **104**(1), 010502 (2010).
10. L. Li, Y. O. Dudin, and A. Kuzmich, "Entanglement between light and an optical atomic excitation," Nature **498**(7455), 466–469 (2013).
11. B. Zhao, M. Muller, K. Hammerer, and P. Zoller, "Efficient quantum repeater based on deterministic rydberg gates," Phys. Rev. A **81**(5), 052329 (2010).
12. C. Nolleke, A. Neuzner, A. Reiserer, C. Hahn, G. Rempe, and S. Ritter, "Efficient teleportation between remote single-atom quantum memories," Phys. Rev. Lett. **110**(14), 140403 (2013).
13. M. Kroutvar, Y. Ducommun, D. Heiss, M. Bichler, D. Schuh, G. Abstreiter, and J. J. Finley, "Optically programmable electron spin memory using semiconductor quantum dots," Nature **432**(7013), 81–84 (2004).
14. K. C. Lee, M. R. Sprague, B. J. Sussman, J. Nunn, N. K. Langford, X.-M. Jin, T. Champion, P. Michelberger, K. F. Reim, D. England, D. Jaksch, and I. A. Walmsley, "Entangling macroscopic diamonds at room temperature," Science **334**(6060), 1253–1256 (2011).

15. A. Kuzmich, W. P. Bowen, A. D. Boozer, A. Boca, C. W. Chou, L.-M. Duan, and H. J. Kimble, "Generation of nonclassical photon pairs for scalable quantum communication with atomic ensembles," Nature **423**(6941), 731–734 (2003).
16. Y. O. Dudin, L. Li, and A. Kuzmich, "Light storage on the time scale of a minute," Phys. Rev. A **87**(3), 031801 (2013).
17. L.-M. Duan, M. D. Lukin, J. I. Cirac, and P. Zoller, "Long-distance quantum communication with atomic ensembles and linear optics," Nature **414**(6862), 413–418 (2001).
18. D. Braje, V. Balic, S. Goda, G. Yin, and S. Harris, "Frequency mixing using electromagnetically induced transparency in cold atoms," Phys. Rev. Lett. **93**(18), 183601 (2004).
19. C. Kupchak, T. Mittiga, B. Jordaan, M. Namazi, C. Nolleke, and E. Figueroa, "Room-temperature quantum memory for polarization states," arXiv:1405.6117 [quant-ph] (2014).
20. X. Fernandez-Gonzalvo, G. Corrielli, B. Albrecht, M. Grimau, M. Cristiani, and H. de Riedmatten. "Quantum frequency conversion of quantum memory compatible photons to telecommunication wavelengths," Opt. Express **21**(17), 19473–19487 (2013).
21. J. Camparo, "The rubidium atomic clock and basic research," Phys. Today **60**(11), 33–39 (2007).
22. M. D. Eisaman, L. Childress, A. André, F. Massou, A. S. Zibrov, M. D. Lukin. "Shaping quantum pulses of light via coherent atomic memory," Phys. Rev. Lett. **93**(23), 233602 (2004).
23. A. Heifetz, A. Agarwal, G. C. Cardoso, V. Gopal, P. Kumar, and M.S. Shahriar, "Super efficient absorption filter for quantum memory using atomic ensembles in a vapor," Opt. Commun. **232**(1-6), 289–293 (2004).
24. S. Manz, T. Fernholz, J. Schmiedmayer, and J.-W. Pan, "Collisional decoherence during writing and reading quantum states," Phys. Rev. A **75**(4), 040101 (2007).
25. M. Bashkansky, F. K. Fatemi, and I. Vurgaftman, "Quantum memory in warm rubidium vapor with buffer gas," Opt. Lett. **37**(2), 142–144 (2012).
26. P. W. Milonni and J. H. Eberly, *Laser Physics* (John Wiley & Sons, 2010).
27. D. A Steck, Rubidium 87 d line data, 2001.
28. B. M. Sparkes, J. Bernu, M. Hosseini, J. Geng, Q. Glorieux, P. A. Altin, P. K. Lam, N. P. Robins, and B. C. Buchler. "Gradient echo memory in an ultra-high optical depth cold atomic ensemble," New J. Phys. **15**(8), 085027 (2013).

1. Introduction

Distribution of entangled quantum states over significant distances is important to the development of future quantum technologies such as long-distance cryptography, networks of atomic clocks, distributed quantum computing, etc. [1–5]. Quantum repeaters can overcome the problems of exponential losses in direct transmission of single photons over quantum channels through entanglement swapping of remotely placed quantum memories via single photon detection [6]. Long-lived quantum memories and single photon sources are building blocks for systems capable of efficiently and securely transferring quantum information over extremely long distances. Quantum memories are a very active area of research with many different quantum systems as viable candidates, including ions [7], neutral atom ensembles [8], Rydberg atoms [9–11], single neutral atoms [12], quantum dots [13], and nitrogen vacancy centers [14]. Cold ensembles of neutral atoms are a favorable platform for quantum memories and single photon sources as they can store single excitations in long-lived ground states that lead to extremely long coherence times [15, 16].

The ability to store and retrieve single excitations efficiently and background-free is crucial to building quantum memories based on neutral atom ensembles [17]. The generation (retrieval) of these excitations usually requires a strong laser beam to create a coherent excitation in the atomic ensemble that can be heralded (read out) by the detection of a single photon from the ensemble. The detection of classical pump photons at the single photon detector is a source of error in standard quantum communication protocols that needs to be eliminated. This strong pump can be filtered by a variety of means: spatial, polarization, frequency, etc. Spatial filtering is achieved using the off-axis geometry in a cold atomic ensemble pioneered in [18]. By aligning the single photon arms a few degrees off-axis from the pump arms, noise suppression > 40 dB is possible, usually limited by scattering off the surfaces near the memory. Polarization filtering is accomplished by post-selecting single photons that are orthogonally polarized to the

corresponding pump fields using properly aligned waveplates and polarizing optical elements. Birefringence of optical elements and imperfect polarizers usually limit noise suppression to ~ 40 dB as well [19]. Optical cavities [12], optically pumped atomic vapor cells [15], and fiber Bragg gratings [20] are just a few examples of frequency selective elements that have been used in various quantum memory experiments to reject sources of noise. It is possible to achieve extremely high levels of noise rejection (> 100 dB) though usually at the cost of lower transmission probability ($\approx 10\%$) [19]. Each of these frequency filters require complicated electronics, significant temperature stabilization, external references, or additional lasers.

In this paper, we show how the serendipitous near degeneracy of spectral lines in ^{85}Rb and ^{87}Rb allow one to construct an efficient frequency filter for both the classical pump beams and erroneous atomic decays in a neutral atom quantum memory, without strong filtering of the desired signal that herald the creation of these coherent excitations. To accomplish this we use the two naturally-occurring isotope of rubidium, ^{87}Rb for use as a quantum memory and a vapor cell filled with isotopically-pure ^{85}Rb to filter the pump photons associated with this process (Fig. 1). By properly choosing the correct transition in ^{87}Rb for the creation of spin-waves, the frequency of the Write beam and Noise single photons are nearly resonant with a transition in ^{85}Rb, while the single photons that are correlated to the created spin-waves are much further detuned from any transition in ^{85}Rb. The Noise single photons arise from spontaneous decays back to the original ground state ($5S_{1/2}, F = 2$). This method for filtering radiation is well known in the atomic clock community [21], and has been used in warm vapor quantum memory experiments previously [22–25]. Such a filter cell is attractive due to its relative simplicity, without the need for an optical reference to lock an external cavity, drifts from cavities or etalons, significant temperature stabilization, or additional lasers for optical pumping.

First, we build a simple model to predict the utility of such a filter under conditions that can be verified experimentally. Then, we perform an experiment where the filter is used to block spontaneously emitted photons not associated with the creation of spin-waves, which would contribute to a reduced retrieval efficiency. The result is a quantum memory with higher retrieval efficiency, hence higher single photon rates and greater nonclassical correlations.

2. Theory

To construct a frequency filter that is capable of attenuating the undesired background radiation it will be necessary to calculate the strength and the lineshape of the filter as a function of vapor cell temperature and buffer gas pressure. In the limit that the frequency of the input light is much more narrow-band (roughly the atomic linewidth $\Gamma/2\pi \approx 5.8$ MHz) than the bandwidth of the frequency filter ($\gg 100$ MHz) [26],

$$\frac{I_{OUT}(z)}{I_{IN}} = e^{-a(\delta,T,P)z} \tag{1}$$

where $a(\delta,T,P)$is the attenuation per unit length that depends on the detuning from the nearest resonance line δ, temperature of the filter cell T, and buffer gas pressure P, while z is the length of the filter cell. The lineshape of the filter function may depend on both the inhomogeneous broadening due to the Doppler effect of atoms at a temperature T with a characteristic FWHM of $\delta\nu_D(T)$ and the homogeneous broadening due to collisions with a buffer gas at pressure P with a characteristic FWHM of $\gamma(P)$. The vapor cell filter is considered in two limits: when Doppler effects dominate and when atomic collisions dominate.

In the Doppler-broadened case:

$$a(T) = f(T)\exp[\frac{-4\ln 2\delta_i^2}{(\delta\nu_D(T))^2}] \tag{2}$$

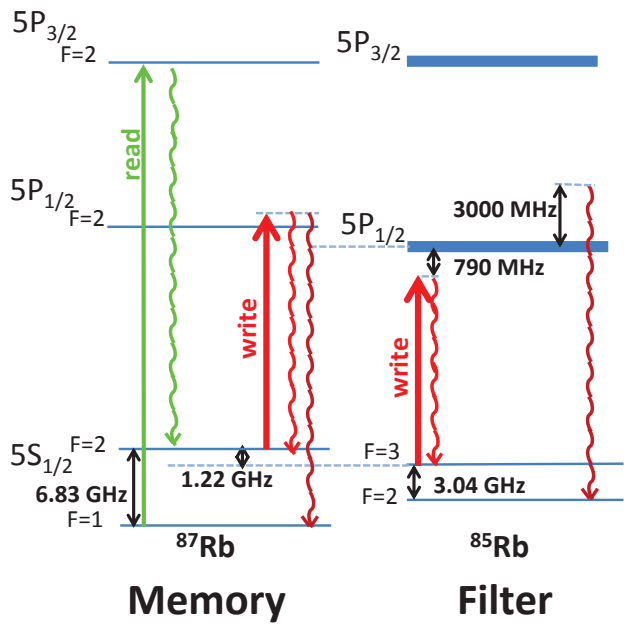

Fig. 1. The relevant energy levels and transitions of ^{87}Rb and ^{85}Rb used in this paper. The write beam is 20, 40, or 60 MHz blue-detuned from the $5S_{1/2}, F = 2 \rightarrow 5P_{1/2}, F = 2$ (D1) transition. Atoms excited to the $5P_{1/2}, F = 2$ state can decay to either the $5S_{1/2}, F = 1$ or the $5S_{1/2}, F = 2$ ground state in ^{87}Rb. The write beam and the emission from the $5P_{1/2}, F = 2 \rightarrow 5S_{1/2}, F = 2$ state are detuned from the Doppler-broadened $5S_{1/2}, F = 3 \rightarrow 5P_{1/2}$ transition in ^{85}Rb by $\approx$ 790 MHz. The emission from the $5P_{1/2}, F = 2 \rightarrow 5S_{1/2}, F = 1$ state is detuned from the Doppler-broadened $5S_{1/2}, F = 2 \rightarrow 5P_{1/2}$ transition in ^{85}Rb by $\approx$ 3000 MHz. This difference in the detuning of these transitions serves as the basis for using a ^{85}Rb vapor cell as a frequency filter in our quantum memory experiment. The read beam is resonant with the $5S_{1/2}, F = 1 \rightarrow 5P_{3/2}, F = 2$ (D2) transition in ^{87}Rb. Drawing not to scale.

where $f(T)$ is proportional to the vapor cell atom number and increases exponentially with cell temperature [27], $\delta\nu_D(T)$ is the Doppler-broadened FWHM of the ^{85}Rb lines, and δ_i is either the Noise or Signal frequency detuning from the nearest ^{85}Rb resonance shown in Fig. 1(a).

One would like a simple/passive frequency filter for strong attenuation of unwanted background radiation with weak attenuation of the signal photons associated with the created spin waves. Figure 2(a) shows that an optically thick vapor cell of pure ^{85}Rb with no buffer gas would accomplish this due to the exponential falloff of the filter strength as a function of δ^2 and the detuning of the light associated with the desired transition is roughly four times further detuned than the light associated with the undesired transition (790 MHz vs 3000 MHz). However, contamination of the cell with a small amount of near-resonant ^{87}Rb can have a significant effect on the attenuation of the Signal photons. If the ratio of ^{87}Rb/^{85}Rb is on the order of a few times 10^{-3} (which is roughly the level of purification available commercially) this will result in roughly equal attenuation of the Noise photons by ^{85}Rb and Signal photons by ^{87}Rb, negating the utility of the frequency filter in Fig. 2(b). It is therefore prudent to consider the frequency filter in the presence of a buffer gas to see if the effect of ^{87}Rb can be mitigated.

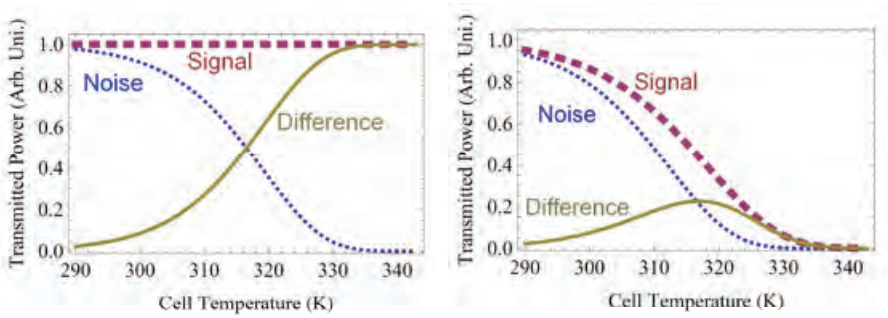

(a) (b)

Fig. 2. Plots of the transmitted light through the vapor cell filter as a function of temperature in the Doppler-broadened limit (Eq. (2)) for a filter cell length of 1 inch. **(a)** The pure ^{85}Rb filter cell acts nearly perfectly by attenuating the undesired light strongly (blue, dotted) and no attenuation of the signal (magenta, dashed) leading to large difference in attenuation between the two signals (gold, solid). **(b)** Small concentrations of ^{87}Rb (^{87}Rb/^{85}Rb fraction of 0.2%) result in strong attenuation of the resonant background and signal fields. The emission from the cold ^{87}Rb ensemble is assumed to be hyperfine specific but the absorption by the warm ^{85}Rb vapor cell transitions are assumed to be Doppler-broadened and not hyperfine specific (See Fig. 1).

In the pressure-broadened case [26]:

$$a(T,P) = f(T)\frac{\alpha P}{\pi(\delta_i - \beta P)^2 - (\frac{\alpha P}{2})^2} \tag{3}$$

where β is the coefficient for the linear frequency shift with a value of -6.7 MHz/Torr and α is the linear coefficient for the pressure-broadened linewidth with a value of 21 MHz/Torr at $T = 300$ K for the D1 transition due to collisions of Rb with an Argon buffer gas. Since we will only vary the temperature of the vapor cell by $\sim 10\%$ it will be a good approximation to say that these pressure-dependent coefficients are constant as a function of temperature. Figure 3 is a plot of Eq. (1) with $a(T,P)$ from Eq. (3) which shows how the introduction of 47 Torr of an Ar buffer gas changes the filter response as a function of vapor cell temperature. The Ar pressure of 47 Torr was chosen such that the filter could be modeled in the pressure-broadened limit ($\alpha P > \delta\nu_D$) where the filter is most effective. Increasing the buffer gas pressure significantly would dilute the filter strength by broadening the filter response function.

Signal absorption decreases from the Doppler-broadened filter (Fig. 2(b)) to the pressure-broadened filter (Fig. 3) due to the differences between the Gaussian and Lorentzian lineshapes of their absorption profiles respectively. The Signal is absorbed strongly in the Doppler-broadened filter due to the strong central peak of the Gaussian-shaped absorption profile of the near-resonant ^{87}Rb present in the vapor cell filter. Whereas, the Lorentzian lineshape of the pressure-broadened vapor cell contains significantly more absorption in the wings of its profile and less near resonance thus leading to less Signal absorption in the presence of a buffer gas. For Noise photons, the weakening of the ^{87}Rb component in the pressure-broadened filter is counterbalanced by an increase of filter strength of the far-detuned ^{85}Rb component as one transitions from a Gaussian absorption profile to a Lorentzian absorption profile. The result is a frequency filter that absorbs Noise photons more strongly than Signal photons. From Fig. 3 one can extract an 18 dB attenuation from the Noise for every 1 dB attenuation of the Signal over the range of filter cell temperatures measured. Disagreements between data and theory at

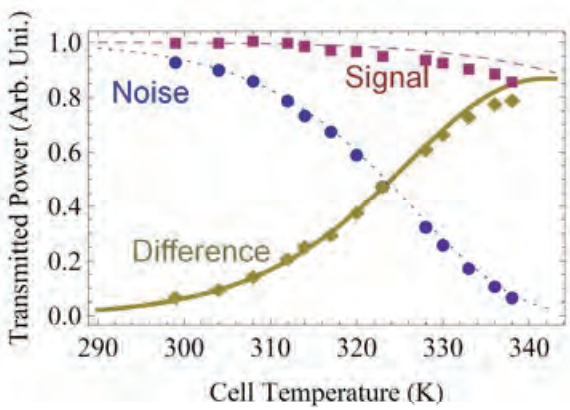

Fig. 3. Normalized measured transmission of classical laser light at the Noise (circles) and Signal (squares) frequencies and the difference between the two signals (diamonds) at a variety of vapor cell temperatures with 47 Torr of Ar in a 1 inch long ^{85}Rb vapor cell. The corresponding solid lines are calculations of the transmitted light through the vapor cell filter as a function of temperature with 47 Torr of Ar using the filter response from Eq. (3).

higher filter cell temperatures may be explained by either violations of assumptions made in our simple model (such as temperature independent $\gamma(P)$) or greater ^{87}Rb contamination in the vapor cell than the specification from the manufacturer (^{87}Rb/^{85}Rb $\approx 0.2\%$)

The optimum operating temperature for the vapor cell filter should correspond to roughly the maximum difference between the Signal and Noise if one assumes roughly equal contributions of Signal and Noise before the frequency filter. This strikes a balance between increasing the Retrieval Efficiency and $g^{(2)}$ correlations (strong attenuation of Noise) while maximizing the coincident count rate (weak attenuation of Signal). With a buffer gas of sufficient pressure and high enough operating temperature it is possible to achieve significant attenuation of the background light with only a small amount of signal loss.

3. Experimental results and methods

3.1. Neutral atom quantum memory

A magneto-optical trap (MOT) of ^{87}Rb atoms produces an optically thick atomic ensemble for our experiment (Fig. 4(a)). Approximately 25 mW/cm^2 of cooling light, detuned 15 MHz below the $5S_{1/2}, F = 2 \rightarrow 5P_{3/2}, F = 3$ transition in ^{87}Rb, and 5 mW of repump light, on resonance with the $5S_{1/2}, F = 1 \rightarrow 5P_{3/2}, F = 2$ transition, are delivered collinearly to the vacuum system. Loading from a room-temperature Rb vapor, a cloud of $\sim 1.8 \times 10^8$ atoms at a temperature of $\sim$100 μK is produced in roughly 5 seconds with a magnetic field gradient of 10 G/cm (subsequent reloading of the MOT is performed in 30 ms as seen in Fig. 4(b)). This is then followed by a compressed MOT stage that consists of simultaneously lowering the intensity of the repump and increasing the gradient of the quadrupole magnetic field to 22 G/cm for 6 ms before turning the field off. The cooling light is turned off 100 μs later, and the repump light 2 μs after that, leaving all of the atoms in the $5S_{1/2}, F = 2$ ground state.

A sequence of 1000 trials with individual durations of $\sim 1\,\mu s$ is performed as follows: a weak, linearly-polarized, Write pulse, tuned 20, 40, or 60 MHz above the $5S_{1/2}, F = 2 \rightarrow 5P_{1/2}, F = 2$ (See Fig. 1) transition is shone on the atomic ensemble. The Write pulse has a 400 μm waist and 50 ns duration set by acousto-optical modulator and an electro-optic modulator. For low

enough excitation probability ($10^{-2} - 10^{-4}$) a photon detection within an 80 ns time interval at Si avalanche photodiode (APD) A heralds the transfer of one ^{87}Rb atom in the ensemble from the $F = 2$ ground state to the $F = 1$ ground state in a particular spatial mode. The polarization of the generated single photon is post-selected to be orthogonal to the Write pulse with appropriate waveplates and linear polarizers. After a hold time of 200 ns, a strong, linearly-polarized (orthogonal to the Write), resonant Read pulse of duration 300 ns and 400 μm waist interacts with the ensemble, producing a photon that is detected by APD B within a 100 ns window. The generated photon has a polarization orthogonal to the Read pulse. The single photon detection arms are aligned at an angle of 3° relative to the classical pump beams. By aligning the single photon arms a few degrees off-axis from the pump arms, the pump light is suppressed by a measured value of ≈ 40 dB in the single photon detection arms. The APD signals are sent to a time-interval analyzer (TIA) for data collection and analysis.

The strength of the correlations between the photon-pairs generated by the atomic ensemble can be measured by the normalized intensity cross-correlation function:

$$g^{(2)}_{A,B} = \frac{p_{AB}}{p_A p_B} = \frac{RE}{p_B} \tag{4}$$

where p_{AB} is the probability to detect a photon pair, p_i is the probability for an event click at detector i, and RE is the retrieval efficiency defined as p_{AB}/p_A. A plot of $g^{(2)}_{A,B}$ over a range of different write probabilities, p_A, is shown in Fig. 4(c). Figure 4(c) shows a series of measurement of $g^{(2)}_{A,B}$ over a range of values for p_A ($10^{-2} - 10^{-4}$) with $\Delta_w/2\pi = 20$ MHz and a constant filter cell temperature of 336 K. The value of $g^2_{A,B}$ saturates at low p_A due to dark counts in the APDs and contamination of the readout arm by classical Read light. The transmission values for the Noise and Signal photons in Fig. 3 at a filter cell temperature of 336 K are 12% and 88% respectively. The filter cell attenuates the Noise photons significantly which increases the measured F and $g^{(2)}_{A,B}$ for a given p_A while not significantly attenuating the Signal photons. Attenuation of the Signal photons would lead directly to a decrease in the coincidence probability, p_{AB}, an undesirable outcome for entanglement creation and entanglement swapping operations.

3.2. Filtering single photon noise

In this section we study the effect of a ^{85}Rb filter on the operation of a cold ^{87}Rb quantum memory. This was done by varying the temperature of AR-coated vapor cell filled with isotopically-pure ^{85}Rb and 47 Torr of Argon from 298 K to 336 K. Based upon Fig. 3 we would expect the presence of ^{85}Rb vapor cell filter to have only a small effect on the quantum memory parameters (p_A, F, $g^{(2)}_{A,B}$) at an operating temperature of 298 K. At this temperature the filter cell absorbs only 10% of the Noise photons and less than 1% of the Signal photons. However, as the filter cell temperature is increased, an increasing percentage of Noise photons (pump and emitted) are filtered by the cell with corresponding decreases in p_A and increases in F and $g^{(2)}_{A,B}$. Figure 5(a) shows the decrease in write probability as a function of filter cell temperature. For $\Delta_w/2\pi = 20$ MHz the Write probability decreases from a value of 6.5×10^{-4} to 5×10^{-4} as the filter cell temperature is increased from 298 K to 336 K. For Write detunings of 40 MHz and 60 MHz the Write probability decreases from 7×10^{-4} to 5×10^{-4} over the same temperature range. Most of this decrease can be attributed to the vapor cell filter absorption of Noise photons emitted by the cold ensemble taking into account the results of Fig. 3. At a filter cell temperature of 336 K only 6% of Noise photons are transmitted through the vapor cell while $> 85\%$ of Signal photons are transmitted. The vapor cell also filters out pump photons from the Write beam that scatter off of the vacuum system glass walls. However the effect on the quantum memory parameters is minimal because the pump contamination in the Write detection

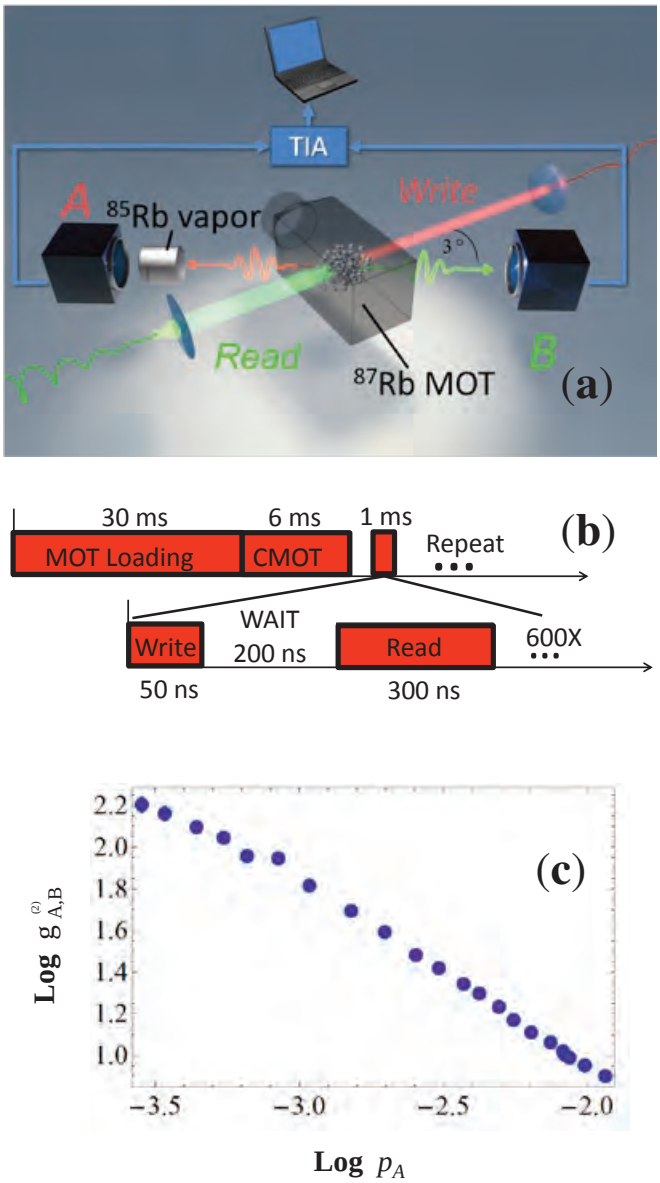

Fig. 4. **(a)** Counter-propagating Write and Read light pulses interact with a cold ^{87}Rb ensemble while emitted single photons are detected off-axis by Si APDs. Arrival times of the photons are measured by a time-interval analyzer (TIA). Emitted Write photons are filtered by a warm ^{85}Rb vapor cell to attenuate Noise photons. **(b)** A MOT is loaded and compressed to create a cold, dense cloud at a rate of 27 Hz. The MOT magnetic and laser fields are then extinguished for a 1 ms duration and a series of 600 Read-Write pulses interact with the system. **(c)** Log-Log plot of $g^2_{A,B}$ as a function of p_A with filter cell at 336 K and $\Delta_w/2\pi = 20$ MHz. Write probability (p_A) is varied from $10^{-2} - 10^{-4}$ and the corresponding values of $g^2_{A,B}$ increase from ≈ 8 to > 160.

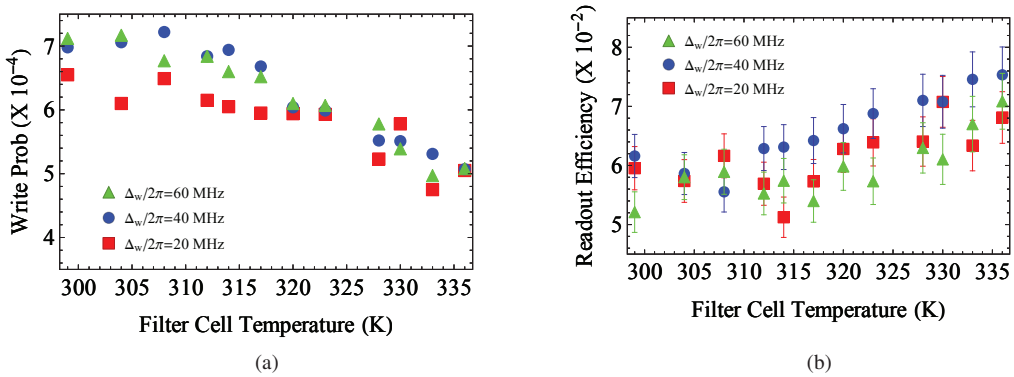

(a) (b)

Fig. 5. Probability of detecting a write photon and Retrieval Efficiency as a function of the filter cell temperature for $\Delta_w/2\pi$ =20, 40, and 60 MHz. **(a)** The write probability decreases by $\approx 40\%$ over the range of filter cell temperatures used in this experiment for each write beam detuning. **(b)** A significant increase in Retrieval Efficiency as the filter cell temperature is increased is observed. The decrease in Noise photon detection in the Write arm leads to an $\approx 35\%$ increase in the Retrieval Efficiency for $\Delta_w/2\pi = 40$ and 60 MHz and $\approx 15\%$ for $\Delta_w/2\pi = 20$ MHz. Each point in plots (a) and (b) correspond to ~ 10000 write detection events and ~ 500 coincident counts respectively. The running time required to obtain a single data point is ≈ 12 minutes. Error bars are calculated assuming Poissonian statistics.

arm is only $\sim 1 \times 10^{-5}$. Since the filter cell has little effect on the coincident counts between detectors A and B, there is then a corresponding increase of $\approx 35\%$ in the measured Retrieval Efficiency as seen in Fig. 5(b) for $\Delta_w/2\pi = 40$ and 60 MHz and $\approx 15\%$ for $\Delta_w/2\pi = 20$ MHz. Retrieval Efficiency increases from 6% to 7% for a Write detuning of 20 MHz, from 5.8% to 7.5% for a Write detuning of 40 MHz, and 5.5% to 7% for a Write detuning of 60 MHz.

Any change in the Retrieval Efficiency due to the vapor cell filter necessarily should lead to a change in $g^{(2)}_{A,B}$ as the filter cell has no effect on p_B. Following the increases in F seen in Fig. 5(b), a similar $\approx 35\%$ increase in the value of $g^{(2)}_{A,B}$ for $\Delta_w/2\pi = 40$ and 60 MHz is seen in Fig. 6 as the absolute values of $g^{(2)}_{A,B}$ increase from 95 to 130 and 100 to 135 respectively. For $\Delta_w/2\pi = 20$ MHz a smaller increase in $g^{(2)}_{A,B}$ of $\approx 15\%$ (from 95 to 110) corresponds closely to the similar increase of F seen in Fig. 5(b) as well.

The difference in the performance of the vapor cell filter for the three write detunings can be partially explained by effective optical depth of the atomic ensemble at different Write beam detunings. Based upon $\Delta_w/2\pi = 20$ MHz (3.3Γ) and a measured $\mathrm{OD}_{res} = 12$ for the atomic ensemble, one would expect an effective optical depth of the cloud for the created photons to be $\mathrm{OD}_{3.3\Gamma} \approx 0.24$ from the equation: $\mathrm{OD}_\Delta = \mathrm{OD}_{res}(1+(2\Delta/\Gamma)^2)^{-1}$ [28]. However that assumes the emitted single photons interact with the entire ensemble. The probability for excitation is proportional to the atomic density which is largest in the center of the ensemble. As a consequence, the average single photon would only see half the atoms in the cloud. The resulting OD (≈ 0.12) leads to $\approx 11\%$ attenuation of Noise single photons emitted by the ensemble. For the dataset with $\Delta_w/2\pi = 40$ (60) MHz there is only 3% (1%) attenuation of Noise single photons due to the smaller effective optical depth from the larger detuning. Since there are slightly more Noise photons for the larger Write detuning, the vapor cell has a relatively larger effect

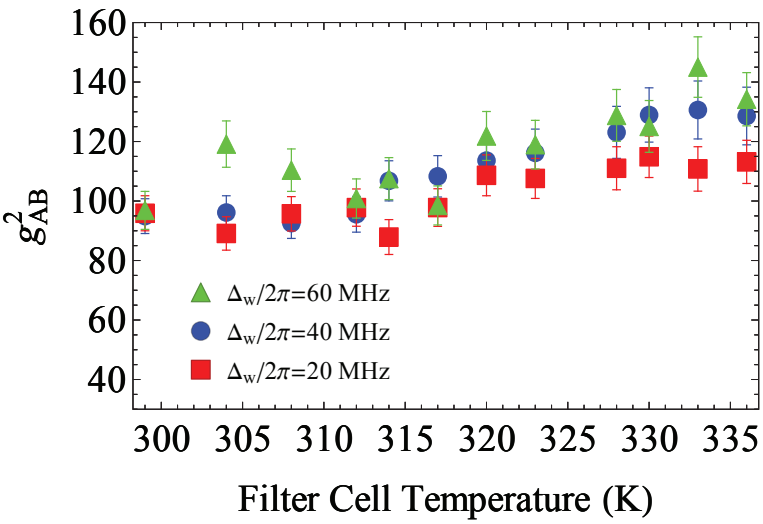

Fig. 6. $g^{(2)}_{A,B}$ correlations as a function of filter cell temperature for $\Delta_w/2\pi$ =20, 40 and 60 MHz. The strength of the correlations increase by $\approx 15\%$ for $\Delta_w/2\pi = 20$ MHz, $\approx 35\%$ for $\Delta_w/2\pi = 40$ MHz, and $\approx 35\%$ for $\Delta_w/2\pi = 40$ MHz. The increase in non-classical correlations follows directly from the increase in Retrieval Efficiency seen in Fig. 5. Error bars are calculated assuming Poissonian statistics.

on the write probability, retrieval efficiency, and non-classical correlations for $\Delta_w/2\pi = 40$ and 60 MHz.

4. Conclusions

In this paper we have shown how a temperature-controlled vapor cell filled with isotopically-pure ^{85}Rb filled with 47 Torr of Ar buffer gas increases the Retrieval Efficiency and the non-classical correlations between the single photons emitted from the cold ^{87}Rb ensemble. The filter cell achieves a substantial reduction in the detection of Noise photons by frequency-selective absorption with little effect on the detection of Signal photons. Our model showed that a buffer gas in the vapor cell was required to eliminate the detrimental effect of the ^{87}Rb contamination in commercially available isotopically-pure ^{85}Rb vapor cells. Our experiments showed that for Write detunings of 40 and 60 MHz the measured Retrieval Efficiency and $g^{(2)}_{A,B}$ of our quantum memory increased by $\approx 35\%$ as the filter cell temperature was tuned from 298 K to 336 K due to the significant decrease in the detection of Noise photons. Less dramatic effects were seen for a Write detuning of 20 MHz which were partially explained by the detuning-dependent optical depth of the cold atomic ensemble. These results are important to maximizing the operating parameters that are critical to the realization of a quantum network based on neutral atom quantum memories.

Acknowledgments

We would like thank N. Solmeyer, D. Matsukevich, and A. Gorshkov for discussions on the quantum memory and P. Kunz for discussions on the vapor cell. DS is an Oak Ridge Associated Universities (ORAU) postdoctoral fellow. Research was sponsored by the Army Research Laboratory. The views and conclusions contained in this document are those of the Authors and should not be interpreted as representing the official policies, either expressed or implied, of the Army Research Laboratory or the U.S. Government. The U.S. Government is authorized to reproduce and distribute reprints for Government purposes notwithstanding any copyright notation herein.

Biographies of ARL Authors

Kwong-Kit Choi is a Senior Research Scientist for Physical Sciences in Sensors and Electron Devices Directorate at ARL. His research focus is devoted to the invention and development of the next generation of advanced sensors and imagers for full spectrum of Army operations; such as in night vision, missile and unmanned aerial systems defense, and helicopter navigation. He also works with NASA in space applications. Dr. Choi received his B.S. from Hong Kong University in 1979 and Ph.D. from Yale University in 1984. After working at Princeton University and AT&T Bell Laboratories, he joint ARL in 1988. Dr. Choi is a Fellow of ARL, American Physical Society, and IEEE, and he is also a member of SPIE. He is an inductee of NASA Space Technology Hall of Fame and a recipient of Distinguished Presidential Rank Award.

Frank De Lucia received his B.S. in Chemistry from Indiana University in 1996, a M.S. in Analytical Chemistry from the Ohio State University in 1999, and a Ph.D. in Analytical Chemistry from the Ohio State University in 2002. He started at the US Army Research Laboratory as a National Research Council Post-Doctoral Fellow in 2002 and was hired in 2003. He is currently a research chemist within the Lethality Division at ARL. In 2009, Dr. De Lucia was a co-recipient of a Research and Development Award for "Stand-off Detection of Explosives." He was the principal investigator for one of the top three FY07 ARL Director's Research Initiative projects (FY07-WMR-04, "Tailored Ultrafast Pulses for Selective Energetic Residue Sampling") and co-investigator for one of the top four FY09 DRI projects (FY09-WMR-03, "Investigation of Chemical Processes Involving Laser-Generated Nanoenergetic Materials"). Dr. De Lucia has written or contributed to 35 peer-reviewed papers and been an invited speaker at four international conferences. His most recent research interest is in the investigation of transient excited states that occur during the initiation of energetic material using ultrafast pump probe experiments. Understanding these excited state dynamics could lead to new pathways for increased chemical energy release. Past research involves elucidating the influence molecular structure and composition has on laser induced plasma emissions in order to discriminate explosives from non-explosives via laser induced breakdown spectroscopy.

Robert J. Drost received the B.S. degree in electrical engineering from the University of Arkansas, Fayetteville, AR, USA, in 2000 and the M.S. degree in electrical engineering, the M.S. degree in mathematics, and the Ph.D. degree in electrical and computer engineering from the University of Illinois at Urbana-Champaign, Champaign, IL, USA, in 2002, 2005, and 2007, respectively. From 2007 to 2009, he was a Digital Signal Processing Design Engineer with Finisar Corporation. He joined the Army Research Laboratory (ARL) in 2010 as a Postdoctoral Fellow and, subsequently, an Electronics Engineer. He has authored several journal and conference papers, receiving the 2013 ARL Honorary Award for Publication. He has also authored two patent applications and has participated as a reviewer and panelist for major organizations such as NSF and IEEE. His research interests include optical communications, signal processing, and graphical models.

Mark Dubinskiy is an expert known for his contributions to advanced solid-state laser development in industry, academia and Government. He has authored over 210 papers, presentations and book chapters. He served as a Program Committee Member, Session Chair and Conference Co-Chair and Chair for a great number of international conferences. Currently he is a Physicist and a Team Leader with the US Army Research Laboratory, where he continues to develop new laser concepts, architectures and advanced laser components geared toward highly efficient high energy solid-state lasers and great variety of advanced tactical lasers applications. For his contributions in laser technology development at ARL he has been honored with the 2007 ARL Honorary Award in Science, the 2008 and 2010 U.S. Army Research and Development Achievement Awards. Dr. Dubinskiy is a Fellow of the Optical Society of America, SPIE Fellow and a Distinguished Member of the ARL Technical Staff – ARL Fellow. He also is a member of the Directed Energy Professional Society.

Ryan W. Enck is an electronics engineer in the Electro-optics and Photonics Division in the Sensor and Electron Devices Directorate at the US Army Research Laboratory. His expertise is in the growth of III-Nitride films by Plasma Assisted Molecular Beam Epitaxy (PAMBE). He is also experienced in X-ray diffraction, photoluminescence, Hall effect, secondary electron microscopy, laser diode fabrication, and atomic force microscopy.

Mikella E. Farrell (nee Hankus) is a research chemist in SEDD at ARL. Research work has included developing surface enhanced Raman scattering (SERS) substrates for Army biological and hazard sensing, biomimetic hazard sensing employing designed peptides, a nanoscale SERS imaging probe, and transitioning a standardized technique for the fabrication of inkjet printed explosive hazard test coupons. She also has also supporting DARPA SERS Fundamentals programs, several university SERS-based research programs, and the evaluation of numerous fielded standoff hazard detection systems. She holds a U.S. patent and has authored over 30 research papers in journals, proceedings and internal Army reports.

Viktor Fromzel has over 30 years of experience in the field of lasers, optics and optoelectronics with his major contributions in the field via academic, industrial and military laser development. His major industrial development of solid-state and fiber lasers originated at Oriel, SES, Inc., and Passat, Inc. He was a principal investigator for several SBIR Phase I & II projects funded by DoD (AF) and NIH. He has authored over 150 scientific publications, and one book on lasers. Since 2010 Dr. Fromzel is a member of the Advanced Solid State Lasers Team, Laser Directed Energy and Protection Branch, Electro-Optics & Photonics Division at the Army Research Laboratory. He works on developing of new concepts and architectures of efficient high energy solid-state and fiber lasers and new laser materials. He has extensive research and development experience in various types of advanced diode-pumped solid state lasers: bulk and fiber, tunable, single-mode, including injection seeded, ultra-short-pulsed, Q-switched, and CW-operated. He has an in-depth knowledge of various laser applications, including lidars, ladars, mass-spectrometry, medicine, biology, military and communication systems, electro-optical instrumentation, and scientific research. He has extensive experience in laser-related modeling: laser parameters, resonators, and nonlinear optic devices.

Jennifer Gottfried received a B.S. in Chemistry (with minors in Physics and Math) from Ohio Northern University in May 2000, a M.S. in Physical Chemistry from the University of Chicago in August 2001, and a Ph.D. in Physical Chemistry from the University of Chicago in August 2005. Dr. Gottfried received numerous fellowships and awards for excellence in academics and research, including the Ohio Northern Recognition Medal (for highest GPA), 2000; Freud Fellowship, 2000; James Franck Fellowship, 2000; National Science Foundation Graduate Fellowship, 2000-2003; and the William Rainey Harper Dissertation Fellowship, 2004-2005. She joined ARL in September 2005 as a postdoctoral fellow and was hired in May 2008. In 2009 Dr. Gottfried was the Gold medal winner for Rookie Employee of the Year - Technical Scientific and Program Support (Excellence in Federal Career Award, Baltimore Federal Executive Board). She was a co-recipient of a 2009 Research and Development Award for "Stand-off Detection of Explosives," co-investigator on one of the top three FY07 ARL Director's Research Initiative (DRI) projects (FY07-WMR-04, "Tailored Ultrafast Pulses for Selective Energetic Residue Sampling"), and principal investigator for one of the top four FY09 DRI projects (FY09-WMR-03, "Investigation of Chemical Processes Involving Laser-Generated Nanoenergetic Materials"). Dr. Gottfried has written two book chapters and has 34 peer-reviewed papers, including four invited reviews and three featured cover articles. She has also published 40 ARL technical reports. She has been an invited speaker at three international conferences, presented her work in more than 60 scientific conference presentations, and taught a short course on chemometric analysis at an international conference. Dr. Gottfried's work is focused on laser spectroscopy of energetic materials for laboratory-scale characterization, model validation, and fundamental understanding of reaction mechanisms during explosive initiation.

Ellen L. Holthoff (nee Shughart) received a B.S. in chemistry from Lebanon Valley College in 2002, and a Ph.D. in chemistry from the University at Buffalo, State University of New York, in 2007. She worked as an Oak Ridge Associated Universities Postdoctoral Fellow at ARL for nearly 2 years before becoming an employee in 2009. Dr. Holthoff works in the Sensors and Electron Devices Directorate where her experimental work includes the development of microelectromechanical systems (MEMS)-scale photoacoustic sensor platforms for gas detection, molecularly imprinted polymers for chemical and biological sensing applications, and drop-on-demand inkjet printing for sample standardization. Other research interests include sol gel chemistry and fluorescence spectroscopy. She has authored and co-authored over 30 research papers and conference proceedings as well as three book chapters and numerous internal Army reports. Most recently, she co-edited a book entitled "Laser Based Optical Detection of Explosives" (CRC Press, March 2015). In recognition of her research in chemical sensing platforms for threat sensing applications, Dr. Holthoff received the 2010 Army Research and Development Achievement Award (RDA) and the 2015 Sensors best paper award.

John W. Little is a Research Scientist for the Energy and Power Division of the US Army Research Laboratory. His research interest are focused on semiconductor electro-optic devices, infrared detectors, and, currently, photovoltaic devices. He received his Ph.D. from the University of Tennessee, Knoxville in 1982, and spent a year at Oak Ridge National Laboratory as a Post-Doctoral Fellow. He was at Martin Marietta's Corporate Research Laboratory for 10 years and was awarded Corporate Inventor of the Year for the development of a new type of quantum well infrared detector. He has been at his current position at ARL since 1996 and received the Department of the Army Research and Development Achievement Award for Technical Excellence in 2006.

Yongle Pan received the B.S., M.S., and Ph.D. degree in in Laser Physics and Optics from East China Normal University, was an associate professor at Fudan University, then a senior research scientist (full research professor) at Yale University before joined the Army Research Laboratory (ARL) in 2009. He is a research physicist and also a Fellow of ARL in Adelphi Research Center. His research focus in the field of aerosol detection and characterization, high-resolution laser spectroscopy, and optical properties of micro-cavities. He has been developing innovative real-time, in-situ point-detection methods for detecting, discriminating, and identifying chemical and biological aerosols from various complicate atmospheric environments. He has published over 90 peer-reviewed journal articles, three book chapters and received 8 U.S. patents. His publications have been cited more than 2,000 times in open literatures, accomplished more than 20 scientific research projects as a principal investigator (PI) and Co-

PI, with support from DTRA, DARPA, JPEO-CBD, JSTO-CBD, DHS, DOE, and ARL. He is a member of the American Association of Aerosol Research (AAAR) and the Optical Society of America (OSA).

Qudsia Quraishi received her PhD from the University of Colorado working at JILA and the Time and Frequency Division at the National Institute of Standards and Technology (NIST), Boulder, CO. She was selected for an Intelligence Community (IC) Postdoctoral Fellowship at the Joint Quantum Institute, Univ. of Maryland, to work on quantum information with trapped ions. She was an ARL National Research Council (NRC) Postdoctoral Fellow working on neutral-atom quantum control. Currently, she is the Team Leader for the Quantum Sciences Group, Adelphi, MD. Her work focuses on investigating quantum memories based on neutral atoms and ions capable of generating, storing and processing entangled quantum information. The aim is to develop an entangled quantum network of quantum memories connected through fiber and free-space. This work involves developing modular components needed for remote entanglement between quantum memories, including quantum frequency conversion, high efficiency photon retrieval/detection and chip-based integrated photon interference. She has received the APS Women's Physicist of the Month Award, is the Guest Editor of a Special Issue on Trapped Ion Quantum Information Processing, member of the CLEO sub-committee on Quantum Science, Engineering and Technology and organizing committee for the first Workshop on Quantum Repeaters and Networks.

Kimberly A. Sablon received her Ph.D. degree in Microelectronics-Photonics from the University of Arkansas, Fayetteville AR in 2009. After graduating from the University of Arkansas, Dr. Sablon worked at the Army Research Laboratory (ARL) as an Oak Ridge Associated University (ORAU) post-doctoral fellow and was later hired as a Research Physicist. Dr. Sablon has published over 30 papers in refereed journals, including high rank journals such as NanoLetters, Applied Physics Letters, and NanoEnergy. Dr. Sablon's current interests are in the area of growth and characterization of III-V semiconductor heterostructures, low dimensional semiconductor nanostructures and 2D materials. She is currently leading the photovoltaic program at the Army Research Laboratory with emphasis on bandgap engineering, optical and transport properties in nano-structured systems for alternative energy and sensing applications.

Brian M. Sadler received the B.S. and M.S. degrees from the University of Maryland, College Park,MD, USA, and the Ph.D. degree from the University of Virginia, Charlottesville, VA, USA, all in electrical engineering. He is a Fellow of the Army Research Laboratory (ARL) in Adelphi, MD, USA. His research interests include information science, networked and autonomous systems, sensing, and mixed-signal integrated circuit architectures. Dr. Sadler is an associate editor for IEEE TRANSACTIONS ON SIGNAL PROCESSING and EURASIP Signal Processing, was an associate editor for IEEE SIGNAL PROCESSING LETTERS, and has been a guest editor for several journals including IEEE JSTSP, IEEE JSAC, the IEEE SP Magazine, and the International Journal of Robotics Research. He is a member of the IEEE Signal Processing Society Sensor Array and Multi-channel Technical Committee and Co-Chair of the IEEE Robotics and Automation Society Technical Committee on Networked Robotics. He received Best Paper Awards from the Signal Processing Society in 2006 and 2010. He has received several ARL and Army R&D awards, as well as a 2008 Outstanding Invention of the Year Award from the University of Maryland.

Anand Sampath is an engineer in the Electro-optics and Photonics Division in the Sensor and Electron Devices Directorate at the US Army Research Laboratory. His research interests include the development of III-Nitride semiconductor materials and optoelectronics devices include avalanche photodetectors, light emitting diodes and laser diodes. He has significant expertise in the growth of III-Nitride semiconductors by plasma-assisted molecular beam epitaxy and the characterization of these materials by Hall Effect and X-ray diffraction. He has authored or co-authored over 80 technical publications or presentations and has 5 patents granted by the United States Patent and Trademark Office. He has received the Department of the Army Research and Development achievement award in 2005 and 2013 as well as the ARL Award for Science.

Dimitra N. Stratis-Cullum received her B.S. degree in chemistry from Marist College, NY 1996 and her Ph.D. in Chemistry from the University of South Carolina in 2000. Prior to joining ARL in 2002, she was a postdoctoral fellowship at U.S. Department of Energy Oak Ridge National Laboratory, TN. Currently leads the biomaterials team at the U.S. Army Research laboratory (ARL). Dimitra Stratis-Cullum's primary research interests relate to improving the fundamental understanding of biomolecular interactions and developing genetically engineered peptides for biological-threat sensing and hybrid material integration. Her interdisciplinary research focuses on developing new tools for understanding the biomolecular peptide recognition and biomaterials discovery. She has 19 years of experience as an analytical chemist including 15 years on enabling technologies for chemical and biological detection with emphasis on novel transduction and synthetic molecular recognition technologies (e.g., peptides). Her scientific advances are evidenced by over 100 publications and several invention disclosures. These publications have been favorably cited over 1350 times. In recognition of her fundamental and applied research in synthetic recognition materials for threat sensing applications, Dr. Stratis-Cullum received the 2012 Army Research and Development Achievement Award (RDA), the 2014 ARL Honorary Award for Science, and the 2015 Sensors best paper award.

Jason Sun is a Physicist at US Army Research Lab, Adelphi, MD. He has experiences in a wide range of optoelectronic and RF device physics and fabrication. He conducted research and development on tunable RF capacitor design and characterization, silicon uncooled micro bolometer FPAs and thermal electric cooler design and fabrication. He developed and patented a vertical structure barium strontium titanate (BST) capacitor, both tunability and break down voltage of the capacitor reached record high. He has many year experiences in research on conventional and high-Tc superconductors and expertise in high-critical temperature (Tc) superconductor epitaxial thin film growth and characterizations. His technical contributions to this area include (1) created a world record of highest critical temperature of superconductors; (2) optimized a process of depositing YBCO thin film on metal tapes; (3) Designed, installed and test 10-meter YBCO tape production line, that was the first YBCO tape production line in US. He and his group have been funded by Navy, Oak Ridge Nation Lab, and several private investment companies. In 2007, he has joined ARL and worked on QWIP project. His current research focuses on QWIP FPA design and fabrication. He advanced two inductively coupled plasma (ICP) etching processes (selective and non-selective) to fabricate C-QWIP and R-QWIP FPAs. The selective etching process has a nearly infinite selectivity for etching GaAs substrate over AlGaAs stop etching layer and been used to remove GaAs substrates of devices successfully. He got an Exceptional Achievement Award from NASA in 2013. He hold five US patents and has published in excess of 60 research papers.

Nikolay Ter-Gabrielyan received his PhD in laser physics from the Institute for Radioengineering and Electronics at Russian Academy of Sciences where he studied Random Lasers. Prior to joining ARL, he worked at Fibertek, Inc. on developing diode pumped MOPA systems for DEW and at Ball Aerospace & Technologies Corp. working on modeling beam propagation through turbulent atmosphere, on LIDAR simulations and on precision interferometry for various Space missions. At ARL Dr. Ter-Gabrielyan, is developing advanced pulsed and CW lasers. He has authored over 50 papers in refereed journals and proceedings on solid-state lasers and materials. For his contribution to the eye-safe HPL development in 2007 he received the Army Research and Development Achievement Award.

Michael Wraback received his Ph.D. in physics from Brown University. During his tenure at ARL, he has used optical techniques to investigate coherent and incoherent excitonic optical nonlinearities and nonequilibrium electron and phonon dynamics and transport in semiconductor heterostructures and optoelectronic devices. He has also presided over research and development of semiconductor ultraviolet and visible light sources and detectors, and optical generation and detection of terahertz radiation. He has authored or coauthored more than 200 papers and presentations addressing the physics of semiconductor materials and devices and holds 13 U.S. patents. He has received the ARL Award for Scientific Achievement in 2005, and Department of the Army Research and Development Achievement Awards in 1994, 1997, 2002, 2005, 2009, and 2013. Dr. Wraback is a Fellow of the American Physical Society, the Optical Society of America, and the Army Research Laboratory, and is currently the Chief Scientist of the Sensors and Electron Devices Directorate at ARL.

U.S. ARMY

U.S. ARMY RDECOM®